Titre: Title:	The Diffusion Bubble Model: A Spectrum-Based Diffusion MRI Framework for Neonatal Brain Segmentation, Developmental Assessment, and Injury Characterization
Auteur: Author:	Erjun Zhang
Date:	2025
Type:	Mémoire ou thèse / Dissertation or Thesis
Référence: Citation:	Zhang, E. (2025). The Diffusion Bubble Model: A Spectrum-Based Diffusion MRI Framework for Neonatal Brain Segmentation, Developmental Assessment, and Injury Characterization [Thèse de doctorat, Polytechnique Montréal]. PolyPublie. https://publications.polymtl.ca/67796/

POLYTECHNIQUE MONTRÉAL
affiliée à l'Université de Montréal

The Diffusion Bubble Model: A Spectrum-Based Diffusion MRI Framework for Neonatal Brain Segmentation, Developmental Assessment, and Injury Characterization

ERJUN ZHANG
Institut de génie biomédical

Thèse présentée en vue de l'obtention du diplôme de *Philosophiæ Doctor*

Génie biomédical

Septembre 2025

POLYTECHNIQUE MONTRÉAL
affiliée à l'Université de Montréal

Cette thèse intitulée :

The Diffusion Bubble Model: A Spectrum-Based Diffusion MRI Framework for Neonatal Brain Segmentation, Developmental Assessment, and Injury Characterization

présentée par **Erjun ZHANG**
en vue de l'obtention du diplôme de *Philosophiæ Doctor*
a été dûment acceptée par le jury d'examen constitué de :

Jean PROVOST, président
Benjamin DE LEENER, membre et directeur de recherche
Gregory LODYGENSKY, membre et codirecteur de recherche
Samuel KADOURY, membre
Matthew D. BUDDE, membre externe

DEDICATION

To my family, with love

乡愁，是一次次的视频通话
我在这头，家在那头

Le mal du pays, scandé par nos appels vidéo
moi ici, la maison de l'autre côté de l'écran

Homesickness, the rhythm of our video calls
me here, home across the screen

ACKNOWLEDGEMENTS

I would like to sincerely thank the jury president, Professor Jean Provost, the jury members, Professor Samuel Kadoury—who also chaired my PhD qualifying exam—and Professor Matthew D. Budde (External Member, Medical College of Wisconsin), and my supervisors, Professor Benjamin De Leener and Professor Gregory Lodygensky, for their expert evaluations and thoughtful feedback on my dissertation and defense.

I also thank Professor Christine Tardif for serving as external examiner on my PhD qualifying exam committee and for her expert comments and guidance.

I am deeply grateful to Professor Xin Liu, who encouraged me to pursue a PhD and generously opened the door to my doctoral studies. I extend my heartfelt thanks to Professors Feijun Song, Kuanxin Yu, and Jian Wu for their support and for writing recommendation letters that made this journey possible. I am also grateful to Professor Maksim Skorobogatiy for welcoming me to his laboratory for a year, an experience that, while challenging at times, proved profoundly instructive. My deepest appreciation goes to my supervisors, Professor Benjamin De Leener and Professor Gregory Lodygensky, for their guidance, mentorship, encouragement, trust, and unwavering support throughout this entire journey—without whom I could not have completed my PhD.

This thesis benefited greatly from insightful discussions on deep learning with Jiaqi Li, Andjela Dimitrijevic, and Farzad Beizaee, which were instrumental to the segmentation chapter. I warmly thank Kylie Xu, Sara Hernandez, Hanna Ton That, Josephine Emadoye, Hoi Ching Wat, Feodor Gornostayev, and Keiara Baker for their meticulous efforts in identifying and delineating punctate white matter lesions, without whom the PWML-related chapter would not exist. I am also grateful to research nurses—Karine Fondrouge, Karine Marcotte, Muriel Marie, and Kate St-Arneault—and MRI technologists at CHU Sainte-Justine (CHUSJ), and to members of Dr. Lodygensky's lab—Alexandra Verreault, Océane-Rose Leloutre-Salat and Ophélia Dalkiriadis—for participant recruitment, demographic curation, and image acquisition in the preterm and term cohorts. I also thank Samuelle St-Onge for her support with dMRI data processing. I further thank Professor Anne Gallagher and Professor Elana Pinchefsky, investigators in the Prémasucré project, for their contributions and support, and Natacha Paquette, Janie Damien, and Laurence Petitpas for their assistance with the preterm study. I am profoundly grateful to the participating infants and their families in the preterm study for their time, trust, and generosity.

My thanks to Professor Sheng-Kwei Song and Professor Peng Sun at Washington University

in St. Louis for their inspiration and guidance on dMRI (DBSI) concepts and sequence parameterization. I also thank Sylvain Deschênes, Daniel Papp, and Vicente Enguix for their expertise in MRI setup and scanning for the preterm brain development project. I also thank Irene Londono, Jérémie Fouquet, and Mila Urosevic for their helpful discussions and assistance in animal handling, phantom preparation, MRI scanning during the model-development phase and the ex vivo MRI study.

The projects in this dissertation were conducted at Lodygensky's lab (CHUSJ), the MAGIC Lab (TransMedTech Institute, CHUSJ), and NeuroPoly at Polytechnique Montréal (PolyMTL). The neonatal MRI data from the Developing Human Connectome Project (dHCP) used in this thesis were kindly shared by the dHCP consortium. I am grateful for financial support from the China Scholarship Council–UdeM Joint Scholarship, and I also thank my two supervisors for their financial support. I further thank Camélia Dadouchi, Representative of the Graduate Studies Office at my defense, for her support throughout the defense process, and Amal Bennani, Graduate Student Records Officer of Institute of Biomedical Engineering (PolyMTL), for her kind and invaluable assistance with student affairs throughout my PhD.

To my family: your support, trust, patience, and unconditional acceptance have been the bedrock of my resilience. You gave me the courage, confidence, and strength to keep going.

To my friends, classmates, and lab members—named and unnamed—thank you for your companionship. Walking this path together made the journey far less solitary; I feel fortunate to have shared it with you.

On a personal note, my PhD often felt like an expedition. For years, I'd heard rumors from graduates about a groundhog with a regal bearing living beneath the blue-gray rocks outside the mathematics library, reputed to have its own "throne". Only recently did I finally see it—an impressively large groundhog, seated like a king on a jutting rock ledge and gazing into the distance, with a brown rabbit as a neighbor—and, in that moment, the stories made sense. That sight felt like a light-hearted sign that the journey was nearing its end.

RÉSUMÉ

La naissance prématurée (≈ 10% des naissances vivantes) expose le cerveau néonatal à un risque élevé de lésions et de handicaps à long terme, soulignant la nécessité urgente de biomarqueurs microstructuraux à la fois biologiquement spécifiques et cliniquement applicables. L'imagerie par résonance magnétique de diffusion (IRMd) se prête bien à cette tâche ; toutefois, les modèles tensoriels classiques confondent divers processus en quelques moyennes globales, tandis que de nombreuses approches basées sur le spectre nécessitent des acquisitions longues et sensibles au mouvement, peu adaptées aux soins néonatals.

Cette thèse introduit le Diffusion Bubble Model (DBM), un cadre d'analyse fondé sur le spectre qui reconstruit le spectre de diffusivité isotropique et fournit des métriques compactes et interprétables allant au-delà des moyennes tensorielles. Le DBM minimise la dépendance à l'orientation et localise les variations le long de l'axe de diffusivité, en distinguant les fluctuations de la composante à diffusion rapide de celles du pic dominé par les tissus. Validé par simulations et in vivo auprès de 248 nouveau-nés (prématurés modérés à tardifs jusqu'à 43 semaines d'âge post-menstruel), le DBM montre une forte concordance avec les métriques scalaires établies tout en ajoutant une localisation spectrale révélant des signatures tissulaires spécifiques et des évolutions dépendantes de l'âge.

Pour permettre son déploiement lorsque les images structurelles sont absentes ou inutilisables, le DBM est associé à un réseau de segmentation nnU-Net fondé uniquement sur la diffusion, constituant une chaîne de traitement d'IRMd complète et native. Ce modèle, de diffusion seule, atteint une excellente précision interne et une meilleure généralisation inter-sites que les modèles fondés sur les images pondérées en T2, permettant d'inclure 14 sur 88 (16.0%) nourrissons dépourvus de T2w utilisable dans les analyses ultérieures et favorisant des études à grande échelle harmonisées.

Deux applications illustrent sa valeur biologique et clinique. Pour l'évaluation du développement, les trajectoires de maturation des prématurés et des nouveau-nés à terme sont globalement parallèles mais décalées dans le temps, indiquant un début de maturation retardé avec une immaturité résiduelle concentrée dans les voies frontales et temporales à l'âge équivalent au terme, malgré une croissance volumétrique compensée. Pour la caractérisation des lésions, le DBM distingue deux phénotypes de lésions ponctuées de la substance blanche : l'un dominé par l'œdème (« humide »), l'autre par la réorganisation tissulaire (« sèche »), qui paraissent similaires en IRM structurelle et sur les tenseurs, mais diffèrent par leurs signatures spectrales, offrant ainsi une spécificité mécaniste utile pour le suivi et le pronostic.

En conclusion, ce travail établit le DBM comme une approche pratique et biologiquement

interprétable, allant au-delà des moyennes scalaires pour révéler où la maturation et la pathologie se manifestent au sein du spectre de diffusivité, faisant progresser la segmentation, l'évaluation développementale et la caractérisation des lésions par IRMd néonatale.

Mots-clés: Diffusion Bubble Model; IRM de diffusion; modélisation fondée sur le spectre; segmentation par diffusion seule; développement cérébral néonatal; lésions ponctuées de la substance blanche; caractérisation des lésions.

ABSTRACT

Preterm birth ($\approx 10\%$ of live births) exposes the neonatal brain to a high risk of injury and long-term disability, creating an urgent need for microstructural biomarkers that are both biologically specific and clinically feasible. Diffusion magnetic resonance imaging (dMRI) is well suited to this task, yet conventional tensor models conflate diverse processes into a few averages, whereas many spectrum-based approaches require lengthy, motion-sensitive scans that are impractical in neonatal care.

This dissertation introduces the Diffusion Bubble Model (DBM), a spectrum-based framework that reconstructs the isotropic diffusion spectrum and yields compact, interpretable metrics beyond tensor averages. DBM minimizes orientation dependence and localizes change along the diffusion axis, distinguishing fast water tail fluctuations from shifts of the tissue-dominated peak. Validated in simulations and in vivo across 248 neonates (moderate-late preterm to 43 weeks postmenstrual age), DBM aligns closely with established scalar metrics while adding spectral localization that reveals tissue-specific fingerprints and age-dependent shifts.

To enable deployment when structural MRI is missing or unusable, DBM is paired with a diffusion-only nnU-Net, delivering an end-to-end, dMRI-native workflow. The diffusion-only model achieves strong internal accuracy and more stable cross-site generalization than T2-weighted baselines, enabling inclusion of 14/88 (16.0%) infants without usable T2w in downstream analyses and supporting large-scale, harmonized studies.

Two applications demonstrate biological and clinical utility. For developmental assessment, preterm and term trajectories are broadly parallel but time-shifted, indicating a delayed onset of maturation with residual immaturity concentrated in frontal and temporal pathways at term-equivalent age despite volumetric catch-up. For injury characterization, DBM separates punctate white matter lesions into edema-dominant ("wet") and reorganization-dominant ("dry") phenotypes that appear similar on tensors and structural MRI, providing mechanistic specificity relevant to monitoring and prognosis.

In conclusion, this work establishes DBM as a practical, biomedically interpretable approach that moves beyond scalar averages to reveal where maturation and pathology manifest within the diffusivity spectrum, advancing diffusion-based segmentation, developmental assessment, and injury characterization in neonatal dMRI.

Keywords: Diffusion Bubble Model; diffusion MRI; spectrum-based modeling; diffusion-only segmentation; neonatal brain development; punctate white matter lesions; injury characterization.

TABLE OF CONTENTS

LIST OF TABLES

LIST OF FIGURES

LIST OF SYMBOLS AND ACRONYMS

AD	Axial diffusivity (principal eigenvalue of DTI tensor)
ADC	Apparent Diffusion Coefficient
ALIC	Anterior Limb of the Internal Capsule
AK	Axial Kurtosis (from DKI)
β	Regression slope / model coefficient (in this thesis)
b	strength of diffusion-sensitizing gradients
CC	Corpus Callosum
CHUSJ	CHU Sainte-Justine Hospital
CHARMED	Composite hindered and restricted model of diffusion, a dMRI model
CSD	Constrained Spherical Deconvolution
CST	Corticospinal Tract
DBM	Diffusion Bubble Model
DBSI	Diffusion Basis Spectrum Imaging
dHCP	Developing Human Connectome Project
DKI	Diffusion Kurtosis Imaging
dMRI	Diffusion Magnetic Resonance Imaging
DWI	diffusion-weighted imaging
DTI	Diffusion Tensor Imaging
DSI	Diffusion Spectrum Imaging
EC	External Capsule
FA	Fractional Anisotropy
FBA	Fixel-Based Analysis (fibre-specific dMRI)
FC	Fibre Cross-section (fixel metric; macrostructural)
FDC	Combined Fibre Density and Cross-section (fixel metric)
FD	Fibre Density (fixel metric; microstructural)
FWE	Free-Water Elimination (dMRI model)
GA	Gestational Age
GBSS	Gray-Matter-Based Spatial Statistics
GMM	Gaussian Mixture Model (for dMRI signal; e.g., RTOP/RTAP)
GM	Gray Matter
ILF	Inferior Longitudinal Fasciculus
LOA	Limits of agreement
MD	Mean Diffusivity: MD or $\mathrm{MD}_{\mathrm{DTI}}$ for DTI, $\mathrm{MD}_{\mathrm{DBM}}$ for DBM

MK	Mean Kurtosis (from DKI)
MRI	Magnetic Resonance Imaging
MSMT-CSD	Multi-Shell Multi-Tissue CSD
MSN	Morphometric Similarity Network
μFA	micro–Fractional Anisotropy (from SMT/SMSI)
NODDI	Neurite Orientation Dispersion and Density Imaging
NDI	Neurite Density Index (from NODDI)
ODF	Orientation Distribution Function
OR	Optic Radiation
PMA	Postmenstrual Age
PLIC	Posterior Limb of the Internal Capsule
PT-34W	Preterm-born Infants (scanned) at age of 34 gestational weeks
PT-TEA	Preterm-born Infants (scanned) at Term-equivalent Age (group, cohort)
PWML	Punctate White Matter Lesion
RD	Radial Diffusivity (from DTI)
RK	Radial Kurtosis (from DKI)
ROI	Region of Interest
RTAP	Return-To-the-Axis Probability (GMM-derived)
RTOP	Return-To-the-Origin Probability (GMM-derived)
SHARD	Scattered-slice HARDI (motion-robust reconstruction)
SLF	Superior Longitudinal Fasciculus
SMSI	Spherical Mean Spectrum Imaging
SMT	Spherical Mean Technique (yields μFA)
SNR	Signal to Noise Ratio
SS3T-CSD	Single-Shell 3-Tissue CSD
T1w/T2w	T1-weighted / T2-weighted MRI sequence (or image)
TBSS	Tract-based Spatial Statistics
TC-40W	Term-born Control Infants (scanned) at age of 40 gestational weeks
TEA	Term-Equivalent Age (40 weeks GA in this thesis)
v_i	Intra-neurite volume fraction (from NODDI)
v_{iso}	Isotropic (free-water) volume fraction (from NODDI)
WK (wk)	week
WM	White Matter
WMTI	White Matter Tract Integrity model (from DKI)

LIST OF APPENDICES

CHAPTER 1 INTRODUCTION

1.1 Background

Preterm birth (gestational age, GA < 37 weeks, Fig. 1.1) complicates approximately 10% of live births worldwide (roughly 13.4 million annually) and remains a leading cause of long-term neurodevelopmental disability [1]. This challenge is also evident in Canada, where the rate of preterm birth has shown a concerning upward trend, despite a slight overall decrease in the total number of births over the past three decades (Fig. 1.2), underscoring the growing need for effective early-life biomarkers. While survival is high among moderate-to-late preterm infants ($32-37$ weeks GA), around 20% exhibit cognitive impairment and 30% have behavioral difficulties that persist into school age [2,3]. These adverse outcomes are believed to stem, in part, from disruptions in gray and white matter maturation during the critical third trimester—a period marked by rapid axonal organization, accelerating myelination, and significant shifts in extracellular water content [4].

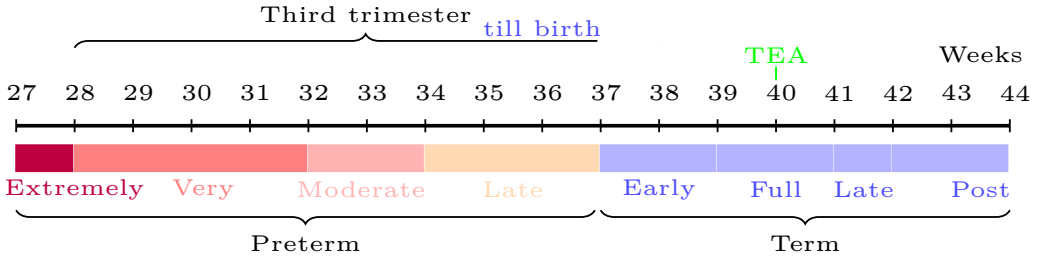

Figure 1.1 Timeline of neonatal age terms used in this thesis. Horizontal axis shows gestational age (GA) and post-menstrual age (PMA) in weeks before and after birth. Shaded bands mark commonly used ranges; the third trimester spans from 28 week GA till birth age. Term-equivalent age (TEA) is ≈ 40 week PMA.

Punctate white matter lesions (PWML) are the most common focal injuries observed on neonatal magnetic resonance imaging (MRI) [5]. Although typically small ($< 5\,\text{mm}$) and often clinically silent in the nursery, PWMLs have been associated with later motor delay and network-level functional alterations [6, 7]. Histopathology and advanced MRI indicate heterogeneous substrates for punctate white matter lesions—including microscopic hemorrhage, gliosis, and oligodendroglial dysmaturation [8]. This underlying biological heterogeneity is mirrored by its variable appearance on conventional MRI, as illustrated in Fig. 1.3. For example, a single PWML can present with a distinct "exclamation-mark" shape on T1-weighted imaging, appear fragmented on T2-weighted imaging, and manifest as only a focal

abnormality on mean diffusivity maps. This underlying heterogeneity complicates prognostic assessment when relying solely on conventional structural imaging, motivating the search for tissue-specific diffusion biomarkers that can capture both global maturation and subtle focal injury at term-equivalent age (TEA, ≈40 wk postmenstrual age, PMA).

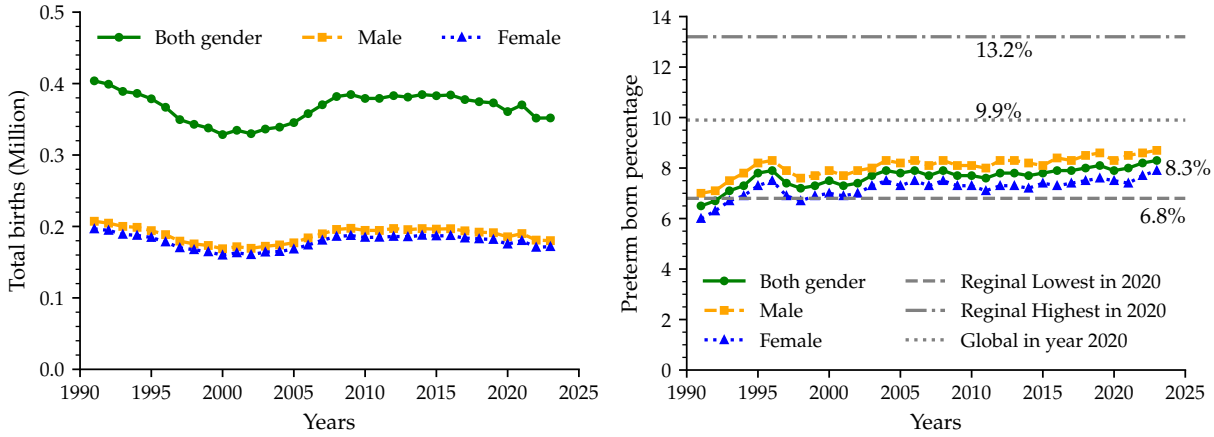

(a) Total births in Canada

(b) Preterm birth rate in Canada

Figure 1.2 Total births and preterm birth rate in Canada (1990–2023). Despite a slight overall decrease in the total number of births over the period (a), the rate has steadily increased, reaching 8.3% in 2023 (green line) (b). Reference lines show 2020 global benchmarks: 9.9% average (dotted gray), 13.2% highest (dot-dashed gray), and 6.8% lowest (dashed gray). Raw preterm birth rate in Canada is from Statistics Canada [link]. Global preterm birth rate in 2020 is from publication [1].

Diffusion MRI (dMRI) can probe neonatal microstructure, provided acquisition and modeling are tailored to the rapidly evolving neonatal brain [9–12]. However, many established microstructural models were developed for adult populations, relying on assumptions of long scan times, high signal-to-noise ratio (SNR), and stable tissue composition, conditions rarely met when imaging a restless newborn in a clinical 3T scanner. In addition, classic tensor metrics conflate concurrent shifts in slow and fast diffusion, limiting specificity to developmental and injury-related processes.

To address these limitations, this thesis introduces a framework that uses data that are scanned in clinical environment, a segmentation method suitable for dMRI, with proposed Diffusion Bubble Model (DBM). DBM adjusts apparent anisotropy to approximate an isotropic signal and decomposes it into a continuous diffusivity spectrum, yielding positional (e.g., quartile diffusivity) and shape (e.g., mean diffusivity) metrics. We test the hypothesis that this protocol-plus-model pipeline improves sensitivity and specificity to brain maturation and PWML-related change compared with conventional diffusion tensor imaging (DTI) at TEA.

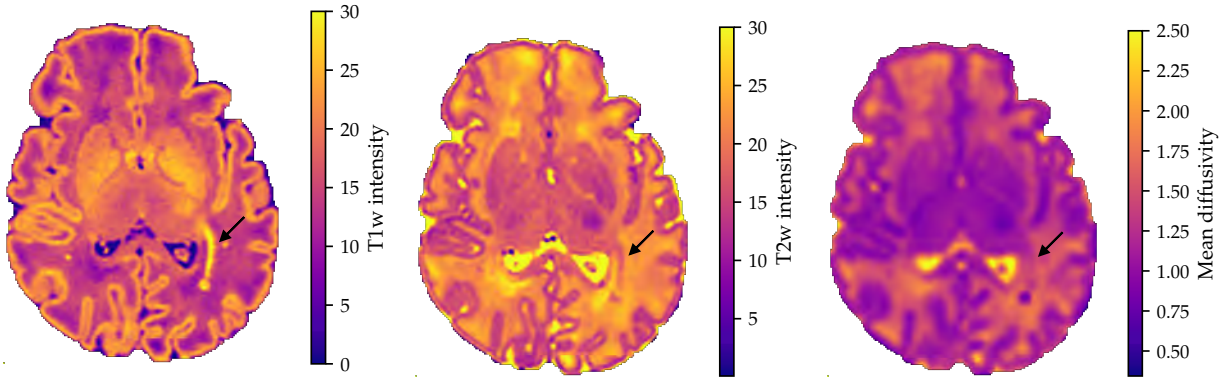

(a) PWML on T1w image (b) PWML on T2w image (c) PWML on MD map

Figure 1.3 Visualizing the challenge: heterogeneous appearance of a punctate white matter lesion (PWML) in optic radiation across conventional MRI modalities. (a) T1-weighted MRI demonstrates a hyperintense "exclamation-mark" configuration (dot+streak) along the right OR. (b) On T2-weighted MRI the lesion is less conspicuous, with a larger gap between the dot and the linear component. (c) The mean diffusivity (MD) map depicts only an enlarged dot of reduced diffusivity, missing the lesion's full structure. This variability complicates diagnosis and underscores the need for more consistent biomarkers. Figure generated from our PWML cohort and created by author.

1.2 Research Framework

1.2.1 Research objective

The overall objective is to develop and validate a clinically feasible diffusion MRI framework to characterize neonatal brain maturation and injury in preterm and term infants. Specifically, we aim to:

1. *Model development*: Develop and validate a spectrum-based diffusion MRI model to characterize neonatal brain tissue and microstructures.

2. *Segmentation framework*: Develop and validate a dMRI-driven segmentation pipeline for neonatal brain structures when structural MRI data is unavailable for segmentation.

3. *Developmental application*: Apply DBM and segmentation developed to quantify regional maturation trajectories from late-preterm to term-equivalent age.

4. *Lesion application*: Apply DBM proposed to characterize PWML microstructure by comparing lesion, contralateral, and term-control and evaluate spectrum reshaping.

1.2.2 Research questions

Technical Questions

1. Can a spectrum-based diffusion model (DBM) provide added specificity beyond DTI by localizing changes along the diffusivity axis using positional and shape metrics (e.g., quartile diffusivities $D_{25,50,75}$, spectral moments $\mathrm{MD}_{\mathrm{DBM}}$, σ^2_{DBM})? (*primarily Chapter 4*)

2. Does a diffusion-only nnU-Net segmentation pipeline generalize more reliably across scanners and protocols than a T2w-based baseline, enabling robust dMRI-native region of interest (ROI) definitions for downstream quantification? (*Chapter 5*)

Clinical Questions:

1. At term equivalent age, how similar are regional and global brain microstructural measures in infants born preterm to those in term-born controls?(*Chapter 6*)

2. Do neonatal punctate white matter lesions show detectable microstructural alterations within the lesion relative to contralateral tissue and term controls? (*Chapter 7*)

1.2.3 Research hypotheses

Normal maturation and many neonatal injuries involve concurrent shifts in slow and fast diffusion that classic tensor metrics tend to conflate. DBM aims to separate these processes by estimating an isotropic diffusivity spectrum. We hypothesize that:

1. **H1 (DBM added specificity)**: Compared to DTI, DBM yields larger effect sizes and stronger age associations by localizing changes along the diffusivity axis. (*addressed primarily in Chapter 4*)

2. **H2 (Segmentation generalization)**: A diffusion-only nnU-Net exhibits smaller external-validation performance drops than a T2w-based model under vendor/protocol shift (non-inferiority in Dice and boundary metrics). (*Chapter 5*)

3. **H3 (Preterm maturation: timing vs. rate)**: From late-preterm to term-equivalent age, preterm–term differences are explained primarily by a timing shift (delayed onset) rather than persistently different rates of maturation; and DBM can capture these residuals more sensitively than DTI. (*Chapter 6*)

4. **H4 (PWML characterization)**: PWMLs perturb the fast-diffusion fraction and reshape the isotropic spectrum within the lesion, DBM can detect and characterize these changes. (*Chapter 7*)

1.3 Framework of Thesis

This thesis is structured around a central narrative of methodological innovation driving biomedical and clinical discovery (Fig. 1.4). It presents a cohesive journey that begins with the creation and rigorous validation of a novel analytical model (Chapter 3 & Chapter 4), continues with the development of an essential tool to maximize its utility (Chapter 5), and culminates in its application to resolve fundamental questions in both typical brain development and injury (Chapter 6 & Chapter 7).

To achieve the general objective of developing and validating a clinically feasible diffusion MRI framework to characterize neonatal brain maturation and injury, the thesis is organized as follows:

1. **Chapter 1** establishes the clinical and technical context and states the research questions and hypotheses.

2. **Chapter 2** reviews the relevant literature on diffusion MRI (dMRI) models, preterm versus term infant brain development, characterization of punctate white matter lesions, and strategies for segmentation of the neonatal brain.

3. **Chapter 3** introduces the proposed Diffusion Bubble Model (DBM) and the general methods used to address the four primary research goals.

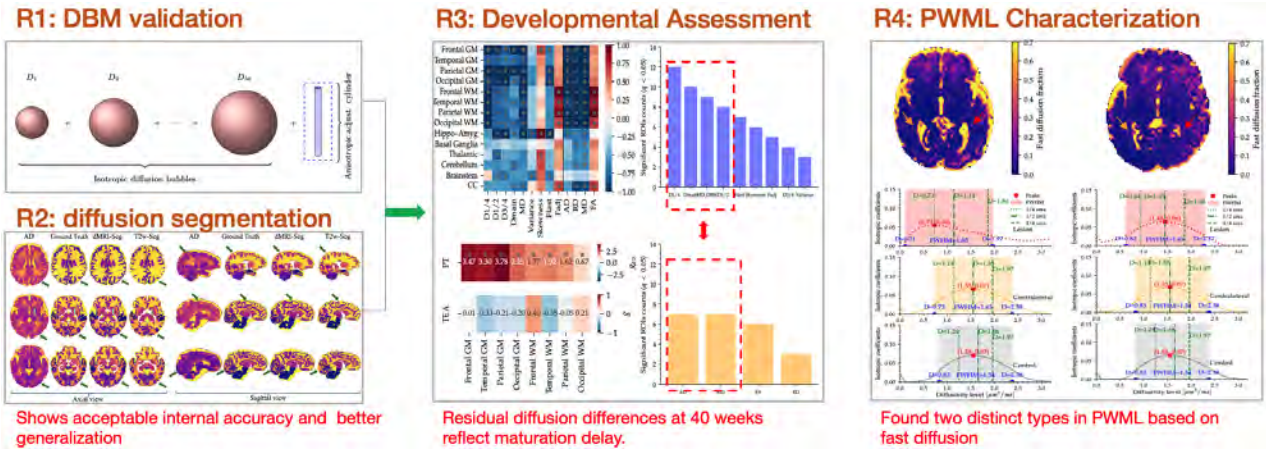

Figure 1.4 Overall logical framework of thesis result chapters. The framework begins with the creation and rigorous validation of a novel analytical model (Result 1: Chapter 4), continues with the development of an essential brain segmentation tool to maximize its utility (Result 2: Chapter 5), and culminates in DBM application to resolve fundamental questions in both typical brain development and injury (Result 3: Chapter 6, and Result 4: Chapter 7).

The logical progression of the four result chapters is as follows:

- **Chapter 4 validates the fundamental tool**. It quantitatively validates Diffusion Bubble Model we introduced, a novel spectrum-based dMRI framework designed for the specific constraints of neonatal imaging. This chapter answers the critical question: "Is the model itself reliable, robust, and capable of capturing biologically meaningful information?"

- **Chapter 5 builds an essential brain structure segmentation tool** to maximize the utility of data for this model. To deploy DBM on large-scale and clinically heterogeneous datasets, a major practical bottleneck must be overcome: the frequent absence of high-quality structural scans for tissue segmentation. This chapter develops and validates a diffusion-only deep learning-based segmentation tool, allowing the application of advanced microstructural models to a broader range of clinical data.

- **Chapter 6 resolves a core biological question**. Armed with a validated model (DBM) and a robust segmentation tool, the thesis transitions to application. This chapter investigates a central controversy in developmental neuroscience: the nature of microstructural differences in preterm infants at term age. It leverages the spectral specificity of DBM to empirically distinguish between a simple "timing shift" and a persistent "rate difference" in maturation.

- **Chapter 7 targets a specific clinical challenge**. Finally, the analytical power of DBM is focused on a common and precise form of neonatal brain injury—Punctate White Matter Lesions. This chapter goes beyond macroscopic description to provide a quantitative microstructural phenotyping of lesions, demonstrating the clinical translatability and superior sensitivity of the proposed framework.

Finally, Chapter 8 synthesizes and contextualizes the findings—positioning DBM within diffusion modeling, outlining clinical feasibility, limitations, and future directions—while Chapter 9 provides a concise summary of contributions and overarching implications.

CHAPTER 2 LITERATURE REVIEW

2.1 Introduction

Neonatal brain development is fast, heterogeneous, and clinically consequential. This review establishes the methodological and biological background for the thesis by integrating four strands: (i) diffusion MRI (dMRI) models; (ii) preterm versus term differences at term-equivalent age (TEA) from both volumetry and diffusion perspectives; (iii) punctate white-matter lesions (PWML) as focal disruptions superimposed on network-level maturation; and (iv) segmentation strategies that underpin region- and tract-level analyses.

We begin by introducing the biophysical sources of the dMRI signal and organizing models into major categories, with particular attention to spectrum-based approaches. Then we summarize the maturation patterns of the neonatal brain throughout late gestation to term-equivalent age. Next, we define punctate white matter lesions and review dMRI study on this lesion. Then, methodologically, we review traditional (manual, atlas- and model-based) and deep learning segmentation approaches, including diffusion-native pipelines that operate directly in DWI space. This context motivates the thesis strategy: a dMRI-focused pipeline and spectrum-informed modeling to characterize neonatal microstructure when structural scans are limited or unavailable.

2.2 Diffusion Magnetic Resonance Imaging Models

This thesis addresses two neonatal problems: (i) quantifying developmental differences between brain tissues and structures (e.g., preterm versus term at TEA), and (ii) characterizing how punctate white matter lesions perturb otherwise typical tissue. Overall diffusivity alone is ambiguous; both maturation and pathology can shift it in overlapping ways. A voxel-wise distribution of diffusivity (the diffusion spectrum) offers greater discriminative power by revealing changes in location, width, and tails (fast or free-water versus restricted components) [13, 14].

Most diffusion-MRI models approach this in one of two ways: they either reconstruct this distribution explicitly (e.g., diffusivity spectra or displacement propagators) or summarize it implicitly through moments or parametric surrogates (e.g., kurtosis, stretched-exponential α, diffusional variance) [13–16]. Below, we evaluate both families through a neonatal lens: weighing biological specificity against acquisition feasibility, and identify the features a spectrum method must have to serve our aims in development and PWML.

Biophysical sources and practical constraints

Brain tissue comprises multiple microstructural constituents: neuronal soma and dendrites, axons that are covered with / without myelin, glial cells, vasculature, and extracellular space [17, 18]. The axonal calibers span roughly 0.2–20 μm, and individual axons can extend from several millimeters to more than a meter in length [19]. Typical in-vivo diffusion MRI uses 1–2 mm isotropic voxels, whereas water displacements over clinically practical diffusion times ($\Delta \approx$ 30–80 ms) are on the order of only a few to $\sim 10\,\mu$m ($\approx \sqrt{2D\Delta}$ with $D \sim$ 0.7–1.0 μm^2/ms) [20–22]. This large-scale mismatch means that each voxel averages signal from an enormous number of distinct microenvironment (multiple cell types, sizes, orientations and extracellular compartments), for example, order-of-millions times the volume of a typical soma. Consequently, the measured signal is an ensemble average of diffusion processes, rather than a readout from a single structure.

These biophysical realities, coupled with practical acquisition limits: finite gradient strength and limited achievable b value and diffusion times, echo-time and signal noise ratio (SNR) constraints, motion sensitivity (especially in neonates), and Echo-planar imaging (EPI) related distortions, make direct imaging of single cellular components infeasible in routine dMRI. Modeling therefore trades biological specificity against data demand and robustness.

Aims of dMRI Modeling

A dMRI model should convert voxelwise DWI signal decays into descriptors that are (i) biologically meaningful, (ii) stable and reproducible, and (iii) practical for clinical or research use. Objectives include: (i) *Compartmental characterization*: Separate broad microstructural compartments (e.g., intra-axonal, extra-axonal, free water) and estimate their volume fractions and other diffusion properties (e.g., apparent diffusivity, exchange rates). (ii) *Orientation-resolved architecture*: Recover the shape and orientation dispersion of anisotropic structures (e.g., fiber orientation distributions, crossing fibers) and, when possible, derive tract- or fiber-specific metrics. (iii) *Non-Gaussianity and heterogeneity*: Capture deviations from mono-exponential (Gaussian) diffusion caused by restriction and hindrance, either via explicit diffusivity spectra / propagators or implicit parameters (e.g., kurtosis, stretched-exponential parameters). (iv) *Scale specificity*: Leverage contrasts that vary with the acquisition scale (e.g., b value, diffusion time or frequency, coupling to T_1 and T_2) to gain sensitivity to microstructural size and time scales without overfitting. (v) *Biomarker utility*: Provide interpretable metrics that correlate with development, disease, or treatment response and exhibit strong effect sizes, repeatability of test-retest, and robustness between scanners, protocols, and sites. (vi) *Practicality and robustness*: Remain identifiable at clinically feasible

SNRs and scan times; minimize fragile hyper-parameters; and expose uncertainty and quality control indicators to guard against implausible estimates.

We seek methods that: run at moderate b and short scans; provide information beyond DTI (e.g., distinguish fast water vs. restricted changes and capture shape shifts, narrowing, tail inflation); remain informative in low-FA tissues (cortex, deep GM); and are robust across sites with clear assumptions.

2.2.1 Diffusion MRI model categories

Diffusion-MRI methods can be organized along several axes (acquisition, reconstruction, mathematical form). Here we use a representation-centric taxonomy because it best highlights how models capture microstructural heterogeneity. We group the methods into three families (Table 2.1), noting that hybrids exist and some methods straddle categories [23, 24]. When models span families, we place them with their predominant assumption.

Table 2.1 Different category of dMRI models. Statistical model is also named signal representation model. Note: Black color: general diffusion, red color: isotropic diffusion, blue color: anisotropic diffusion.

Category: Definition	Models	
Statistical model: Empirically capture signal shape without explicit tissue assumptions	DTI [16]	$e^{-b_k \mathbf{g_k^T D g_k}}$
	Stretched-exponential [14]	$e^{-(b\times DDC)^{\alpha}}$
	DKI [15]	$e^{-b\sum_{i,j=1}^{3} D_{ij}g_ig_j+\frac{1}{6}b^2D_{\text{avg}}^2\sum_{i,j,k,l=1}^{3} W_{ijkl}g_ig_jg_kg_l}$
Multi-compartment model: Represent tissue as a small set (≤ 4) of predefined compartments	FWE [25]	$(1-f_{\text{iso}})e^{-b_k \mathbf{g_k^T D g_k}} + f_{\text{iso}}e^{-b_k D_{\text{iso}}}$
	NODDI [26]	$f_{\text{ic}}\cdot e^{-bD_{\text{ic}}(\theta\cdot\mathbf{n})^2}\cdot \text{Watson}(\kappa) + f_{\text{ec}}\cdot e^{-bD_{\text{ec}}} + f_{\text{iso}}\cdot e^{-bD_{\text{iso}}}$
	SANDI [17]	$f_{\text{neurite}}\cdot e^{-b_{\text{neurite}}} + f_{\text{soma}}\cdot\left(\frac{\sin(qa)}{qa}\right)^2 + f_{\text{ec}}\cdot e^{-bD_{\text{ec}}}$
Spectrum model: a continuum of components spanning a range of diffusivity, or ≥ 5 compart. with clear diffusion scale order)	DSI [13]	$S(q,\Delta)=\int P(\mathbf{R},\Delta)e^{-2\pi\mathbf{q}\cdot\mathbf{R}}d^3\mathbf{R}$
	DBSI [27]	$\int_a^b f(D)e^{-\lvert b_k\rvert D}dD + \sum_{i=1}^{N_{An}i} f_i e^{-\lvert\vec{b}_k\rvert\lambda_{\perp i}}e^{-\lvert b_k\rvert(\lambda_{\parallel i}-\lambda_{\perp i})\cdot\cos^2\psi_{ik}}$
	RSI [28]	$\sum_{i=1}^{M} f_{D_i}e^{-bD_i}$
	DBM [24]	$\sum_{i=1}^{M} f_{D_i}e^{-b_k \mathbf{g_k^T D_i g_k}} + \sum_{j=1}^{N} f_{D_j}e^{-b_k \mathbf{g_k^T D_j g_k}} + \epsilon_k$

1. Statistical (signal-descriptive) models empirically reproduce the diffusion-weighted imaging signal without explicit microstructural assumptions. Classic examples include DTI, the stretched-exponential model, and DKI, whose compact parameterizations (e.g. mean diffusivity, kurtosis) are simple but biologically nonspecific [14–16].

2. Discrete multi-compartment (biophysical) models represent each voxel as a weighted sum of a small set of predefined tissue pools, typically ≤ 4 (e.g., intra-axonal, extra-axonal, free water). FWE, NODDI, and SANDI fall into this category [17, 25, 26]. Their

parameters, volume fractions, and compartment-specific diffusivities, are more directly interpretable, but the fixed, low-dimensional compartment set may be overly restrictive in complex tissues [29].

3. Spectrum-based (continuous) models extend compartmentalization to either a mathematical continuum or a larger discrete set (≥ 5) ordered by diffusivity or restriction scale [24]. DSI, DBSI and RSI–and our DBM introduced later belongs here–exemplify this family [13, 27, 28]. By allowing a continuous or high-resolution spectrum, these models can accommodate intricate lesion microstructure, but they demand denser q-space sampling or invoke regularisation to stabilise fitting.

2.2.2 Explicit spectrum models

Diffusion Spectrum Imaging (DSI)

What it estimates: DSI densely samples the diffusion signal on a Cartesian grid in q-space and uses the Fourier relationship to reconstruct the ensemble average propagator (EAP, the full 3-D displacement distribution) at each voxel [30]. From the EAP, orientation information (e.g., ODFs) and distribution-shaped scalars can be derived [31–33]. The main advantage is precisely this recovery of the full 3-D diffusion spectrum or EAP (not just angular features), which helps resolve complex fiber configurations.

Why it matters for a spectrum view: It is a canonical example of an explicit distribution method: instead of summarizing in moments, DSI recovers the underlying distribution itself.

Neonatal feasibility: Classic DSI requires dense Cartesian q-space sampling (typically 102–515 gradient directions) and high b-values (6000–12000 $\mathrm{s/mm^2}$), leading to scan times $>$ 35 min, which is impossible to routine neonatal imaging [13, 34]. Several variants have been developed in the past, but their acquisition burden still limits routine clinical adoption [34–36]. Thus, it could be a conceptual benchmark but not suitable for our cohort of neonatal scans.

Diffusion Basis Spectrum Imaging (DBSI)

What it estimates: DBSI models each voxel as a linear combination of multiple anisotropic, axially symmetric tensors (for oriented axonal populations) plus a continuous set of isotropic diffusion tensors [27, 37]. It explicitly defines an isotropic diffusivity spectrum and partitions it into restricted and non-restricted components. The anisotropic part enables tractography, while the isotropic part quantifies restricted versus hindered isotropic signal fractions [27].

Why it matters for a spectrum view: DBSI's isotropic part is an explicit $f(D)$ estimate. To our knowledge, DBSI explicitly estimated and plotted the isotropic diffusion spectrum (the voxelwise $f(D)$ "spectrum curve") and showed differences between injury and control [27]. However, most studies summarize spectrum information using threshold bands (e.g., "restricted" versus "non-restricted"), which is practical but introduces cut-point variability across studies. In practice, many reports use $0.3\,\mu m^2/ms$ to separate "restricted" from "non-restricted" [38], but other thresholds also appear in the literature, complicating standardization (e.g., boundaries near $0.10\,\mu m^2/ms$) [38–40]. In addition, DBSI first estimates multiple anisotropic tensors and then subtracts their contribution to recover the isotropic part [27]; inaccuracies or model mismatch in those initial tensor fits can propagate and destabilize the isotropic spectrum [41].

Neonatal feasibility: DBSI has been demonstrated with compact, 99-direction and 25-direction schemes in coherent white matter tracts (e.g., optic nerve), with histologic validation [37]; this clinical implementation is sometimes referred to as neuro-inflammation imaging [42]. Broader use of the whole brain for neonatal use is currently limited by software availability and threshold conventions.

DBSI has been used to detect and distinguish axonal injury, demyelination, and inflammation in multiple sclerosis animals and patients [38,43]; to characterize spinal cord compression [44]; and as an adjunct to the evaluation and progression evaluation of brain tumors [41]. But most of the applications were limited to the related labs [23], and also the reliance on thresholding has to be decided.

Restriction Spectrum Imaging (RSI)

What it estimates: RSI was introduced as a multi-scale framework with oriented response functions whose axial diffusivity is fixed while radial diffusivity varies across a continuum of restriction scales (spectrum), and report rotation-invariant metrics [25]. Recent RSI applications used a small and fixed set of compartments (≤ 5) and required a collapse of all measurements within the same b-shell into an averaged value before fitting, which removes direction-specific signals and limits the spatial resolution of the spectrum [28, 45].

Why it matters for a spectrum view: RSI's roots are continuum-based; in practice, its compact implementations act like semi-continuous/implicit spectrum surrogates that distinguish restricted versus hindered pools without plotting an explicit $f(D)$. We listed this model as a spectrum model; In addition to its original continuous diffusion map, in their recent publication, the RSI with 5 compartments also showed the left shift restriction phenomenon [28].

Neonatal feasibility: RSI is strong in tissues with low anisotropy (cortex, deep GM) and has been implemented at moderate b values [46, 47], making it attractive for developmental applications and conditions where FA is modest; large cohorts have reported age-related effects using its metric maps [46, 47]. However, many clinical implementations, especially in oncology and prostate magnetic resonance imaging, are based on relatively high values of b values (often $b \geq 3000\,\mathrm{s/mm^2}$ and up to 4000–6000 $\mathrm{s/mm^2}$) to improve the contrast between restricted units [48–50]. This trade-off (higher b for specificity versus SNR and scan-time limits) is an important consideration for neonatal imaging.

2.2.3 Implicit spectrum models

Stretched-Exponential Model (SEM)

What it summarizes: SEM models the diffusion-weighted signal as $S(b) = S_0 e^{-(bDDC)^{\alpha}}$ [14]. DDC is the distributed diffusion coefficient and $0 < \alpha \leq 1$ is a heterogeneity index that summarizes the breadth of intravoxel diffusion rates. Lower α refers to broader heterogeneity [14, 51, 52]. This is an implicit spectrum, which is mathematically equivalent to a continuous superposition of monoexponentials without reconstructing $f(D)$ explicitly [14,51].

Why it matters for a spectrum view: SEM gives voxel-wise heterogeneity α and central tendency DDC, so diffusion shift, broadening or narrowing with development and lesions can be tracked, even in low-FA tissue.

Neonatal feasibility: Works with multi-b data at moderate b (often $\leq 2000 - 3000\,\mathrm{s/mm^2}$) [14, 53–55]; direction-light and robust in cortex and deep GM [52–56]. Manage high-b SNR when pushing beyond clinical b values [53].

Statistical model for diffusion-attenuated MR signal

What it summarizes: The signal is a superposition of exponentials with a continuous diffusivity distribution $P(D)$ ($S(b) = \int_0^{\infty} P(D)\, e^{-bD}\, dD$) [29]. Rather than inverting $P(D)$ nonparametrically, these models assume a functional form (e.g., Gaussian or Gamma) and estimate parameters such as peak, mean diffusivity and distribution width [29].

Why it matters for a spectrum view: Provides shape information (spread, skew) and band-wise fractions that can map to maturation (narrowing and left-shift) and PWML (broadening and left-shift), while staying data-efficient. In vivo brain data acquired over b up to $\approx 2000\,\mathrm{s/mm^2}$ were well described by this model, with a substantial width ($\approx 36\%$ of ADC) across regions; it also accounts for biexponential fits as special cases [29].

Neonatal feasibility: Moderate multi-b requirements; performance depends on the assumed $P(D)$ and SNR. Transparency about priors/cutoffs is essential for cross-study use.

2.2.4 Conclusion of dMRI Model review

Based on the review, several patterns emerge. (i) The explicit spectrum approaches align closely with the objective of describing an underlying distribution. However, they either require data beyond typical neonatal protocols (e.g., dense $q-$space, high b values, or long-time scans) or rely on threshold choices that complicate cross-study comparability. (ii) The implicit spectrum approaches offer feasible and robust summaries of distribution shape on moderate multi-shell data, particularly in low-FA neonatal tissue, but they do not reconstruct $f(D)$ and can blur spectral detail. (iii) Spectrum-oriented variants have been customized for body imaging [57], prostate [28, 58, 59], breast [60], and musculoskeletal applications [61]. However, no neonatal-feasible and safety-conscious implementation tailored to the immature brain has been reported. (iv) A further limitation is the transfer of adult WM priors to infants [62]. Many advanced models are calibrated in tissues with high FA, whereas in newborns they cannot meet due to the high free water fraction. Applying adult-tuned parameters can bias compartment fractions and mask subtle effects of maturation or injury.

Implication for this thesis For neonatal development, we need reproducible isotropic readouts that indicate where along the diffusivity axis changes occur without heavy acquisitions. For PWML, we need edema versus restriction disentanglement and quantification of spectrum shape (shift, width, tails) without fragile thresholds. These motivate a spectrum-based approach tailored to neonatal data—introduced in the next chapter.

2.3 Preterm vs. Term at Term-Equivalent Age: Volumetry and Diffusion MRI

2.3.1 Volumetry from birth to TEA: catch-up and residual gaps

Across the third-trimester window, preterm-born infants undergo substantial increases in brain volume, yet growth is tissue-specific and only partially closes the gap with term controls by term-equivalent age (TEA).

Absolute growth Total brain volume (TBV) rises steeply from birth to TEA. Longitudinal segmentation shows the fastest expansion in cortical gray matter ($11.94 \pm 2.1\,\mathrm{mL/wk}$) and the cerebellum (CB; $1.76 \pm 0.3\,\mathrm{mL/wk}$), with more modest gains in unmyelinated white matter ($6.51 \pm 1.3\,\mathrm{mL/wk}$) and deep gray matter (Deep GM; $1.05 \pm 0.2\,\mathrm{mL/wk}$) [63]. CSF ($5.77 \pm 1.9\,\mathrm{mL/wk}$) can also increase as sulcation deepens, underscoring parallel changes in

tissue and extra-axial compartments [63].

Changing tissue proportions As a fraction of intracranial volume, cerebellum, cortical GM and CSF typically increase between birth and TEA, whereas unmyelinated white matter and deep GM fractions decline—consistent with rapid cortical expansion and compartmental remodeling during late gestation [63, 64].

Ex utero versus in utero velocity Across the cerebrum, cerebellum and brainstem, postnatal growth rates during the third trimester are generally lower than in utero trajectories, arguing for partial rather than complete catch-up by TEA [65].

Hemispheric asymmetry At birth, cortical GM and deep GM volumes tend to be relatively larger on the left and unmyelinated WM larger on the right. By TEA, most tissue asymmetries attenuate, and unmyelinated WM asymmetry is more likely to persist than cortical GM and deep GM asymmetries [63].

Modifiers of growth Lower gestational age at birth is associated with slower neonatal growth, most clearly for CGM and CB, and with smaller lobar volumes and larger CSF beyond the neonatal window (around 12 months), following a frontal > parietal > temporal > occipital gradient [66]. Selected perinatal morbidity further dampens growth trajectories. The evidence for sex differences in absolute size (e.g., larger TBV and WM in males, proportionally more CGM in females) is fairly consistent, whereas sex-specific growth rates within the neonatal window remain mixed [63, 66, 67].

Links to outcome At TEA, smaller volumes of total brain tissue, cerebrum, frontal lobes, basal ganglia, thalamus and cerebellum are often seen in infants with neurodevelopmental impairments [68]. Several studies report that larger TBV, WM and CB at TEA, and steeper birth-to-TEA gains, relate to better early motor and cognitive outcomes [69, 70]; conversely, smaller cerebellar volumes have been linked to poorer neurological performance at 2 years' corrected age [68]. However, other cohorts find attenuated or nonsignificant associations after adjustment for perinatal and socio-environmental covariates, highlighting heterogeneity in effect sizes and model specification [71].

These patterns provide a mechanistic backdrop for the residual TBV and regional volume gaps frequently observed when preterm cohorts are compared with term-born peers at TEA, and they motivate careful adjustment for GA and clinical covariates when quantifying "catch-up". Reference ranges at TEA synthesized across cohorts can aid interpretation of absolute and relative tissue volumes [64].

2.3.2 Diffusion MRI from birth to TEA: DTI consensus and model-based specificity

Preterm birth remains a major global health burden and motivates sensitive imaging markers of early-life brain development [72–74]. We summarize TEA-stage group contrasts and prognostic evidence in preterm cohorts in Table 2.2, and we assemble model-focused neonatal dMRI studies that clarify dispersion versus density, deep GM sensitivity, and fibre-population localization without requiring an explicit preterm–term contrast in Table 2.3.

Developmental context The development of white matter begins in mid-gestation with limbic, projection, and commissural pathways, followed by thalamocortical and association systems between 24 to 32 weeks, and accelerates during the first two postnatal years [75]. Histology describes a sequence of axon outgrowth, synaptic overproduction and pruning, pre–myelination, and myelination, providing a cellular substrate for diffusion-derived trajectories [75]. During 30 to 45 weeks of PMA, diffusion MRI typically shows decreases in MD and increases in FA in the major tracts, consistent with axonal packing and premyelinating changes, while sensitive metrics of myelin (e.g. T_1/T_2, fraction of myelin water) increase rapidly in early childhood [76–78]. Classical neuroanatomy and infant magnetic resonance imaging converge on a posterior to anterior gradient: the occipital and central systems mature earliest, the parietal follows, and the cortices of the frontal and anterior temporal association lag; cortical microstructural trajectories mirror this gradient [77–80].

DTI consensus at TEA (evidence base in Table 2.2) Across multiple cohorts, preterm infants scanned at TEA exhibit lower FA and higher diffusivities in PLIC, corpus callosum and association pathways relative to term controls, supporting a dysmaturation account rather than focal loss [81–83]. PLIC FA at TEA stratifies abnormal 18–24-month outcomes in low-birth-weight infants, highlighting the sensitivity of early-myelinating tracts [84]. Tract-Based Spatial Statistics (TBSS) analysis shows widespread white matter skeleton effects and relate neonatal FA and RD patterns to 18-month motor and cognitive performance, though effect sizes and covariate robustness vary across studies [81, 85]. Tract-specific development within the corpus callosum scales with gestational age at birth at TEA [86]. Sex differences in tracts at TEA also associate with two-year outcomes in some cohorts [87].

PMA-dependent trajectories Across late gestation, FA typically increases and MD and RD decrease with PMA, reflecting ongoing axonal packing and early myelination; tract profiling shows asynchronous maturation across corticospinal, callosal, limbic, and visual pathways, with additional modulation by gestational age and sex [88]. Normative diffusion and NODDI maps in term infants around one month of age provide a useful reference frame for interpreting TEA findings under unsedated protocols and heterogeneous acquisition settings [89].

What model-based diffusion adds (study details in Table 2.3)

Compartment models (NODDI) In preterm infants scanned longitudinally between the preterm and TEA time-points, cortical FA decreases while orientation dispersion index (ODI) increases and v_{iso} decreases, whereas thalamic v_i increases, indicating that much of the cortical FA change is driven by rising orientation dispersion rather than reduced neurite content and that deep GM shows increasing tissue packing not separable by tensor metrics [90]. Cross-sectionally at TEA, cortex-wise NODDI reveals lower neurite density index (NDI) and higher tissue water in preterm cohorts relative to term controls, with posterior > anterior gradients and limited outcome associations after stringent covariate adjustment [91]. A dHCP-style analysis further reports regional NDI and ODI alterations in preterm infants at TEA, reinforcing a region-selective cortical signature of prematurity [92].

Kurtosis-derived models (DKI and WMTI) DKI demonstrates greater sensitivity than DTI to maturation in deep GM (basal ganglia and thalamus) and periventricular WM at TEA, with MK and RK reductions in preterm infants suggesting delayed microstructural development [93, 94]. Building on these contrasts, WMTI and combined DT+KT multivariate indices yield composite "maturity" scores that track PMA and early behavioral measures more strongly than DTI alone [95].

Fibre-specific modelling (CSD and FBA) and connectomics Fixel-based analysis separates microstructural density (FD) from macrostructural cross-section (FC), localizing fibre-population deficits at TEA beyond voxel-averaged tensor maps; in very preterm cohorts, FD/FC/FDC are reduced relative to term and associate with 1–3-year motor and cognitive outcomes, while perinatal risk factors often map preferentially to FC [96–98]. Structural connectome work that integrates CSD with NODDI and FA weighting suggests relative preservation of core long-range connections but vulnerability in thalamo-cerebellar and perisylvian systems, aligning macro-scale topology with microstructural loadings [99]. Prognostic pipelines that combine FBA metrics with connectomic features further indicate incremental value for classifying adverse outcomes in neonatal clinical cohorts [100].

Cortical diffusion and outcome Beyond the WM-centric view, neonatal cortical diffusion microstructure carries predictive information: parcel-wise cortical FA at birth relates to 2-year cognitive and language scores, implicating frontal-parietal and limbic territories in distinct behavioral domains [101]. In clinical term cohorts with congenital heart disease, lower cortical ODI and higher FA covary with reduced cerebral oxygen delivery, consistent with impaired dendritic arborization and demonstrating that dMRI-derived cortical metrics can couple to physiology [102].

Infrastructure that enables reliable neonatal dMRI Reproducible inference of new-

borns depends on motion-robust acquisition and reconstruction. The dHCP pipeline standardizes denoising, distortion correction, and multi-shell modeling, and a multi-tissue and time neonatal diffusion template enables voxel- or fixel-wise group analyzes across PMA [62, 103]. SHARD reconstruction mitigates slice-wise motion and outliers in multi-shell HARDI, improving downstream CSD, NODDI and FBA estimates [104]. SMSI offers orientation invariant microstructural contrasts including μFA from spherical mean signal, showing feasibility for mapping the neonatal brain [105]. Atlas resources covering $0-3$ months provide age-specific diffusion maps and tract-level norms to contextualize cohort effects [106]. Finally, high-angular tractography can resolve crossing - fiber systems and sub-bundles (e.g., SLF I, II and III) even at birth, allowing finer-grain development comparisons [107, 108].

Table 2.2: Diffusion MRI studies of preterm-born infants from birth to term-equivalent age (Birth→TEA; study-centric). dMRI protocol column shows: X-tesla scanner (e.g., 1.5T, 3T), number of distinct b-value shells (e.g., 2-shell, 3-shell), Total noncollinear diffusion-encoding directions (e.g., 32-dir, 64-dir), b values (e.g., 32 $b1000$ means shell at $b = 1000\,\mathrm{s/mm^2}$ with 32 diffusion-encoding directions). Region and ROI column lists the principal regions/tracts and the ROI definition method (e.g., manual, tractography, TBSS/GBSS skeleton, atlas-based). Main findings and outcome states key results and whether a longer-term outcome was reported (YES/NO). Abbreviations: see list of symbols and acronyms.

No.	Study	Design & cohort	dMRI protocol	Region / ROI	Main findings / Outcome
1	Arzouman., 2003 [84]	63 low-birth-weight PT at TEA; cross-sectional; 18–24 month follow-up	1.5T; DTI (6-dir, $b1000$; ADC/FA)	Manual ROIs: whole brain, CC, WM, PLIC	Lower PLIC FA at TEA predicted abnormal neuro-development at 18–24 mo (YES).
2	Anjari, 2007 [81]	26 PT vs. 6 term at TEA (mean 41.3 wk PMA), cross-sectional	3T; DTI (15-dir, $b750$); TBSS; T1w/T2w	Centrum semiovale, frontal WM, genu CC, PLIC, EC	PT < term: FA↓/RD↑ across widespread WM, (NO).
3	Hasegawa, 2011 [86]	PT at TEA (40 wk) in 3 birth-GA strata (cross-sectional)	1.5T; DTI (15-dir, $b1000$)	CC (tractography + manual ROIs)	Posterior CC maturation varied with birth GA (No follow-up, NO).
4	Van Kooij, 2011 [87]	PT at TEA (41 wk); male (n=38) vs. female (n=29) (cross-sectional); 2 y outcomes	1.5T; DTI (32-dir, $b800$); tractography	Fiber tracking: CC, PLIC	Sex-related tract differences linked to 2 y motor/cognitive outcomes; female-CC-cognitive and motor and male left PLIC-motor (YES).
5	Van Pul, 2012 [82]	89 PT at TEA (41.7 wk); WMI scored on T1w/T2w (cross-sectional)	3T; DTI (32-dir, $b800$; 4 metrics); tractography	Fiber tracking: CC, PLIC; WM injury score	Higher WMI burden associated with FA↓/diffusivity↑ in CC/-PLIC at TEA (NO).
6	Liu, 2012 [83]	PT at TEA: 41 normal, 27 mild, 2 moderate WMA (cross-sectional)	1.5T; DTI (32-dir, $b600$)	Probabilistic tractography: 15 major tracts (incl. CC, internal capsule)	Greater WMA associated with tract-specific DTI abnormalities (notably $\lambda_\perp$) (NO).

Continued on next page

No.	Study	Design & cohort	dMRI protocol	Region / ROI	Main findings / Outcome
7	Duerden, 2015 [85]	75 PT at 32 wk, 78 PT at 40 wk, 27 term at 39 wk; 18 mo follow-up	1.5T; DTI (12-dir, *b*600/700); TBSS; T1w/T2w	WM skeleton; CC	From PT to TEA, FA showed stronger associations with 18 mo cognition; AD/RD (PT/TEA) predicted motor outcome.
8	Pannek, 2018 [96]	PT at TEA with-/without abnormality; term at 40 wk (cross-sectional)	3T; DTI (30-dir, *b*1000) + CSD/FBA (64-dir, *b*2000)	Multiple tracts: CC, CST, association fibres	PT at TEA < term: FD/FC/FDC↓ (fibre-specific); PMA at MRI and brain volume influenced microstructural measures (NO).
9	Pannek, 2020 [97]	80 very-preterm at TEA; Bayley-III at 1–2 y (cross-sectional)	3T; CSD/FBA (64-dir, *b*2000)	CST, CC, long association tracts	Fixel metrics at TEA associated with 1–3 y motor/cognitive outcomes (YES).
10	Dimitrova, 2021 [91]	76 PT at TEA (40.9 wk) vs. 259 term; 18 mo outcome tested (cross-sectional)	dHCP protocol: 64 *b*400, 88 *b*1000, 128 *b*2600; cortical NODDI + quantitative MRI	DrawEM: 9 tissues, cerebral cortex (posterior>anterior gradient)	Term: heterogeneous and regionally specific associations between age at scan and measures of cortical morphology and microstructure; PT: cortical NDI↓, tissue water↑ with deviations↑; limited associations with outcomes after covariates (Mixed/NO).
11	Zhao, 2021 [94]	26 PT at TEA vs. 26 term (40 wk) (cross-sectional)	3T; DKI and DTI (30-dir *b*1000/2000)	7 manual ROIs: ALIC/PLIC, genu/splenium CC, parietal WM, thalamus, lentiform nucleus	PT at TEA: MK/RK↓ (reflecting deep GM maturity); DKI more sensitive than FA/MD for delayed maturation (NO).
12	Wang, 2023 [92]	73 PT at TEA (40 wk) vs. 69 term; dHCP-like processing (cross-sectional)	3T; dHCP (64 *b*400, 88 *b*1000, 128 *b*2600); cortical NODDI; GBSS	Cortex (JHU-neonate registered), 26 cortical ROIs	PT < term: regional specific NDI/ODI alterations at TEA (NO).

What is consistent, what is conditional Across methods, three patterns are well supported: (i) TEA-stage microstructural gaps in preterm cohorts, especially in early myelinating projection and callosal pathways [81–83]; (ii) PMA-dependent maturation with FA↑, MD↓ and NDI↑ but asynchronous across tracts [88, 89]; and (iii) model-specific sensitivity—NODDI clarifies dispersion versus density, DKI and WMTI heighten deep GM and microstructural kurtosis contrasts, and FBA localizes fibre-population-specific effects with outcome links [90, 93, 95, 97]. At the same time, associations with later outcomes attenuate in some studies after rigorous adjustment for perinatal and socio-environmental covariates, underscoring heterogeneity in effect sizes and model specification and the importance of harmonized protocols and covariate frameworks [85, 91].

Implications for this thesis From moderate-late preterm to TEA, neonatal brain growth is steep, yet asynchronous. Preterm cohorts show partial catch-up with residual regional gaps at TEA, consistent with dysmaturation rather than overt tissue loss. The metrics of the diffusion MRI model refine the biological specificity and, in some cohorts, relate to early motor and cognitive outcomes. Systemic, model-rich studies across the whole preterm brain

remain limited.

Table 2.3: Diffusion MRI studies of neonatal brains (no explicit PT–term contrast as the main analysis, model-focused). Notation and column conventions as in Table 2.2.

No.	Study	Design & cohort	dMRI protocol	Region / ROI	Main findings / Outcome
1	Kunz, 2014 [109]	13 newborns (near TEA), cross-sectional	3T; 6-shell (6 b50, 9 b250, 12 b700, 16 b1400, 20 b2500); NODDI, CHARMED, DTI	DTI-TK: 20 manual WM ROIs: CC; PLIC/ALIC; EC; periventricular crossroads	Feasibility of multi-compartment models; compact CC: FA↑, NDI/ν_{in} ↑, ODI↓; posterior vs. anterior IC separable; late-maturing regions: ν_{in} ↓, ODI↑ (NO).
2	Eaton-Rosen, 2015 [90]	Preterm longitudinal (12 preterm → 7 TEA; two time-points)	3T; 2-shell (15 b750, 32 b2000); NODDI (first time on PT), DTI (histogram of parameters in regions)	Cortex; thalamus (GM)	Cortex with PMA: FA↓, ODI↑, v_{iso} ↓, v_i ≈stable; thalamus: v_i ↑; dispersion-based interpretation of FA; adds GM specificity (NO).
3	Kansagra, 2016 [110]	Neonatal encephalopathy; scans at birth (n=12) and ∼6 mo (n=13) (longitudinal)	3T; 3-shell (b700, b2000, b3000); NODDI, DTI	Manual ROIs on FA: major WM tracts (ALIC/PLIC/CC/associations)	Early injury pattern in ODI/NDI; NODDI tracked maturation/repair beyond DTI (NO).
4	Shi, 2016 [93]	35 PT at 33–44 wk PMA, cross-sectional	3T; 2-shell (25 b1250 and b2500); DKI, DTI	8 manual ROIs: PLIC; CC (genu/splenium); frontal WM and GM; lentiform nucleus; CR; deep GM	MK tracked maturation; DKI more sensitive than FA/MD in deep GM; neonatal feasibility (NO).
5	Dean, 2017 [89]	104 term (1 mo), cross-sectional	3T; 3-shell (9 b350, 18 b800, 36 b1500); NODDI, DTI	DTI-TK: major WM tracts (atlas-based)	Normative neonatal NODDI/DTI maps; asymmetric/regional maturation patterns in early age (NO).
6	Batalle, 2017 [99]	65 newborns at 25–45 wk PMA; connectomics with prematurity tested, cross-sectional	3T; 2-shell (32 b750, 64 b2500); CSD, DTI, NODDI; connectome	CSD tractograhy: whole-brain network; thalami-cerebellar; perisylvian	Regional differences in brain maturation: deep GM shows fastest developmental changes; Multi-model network weighting; core connections relatively preserved by birth GA; local systems vulnerable (NO).
7	Karmach., 2018 [111]	Healthy (n=16, 38-47 wk PMA) vs. CHD (n=19, 37-41 wk PMA) neonates; cross-sectional	3T; 2-shell (30 b1000, 30 b2000); DTI, NODDI, non-parametric GMM	Atlas-based ROIs: 22 WM tracts (association/projection/callosal)	All models tracked maturation; GMM (e.g., RTOP/RTAP) showed larger effect sizes for CHD-related deviations vs. DTI/NODDI; NDI increased with age (NO).
8	Pecheva, 2019 [98]	50 very-preterm at TEA; perinatal risk factors	3T; single-shell (64 b2500); CSD, FBA	Fixel-wise WM (whole-brain)	FBA disentangled micro- (FD) vs. macro-structure (FC); FD and FA corelated with GA at birth; perinatal risks related more to FC than FD (NO).

Continued on next page

No.	Study	Design & cohort	dMRI protocol	Region / ROI	Main findings / Outcome
9	Pietsch, 2019 [62]	dHCP cohort (n=113, 33–44 wk PMA); methods/resource	MSMT-CSD; multi-tissue diffusion (1 isotropic and 2 anisotrpic components)	Whole brain (voxel/-fixel, diffuison atlas was built)	Providing neonatal-specific modelling/processing strategies; Enables neonatal fixel-wise analyses and atlas-building; infrastructure for fiber-specific metrics (NO).
10	Bastiani, 2019 [103]	dHCP processing pipeline; methods/resource	Automated neonatal dMRI pre-processing (denoise, eddy/-topup, distortion corr.)	Whole brain (pipeline)	Standardized pipeline; prerequisite for robust NODDI/CSD/FBA in unsedated neonates (NO).
11	Kelly, 2019 [102]	48 CHD vs. 48 healthy term neonates, cross-sectional	3T; 3-shell (dHCP protocol); NODDI, GBSS; CBF/O_2 measures	Cerebral cortex (GBSS-based)	Lower cortical ODI (and higher FA) associated with reduced cerebral oxygen delivery; dendritic arborization hypothesis (NO).
12	Huynh, 2020 [105]	Methods/feasibility; neonatal application; Simulation and 2 subjects (2 time-point scan each), cross-sectional	3T; 3- to 21- shell (b500 to b3000); SMSI (orientation-invariant indices incl. μFA)	Whole brain (WM/GM capable)	First neonatal application of SMSI; SMSI provides microstructure contrasts beyond tensor/kurtosis; neonatal-feasible; b-shell contributions to isotropic fraction noted; Isotropic fraction volume benefits more from b500 shell than from b1000 (NO).
13	Fenchel, 2020 [112]	241 term (37–44 wk PMA); cross-sectional normative networks	dHCP-style multi-shell; DTI, NODDI features into cortical profiles/MSN	Cerebral cortex (surface-based)	Cortical morphometric–microstructural profiles form modules aligned with cytoarchitecture; posterior networks strengthen with age (NO).
14	Ouyang, 2020 [101]	87 neonates (31.9–41.7 wk PMA); cross-sectional; 2 y follow-up	3T; single-shell DTI (30-dir, b1000); cortical FA on skeleton	Atlas registration: whole-cortex parcels	Neonatal cortical diffusion microstructure predicted 2 y cognitive/language outcomes; lobar GM weights differently: frontal and parietal ↔ cognitive outcomes, frontal and limbic gyri ↔ language outcomes (Yes).
15	Kimpton, 2021 [88]	31 preterm; cross-PMA (25–45 wk); 2 y outcome subset	3T; 2-shell (32 b750, 64 b2500); NODDI, DTI, CSD tractography	Fiber tracking (CSD): CST, fornix, OR, ILF, callosal tracts	With PMA: FA↑/MD↓/NDI↑; GA and sex effects on NDI; asynchronous tract maturation (NO).
16	Uus, 2021 [113]	dHCP resource; 40 PT AND 140 term at TEA	3T; 3-shell (dHCP protocol); multi-channel atlas incl. SMT-based μFA, DKI, NODDI, DTI	Whole brain; WM parcellations; transient WM regions	Neonatal 4D parametric atlas (incl. μFA) enabling age-resolved analyses; methods/resource (NO).
17	Christiaens, 2021 [104]	Motion-robust reconstruction; cohort-scale feasibility	3T; multi-shell (dHCP); SHARD scattered-slice reconstruction	Whole brain (reconstruction), motion correction	Slice-level motion correction/outlier handling improves multi-shell HARDI for CSD/FBA/NODDI (NO).

Continued on next page

No.	Study	Design & cohort	dMRI protocol	Region / ROI	Main findings / Outcome
18	Bobba, 2022 [106]	55 newborns (0–3 mo ADC/DTI subsets); cross-sectional	3T; 2-shell (b500, b1000 for ADC) & single-shell DTI (30 b1000); online atlas	TBSS: Voxelwise + tract-level maps	Age-specific diffusion atlases; rapid neonatal changes; highest growth rates in subcotical WM, cortical spinal tract, cerebellar WM and vermis; prematurity and low GA at birth may result in lasting delay in CC; public resource (NO).
19	Li, 2022 [95]	50 term (37–44 wk PMA); behavior scores; cross-sectional	3T; 4-shell (18 b500, 18 b1000, 18 b2000, 18 b2500); DKI, WMTI, DTI	TBSS: WM skeleton + tract ROIs	DT+KT Mahalanobis "maturity index" tracked PMA/behavior better than DTI alone (YES).
20	Liang, 2022 [107]	40 term vs. 40 adults; developmental contrast, cross-sectional	3T; 3-shell (dHCP protocol); MSMT-CSD tractography; DTI/NODDI metrics	SLF I/II/III subbundles	Resolved SLF subdivisions at birth; heterochromous maturity (SLF II least mature); FA driven by NDI more than ODI (NO).
21	Jeong, 2022 [100]	15 term newborns grouped by outcome (normal, abnormal, death); prognostic focus, cross-sectional	3T; 3-shell (b700, 33 b800); CSD, FBA; connectome;	Major tracts; fixel metrics (FD/FC/FDC), ML classifier	Fixel metrics/connectivity at TEA related to later motor/cognitive outcomes; prognostic utility beyond DTI (YES).
22	Wang, 2023 [114]	42 term neonates (≤28 d), cross-sectional	3T; 2-shell (25-dir, b1000, b2000); DKI	11 manual ROIs: PLIC/ALIC; CC (genu/splenium); frontal/central/parietal WM; caudate; GP; putamen; thalamus	Normative DKI patterns: MK increased and diffusivity decreased with age across WM/GM (NO).
23	DiPiero, 2024 [115]	91 pne-month infants; GBSS framework (no case–control focus)	3-shell (9 b350, 18 b800, 36 b1500); GBSS for infant cortex; DTI, NODDI	Cortex (GM skeleton)	Refined GBSS for infant cortex; improved registration/delineation; PMA-related cortical microstructural trends; no sex effect (NO).
24	Verschuur, 2024 [108]	Exemplar TEA scans (late-preterm + dHCP case); feasibility, cross-sectional	3T; two-shell (45-dir, b800, b2000) or dHCP; DTI + CSD/SS3T-CSD tractography	Manual ROIs in fiber bundles: CC; CST; crossing-fiber regions	Guidance for reconstructing crossing fibers in neonatal dMRI; sensitivity to angular/spatial resolution and processing choices (NO).

2.4 Neonatal PWML: Definitions, Imaging, Quantification, and Outcomes

Neonatal PWML are frequent, clinically relevant, and heterogeneous. Their multimodal MRI signatures indicate complementary facets of the lesion: a T1-defined core, a T2 and MD penumbra, and, in a subset, SWI evidence of hemorrhagic and perivenular components, while diffusion metrics capture tract-level effects that relate to burden and outcomes. Despite this progress, tract-specific applications of advanced diffusion models to optic-radiation PWML are rare. This review integrates definitions, cross-modality imaging, quantitative diffusion findings, and outcome links, and motivating our Diffusion Bubble Model to phenotype OR-

PWML beyond conventional tensors.

2.4.1 Definition of PWML

Punctate white matter lesions are common in neonates, especially those born preterm, and have been associated with later neurodevelopmental deficits [5, 6, 116, 117]. Radiologically, PWML are classically defined as small, non-cystic foci within predominantly unmyelinated white matter that appear hyperintense on T1-weighted images and iso- to hypointense on T2-weighted images [116, 118–122]. Several clarifications are warranted: (i) Historically, PWML occupies the punctate noncystic end of the periventricular leukomalacia spectrum (PVL). In the ultrasound era, severe cystic PVL was most readily detected, while the advent of MRI, particularly T1-weighted imaging, brought attention to early focal noncystic lesions; related terms in the literature include "non-cystic PVL", "punctate (or focal) white matter abnormality" and "punctate (white matter or brain) lesion" [122–126]. (ii) Subsequent reports noted that the T2-weighted signal of PWML is not invariably hypointense. Iso-intense foci have been described and incorporated into working definitions [127,128]. (iii) To avoid confounders of intrinsic T1 hyperintensity of normally myelinating tissue, some studies excluded regions undergoing active myelination from PWML counts and analyzes (e.g., [122]). (iv) Neonatal PWML should be distinguished from adult punctate white matter hyperintensities, which differ in tissue environment, imaging criteria, and pathogenesis.

In practice, however, PWML exhibit developmental variability: they cluster in periventricular and deep white matter, may border regions entering early myelination at term-equivalent age, and show diffusion changes that are frequent but not invariable.

2.4.2 PWML locations

PWML mainly involve the periventricular and deep white matter, notably the peritrigonal region, centrum semiovale, and posterior radiations, including the optic radiations. This topography is well documented across cohorts of preterm infants [117, 129]. It likely reflects several converging vulnerabilities in the late-gestation brain: (i) long medullary vascular trajectories with relatively sparse collaterals, together with dependence on deep medullary venous drainage, predispose periventricular white matter to hypoperfusion and venous congestion, though this "end-zone" hypothesis remains debated [130]; (ii) metabolic demands are high as axons and glia rapidly mature [130]; (iii) and preoligodendrocytes in incompletely myelinated tissue are especially susceptible to hypoxia–ischemia and inflammatory insults [131, 132]. In addition, barrier and immune signaling is still maturing in early life, and systemic illness or inflammation can modulate risk, although infection is neither necessary nor sufficient for

PWML [133].

Incidence varies widely across cohorts owing to differences in definitions, imaging protocols, and case mix. One early series reported an overall neonatal incidence of approximately 23%, with 86% of cases occurring in preterm infants [123]. Another study given mean incidece of isolated PWML was 22.1% through study 1655 patients [6]. In preterm populations specifically, reported rates range from 10–50% [5, 117]. Regional predilection for posterior pathways has been repeatedly noted; for example, Childs et al. observed that 9 of 12 minor PWML were located along the optic radiations [123]. Posterior lesions (including OR) were reported in 23 to 53% of cases. Bassi reported 12/19 in optic radiation of preterm scan [126]. Li et al reported 8 anterior, 25 central, and 22 posterial lesions [129]. While Kersbergen et al. only reported 5 out of 112 appered in posteri white matter or along the optic radiation in preterm infants PWML study [117].

2.4.3 Morphologic patterns

In neonatal MRI practice, PWML are most commonly described using three descriptive patterns: (i) punctate: small, discrete foci; (ii) linear or striated: radially oriented streaks that tend to follow deep medullary veins or fiber directions; and (iii) clustered: aggregations of adjacent punctate lesions that form a larger region of involvement [5, 117]. These labels are descriptive, not pathognomonic, and are illustrated in Fig. 2.1. Punctate foci can reflect microvascular hypoperfusion, microhemorrhage, or focal inflammatory injury; linear foci can accompany perivenular injury or early myelin–axon involvement; and clustered lesions often indicate a higher local burden of multifocal injury [122].

Etiologic framework PWML likely arises from intersecting mechanisms operating in the late-gestation white matter: (i) *Hypoxic–ischemic/low-flow injury*, particularly in periventricular and deep white matter supplied by long medullary end arteries with limited collateralization. Energy failure in premyelinating oligodendrocytes and axons leads to membrane disruption and focal necrosis [5, 117]. (ii) *Inflammatory–immune injury*, including fetal or perinatal systemic inflammation and, less commonly, infection-related processes, which amplify glial activation and microvascular dysfunction [5]. (iii) *Hemorrhagic/vascular injury*, where microbleeds or perivenular congestion contribute to punctate foci, often detectable as susceptibility effects in SWI and aligned with the anatomy of the deep medullary venous [117, 122]. These pathways frequently cooccur, and individual lesions may reflect mixed pathology [5, 117].

Temporal stages PWML evolve along a developmental timeline from an acute stage, characterized on imaging by small T1-hyperintense foci with frequent diffusion restriction in

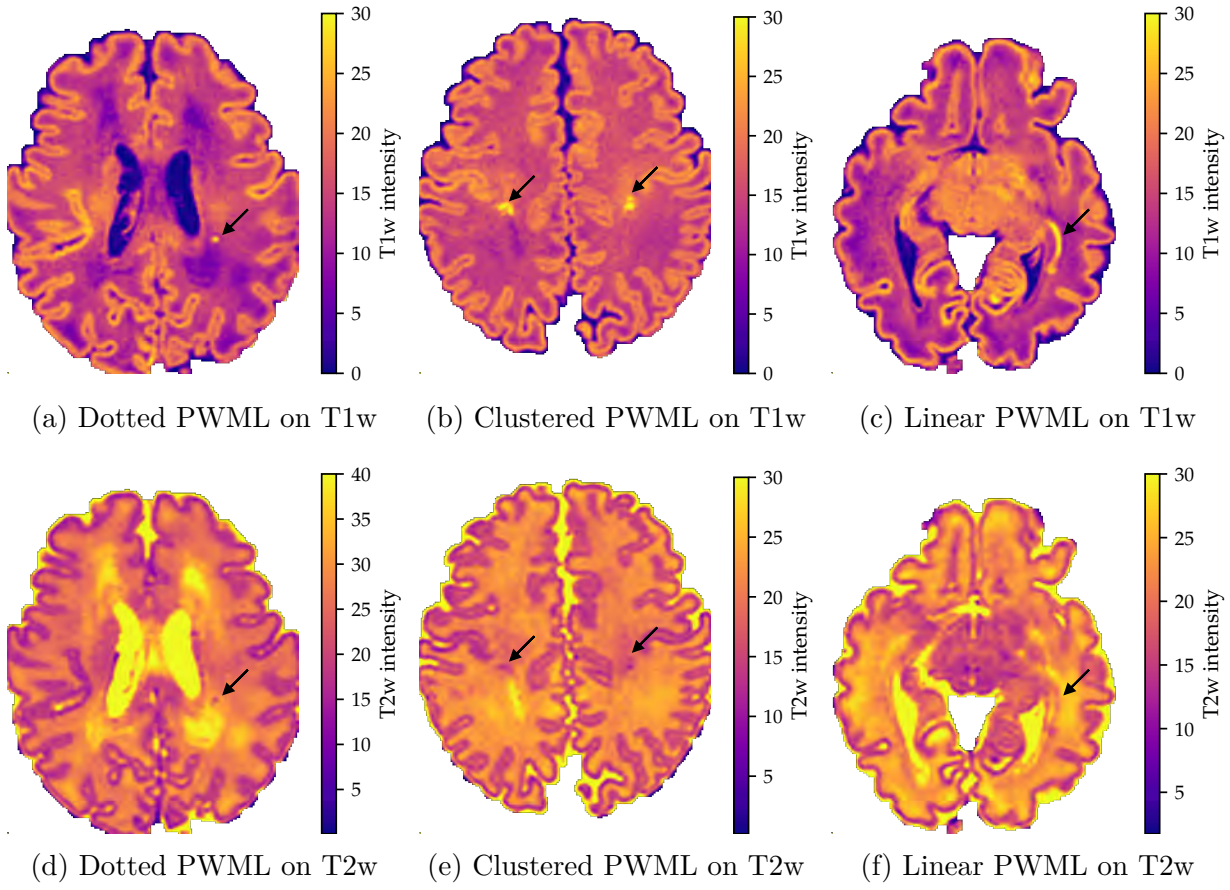

(a) Dotted PWML on T1w (b) Clustered PWML on T1w (c) Linear PWML on T1w

(d) Dotted PWML on T2w (e) Clustered PWML on T2w (f) Linear PWML on T2w

Figure 2.1 Representative morphologic patterns of PWML on structural MRI (dHCP). Top row: T1-weighted; bottom row: T2-weighted. Columns illustrate (left) punctate, (middle) clustered, and (right) linear PWML patterns in axial planes. Consistent windowing and matched slice levels are used; lesions are highlighted with arrows. Provenance: author-generated examples from the dHCP dataset.

clustered lesions and/or susceptibility on SWI in linear lesions, to a subacute stage with resolution of edema and inflammation alongside reactive gliosis, oligodendroglial progenitor proliferation, and early vascular remodeling; in a subset, a chronic stage follows, leaving gliotic residua or subtle scarring [117, 122, 134]. A proportion of lesions partially or completely regress radiologically, reflecting both biological recovery and maturational remodeling, but persistent microstructural alterations can remain, especially with clustered or tract-involving lesions [7, 117, 126].

2.4.4 Imaging characteristics across modalities

Cranial ultrasound is widely available and useful for bedside screening but has limited sensitivity to small punctate foci; therefore, magnetic resonance imaging is the modality of choice [5]. On MRI, PWML are typically T1-hyperintense and isointense to hypointense on T2-weighted images (see Fig. 7.3 (a), Fig. B.1 (b), Fig. 2.1, and Fig. 1.3); importantly, T2 hypointensity is not invariable and isointense foci have been reported [116, 118–122, 128]. Diffusion changes, lower mean diffusivity, are frequent, but not universal and depend on the timing and composition of the lesion [117].

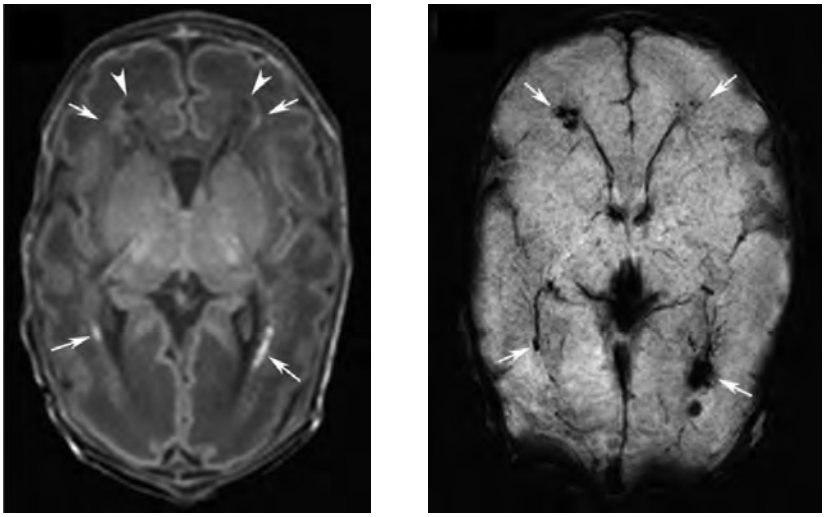

(a) PWML on T1w (b) PWML on SWI

Figure 2.2 PWML in the optic radiations: T1-weighted core versus SWI hemorrhagic footprint (literature case). (a) T1-weighted MRI shows punctate hyperintense lesions confined to the left and right optic radiations. (b) Susceptibility-weighted imaging (same slice) reveals a broader susceptibility footprint consistent with microhemorrhage, with shape and extent—particularly on the right—differing from the T1-defined foci. Reproduced from publication under the terms of the Creative Commons Attribution–NonCommercial (CC BY–NC) License [122].

Across modalities, lesion extents can be non-congruent: T1-weighted images often delineate a compact core, whereas T2-weighted or MD maps depict a broader abnormal penumbra [126]. Susceptibility-weighted imaging can additionally reveal a hemorrhagic and perivenular component in a subset, which can extend beyond the T1-defined core (Fig. 1.3 and Fig. 2.2) [117, 122].

2.4.5 Quantitative biomarkers and diffusion MRI

Quantitative descriptions vary across studies owing to differences in acquisition and timing. In general, acute lesions show lower MD consistent with restricted diffusion, with partial normalization during subacute recovery; chronic residua may exhibit subtle T1 and T2 changes with near-normal MD but altered microstructural indices.

Diffusion MRI has yielded two complementary streams of evidence for PWML. First, cohort studies have applied DWI and DTI to PWML since the early 2000s and demonstrated tract-level alterations (for example, FA reductions) and burden–effect relationships [7, 125, 126]. Second, tract-specific work in the visual pathway underscores the functional relevance of the optic radiations, even when PWML is not the primary exposure [135]. As summarized in Table 2.4, clustered lesions more often exhibit restricted diffusion, linear lesions more often show susceptibility on SWI, lesion burden relates to widespread DTI alterations, and optic radiation microstructure correlates with early visual performance [117, 122, 126, 135].

2.4.6 Clinical correlations and outcomes

The outcomes after neonatal PWML are heterogeneous, reflecting the variability in the burden of the lesion, location, imaging phenotype, and prematurity comorbidities. In general, a higher burden of PWML and tract-associated lesions are associated with a greater risk of adverse neurodevelopment, while small isolated foci often carry minimal sequelae [6, 7, 117]. Infants with PWML in the setting of a genetic disorder appeared to be more at risk of poor outcome [119]. (i) *Motor outcomes* Across cohorts, PWML burden relates to wider microstructural alterations on DTI and to poorer early motor performance, consistent with a dose–effect relationship [7]. Tract-level analyses demonstrate reduced FA within major pathways in infants with PWML, supporting the idea that focal lesions can have distributed tract effects [126]. Lesions close to corticospinal projections (e.g., centrum semiovale or PLIC vicinity) plausibly contribute to motor risk, although effect sizes vary by cohort and timing [7, 117]. (ii) *Visual and visuocognitive outcomes* When PWML extend into posterior pathways, involvement of the optic radiations (OR) raises concern for later visuocognitive vulnerabilities. Although not PWML-centered, neonatal DTI studies show that OR microstructure correlates with early visual performance, providing a tract-specific functional context [135]. This makes OR-involving PWML a biologically plausible substrate for later visual difficulties and motivates tract-anchored analyses. (iii) *Cognitive and language outcomes* Evidence is mixed, with some studies reporting subtle group-level decrements that attenuate after adjustment for prematurity-related confounders, whereas lesion burden and distribution remain more consistent predictors than any single sequence readout [5, 7]. Methodological

Table 2.4 Neonatal PWML and diffusion MRI studies with an emphasis on the optic radiations. Studies include PWML-focused cohorts and OR-focused background work. Columns summarize cohort, whether the OR was explicitly analyzed, the diffusion model used (DWI/DTI or advanced), and the key PWML-related finding. This overview highlights tract-level evidence, cross-modality complements (e.g., SWI), and the limited use of higher-order dMRI models directly targeting PWML.

Study (year)	**Cohort**	**OR focus**	**dMRI model**	**Key finding (PWML-related)**
Berman et al., 2009 [135]	36 preterm at 29-41W GA	**Yes** (OR)	DTI	OR microstructure correlates with visual performance; not PWML-focused.
Bassi et al., 2011 [126]	23 PWML vs. 23 controls; TEA	Main WM tracts, including OR	TBSS, DTI	Lower FA in major tracts; burden–effect relation in PWML at TEA.
Niwa et al., 2011 [122]	17 preterm, 7 term	OR examples	SWI	SWI reveals hemorrhagic/perivenular components beyond T1 core (complement to dMRI).
Kersbergen et al., 2014 [117]	112 preterm; 30W PMA + TEA	Posterior regions seen esp. with higher lesion load	DWI, SWI	Linear+SWI vs. clustered+DWI patterns; temporal evolution; many low-burden foci regress by TEA.
Li et al., 2017 [129]	33 PWML vs. 33 controls	PWML adjacent, main fiber tracks, including OR	TBSS, DTI	Grade III shows AD↑/RD↑/FA↓ near lesions; milder grades smaller effects.
Tusor et al., 2017 [7]	511 preterm, 122 PWML, 42W PMA	No. PLIC and other WM	TBSS, DTI	PWML burden associates with widespread microstructural alterations; links to early motor outcome; FA↓, RD↑ found.
Tro et al., 2022 [136]	9 PWML, 8 control, TEA	No (spinal cord)	DKI	DKI is more sensitive than DTI-related measures to alterations caused by PWML.
Zhang et al., 2025 [24]	Neonatal OR-PWML	**Yes** (OR)	**DBM**	**Our study:** Isotropic diffusion spectrum / free-water separates "wet" vs. "dry" PWML phenotypes in OR.

diversity in follow-up age and instruments (e.g., Bayley-III vs. later school-age tests) likely contributes to between-study variability. (iv) *Imaging correlates that modify risk* Imaging phenotype appears to matter: clustered lesions more often show restricted diffusion and are linked to broader tissue effects, whereas linear (or striated) lesions more often show susceptibility on SWI and may represent a different pathophysiological mix; many low-burden foci become inconspicuous by term-equivalent age [117]. Severity grading also relates to nearby tissue change, with higher-grade PWML showing more pronounced increases in AD and RD and reductions in FA adjacent to lesions [129]. Importantly, radiological "regression" does not necessarily imply full microstructural recovery, as tract-level abnormalities can persist at term [7, 126]. (v) The prognosis of these typical lesions is determined by early management, particularly in the first year [6, 137].

Motivation for applying DBM to OR-PWML Prior work establishes prevalence, heterogeneity, posterior involvement, and complementary multi-sequence signatures. However, most studies are based on tensors; advanced models applied directly to OR-anchored PWML remain scarce. In Chapter 7 we use a spectrum-based approach (DBM) to estimate diffusivity distributions and free-water content within lesions, providing a dMRI framework to localize which portions of the isotropic spectrum are perturbed.

2.5 Review of Neonatal Brain Tissue and Structure Segmentation

2.5.1 Traditional segmentation methods

Manual delineation: Manual slice-by-slice tracing by expert raters has long been considered the reference standard for neonatal MRI segmentation because it can capture subtle anatomy when performed carefully. However, it is labor-intensive, time-consuming, and subject to inter- and intra-rater variability, which limits scalability to large cohorts and motivates automated alternatives [138–140]. In practice, manual delineation today is mainly used to create atlases and to validate automated methods (like our PWML labeling and segmentation in Chapter 7).

Atlas-based segmentation: Atlas methods propagate labels from one or more annotated reference images to a target image via deformable registration, optionally combining multiple atlases with label-fusion strategies to improve robustness [141–143]. In neonates, age-appropriate atlases are crucial due to rapid developmental changes; registration errors and anatomical variability can degrade pure atlas-based transfer. Contemporary neonatal pipelines therefore blend atlas priors with intensity modeling and iterative refinement. A prominent example is Draw-EM (Developing brain Region Annotation with Expectation–Maximization), used in the dHCP structural pipeline, which couples probabilistic atlases with EM-based tissue modeling to achieve robust multi-tissue segmentations on T2-weighted images across a wide gestational-age range [144, 145].

Statistical/parametric segmentation: Intensity-based parametric models treat voxel intensities as draws from class-specific distributions and estimate class memberships via EM. Classical approaches include finite or mixture models and hidden Markov random field models to encode spatial smoothness and correct for bias-field inhomogeneity [146–148]. These methods can be combined with atlas priors (as in Draw-EM), initialized from coarse segmentations, and iteratively refined [145]. Other traditional approaches include unsupervised clustering (e.g., k mean, fuzzy c mean) and supervised voxel-wise classifiers (e.g., k-NN, Naive Bayes, random forests, SVMs) using intensity and spatial location features; for newborns, k-NN and

random forest frameworks have been successfully used to segment T2-weighted data into WM, GM and CSF and related classes [149, 150]. Although effective and less labor-intensive than manual annotation, these methods rely on hand-crafted features and often under-perform modern deep learning when large labeled datasets are available.

Statistical shape modeling and deformable models: Deformable models incorporate prior shape information and image-driven forces to refine boundaries, typically via active contours or level-set evolutions [151, 152]. In neonatal MRI, such models have been applied to structures like cortex or ventricles, sometimes in morphology-driven frameworks, and are frequently coupled with atlas or intensity models to improve anatomical plausibility [153, 154]. These methods can sharpen boundaries and enforce realistic shapes but generally require good initialization and may struggle with the pronounced inter-subject variability and contrast changes in early life.

2.5.2 Deep learning–based segmentation

Deep learning has markedly advanced brain MRI segmentation, including in neonates. Convolutional neural networks (CNNs) learn hierarchical features directly from data and have shown superior accuracy and consistency over classical pipelines when sufficient training labels are available. The U-Net architecture introduced an encoder–decoder with skip connections that preserves localization while leveraging deep, multi-scale features, and U-Net variants dominate many medical segmentation benchmarks [155]. For neonatal imaging specifically, early CNN work (e.g., multi-scale, patch-based CNNs) reported Dice scores around 0.80–0.87 for neonatal tissues, demonstrating feasibility despite challenging contrast [156].

Fully 3D architectures further improved volumetric consistency. V-Net extended the U-shaped design to volumetric convolutions and popularized Dice-based losses that help with class imbalance in medical images [157]. More recently, nnU-Net automated much of the configuration burden (patch size, preprocessing, network depth, postprocessing) and delivered top-tier performance across diverse tasks, including brain tissue and structure segmentation, without manual tuning, showing that robust data-driven configuration can rival bespoke architectures [158]. This thesis also choose nnU-Net as the method for segmentation (Chapter 5).

To better capture long-range dependencies, transformer-based or hybrid CNN–transformer models have been introduced. UNETR and Swin UNETR use transformer encoders (with hierarchical, shifted-window self-attention for the latter) within a U-shaped decoder, and have achieved strong results on challenging benchmarks such as BraTS 2021 [159, 160]. These models often require substantial compute and training data, but current evidence suggests

they can match or exceed CNN-only baselines when well trained.

In general, deep learning methods are now the state of the art for neonatal brain magnetic resonance imaging segmentation in many settings. Their main limitation is dependence on reliable training labels, which are scarce and expensive in neonates (often derived from dHCP, Draw-EM or expert annotations). Nevertheless, with transfer learning, data augmentation, and semi-supervised strategies, CNNs and hybrid models provide accurate and consistent tissue and structure delineations across neonatal cohorts [140, 161].

2.5.3 Segmentation using diffusion MRI data

Accurate tissue segmentation is central to studying neonatal brain development and pathology. In practice, infant segmentation pipelines rely primarily on high-resolution structural MRI, with T2-weighted images preferred during the neonatal period because they offer clearer gray-white matter delineation than T1-weighted images prior to substantial myelination [10, 162, 163]. The dHCP structural pipeline (DRAW-EM) is a representative example: it segments the T2w volume into multiple tissue classes and cortical parcels and has become a standard for neonatal datasets [103, 162].

A practical limitation of structural-first workflows is that anatomical labels must be transferred into diffusion space. Diffusion MRI is typically acquired with single-shot EPI for speed, which introduces susceptibility- and eddy-current–induced geometric distortions that vary with phase-encoding and anatomy [164, 165]; in neonates these distortions compound with small head size and high water content [166]. Additionally, DWIs typically encompass multiple volumes that may not align properly due to infant movement during scans [167]. This resolution disparity, different distortions and misalignment between diffusion MRIs and T2-weighted images can result in inaccuracies in segmentation placement, thereby affecting the reliability of statistical outcomes. Even with correction, residual mismatch between structural and DWI spaces can degrade label placement and tractography constraints [165].

These challenges have motivated diffusion-native space segmentation: learning tissue labels directly from DWI or diffusion-derived maps, thus avoiding intermodality registration. Zhang et al. proposed *DDSeg*, a CNN that predicts WM, GM and CSF from diffusion features (DTI and corrected DKI contrasts) trained on HCP data and then applied to diverse acquisitions without requiring T1 and T2 inputs [168]. More recently, Theaud et al. introduced *DORIS*, a DWI-based deep network that outputs 10 tissue classes, including ventricles and key subcortical nuclei, specifically to improve anatomically constrained tractography; in lieu of a diffusion-space ground truth, it uses a silver standard derived from FreeSurfer labels registered to DWI [169]. Reviews of machine learning for diffusion MRI likewise highlight

diffusion-only segmentation as a growing, viable track for sites lacking structural scans [170].

In conclusion, the appropriate age-appropriate atlas and EM frameworks on the T2-weighted anatomy remain reliable throughout the TEA window; modern CNN improve the accuracy and consistency of brain segmentation when labels exist. Diffusion-native segmentation reduces the cross-modal registration error and is valuable when structural scans are missing.

This review motivates two pragmatic design choices for the rest of the thesis: (i) working directly in diffusion space with a diffusion-only segmentation pipeline to avoid cross-modal registration error and to enable analyzes when structural MRI is unavailable; and (ii) adopting a spectrum-based diffusion model that localizes shifts, width, and tail changes in the isotropic spectrum, disentangling free-water–like from restriction-dominated effects. The next chapter introduces our proposed model—the Diffusion Bubble Model (DBM)—and outlines its formulation, algorithm, and chapter-by-chapter plan.

CHAPTER 3 METHODOLOGY

Introduction

This chapter provides the methodological backbone for the four results chapters. It is organized in two parts. First, it introduces the proposed Diffusion Bubble Model (DBM), a spectrum-based dMRI framework that reconstructs the isotropic diffusivity spectrum while minimally adjusting for anisotropy. Second, it outlines the general research plan for each of the result chapters.

3.1 Proposed Diffusion MRI Model: Diffusion Bubble Model (DBM)

Advanced diffusion MRI models balance biological realism with mathematical tractability [171]. Conventional compartment models either (i) fit a single diffusion tensor to an entire voxel or (ii) decompose the diffusion-weighted signals into a small, fixed set of compartments, both of which can oversimplify the complex microstructure present within brain tissue voxels [17, 25, 26, 29]. At the other extreme, diffusion spectrum approaches aim to recover a full displacement or diffusion spectrum (for isotropic and/or anisotropic components) but typically require a heavy acquisition burden and complex reconstruction strategy [23, 172, 173].

The proposed Diffusion Bubble Model offers a middle ground: it preserves the sensitivity needed for anisotropic diffusion analysis while modeling the isotropic part of the signal as a continuous one-dimensional spectrum of "diffusion bubbles" [24]. Because the spectrum spans from highly restricted to highly free diffusion water, DBM is expected to be sensitive to subtle microstructural changes associated with brain maturation and injuries.

3.1.1 Model concept

DBM assumes that the normalized diffusion-weighted signal can be decomposed into two additive terms (Fig. 3.1):

1. *Isotropic diffusion bubbles*: a continuum of (near-) isotropic tensors, each characterized by limit number of parameters set (for isotropic tensors, a scalar diffusivity D_i); Together, their coefficients (weights) form an isotropic diffusivity spectrum.

2. *Anisotropic adjustment tensors*: a small set of cylindrically tensors that absorb the residual direction-dependent signal.

Operationally, DBM first estimates the anisotropic adjustment to minimize its influence on the isotropic fits, and then performs a stable, high-resolution recovery of the isotropic spectrum. Plotting the coefficients against their corresponding diffusivity (or effective bubble diameters) produces the isotropic spectrum (Fig. 3.2).

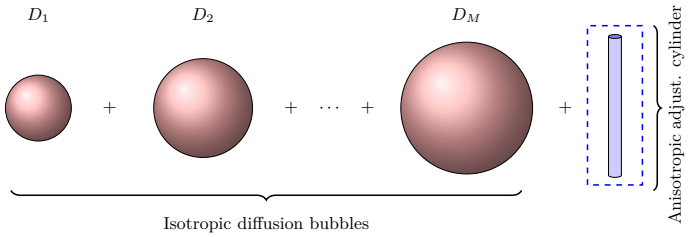

Figure 3.1 Schematic of the Diffusion Bubble Model (DBM). Red spheres depict isotropic diffusion "bubbles" spanning a continuum of scalar diffusivity D_i; the blue cylinder denotes a cylindrically symmetric anisotropic adjustment aligned with a dominant fiber direction (a single cylinder is shown for clarity). Decomposing the normalized diffusion-weighted signal into these isotropic and anisotropic terms yields an isotropic diffusivity spectrum while retaining directional sensitivity beyond conventional single-tensor models. Figure was from our prior open-access article with author permission [24].

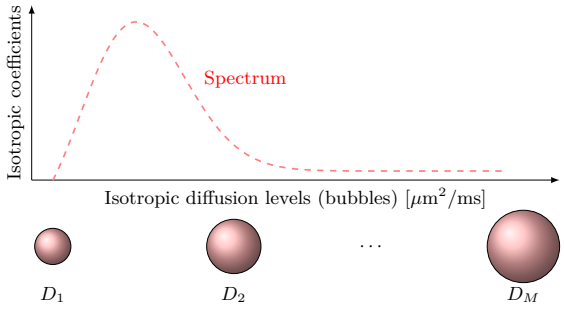

Figure 3.2 Conceptual DBM isotropic diffusion spectrum. The curve plots isotropic decomposition coefficients (along y-axis) against isotropic bubble diffusivity (equivalently, effective bubble diameter, along x-axis).

3.1.2 Mathematical formulation

Let S_k be the diffusion-weighted magnitude signal acquired with b-value b_k and and unit gradient direction $\mathbf{g_k}$ ($|\mathbf{g_k}| = 1$); let S_0 be the non-diffusion-weighted signal. We model the normalized signal S_k/S_0. For a single diffusion tensor $\mathbf{D}$, the mono-exponential relation is

$$S_k/S_0 = e^{-b_k \mathbf{g_k^T D_i g_k}} \tag{3.1}$$

Rather than a single $\mathbf{D}$, DBM represents the DWIs as the sum of the isotropic compartment by a continuum of isotropic diffusion tensors $\mathbf{D_i}$ and anisotropic adjustment part as anisotropic tensors $\mathbf{D_j}$. Thus, for the k-th acquisition (b-value b_k, unit gradient $\mathbf{g_k}$), the complete model combines both terms with noise/mismatch:

$$S_k/S_0 = \underbrace{\sum_{i=1}^{M} f_{D_i} e^{-b_k \mathbf{g_k^T D_i g_k}}}_{S_{\text{iso}}} + \underbrace{\sum_{j=1}^{N} f_{D_j} e^{-b_k \mathbf{g_k^T D_j g_k}}}_{S_{\text{aniso}}} + \epsilon_k \tag{3.2}$$

with S_0 the non-diffusion-weighted signal.

1. M and N are the numbers of isotropic bubbles and anisotropic tensors, respectively (DBM reduces to a purely isotropic model when $N = 0$);
2. $\mathbf{D_i} = D_i\mathbf{I}$ is an isotropic tensor, whereas $\mathbf{D_j} = \text{diag}(\lambda_{\parallel}, \lambda_{\perp 1}, \lambda_{\perp 2})$ is a long narrow tensor;
3. The weights satify $\sum_{i=1}^{M} f_{D_i} + \sum_{j=1}^{N} f_{D_j} = 1$.

The two terms serve complementary purposes:

1. The isotropic spectrum (S_{iso}) captures the full distribution of restricted, hindered and unrestricted water, allowing richer microstructural metrics than scalar quantities such as mean diffusivity.
2. Anisotropic adjustment S_{aniso} absorbs residual directional signal, (i) protecting the isotropic fit from bias, and (ii) retaining biologically relevant orientation information for highly ordered tissues.

Together, these components provide a more complete and biologically interpretable characterisation of neonatal brain tissue than conventional diffusion tensor models.

3.1.3 Algorithm for estimating DBM parameters

The goal is to determine the diffusivities $\mathbf{D}_i$ and $\mathbf{D}_j$ in Eq. (3.2), together with their non-negative weights f_{D_i} and f_{D_j}. We adopt a strategy (Algorithm 1): first reduce the anisotropy of DWI signal, then solve a linear problem for the isotropic spectrum using the non-negative least squares (NNLS) algorithm.

Algorithm 1: DBM Reconstruction Algorithm With Anisotropic Adjustment

Input : DWIs: $S_1, S_2, \cdots, S_n$; b values b, and b vectors $\vec{b}$
Output: f_{D_j}, f_{D_i} and metrics derived: MD_{DBM}, σ_{DBM}

Step 1/2: Obtain $f_{D_j best}$ with fixed $\lambda_{//}, \lambda_{\perp}$
Initialize $Loss_{min} = 1.01$, $f_{D_j best} = 0$, $\lambda_{//} = 3.2\mu m^2/ms$, and $\lambda_{\perp} = 0.1\mu m^2/ms$;
for $f_{D_j} \leftarrow 0.01$ **to** 0.99 *with step of* 0.005 **do**
  compute anisotropic diffusion signal $S_{aniso} = \sum_{j=1}^{N} f_{D_j} e^{-b_k \mathbf{g_k^T D_j g_k}}$;
  compute residual isotropic diffusion signals $S_{iso} = S_k/S_0 - S_{aniso}$;
  fit the isotropic tensor $\sum_{i=1}^{M} f_{D_i} e^{-b_k \mathbf{g_k^T D_i g_k}}$;
  $Loss = \frac{1}{M} \sum_{i=1}^{M} |sphericity(\mathbf{D_i}) - 1|$;
  if *(Loss > tol) and (Loss < Loss$_{min}$)* **then**
    $f_{D_j best} = f_{D_j}$, $Loss_{min} = Loss$
  else
    break
  end
end

Step 2/2: Determining Isotropic Diffusion Coefficients f_{D_i}
Set $D_1, D_2, \cdots, D_M$;
Compute S_{aniso} using $f_{D_j best}$, $\lambda_{//}$, and $\lambda_{\perp}$;
Removing S_{aniso} from S_k, got $S_{iso} = \sum_{i=1}^{M} f_{D_i} e^{-b_k \mathbf{g_k^T D_i g_k}}$;
Create design matrix $A = e^{-b\mathbf{g^T D_j g}}$;
Fit $S_{iso} = AF$, $F = [f_{D_i}, f_{D_i}, \cdots, f_{D_M}]^T$ using NNLS;
return $f_{D_i}, f_{D_i}, \cdots, f_{D_M}$ `// For later metric derivation`

$$S_k/S_0 - S_{aniso} = \sum_{i=1}^{M} f_{D_i} e^{-b_k \mathbf{g_k^T D_i g_k}} \tag{3.3}$$

$$Loss = \frac{1}{M} \sum_{i=1}^{M} |sphericity(\mathbf{D_i}) - 1| \tag{3.4}$$

Rationale for Stage A

The diffusion in brain tissues is usually anisotropic, especially for white matter. Although any residual anisotropy biases the isotropic spectrum, we first subtract DWIs arising from a single highly elongated tensor (eigenvalues of $(3.2, 0.1, 0.1)\,\mu\mathrm{m}^2/\,\mathrm{ms}$ in the thesis) [25, 174]. The anisotropic adjustment coefficient f_{adj} was looped from 0.01 to 0.99 in small steps. Optimal f_{adj} is found by enforcing the sphericity of the remaining isotropic fit, the sphericity

of 1 indicating a perfect sphere. If needed, after coarse looping feeding the optimal f_{adj_0}, a nonlinear optimization can be performed by setting boundary from $\max\{f_{\text{adj}_0} - 0.1, 0\}$ to $\min\{f_{\text{adj}_0} + 0.1, 1\}$ minimizing the loss (Equation 3.4).

Rationale for Stage B

With the anisotropic term fixed, Eq. (3.3) becomes linear in f_{D_i}. Constraining D_i to the biophysically plausible range $0.1 - 3.2\,\mu\text{m}^2/\text{ms}$ and enforcing non-negativity yields a well-posed NNLS problem whose solution defines the voxel's isotropic diffusion spectrum.

3.1.4 DBM-derived metrics

Because there is no universally agreed diffusivity cutoff that cleanly separates "restricted" from "non-restricted" diffusion within a voxel (such thresholds are protocol- and tissue-dependent), we summarize the isotropic spectrum using threshold-free distributional descriptors rather than fixed cut points (as advocated in prior work) [38–40]. For each voxel, we compute the metrics listed in Table 3.1, grouped as anisotropic metric (f_{adj}), diffusion positional metrics (D_{25}, D_{50}, D_{75}, D_{main}, D_{peak}, f_{main}, f_{peak}, and f_{fast}) and general (shape) metrics (MD_{DBM}, σ^2_{DBM}, Sk_{DBM} and K_{DBM}).

Table 3.1 DBM metrics: definitions and interpretation. Statistical moments are computed over the normalised isotropic spectrum f_{D_i}; Sk_{DBM} (skewness) and K_{DBM} (kurtosis) are dimensionless (kurtosis reported as Fisher excess unless stated). All diffusivity quantities (D, D_{peak}, $D_{1/4}$, $D_{1/2}$, $D_{3/4}$, and FWHM) are postional metrics, expressed in $\mu\text{m}^2/\text{ms}$ (i.e., 10^{-3} mm^2/s). f_{fast} sums spectral weights with $D \geq 2.5$ $\mu\text{m}^2/\text{ms}$ (free-water–like range). In this thesis, $D_{1/4} = D25 = D_{25}$, $D_{1/2} = D50 = D_{50}$, $D_{3/4} = D75 = D_{75}$.

Symbol	**Statistical definition**	**Practical interpretation**
MD_{DBM}	First moment (mean)	Mean diffusivity after aniso. adjut
σ^2_{DBM}	Second *central* moment (variance)	Overall spread of diffusivities
Sk_{DBM}	Third *standardised* moment (skewness)	Asymmetry of the spectrum
K_{DBM}	Fourth *standardised* moment (kurtosis)	Peakedness / tail heaviness
D_{peak} (D_{main})	Diffusivity at the main spectral peak	Predominant diffusion scale
f_{peak} (f_{main})	Weight at D_{peak}	Dominant diffusion fraction
FWHM	Full width at half maximum	Breadth of the main lobe
$\text{FWHM}_{\text{L/R}}$	Left / right edge of FWHM window	Low / high diffusivity limits
$D_{25,50,75}$	Diffusivity at quartile cumulative area	Quartile markers (shift with pathology)
f_{fast}	$\sum_{D_i>2.5} f_{D_i}$	Fraction of "free-water" components
f_{adj}	Weight of anisotropic adjustment tensor	Proxy for fibre content (FA-like)

These threshold-free descriptors let us detect microstructural shifts: for punctate white matter lesions, we expect, for instance, a broader FWHM and a leftward shift of D_{25}, and higher f_{fast} reflecting extra free water.

3.2 Chapter-by-Chapter Research Plan

3.2.1 Chapter 4 Quantitative Evaluation of Diffusion Bubble Model

Motivation In this chapter, we ask the question: Can DBM be a credible, spectrum-based alternative to neonatal dMRI that preserves directional information while resolving isotropic diffusion along a physiologically meaningful continuum?

Objective & Hypothesis We aim to establish DBM as a credible and robust tool for neonatal imaging by rigorously testing its properties under controlled and real-world conditions. We hypothesize that DBM will demonstrate spectral invariance to anisotropy, accurately recover known isotropic fractions, reveal distinct tissue fingerprints in vivo, and our research dMRI-25-dir protocol will have comparable metrics to clinically dMRI-32-direction acquisition protocols.

Method A multi-stage validation framework is employed:

1. **Simulations**: Forward models emulate a neonatal multi-shell acquisition to test core mechanisms: spectral invariance at fixed MD, and recovery of fast and slow isotropic pools with and without an anisotropic compartment.

2. **In-vivo Analysis**: DBM is applied to a cohort of 248 neonates to characterize tissue-specific spectral patterns (cortical GM, deep GM, WM) and developmental trajectories.

3. **Protocol Comparability**: DTI-derived metric agreement between a research dMRI-25-dir protocol and a clinical dMRI-32-dir protocol is quantified using regression, Bland-Altman analysis, equivalence testing (TOST), and intraclass correlation (ICC).

Outcomes This chapter provides a foundational proof-of-concept for DBM. We demonstrate its theoretical construct validity through simulations, its biological plausibility through distinct in vivo tissue fingerprints and age-related trends, and our proposed research dMRI acquisition protocol has robustness and equivalence to the clinical protocol. These results justify the use of DBM in the subsequent applied chapters.

3.2.2 Chapter 5 Segmentation Based on Diffusion Magnetic Resonance Imaging

Motivation In this chapter, we address a critical bottleneck: How can we perform accurate brain tissue segmentation when high-resolution structural scans are unavailable or corrupted—a common scenario in clinical practice—to fully utilize clinical scanned diffusion MRI data?

Objective & Hypothesis We aim to develop and validate a deep learning model that segments neonatal brain tissue directly from native dMRI-derived maps. We hypothesize that this diffusion-only model will perform comparably to a T2w-based baseline on internal data and achieve superior generalization on external data.

Method We train and benchmark two nnU-Net models under an identical framework:

1. **Diffusion-only Model:** Inputs are standard DTI maps (AD, RD, MD, and FA) in native dMRI space.
2. **T2w Baseline Model:** Serves as a state-of-the-art control.
3. **Comparison**: Performance is rigorously evaluated on an internal dataset (dHCP) and an external, multi-scanner dataset (CHUSJ) to test hypothesis.

Outcomes We present a diffusion-only segmentation pipeline that successfully rescues data otherwise excluded from quantitative analysis. The model demonstrates accessible performance on par with the T2w baseline internally and shows enhanced generalization externally. This tool directly enables the cohort-wide applications of DBM in Chapter 6 and expands the potential cohort for the Chapter 7 study by providing reliable tissue and structure labels for clinical-grade dMRI datasets.

3.2.3 Chapter 6 Comparative Study of Preterm and Term-born Infants

Motivation Here, we tackle a fundamental question in developmental neuroscience: Is the altered brain microstructure of preterm infants at term-equivalent age best explained by a simple delay in maturation onset (a timing shift) or by a persistently altered pace of development (a rate difference)?

Objective & Hypothesis We aim to model longitudinal microstructural trajectories from 34 to 40 weeks PMA in preterm infants and contrast them with a term-born reference to empirically distinguish between these competing hypotheses. We hypothesize that differences are primarily due to a timing shift, and that DBM will provide greater specificity than DTI in localizing residual microstructural alterations.

Method Leveraging a prospective cohort scanned in CHUSJ, with longitudinal scans (preterms at 34 and 40 weeks PMA) and cross-sectional controls (terms at 40 weeks PMA), we:

1. Map microstructural differences across tissue classes using both DBM and DTI.
2. Model developmental trajectories to test the timing-shift vs. rate-difference hypotheses.

3. Control for concurrent volumetric changes to isolate true microstructural effects.

Outcomes This chapter delivers a nuanced understanding of preterm brain development. We provide evidence supporting the dominant mechanism (timing versus rate) and identify the regions of the brain that are most vulnerable to residual alterations. Crucially, we demonstrate that DBM offers enhanced biological specificity over DTI by localizing developmental differences to specific parts of the diffusivity spectrum.

3.2.4 Chapter 7 Microstructural Characterization and Subtyping of Neonatal Punctate White Matter Lesions

Motivation In this chapter, we ask: Can the spectral sensitivity of DBM move beyond macroscopic tissue characterization to provide a quantitative, microstructural phenotype of punctate white matter lesions (PWML), thereby revealing injury-specific signatures that are invisible to conventional models?

Objective & Hypothesis We aim to characterize the microstructural signature of PWML within the optic radiation using DBM. We hypothesize that PWML will cause a leftward shift of the isotropic diffusivity spectrum (indicating increased restriction) and that DBM will outperform DTI in detecting these alterations and in distinguishing between proposed lesion subtypes.

Method We conduct a focused analysis on PWML in the optic radiation:

1. Compare DBM spectra and metrics within lesions against (i) contralateral normal-appearing tissue and (ii) healthy control tissue.
2. Benchmark the effect size and sensitivity of DBM against conventional DTI metrics.
3. Explore spectral differences between “wet” and “dry” PWML subtypes.

Outcomes We establish DBM as a sensitive tool for microstructural lesion phenotyping. We demonstrate that PWML are characterized by a specific shift in the DBM spectrum, providing a quantitative biomarker of tissue injury. This work lays the groundwork for a future, microstructure-informed classification system for neonatal brain injuries, with potential implications for prognosis and personalized medicine.

CHAPTER 4 RESULT 1: QUANTITATIVE EVALUATION OF DIFFUSION BUBBLE MODEL

4.1 Introduction

Diffusion magnetic resonance imaging (dMRI) provides non-invasive access to brain microstructure and has become a key tool for studying brain development and injury, particularly the third trimester (from 28 week of GA to birth age, Fig. 1.1), a period marked by rapid and heterogeneous microstructural changes [12, 62, 175]. Diffusion tensor imaging (DTI), as the most widely used one-tensor dMRI model, has revealed general maturational trends of decreasing mean diffusivity (MD) and increasing fractional anisotropy (FA) during this preterm-to-term period [81, 82, 90, 109]. However, it reduced the complex diffusion signal to a single tensor, conflating distinct microstructural compartments and obscuring biologically specific changes along the diffusivity spectrum [23].

Spectrum-based methods address this limitation by estimating a continuous distribution of diffusivity. These methods includes diffusion spectrum imaging (DSI), Diffusion Basis Spectrum Imaging (DBSI) and Restriction Spectrum Imaging (RSI), spherical mean spectrum imaging (SMSI) [13,27,28,105]. However, these approaches either require very dense sampling schemes with many directions and shells or high b values that are infeasible in neonatal imaging [13, 34].

In this context, we previously introduced the Diffusion Bubble Model (DBM) as a practical alternative. DBM preserves essential directional information for the characterization of white matter while representing the isotropic signal component as a continuous spectrum of diffusivity, ranging from highly restricted to fast-diffusing water pools [24]. This formulation is hypothesized to offer increased sensitivity to subtle microstructural changes associated with both typical maturation and pathology, such as punctate white matter lesion (PWML) [24].

To establish DBM as a credible tool for developmental neuroscience, a rigorous evaluation of its properties under realistic neonatal imaging conditions is essential. This study therefore aims to comprehensively validate DBM through a multi-stage framework combining simulations, in vivo analysis, and protocol comparisons. Our specific objectives are threefold: (i) to verify core model mechanisms using forward simulations emulating a widely used neonatal multi-shell acquisition; (ii) to characterize tissue-specific spectral patterns and developmental trajectories across cortical gray matter, deep gray matter, and white matter in a neonatal cohort; (iii) to assess the comparability of DTI metrics derived from a gradient direction

reduced protocol (dMRI-25-direction protocol) against a standard clinical protocol (dMRI-32-direction protocol).

We preregistered four hypotheses aligned with our objectives: (i) The isotropic spectrum remains invariant to changes in anisotropy when its mean diffusivity is held constant. (ii) An anisotropy adjusted fraction derived from DBM correlates with FA, and fast and slow isotropic fractions are recoverable with high fidelity, even in the presence of an anisotropic compartment. (iii) Cortical gray matter, deep gray matter, and white matter exhibit distinct spectral fingerprints in vivo, with age-dependent trends localized to specific regions of the diffusion spectrum. (iv) The dMRI-25-direction protocol yields diffusivity estimates equivalent to those from the dMRI-32-direction protocol, with FA differences within acceptable bounds for downstream applications.

4.2 Method

4.2.1 Subjects

Parameter optimization For DBM hyperparameter tuning progress displaying, we used one healthy, representative infant from the dHCP second release (male; gestational age at birth = 32.29 weeks; postmenstrual age at scan = 35.14 weeks). This dataset was selected for its high diffusion image quality and served only to optimize model parameters that were then held fixed for all subsequent analyzes.

In-vivo validation The primary cohort consisted of 248 singleton infants from the second dHCP release, scanned between 33 and 43 weeks PMA. The inclusion criteria were high-quality diffusion data with the radiology review scores of 1–2 and absence of sedation at scanning. These subjects were used to characterize tissue-specific DBM spectra across different tissues—cortical gray matter, deep gray matter, and white matter—and to model age-related trajectories.

Protocol comparability (within-subject paired acquisitions) To assess cross-protocol agreement, we prospectively enrolled 67 unique healthy infants at CHU Sainte-Justine (Montréal, Canada) between June 2021 and January 2025, with the approval of the CHU Sainte-Justine Recearch Center Authority. Among these enrollments, 45 scan sessions had paired, high-quality acquisitions using both diffusion protocols (the dMRI-25-direction and dMRI-32-direction schemes) suitable for comparability analyses. All infants were born between 27 and 41 weeks' gestational age and were scanned between 31 and 42 weeks PMA. The full participant list are provided in Table A.1, Table A.2 and Table A.3.

4.2.2 MRI acquisition

The complete acquisition parameters are listed in Table 5.2 of the next chapter. Here, we only describe the general settings.

For the dHCP cohort, T2-weighted images were acquired with a fast spin-echo sequence at 0.5 mm isotropic resolution, and diffusion MRI used a multi-shell scheme with 20 $b0$ volumes and three non-zero shells at $b = 400/1000/2600\,\mathrm{s/mm^2}$ (voxel size $1.17 \times 1.17 \times 1.50\,\mathrm{mm^3}$) [103].

For the CHU Sainte-Justine (CHUSJ) cohort, both a clinical 32-direction DTI sequence and a research 25-direction dMRI sequence were acquired with 2.0 mm isotropic voxels, TR / TE of 8000/81 ms, and anterior–posterior phase-encoding with a reverse-phase scan for susceptibility correction. Routine clinical T2w images were acquired alongside diffusion scans.

4.2.3 MRI processing

Full cohort-specific processing pipelines are detailed in the next chapter (dHCP: Section 5.2.3; CHUSJ: Section 6.2.3); here we summarize only the general steps.

For the dHCP dataset, T2-weighted images underwent bias-field correction using N4ITK and skull stripping using FSL-bet, followed by neonatal brain tissue and structure segmentation with Draw-EM [162,176,177]. T2-weighted image and segmentations were transformed to the dMRI space for 87-structure and 9-tissue ROI extraction. dHCP diffusion data processing was used as released (denoising, motion/eddy correction with outlier replacement, susceptibility correction) [103].

For the CHUSJ dataset, T2-weighted images received bias-field correction, skull stripping and segmentation same as dHCP [162,176,177]. The raw diffusion-weighted images were first denoised using Marchenko–Pastur principal-component analysis (MP-PCA) [178]. Susceptibility-induced distortions were then estimated and corrected with FSL TOPUP [176]. Next, all DWI volumes were rigidly aligned to the first b0 to mitigate inter-volume motion [179]. Finally, images were resampled to the same resolution as dHCP using spline interpolation [179].

After preprocessing of both dHCP and CHUSJ, the DTI metrics were reconstructed and extracted using a weighted least squares DTI algorithm [179,180]; DBM isotropic spectrum and the DBM metrics were reconstructed and extracted using our DBM algorithm and optimized parameters previously [24]. The free-water–elimination model was also estimated for simulation and in-vivo validation [181].

4.2.4 Experiments and statistics

We validated the Diffusion Bubble Model in several stages to cover the mechanism, biology, and robustness: (i) Parameter optimization; (ii) Simulation-based validation; (iii) in-vivo validation in neonates. We also performed protocol comparability to use the same data perform DTI reconstruction.

Parameter Optimization and Validation Using Representative Tissue Types

Optimal parameter selection for DBM was performed using representative voxels from three different tissue types: cortical gray matter, white matter, and cerebrospinal fluid in an example subject. This approach ensured that the model parameters were tuned to capture the fundamental diffusion properties of major neonatal brain tissues.

The anisotropic adjustment coefficient was optimized using the algorithm detailed in Section 3.1.3 (Part 1). Oriented by established diffusion properties of brain tissues, we hypothesized that CSF, characterized by isotropic diffusion and very low fractional anisotropy, would produce a value near zero f_{adj}. In contrast, WM, with its highly organized fiber tracts, was expected to exhibit a high f_{adj} value. Cortical GM, which has a more isotropic microstructure than WM but less than CSF, was expected to produce an intermediate value of f_{adj}.

The isotropic diffusion spectrum was reconstructed in a diffusivity range of 0.1 to 3.2 $\mu\text{m}^2/\text{ms}$. To determine the optimal resolution of the spectrum, we evaluated a range of diffusion interval steps (Δd): 0.15, 0.20, 0.25, 0.30, and 0.35 $\mu\text{m}^2/\text{ms}$. The objective was to identify the smallest Δd (the highest spectral resolution) that produced stable, physiologically plausible, and discriminative isotropic decomposition curves in all three types of tissue, without introducing spurious spectral noise.

Simulation-based Validation

To isolate specific biophysical drivers and verify that DBM behaves as theorized, we performed forward simulations that mirror the dHCP multi-shell acquisition. In each experiment, one parameter was varied, while others were kept fixed.

Anisotropy robustness For the anisotropy-robustness experiment, the goal was to test whether (i) the isotropic spectrum remains effectively invariant to anisotropy changes when MD is fixed, and (ii) the DBM anisotropy-adjusted fraction f_{adj} tracks FA_{DTI}.

We synthesized single prolate tensors with fixed mean diffusivity (MD = 1.5 $\mu\text{m}^2/\text{ms}$) and systematically varied fractional anisotropy (FA) from 0 to 0.7, spanning and slightly exceeding

typical neonatal corpus callosum values (FA ≈ 0.5). The eigenvalues were initialized around a neonatal white matter reference ($(\lambda_1, \lambda_{2,3}) = (2.0, 1.0)\,\mu\text{m}^2/\text{ms}$) and then rescaled as needed to preserve the target MD at each FA level; principal orientations were randomized across realizations to avoid directional bias. For each FA condition, we drew 1 000 independent noise realizations.

DBM was fitted with the same basis and regularization used in vivo, yielding the isotropic diffusivity spectrum and the anisotropy-adjusted fraction f_{adj}. A conventional DTI fit on the identical synthetic data provided FA_{DTI} as an external reference.

The spectrum and its 95% confidence intervals of different FA conditions were plotted to check if isotropic diffusion spectrum was stable or not. To examine linkage to anisotropy, we regressed anisotropy-adjusted fraction f_{adj} on FA_{DTI}, reporting slope, intercept, R^2, 95% confidence intervals.

Fast- and slow-water sensitivity For the fast- and slow-water sensitivity experiment, we simulated two-pool isotropic mixtures to test fraction recoverability and spectral localization. The slow and fast components were assigned diffusivity in physiologically plausible ranges, while the programmed fast fraction (f_{fast}, $\text{D}_{\text{fast}} = 3.0\,\mu\text{m}^2/\text{ms}$) changed from 0 to 1 with increments of 0.19.

To verify fast- and slow-water sensitivity in the presence of a directional structure, we repeated these simulations after adding a third compartment: a single anisotropic tensor ($(\lambda_1, \lambda_{2,3}) = (2.0, 1.0)\,\mu\text{m}^2/\text{ms}$, fixed weight 0.3). Acquisition sampling, noise levels, and experiments matched the fast- and slow-water sensitivity experiment without anisotropic tensor.

In-vivo Validation (Neonatal Brain Tissue Fingerprints and Age Trajectories)

To visualize fingerprint differences along the diffusivity axis, tissue-averaged spectra with 95% confidence intervals for cortical GM, WM, and deep GM were plotted. We hypothesize that DBM spectra can show tissue-specific "fingerprints" (WM narrower and right-shifted; cortex GM broader with a fast tail; deep GM intermediate).

To assess correspondence with established models, we performed ordinary-least-squares regressions at the subject–tissue level: f_{adj} versus FA_{DTI}, MD_{DBM} versus MD_{DTI}, F_{fastDBM} versus F_{fastFWE}. For each pairing, we report slope, intercept, R^2.

To model maturation (age trajectories), we fitted linear mixed-effects models with fixed effects for Tissue and Age (PMA in weeks, treated as a continuous variable). For each DBM descriptor (f_{adj}, MD_{DBM}, F_{fastDBM}), we estimated tissue-specific age slopes, obtained fitted

trajectories with 95% confidence intervals, and controlled multiplicity across metrics using FDR.

For comparison, analogous LMEs were fit for DTI (FA_{DTI}, MD_{DTI}) and FWE ($F_{fastFWE}$) to compare the direction and magnitude of age effects with DBM.

As a compact summary, we displayed a heat map of the standardized age effects across tissues (rows = metrics of DBM, DTI, FWE; columns = GM, deep GM, WM). Each cell reports a unit-less effect size $r = sign(\beta)\sqrt{R^2}$ alongside the variance explained. Positive r indicates an increase with PMA; negative r indicates a decrease. Model assumptions (linearity, residual normality) were inspected; When mild deviations were detected, results were verified with robust (sandwich) standard errors in sensitivity analyses.

DTI Protocol Comparability: CHUSJ dMRI-25-dir versus dMRI-32-dir

This experiment evaluated whether the CHUSJ dMRI-25-direction research protocol yields DTI metrics comparable to those from the clinical dMRI-32-direction protocol. Participant characteristics, MRI acquisition parameters, and data preprocessing steps for this analysis are detailed in the previous sections (Subjects, MRI Acquisition, and MRI Processing (CHUSJ)). For each subject and protocol, mean values of AD, RD, MD, and FA were calculated within white matter masks for subsequent statistical analysis.

The agreement between the two protocols was quantified using a suite of complementary statistical approaches, designed to assess different aspects of measurement concordance: linear association, absolute agreement, statistical equivalence, and reliability.

Regression Analysis We performed Deming regression (error-in-variables regression), which accounts for measurement error in both protocols, to model the relationship between the dMRI-25-dir (dependent variable) and dMRI-32-dir (independent variable) metrics. The error variance ratio was set to 1, reflecting the matched signal-to-noise ratio and identical post-processing pipelines for both acquisitions. We reported the slope (β), intercept (α), and their 95% confidence intervals for each DTI metric. Scatter plots visualized the relationship against the line of identity.

Bland–Altman Analysis Bland–Altman plots were constructed to assess absolute agreement between the protocols. For each metric, the mean bias (defined as the mean difference: dMRI-25-dir minus dMRI-32-dir) and the 95% limits of agreement (mean bias $\pm 1.96\times$ standard deviation of the differences) were calculated using WM averaged values per subject.

Equivalence Testing We employed two one-sided tests (TOST) to formally test for statistical equivalence. Equivalence bounds were prespecified based on established repeatability

data within the session: $\pm 0.05\,\mu m^2/ms$ for AD, RD, and MD, and ± 0.02 for FA. The 90% confidence interval for the mean difference was computed; equivalence was declared if this whole interval fell within the prespecified limits.

Reliability Assessment Intraclass correlation coefficients (ICC) were calculated using a two-way mixed effects model to evaluate reliability. We report two distinct metrics: (i) ICC (A,1): a two-way mixed, *absolute-agreement*, single-measure ICC, which assesses the agreement of individual measurements between protocols. (ii) ICC (C,1): a two-way mixed, *consistency*, single-measure ICC, which evaluates the stability of the subject ranking across protocols, irrespective of a systematic offset. The interpretation of ICC values followed established guidelines: < 0.50, poor; 0.50–0.75, moderate; 0.75–0.90, good; > 0.90, excellent [182].

To control the false discovery rate across the four primary DTI metrics, Benjamini–Hochberg adjustment was applied to the respective $p-$values from the equivalence tests. All regression models were inspected for standard assumptions (linearity, homoscedasticity of residuals). Where minor violations were observed, key inferences were verified using nonparametric bootstrap confidence intervals (1000 samples).

4.3 Results

4.3.1 Parameter optimization and validation using representative tissue types

Optimization of the anisotropic adjustment coefficient, from 0 to 0.99 in increments of 0.005, yielded distinct optimal values for the main types of tissue, effectively capturing their known microstructural properties (Fig. 4.1 (a)). The sphericity was maximized at 0.96 for gray matter, 0.51 for white matter, and 0.99 for CSF, corresponding to optimal anisotropic coefficients of 0.07, 0.51, and 0.01, respectively. These results align with established tissue characteristics: near-isotropic diffusion in CSF, low anisotropy in gray matter, and high anisotropy in white matter.

Regarding the robustness of the isotropic diffusivity spectra derived to the choice of diffusion interval step (Δd) of 0.15, 0.20, 0.25, 0.30 and $0.35\,\mu m^2/\,ms$ (Fig. 4.1 (b-d)), the absolute magnitudes of the spectral coefficients varied with Δd, but the overall shape of the spectra and the positions of the characteristic peaks remained highly consistent in each of the three types of tissues. This stability ensured that the discriminative features of the spectra were preserved regardless of the precise Δd value. Based on this analysis, the best resolution ($\Delta d = 0.15, \mu m^2/, ms$) was selected for all subsequent analyzes to maximize DBM spectral detail.

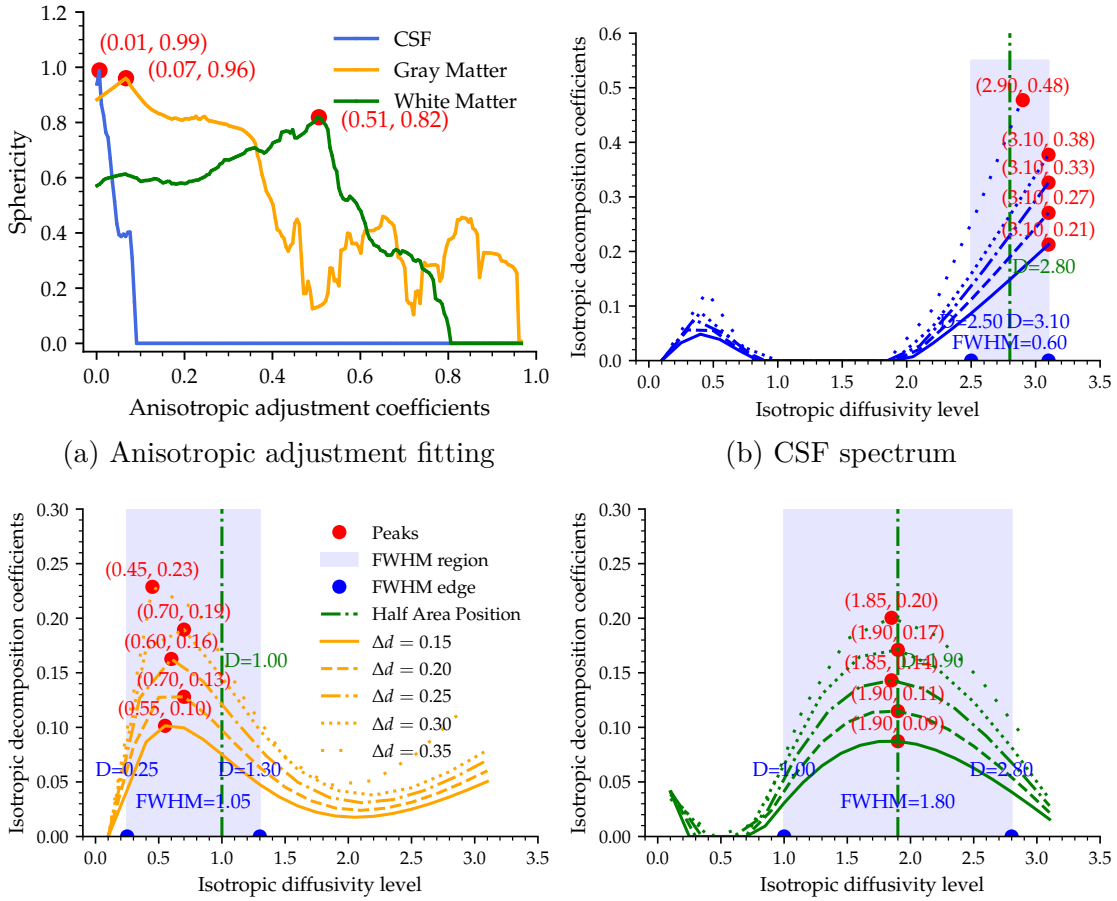

(a) Anisotropic adjustment fitting

(b) CSF spectrum

(c) Cortical gray matter spectrum

(d) White matter spectrum

Figure 4.1 DBM parameter optimization for representative neonatal brain voxels. (a) Anisotropic adjustment fitting progress. Calculation process for isotropic sphericity by looping anisotropic coefficients from 0 to 0.99 in steps of 0.005. (b) Spectrum for CSF; (c) Spectrum for cortical gray matter; (d) Spectrum for white matter.

4.3.2 Simulation-based evaluation of Diffusion Bubble Model

Simulations validated key properties of the Diffusion Bubble Model (DBM) under controlled conditions (Fig. 4.2, Fig. 4.3, and Fig. 4.4).

Anisotropy robustness (Fig. 4.2) When mean diffusivity was held constant, the reconstructed isotropic spectra remained nearly invariant across a wide range of fractional anisotropy (FA from 0 to 0.70), with only a minor deviation observed at the highest FA (Fig. 4.2 (a)). The DBM anisotropy adjustment coefficient (f_{adj}) exhibited a strong linear relationship with conventional DTI FA ($\beta = 0.78$, $R^2 = 0.95$; Fig. 4.2 (b)). This confirms that f_{adj} serves as a robust, linearly proportional proxy for FA while the isotropic spectrum remains stable.

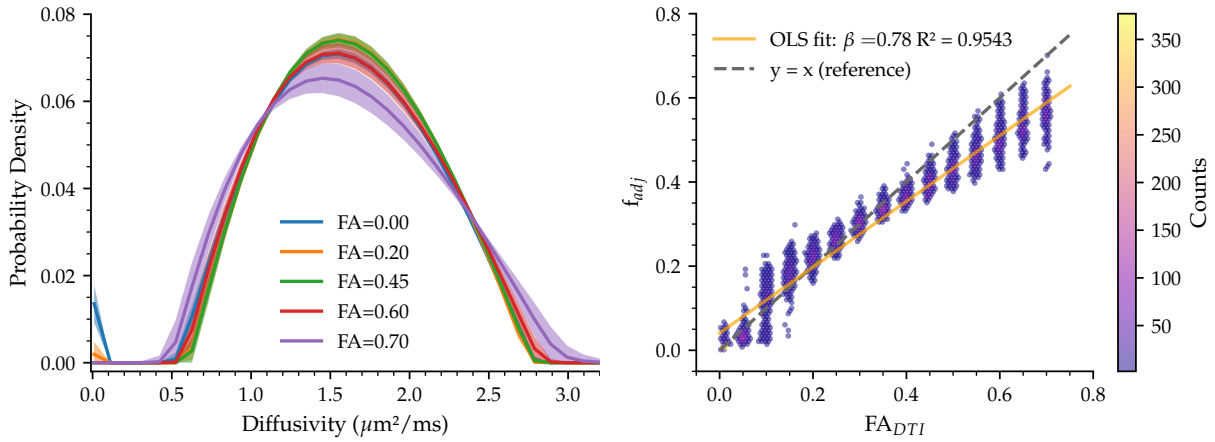

(a) DBM spectrum (b) f_{adj} vs. FA_{DTI}

Figure 4.2 DBM isotropic-spectrum stability across anisotropy levels and correspondence of DBM anisotropy index f_{adj} with FA_{DTI}. (a) Mean isotropic diffusion spectra (solid) and their 95% confidence ribbons (shaded) for five representative FA values (0.00, 0.20, 0.45, 0.60, 0.70) drawn from a Monte-Carlo anisotropy sweep (MD = 1.5 μm^2/ms, SNR = 90, 1000 noise realizations per FA). The near-perfect overlap of all curves demonstrates that the DBM isotropic spectrum remains invariant when only tensor shape changes. (b) Scatter plot (n = 15000 simulated voxels) comparing the DBM anisotropy adjustment coefficient (f_{adj}) with FA_{DTI}.

Fast- and slow-water sensitivity (Fig. 4.3) In simulations incorporating a fixed anisotropic background, DBM accurately recovered the ground-truth fractions of fast and slow isotropic pools.

1. *Fast water sweep*: Increasing the fast-water fraction v_{fast} ($D_{\text{fast}} = 3.0\,\mu\text{m}^2/\text{ms}$) produced a progressive right shift and broadening of the high-diffusivity tail of the spectrum (Fig. 4.3 (a)). DBM-estimated $\text{F}_{\text{fastDBM}}$ showed excellent agreement with the ground truth: $f_{\text{fastDBM}} = 0.82 v_{\text{frac}} - 0.02$ with $R^2 = 0.98$ (Fig. 4.3 (b)).

2. *Slow water sweep*: Increasing the slow-water fraction v_{slow} ($D_{\text{slow}} = 0.3\,\mu\text{m}^2/\text{ms}$) produced a progressive shift to the left and a tiled spectrum (Fig. 4.3 (c)). The recovery was also highly accurate ($f_{\text{slow}} = 0.57 v_{\text{frac}} + 0.01$, $R^2 = 0.97$, Fig. 4.3 (d)).

Bidirectional isotropic trade-off with and without anisotropy (Fig. 4.4) DBM maintained high fidelity in recovering isotropic fractions both in the presence and absence of an anisotropic compartment.

1. In a two-pool (slow + fast) model without anisotropy, the estimated slow fraction

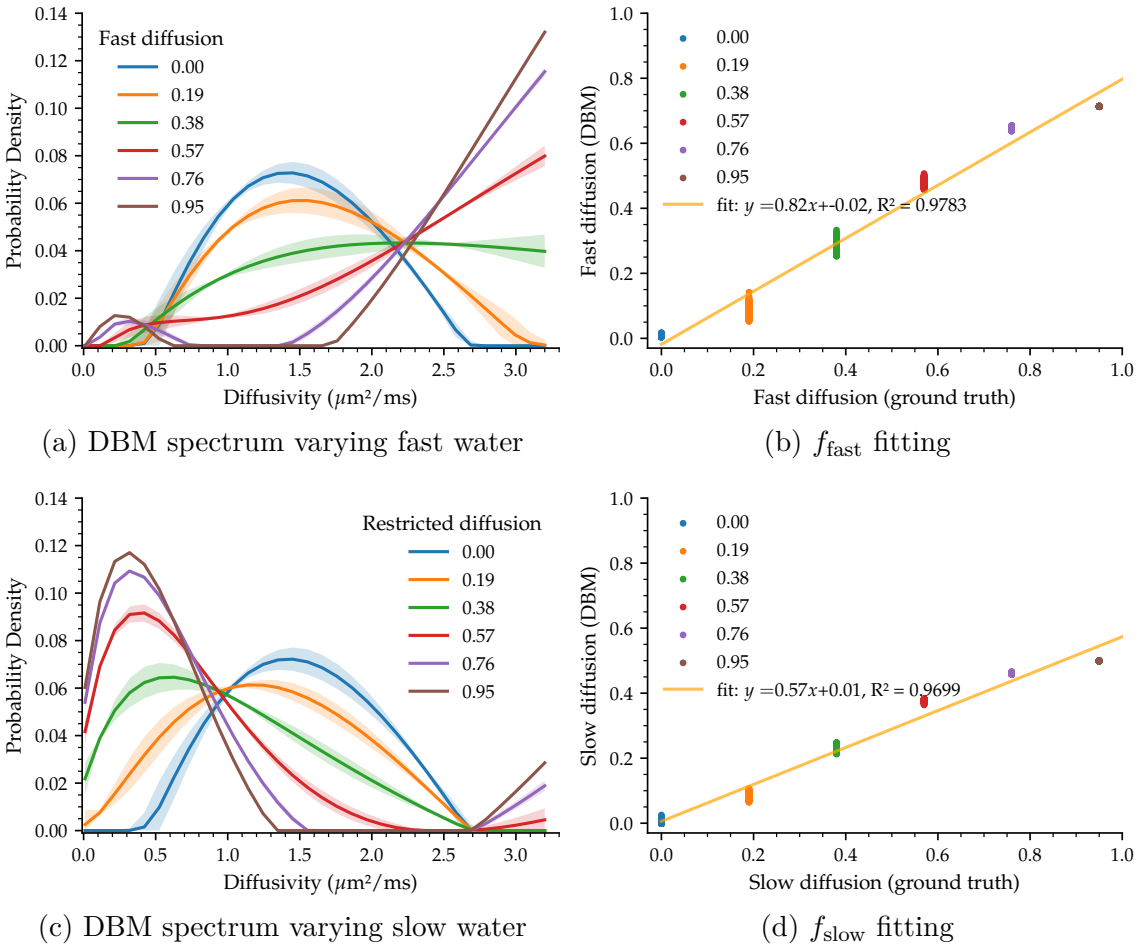

(a) DBM spectrum varying fast water

(b) f_{fast} fitting

(c) DBM spectrum varying slow water

(d) f_{slow} fitting

Figure 4.3 DBM sensitivity to opposite ends of the diffusivity spectrum: fast-water sweep (top row) versus slow-water sweep (bottom row). (a) Isotropic-spectrum curves obtained from a Monte-Carlo mixture model in which the fast-water ($D = 3.0\,\mu\text{m}^2/\text{ms}$) fraction was swept from 0 to 1 in 0.19 increments. The anisotropic signal was with a fixed anisotropic tensor $(\lambda_1, \lambda_{2,3}) = (2.0, 1.0)\,\mu\text{m}^2/\text{ms}$ and $S_0 = 1000$. (b) Corresponding quantitative accuracy: DBM-estimated fast-water fraction (f_{fast}) versus ground-truth v_{frac} for all simulated voxels. (c) Isotropic spectra from a complementary sweep in which the slow-water (restricted) fraction ($D = 0.3\,\mu\text{m}^2/\text{ms}$) was varied over the same range. (d) DBM-estimated slow-water fraction (f_{slow}) versus ground-truth v_{frac}.

closely tracked the ground truth ($f_{\text{fast}} = 0.82 v_{\text{frac}} + 0.05$, $R^2 = 0.99$). Rising slow water progressively shifts the spectral peaks to the left and eliminates the fast-tail hump.

2. In a three-component model (slow + fast + anisotropic) with the anisotropic weight fixed at 0.30, the fast fraction was recovered with equally high precision ($f_{\text{fast}} = 0.79 v_{\text{frac}} + 0.05$ with $R^2 = 0.997$, $R^2 = 0.997$). Rising slow water progressively shifts the spectral peaks to the left and eliminates the fast-tail hump. The slope did not change

much (0.82 versus 0.79) and the intercept did not change in relation to the case of two groups, demonstrating that DBM decouples the isotropic fractions from the anisotropic content.

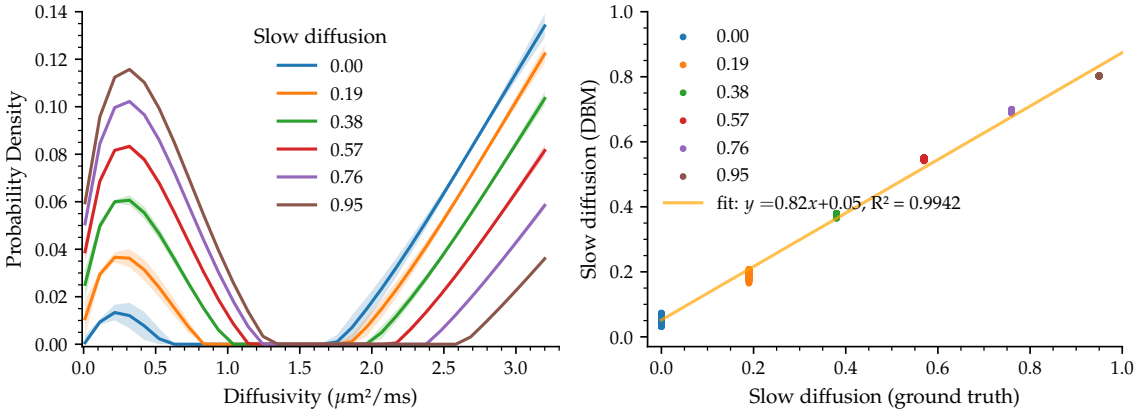

(a) DBM spectrum varying fast water

(b) f_{fast} fitting

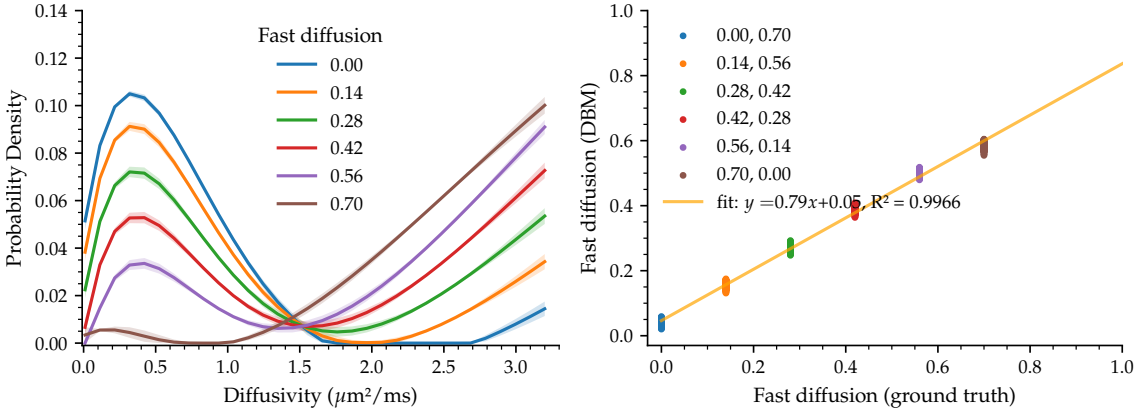

(c) DBM spectrum varying fast water

(d) f_{fast} fitting

Figure 4.4 DBM resolves isotropic mixtures with and without an anisotropic compartment. (a, b) In a two-pool model, increasing the slow fraction ($D = 0.3\,\mu\text{m}^2/\text{ms}$) shifts spectra leftward, and DBM accurately tracks the change ($R^2 = 0.99$). (c, d) Adding a fixed anisotropic tensor (weight 0.30) does not impair quantitative recovery of fast fraction ($R^2 = 0.997$), confirming that DBM effectively separates isotropic and anisotropic contributions.

4.3.3 In-vivo validation (neonatal brain tissue fingerprints and age trajectories)

Having established the theoretical properties of DBM under controlled conditions, we next evaluated its performance in-vivo across a cohort of 248 neonates (33–43 weeks, PMA).

Tissue spectra results in the full cohort (Fig. 4.5) DBM revealed distinct, tissue-specific spectral profiles in neonatal brain tissue. White matter exhibited a compact spectrum with

its peak shifted toward higher diffusivities, while cortical gray matter showed the broadest distribution with a pronounced fast-diffusivity tail, consistent with greater CSF partial volume effects. Deep gray matter displayed an intermediate profile, closely resembling WM in spectral contour. These patterns provide cohort-level spectral 'fingerprints' for each major tissue class.

Quantitative comparisons demonstrated strong agreement between DBM and conventional models across tissues (Fig. 4.5 b-d): f_{adj} versus FA ($R^2 = 0.80 - 0.93$), MD_{DBM} versus MD_{DTI} (($R^2 = 0.66 - 0.96$)), f_{fastDBM} versus $\text{f}_{\text{fastFWE}}$ ($R^2 = 0.50 - 0.60$), with interpretable offsets consistent with model definitions.

Developmental trajectories across tissues (Fig. 4.6) Between 33 and 43 weeks postmenstrual age, all tissues exhibited characteristic maturational patterns. Fast water decreased with age in all tissues (a, FWE: cortical GM $\beta \approx -0.0006$, $R^2 \approx 0.31$; deep GM -0.004 and 0.13; white matter -0.007 and 0.16). The DBM fast water showed the same sign with smaller effect sizes. The mean diffusivity decreased in all tissues for both models (DBM MD: cortical GM $\beta \approx -0.011$, $R^2 \approx 0.33$; deep GM -0.013 and 0.51; white matter -0.014 and 0.37). Anisotropy increased with age in white matter and deep GM and decreased in the cortex. Finally, the fast tail of the spectrum narrowed with age, consistent with a left-shifting sharpening isotropic spectrum.

Age effects across tissues (standardized heatmap) (Fig. 4.7) Analysis of standardized effect sizes $r = \text{sign}(\beta)\sqrt{R^2}$ revealed several key patterns:

(1) *Differential maturational pace*: DTI diffusivity showed the largest effects in deep GM (both RD and MD: $r \approx -0.82$; AD $r \approx -0.77$), smaller magnitudes in WM (RD $r \approx -0.69$, MD $r \approx -0.66$), and the smallest in the cortical GM (RD $r \approx -0.17$). DBM spectral metrics mirrored this: the fast-tail width decreased most in deep GM ($\text{FWHM}_{\text{right}}$ $r \approx -0.72$), less in WM ($r \approx -0.51$) and cortex ($r \approx -0.52$); positional indices MD_{DBM} shows similar results as MD_{DTI}.

(2) *DBM reaches comparable levels and adds spectral specificity*: FA rises with age in white matter and deep GM (both FA: $r \approx +0.71$) and and falls in cortical GM (FA $r \approx -0.59$); DBM's anisotropy adjustment coefficient f_{adj} follows the same pattern with slightly smaller magnitudes (WM: $r \approx +0.55$; deep GM: $r \approx +0.63$; cortical GM: $r \approx -0.40$). DBM mean diffusivity is also strongly age-sensitive (deep GM: $r \approx -0.71$; WM $r \approx -0.61$), approaching DTI MD. What DBM adds is "where" the change happens along the diffusivity axis. In deep GM, the age effect concentrates toward the fast-diffusivity tail: diffusion quartiles (3/4, 1/2, 1/4) gives $r = -0.72, -0.61, -0.52$), indicating pref-

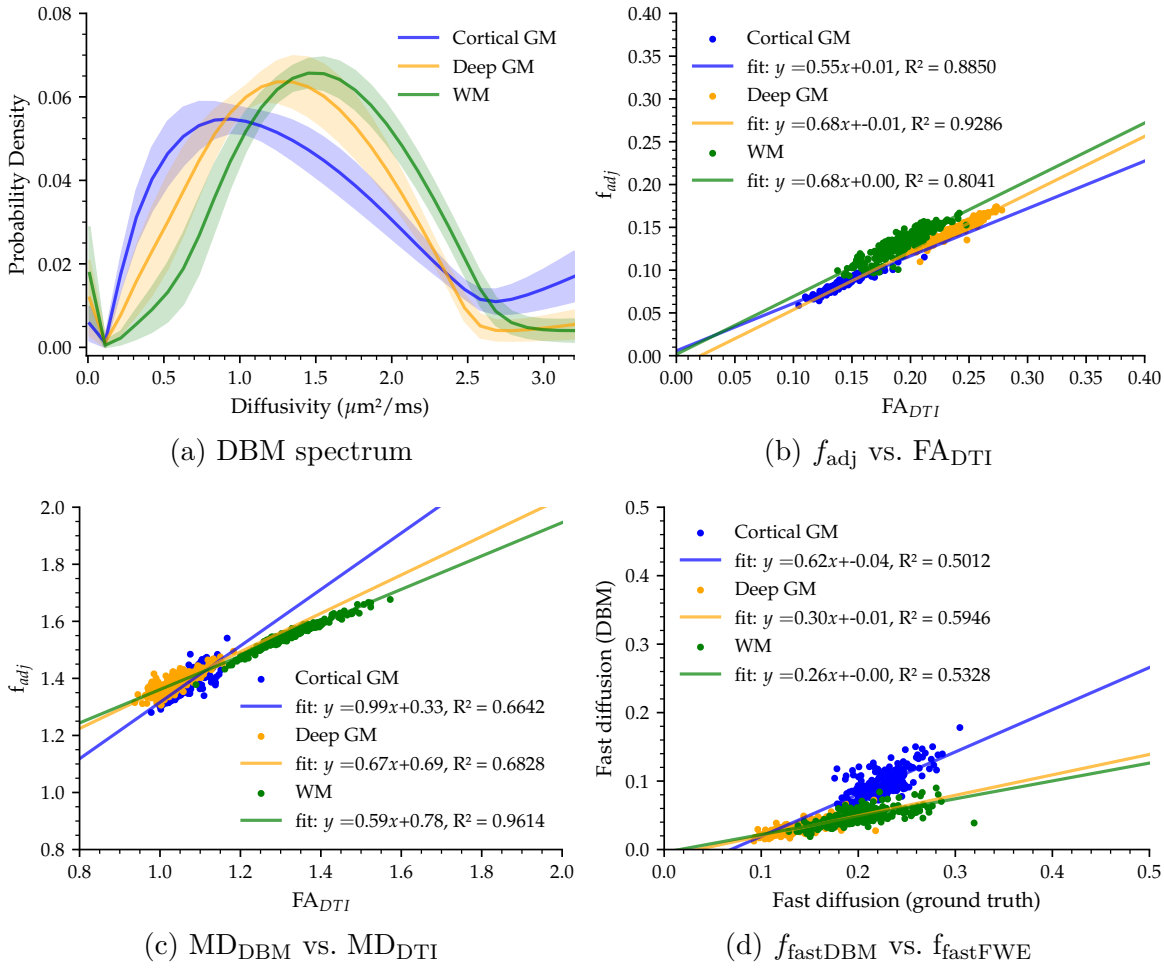

(a) DBM spectrum

(b) f_{adj} vs. FA_{DTI}

(c) MD_{DBM} vs. MD_{DTI}

(d) f_{fastDBM} vs. $\text{f}_{\text{fastFWE}}$

Figure 4.5 Cohort-level DBM isotropic spectra across tissues ($N = 248$; GA at scan: $33 - 43$ weeks). (a) Mean isotropic spectra with 95% CI ribbons for cortical GM (blue), deep GM (orange), and white matter (green). White matter exhibits a narrower spectrum with its peak shifted rightward on the diffusivity axis; deep GM is intermediate and closely follows WM; cortical GM is broader with a more prominent fast-diffusivity tail and a clear leftward tilt. (b) DBM anisotropy index (f_{adj}) versus DTI FA (FA_{DTI}): one point per subject and tissue (colored as in a). Ordinary-least-squares fits indicate excellent linear correspondence ($R^2 = 0.80 - 0.93$) with small intercepts (e.g., WM $\beta \approx 0.676$, $\alpha \approx 0.002$). (c) DBM mean diffusivity versus DTI MD: strong linear mapping in all tissues (WM $R^2 \approx 0.96$; CGM/DGM $R^2 \approx 0.66 - 0.68$) with positive offsets consistent with spectrum-weighted MD (e.g., WM $\beta \approx 0.585$, $\alpha \approx 0.776\,\mu\text{m}^2/\text{ms}$). (d) DBM fast-water versus FWE free-water: moderate-strong agreement ($R^2 \approx 0.50 - 0.60$) with small, consistent negative intercepts (≈ -0.04) and slopes < 1 reflecting DBM's broader fast-diffusivity band.

erential attenuation of faster water region with age; In white matter the pattern flips: the strongest effect is at the slowest quartile ($r = -0.54, -0.63, -0.65$), consistent with a growing slow/restricted pool as myelination progresses. As expected from the model

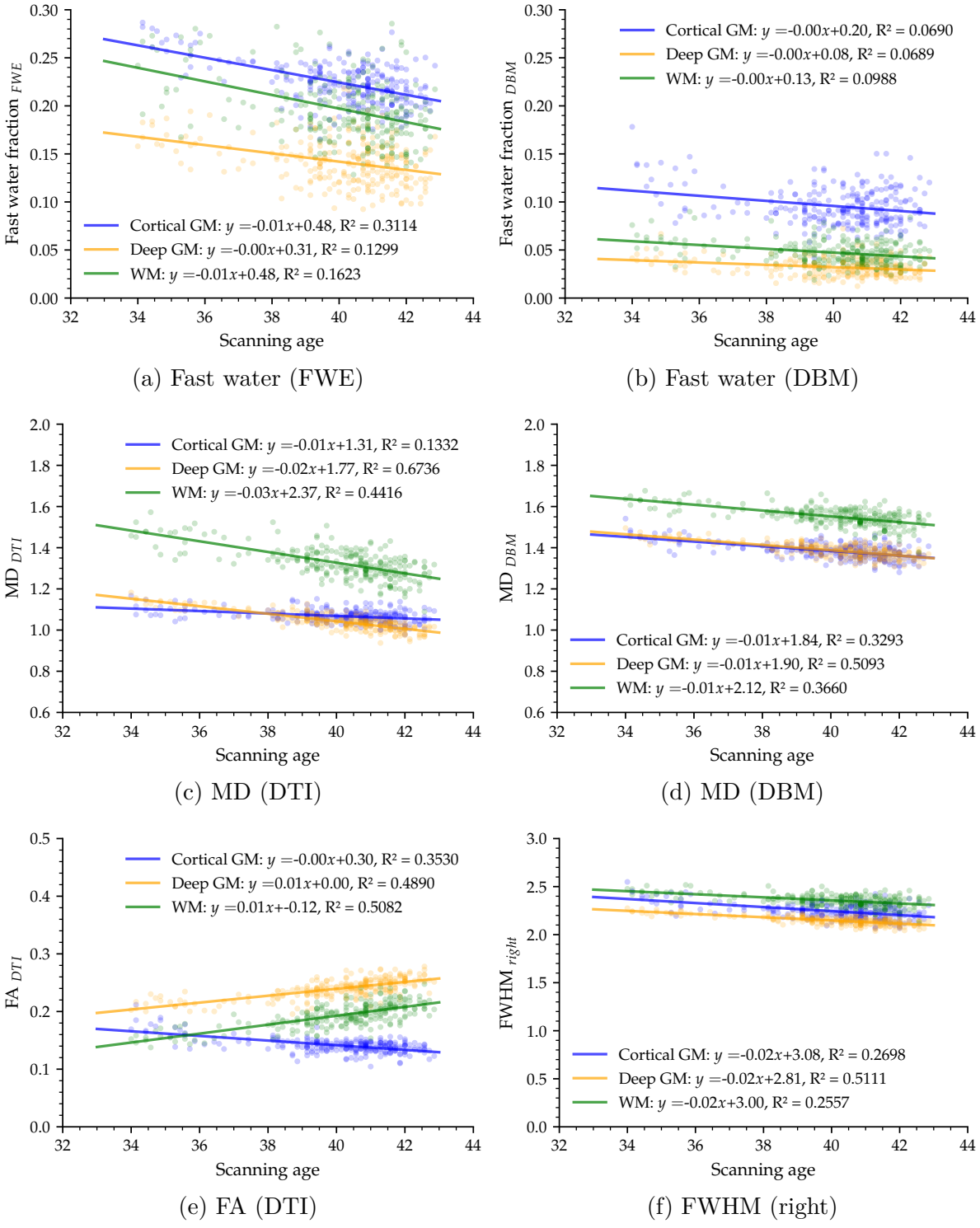

(a) Fast water (FWE)

(b) Fast water (DBM)

(c) MD (DTI)

(d) MD (DBM)

(e) FA (DTI)

(f) FWHM (right)

Figure 4.6 Developmental trajectories of key DBM/DTI metrics across tissues. (a) Fast-water (FWE); (b) Fast-water (DBM); (c) MD (DTI); (d) MD (DBM); (e) FA (DTI); (f) Spectrum width ($\mathrm{FWHM}_{\mathrm{right}}$).

definitions, DBM fast-water shows weaker but consistent declines ($r = -0.26$ to -0.31) compared with the two-compartment FWE index. DBM shape metrics align with this picture: FWHM right edge decreases and skewness moves toward zero, pointing to a narrowing spectrum and a shrinking fast tail with age.

(3) *Diffusivity-related metrics decrease and anisotropy-related metrics increase*: DTI metrics (AD, RD and MD) and DBM MD showed negative age effects in all tissues, consistent with the maturational restriction of water mobility. DBM f_{adj} and FA DTI increased with age in deep GM and WM (FA: $r \approx +0.70$ in both; f_{adj}: $r \approx +0.63$ in deep GM, $+0.55$ in WM) but decreased in cortical GM (FA: $r \approx -0.59$; f_{adj}: $r \approx -0.40$), reflecting the tissue ordering expected at term equivalent age.

(4) *Spectral-shape and positional metrics* indicated a progressive sharpening and leftward re-centring of the isotropic spectrum: the fast-tail width decreased ($\text{FWHM}_{\text{right}}$: $r \approx -0.71$ deep GM; -0.51 WM), skewness moved toward zero (WM: $r \approx +0.60$), and DBM positional indices (d_{domain}, diffusion quartiles) were strongly negative in WM ($r \approx -0.66$ for d_{domain}; -0.65, -0.63, -0.54 for 1/4, 1/2, 3/4 diffusion).

4.3.4 DTI protocol comparability: dMRI-25-dir versus dMRI-32-dir

We evaluated the agreement between the CHUSJ dMRI-25-direction protocol and a clinical dMRI-32-direction protocol in pairs of infants of the same session $n = 45$.

Regression agreement (Fig. 4.8) Scatter plots with dMRI-32-dir on the $x-$axis and dMRI-25-dir on the $y-$axis showed near-identity for diffusivity ($\beta = 0.98 - 0.99$, $\alpha = 0.03 - 0.04$, $R^2 = 0.87 - 0.95$) and a modest scaling for FA ($\beta = 0.88$, $\alpha = 0.01$, $R^2 = 0.59$):

1. AD: $y = 0.98x + 0.04$, $R^2 = 0.87$;
2. RD: $y = 0.99x + 0.04$, $R^2 = 0.95$;
3. MD: $y = 0.99x + 0.03$, $R^2 = 0.95$;
4. FA: $y = 0.88x + 0.01$, $R^2 = 0.59$.

Thus, AD, RD and MD are essentially on the identity line, whereas FA from dMRI-25-dir is slightly compressed at lower FA, as expected with fewer directions.

Bland–Altman analysis (Fig. 4.9) The Bland-Altman analysis showed minimal biases between the dMRI-25-dir and dMRI-32-dir protocols in diffusivity (Fig. 4.9 a-c, $0.005 -$

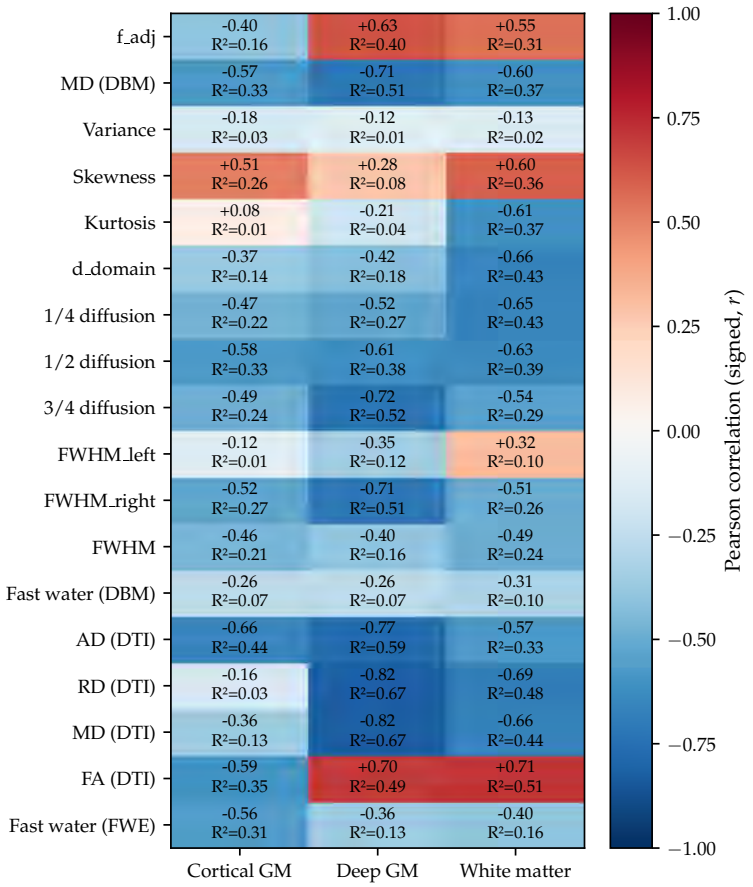

Figure 4.7 Standardized age effects across tissues for DBM, DTI, and FWE metrics. Rows: metric from DBM, DTI, FWE; Columns: cortical GM, deep GM, white matter regions. Unit-less standardized effects $r = sign(\beta)\sqrt{R^2}$ (signed Person's correlation, cell color and first line of the label) together with the variance explained were displayed each cell. Positive r indicates an increase with age; negative r a decrease.

$0.028\,\mu m^2/ms$) and narrow limits of agreement 95% ($\approx (-0.02, 0.08)$), indicating the excellent interchangeability of the dMRI-25−dir and dMRI-32−dir protocols; FA (Fig. 4.9 d) showed a modest negative bias, reflecting the same slope compression seen in the regression.

Equivalence testing (Table 4.1) Two one-sided tests (TOST) with pre-specified bounds (± 0.05 µm²/ms for AD/RD/MD; ± 0.02 for FA) confirmed statistical equivalence for all four metrics. Ninety percent of the CI for the mean differences were completely within the limits (e.g. MD: $0.020\,[0.015, 0.026]\,\mu m^2/ms$; FA: $0.020\,[0.015, 0.026]$, and both values one-sided $p-$ were < 0.001 in each case.

Reliability test (Table 4.2) Intraclass correlations (two-way mixed, absolute-agreement, single-measure; ICC(A,1)) were excellent for AD/MD/RD and moderate for FA: AD: 0.935 (95% CI $[0.88, 0.96]$); RD: 0.943 (95% CI $[0.49, 0.98]$); MD: 0.957 (95% CI $[0.77, 0.98]$); FA:

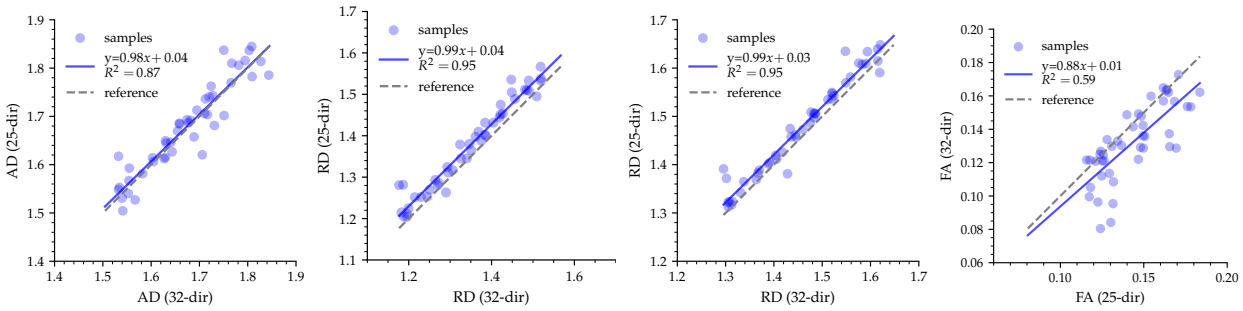

(a) AD (b) RD (c) MD (d) FA

Figure 4.8 Agreement of DTI metrics between CHUSJ 25-direction and 32-direction acquisitions (same-session pairs, $N = 45$ infants). (a) AD: $y = 0.98x + 0.04$, $R^2 = 0.87$; (b) RD: $y = 0.99x + 0.04$, $R^2 = 0.95$; (c) MD: $y = 0.99x + 0.03$, $R^2 = 0.95$; (d) FA: $y = 0.88x + 0.01$, $R^2 = 0.59$. Subject-level white-matter means are plotted with 32−dir on the $x-$axis and 25−dir on the $y-$axis; each point is one infant.

Table 4.1 TOST equivalence between CHUSJ dMRI 25-direction and 32-direction DTI metrics (paired; $N = 45$). Mean difference is Δ = dMRI-25-dir − dMRI-32-dir. AD/RD/MD in $\mu m^2/ms$; FA unitless. p-values < 0.001 are shown as "< 0.001".

Metric	Bounds	Mean Diff.	SD	90% CI	p_{lower}	p_{upper}	Equivalent
AD	[−0.050, 0.050]	+0.005	0.033	[−0.003, +0.013]	< 0.001	< 0.001	Yes
RD	[−0.050, 0.050]	+0.029	0.024	[+0.022, +0.035]	< 0.001	< 0.001	Yes
MD	[−0.050, 0.050]	+0.020	0.023	[+0.015, +0.026]	< 0.001	< 0.001	Yes
FA	[−0.020, 0.020]	−0.011	0.015	[−0.015, −0.008]	< 0.001	< 0.001	Yes

0.664 (95% CI $[0.24, 0.84]$).

The consistency ICCs (ICC (C,1)) were similarly high for diffusivity (0.975 for RD/MD) and higher than the absolute agreement for FA (0.757), indicating a stable rank order even where the absolute FA differs slightly.

4.4 Discussion

This chapter study establishes the Diffusion Bubble Model as a robust and mechanistically informative framework for neonatal diffusion MRI. Using a staged validation strategy: parameter optimization, controlled simulations, and in vivo application, we show that DBM that DBM effectively decouples isotropic diffusion changes from anisotropic effects, providing a spectrally resolved characterization of microstructural development and pathology.

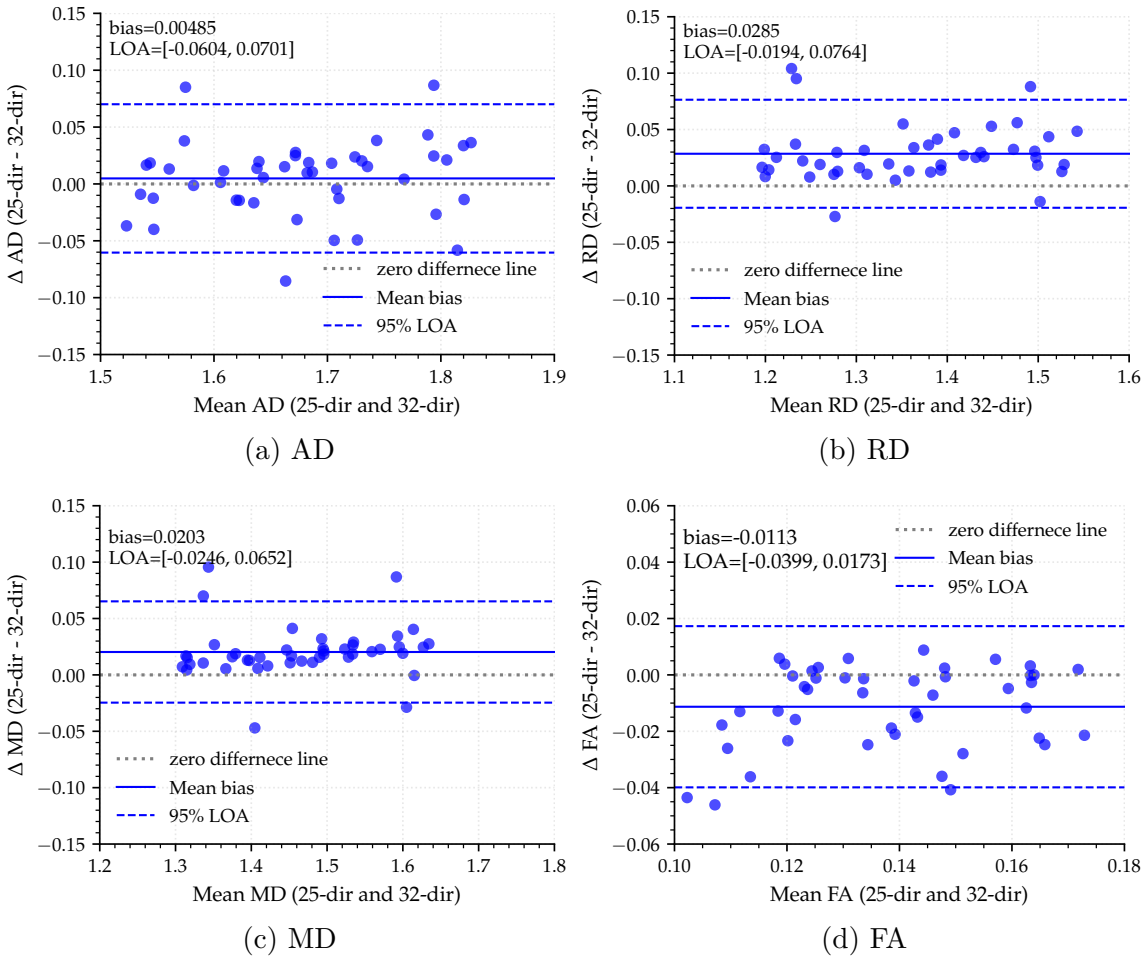

Figure 4.9 Bland–Altman agreement between CHUSJ 25-direction and 32-direction DTI metrics ($N = 45$ infants, same-session pairs). Subject-level white-matter means are plotted as difference $\Delta = 25 - dir - 32 - dir$ versus mean (25-dir + 32-dir)/2. the solid line marks the mean bias; dashed lines show the 95% limits of agreement (LOA = bias $\pm$ 1.96 SD); the dotted line is zero difference. (a) AD (μm^2/ms); (b) RD (μm^2/ms); (c) MD (μm^2/ms); (d) FA (unitless). Each point is one infant.

4.4.1 Experimental validation confirms core DBM principles

Our systematic experimental approach validated three fundamental properties of DBM:

Anisotropy robustness: The simulation experiment with fixed MD and varying FA confirmed DBM's core competency: the isotropic spectrum remained effectively invariant to anisotropy changes, while the anisotropy-adjusted fraction (f_{adj}) strongly tracked DTI-derived FA ($\beta = 0.78$, $R^2 = 0.95$). This validates DBM's ability to isolate isotropic signals from orientation-related effects, a crucial advantage over conventional metrics that conflate these dimensions. Practically, it underscores that b-value bandwidth is the primary driver for

Table 4.2 Intraclass correlation between 25-dir and 32-dir protocols at the subject level. ICC(A,1): two-way mixed, absolute agreement, single measure. ICC(C,1): two-way mixed, consistency, single measure. Interpretation: < 0.50 poor, $0.50 - 0.75$ moderate, $0.75 - 0.90$ good, > 0.90 excellent [182].

Metric	ICC(A,1)			ICC(C,1)			Interpretation
	Estimate	95% CI	p	Estimate	95% CI	p	
AD	0.935	[0.88, 0.96]	< 0.001	0.935	[0.88, 0.96]	< 0.001	Excellent
RD	0.943	[0.49, 0.98]	< 0.001	0.975	[0.95, 0.99]	< 0.001	Excellent
MD	0.957	[0.77, 0.98]	< 0.001	0.975	[0.95, 0.99]	< 0.001	Excellent
FA	0.664	[0.24, 0.84]	< 0.001	0.757	[0.60, 0.86]	< 0.001	Moderate

reconstructing the isotropic spectrum, whereas dense angular sampling is less critical for this specific target, even though it remains important for orientation-resolved modeling and tractography [23, 25, 27].

Fraction recoverability: Two-pool mixture simulations showed high-fidelity recovery of programmed fast fractions across the full physiological range ($R^2 = 0.99$-0.997) in both purely isotropic and anisotropic environments, supporting the use of DBM metrics and spectrum as geometry-light, biologically meaningful readouts. Because increases in restricted components often reflect higher cellularity, reduced extracellular space, or reactive gliosis, whereas changes in fast-diffusion water track fluid-rich compartments and edema [25, 27, 50, 127, 183], DBM's spectral parameters are well positioned to index these processes that underlie scalar DTI changes.

In vivo correspondence: The strong linear relationships between DBM and established metrics (DBM_{MD} vs. MD_{DTI}: R^2 up to 0.96; $f_{\text{fast}DBM}$ vs. $f_{\text{fast}FWE}$: slope near unity) provide crucial convergent validity. Rather than proposing to replace conventional metrics, DBM complements them by adding spectral specificity while maintaining conceptual alignment.

4.4.2 Spectral signatures reveal tissue-specific maturational patterns

Across 248 neonates, DBM revealed distinct spectral fingerprints by tissue class: white matter exhibited narrower, right-shifted spectra, whereas cortical gray matter showed broader spectra with more prominent fast tails. We observed a monotonic decline in DBM fast fraction across cortical GM, WM, and deep GM, with a reproducible ordering: GM > WM > deep GM at a give age. This ordering is physiologically plausible: cortical GM in late gestation has the largest extracellular compartment and prominent CSF partial-volume at gyral crowns, WM is progressively reducing free-water content as pre-myelinating oligodendrocytes prolif-

erate, and deep GM (e.g., thalamus, basal ganglia) is earlier-maturing and comparatively more cellular, yielding the smallest fast-water pool [4, 10, 184–187]. The observed decline in fast fraction aligns with reports of extracellular-space contraction and contemporaneous MD decreases / FA increases during late gestation, as well as prior spectrum/FWE-style analyses showing that separating the high-diffusivity isotropic signal improves biological specificity [62, 106, 188].

DBM also helps resolve a long-standing ambiguity in neonatal diffusion imaging: WM MD > GM WM (with deep GM close to cortical GM), is commonly reported, but the tensor average cannot reveal where this difference arises along the diffusivity axis. DBM shows that the WM–GM MD gap is driven primarily by a right-shift of the spectral peak in WM, not by a larger fast-water tail, indicating more hindered and less restricted tissue-dominated diffusion in WM relative to GM at this age rather than frank free-water excess [10,62,185]. By preserving the entire isotropic distribution rather than collapsing it to a single "free-water" pool, DBM clarifies the mechanistic source of the MD contrast [181, 189].

Age-trajectory analyses from 33 to 43 weeks PMA further showed regionalized spectral localization of maturation: deep gray matter changes were most strongly expressed at the fast-tail quartile ($r \approx -0.72$), consistent with early contraction of fluid-rich components in thalamus and basal ganglia, whereas in WM the most pronounced changes occurred toward the slowest quartile ($r \approx -0.65$), compatible with increasing restriction due to axonal packing and pre-myelination [4,186,187]. Importantly, the FA trajectories diverged by tissue: cortical GM FA decreased linearly with age, plausibly reflecting dendritic arborization and increasing orientation dispersion that reduce anisotropy in the cortical ribbon, while deep GM and lobar WM FA increased linearly, with deep GM often exceeding lobar-average WM within this window due to earlier maturation and coherent thalamocortical projections, even though major WM tracts (e.g., internal capsule) can display high FA locally [4, 10, 186, 187, 190]. Additionally, these patterns support a posterior-to-anterior hierarchy and a timing-shift account of prematurity effects developed in the next chapter, while illustrating how spectral localization sharpens inferences that would otherwise be flattened by tensor averages [88, 190, 191]. This spectral resolution offers a more nuanced view of maturational processes than the uniform decreases in MD (and increases in FA) captured by DTI alone.

4.4.3 Clinical translation and protocol considerations

The current 25-point (dMRI-25-dir) protocol ($\approx$ 4 min) fits the constraints of neonatal time and SNR while supporting DTI and providing sufficient b-value leverage for DBM's isotropic spectrum. Directions follow an icosahedral scheme for stable tensor estimation under limited

time [192], with low–moderate b-values ($\leq 800\text{s/mm}^2$) to maintain SNR and safety in newborns. The idea of using 25 DWI points with linearly increasing b value but in different direction is from DBSI [193]. In practice, this captures the fast-diffusion tail that DBM is sensitive to and yields acceptable DTI maps. The agreement with a standard 32-direction clinical protocol was strong for diffusivity metrics ($R^2 = 0.87$–0.95, narrow Bland–Altman limits; ICC up to 0.96), supporting regional analyses, while a modest FA compression ($y = 0.88x + 0.01$) advises caution for absolute FA comparisons across protocols [22].

Practical caveats First, tractography has not been validated with 25 directions; orientation estimation depends critically on angular density, and more directions may be required for reliable fiber reconstructions. Second, the simulations here were multi-shell, while the clinical scheme is not multi-shell; a systematic comparison of DBM spectra between clinical used acquisition and multi-shell acquisitions is needed to quantify protocol—induced changes and establish harmonization procedures. Short, targeted optimization–directional uniformity in direction, b-value placement tailored to the end points of the DBM, and cross-protocol calibration—should further improve performance without sacrificing clinical feasibility [24, 193].

4.4.4 Limitation and future direction

Despite strong validation, several limitations of the current implementation of the DBM warrant consideration. (i) Validation relied on low–to–moderate b-values; model performance under higher diffusion weighting, broader b-value bandwidth or denser angular sampling remains to be systematically evaluated. (ii) A single fixed prolate tensor was used for the anisotropy adjustment. Although sufficient for neonatal tissue with modest FA, coupling effects may bias the recovered isotropic spectrum in regions of high anisotropy. Adaptive or multi-basis corrections could improve robustness across tissue types. (iii) Benchmarks were limited to DTI and FWE. Future comparisons with other microstructural models (such as NODDI and RSI) will help delineate DBM's unique sensitivity profile. (iv) Validation focused on late gestation infants; earlier developmental stages and broader pathological conditions were not explored.

Future work should therefore go in several directions. (i) Optimize the placement of b-values and angular sampling to jointly serve DTI and DBM to maximize clinical efficiency. (ii) Develop region–aware anisotropy adjustments (e.g., small number of tensors or data–driven and adaptive axial diffusivity) to improve spectrum fidelity across tissue classes. (iii) Compare DBM to NODDI, RSI and related frameworks under matched acquisitions. (iv) Translating DBM into open-source, harmonized pipelines for multi-site neonatal cohorts to establish nor-

mative references and to link spectral metrics with long-term neuro-developmental outcomes.

4.5 Conclusion

This chapter provides multi-level evidence that the Diffusion Bubble Model offers a spectrally localized, biologically interpretable characterization of neonatal brain microstructure. Simulations demonstrated that DBM's isotropic spectrum is robust to anisotropy at fixed MD while an anisotropy-adjusted term tracks FA; mixture experiments showed high-fidelity recovery of compartment fractions across the physiological range; and in-vivo analyses revealed tissue-specific spectral patterns and age-dependent shifts that align with, yet surpass in specificity, conventional DTI summaries. An efficient 25-direction acquisition delivered diffusivity metrics in close agreement with a standard 32-direction protocol, underscoring clinical viability.

Beyond confirming expected trends, DBM clarifies where along the diffusivity axis maturation and pathology emerge—disentangling peak shifts from fast-tail changes that tensor averages cannot resolve. This capacity to localize effects within the isotropic spectrum elevates the biological meaning of diffusion readouts and provides a consistent bridge to complementary models. The technical and biological foundations established here enable the next chapters, where DBM is paired with automated segmentation for large-scale analyses and applied to both typical maturation and neonatal brain injury in preterm and term infants.

CHAPTER 5 RESULT 2: SEGMENTATION BASED ON DIFFUSION MAGNETIC RESONANCE IMAGING

5.1 Introduction

Magnetic resonance imaging (MRI) is an non-invasive tool for characterizing neonatal brain tissues and structures [10, 23]. In particular, diffusion magnetic resonance imaging (dMRI) is widely utilized in neonatal practice, offering unique sensitivity to tissue microstructure at a neurocellular scale [16, 23]. Accurate multiclass segmentation of the neonatal brain is essential for the quantitative analysis of neonatal brain development, disease, and injury. However, this task remains particularly challenging due to the inherently low tissue contrast and high noise levels in neonatal scans, compounded by the frequent absence of high-resolution anatomical images in clinical settings [194, 195].

In recent years, deep convolutional neural networks have dramatically advanced the state of the art in brain MRI segmentation of different age groups, effectively displacing traditional methods such as time-consuming manual delineation and threshold-based techniques prone to high false positive rates [140, 156, 161, 194, 196]. This powerful technique has shown success in a wide range of tasks, from basic tissue classification to the segmentation of complex anatomical structures [168, 196–198]. However, in the newborn population, research efforts remain predominantly focused on structural imaging (T1- and T2-weighted), with considerably fewer studies venturing to train models directly in diffusion space [10, 162, 163]. This gap is noteworthy, as clinical dMRI—often comprising single- or few-shell diffusion tensor imaging (DTI) acquisitions—is widely available and inherently coregistered with the quantitative maps (e.g., mean diffusivity, fractional anisotropy) used for downstream analysis [11]. A diffusion-native segmentation strategy could reduce interpolation and registration error, improve fidelity for diffusion-based studies, and expand inclusion when structural images are degraded or missing [165, 194, 195]. This scenario is a common clinical predicament: In our cohort, for example, subjects 14/88 (16.0%) did not have T2w images or the quality of T2w is not good enough for segmentation, but had high-quality dMRI data, making them ineligible for conventional segmentation pipelines.

To address this methodological gap and practical need, this study aims to develop a diffusion-only segmentation pipeline capable of providing reliable neonatal brain tissue labels across scanners and protocols. In addition, we seek to rigorously benchmark its performance against a conventional T2w-based baseline using both in-domain data (the developing Human Connectome Project, dHCP) and cross-scanner data (CHU Sainte-Justine Hospital, CHUSJ). To

this end, we train a diffusion-only-based nnU-Net model that consumes DTI-derived maps (axial, radial, and mean diffusivity, and fractional anisotropy, namely AD, RD, MD, and FA) to predict anatomical labels directly in the native dMRI space. A T2w baseline nnU-Net model, trained under identical supervision and framework, serves as a baseline, allowing a controlled comparison of the intrinsic information content and generalization capacity of each modality.

We hypothesize that the diffusion-only model will not demonstrate poorer performance compared to the T2w baseline on internal data, while achieving better generalization on external data, due to elimination of intersequence registration errors and improved inherent alignment with diffusion-derived quantitative contrasts [170]. This work not only validates an alternative segmentation pathway, but also promises to rescue valuable clinical data that would otherwise be excluded from quantitative analysis.

5.2 Method

5.2.1 Datasets and cohort definition

Internal dataset (training/validation/testing) (Table 5.1): We used the developing Human Connectome Project data (dHCP, Release 2, scan age between 37 and 43 weeks GA) [103, 162]. Subjects passed quality control with radiology review socre 1–2 for dMRI and T2w. Train, validation, and test partitions were made at the subject level (no slice and scan leakage).

External dataset (hold-out generalization) (Table 5.1): We evaluated on prospectively acquired infants at CHU Sainte-Justine (CHUSJ, Montreal) scanned on GE Discovery MR750 and Siemens Skyra systems. Each session included a research dMRI-25-dir sequence and, when available, a routine clinical single-shell dMRI-32-dir sequence plus a clinical T2w. For this chapter, the two CHUSJ cohorts were combined into a single external test set; no further split or tuning was performed on CHUSJ. When both protocols were available for a subject, only the dMRI-25-dir research was used.

5.2.2 MRI acquisition

dHCP Protocol: T2w images were acquired using a fast spin-echo sequence with 0.5 mm isotropic resolution. dMRI was a multi-shell acquisition, including 20 $b0$ and 3 non-zero shells (including 400/1000/2600 s/mm^2), with voxel size $1.17 \times 1.17 \times 1.50\,\text{mm}^3$. Detailed acquisition parameters are in Table 5.2.

Table 5.1 Demographic characteristics of the three neonatal cohorts used for model development and evaluation. *dHCP-T-Train* is the internal dHCP cohorts used for training, validation, and internal testing. *SJ-T-Test1/2* are out-of-center cohorts scanned at CHU Sainte-Justine on GE and Siemens systems, respectively, serving as external test sets. Values are mean ± SD. GA = gestational age; N = number of subjects.

Cohort	N	Gestational age (wk)		Birth weight	Scanner	Study role
		At birth	At scan	kg		
dHCP-T-Train	152	39.4 ± 0.9	40.9 ± 1.4	3.30 ± 0.57	Philips Achieva	Train/val/test
SJ-T-Test1	24	39.3 ± 0.8	40.8 ± 1.3	3.30 ± 0.57	GE MR750	External test
SJ-T-Test2	24	39.4 ± 0.9	40.9 ± 1.4	3.30 ± 0.57	Siemens Skyra	External test

CHUSJ Protocol: Both clinical (dMRI-32-dir) and research (dMRI-25-dir) diffusion sequences were acquired with 2.0 mm isotropic voxels, TR/TE 8000/81 msand an anterior-posterior (AP) phase-encoding direction with a single reverse-phase (PA) b0 volume for susceptibility distortion correction. Routine clinical T2w images were acquired alongside the diffusion scans. Full parameters are listed in Table 5.2.

Table 5.2 MRI acquisition parameters for the internal dHCP cohorts and external CHU Sainte-Justine (SJ, CHUSJ) cohorts. Each newborn was scanned on a single system (GE or Siemens) but received three sequences: a high-resolution TurboRARE T2-weighted scan and two diffusion scans: one with 32 gradient directions at $b = 700\,\mathrm{s/mm^2}$ and one with 25 directions at $b \leq 800\,\mathrm{s/mm^2}$. All sequences share the same spatial resolution to match the dHCP diffusion voxel size and facilitate cross-scanner comparison.

Scanner (3T)	Sequence	Resolution ($\mathrm{mm^3}$)	TR/TE (ms)	Diffusion scheme
Philips Achieva	T2w (FSE)	$0.50 \times 0.50 \times 0.50$	12 000/156	–
	2D EPI (dMRI-3-shell)	$1.17 \times 1.17 \times 1.50$	3 800/90	20 $b0 + b400, 1000, 2600$
GE Discovery 750	T2w (TurboRARE)	$1.0 \times 0.75 \times 0.75$	5 067/160	–
	2D EPI (dMRI-32-dir)	$2.00 \times 2.00 \times 2.00$	8 000/81	2 $b0 + 32$ dir $b = 700$
	2D EPI (dMRI-25-dir)	$2.00 \times 2.00 \times 2.00$	8 000/81	3 $b0 + 25$ dir, $b \leq 800$
Siemens Skyra	T2w (TurboRARE)	$0.625 \times 0.625 \times 2.0$	11 270/90	–
	2D EPI (dMRI-32-dir)	$2.00 \times 2.00 \times 2.00$	8 000/81	2 $b0$ +32 dir $b = 700$
	2D EPI (dMRI-25-dir)	$2.00 \times 2.00 \times 2.00$	8 000/81	3 $b0$ +25 dir, $b \leq 800$

5.2.3 Preprocessing

Structural (T2w) Preprocessing T2w images underwent the following steps: (i) Bias-field correction using N4ITK and skull-stripping; (ii) Segmentation with Draw-EM to obtain the standard 87-label neonatal atlas and the companion 9-tissue atlas [162, 177]; (iii) For CHUSJ, T2w volumes were optionally reconstructed to isotropic spacing using a validated

super-resolution procedure when needed [199, 200]; the same Draw-EM pipeline was then applied [162, 177].

Diffusion (dMRI) Preprocessing dMRI data were processed as follows: (i) Denoising (dHCP: per consortium pipeline; CHUSJ: Patch2Self [201]); (ii) Motion/eddy-current correction with outlier replacement; susceptibility correction with topup/eddy using the PA b0 field [104]. Gradient reorientation and table consistency checks were applied [103, 162]. (iii) Resampling to the nnU-Net target spacing (dMRI space) kept consistent within each dataset. (iv) DTI fitting with weighted least squares (DIPY 1.8.0) [179]. To ensure protocol comparability with CHUSJ single-shell acquisitions, dHCP tensors were fit using $b \leq 1000\,\mathrm{s/mm^2}$ (the higher-b shell was excluded for DTI reconstruction). (v) Scalar maps AD, RD, MD, and FA were computed for all subjects

Registration: To guarantee identical supervision across modalities, the Draw-EM T2w segmentations were transformed to dMRI $b0$ space via rigid + nonlinear registration (ANTs) [103, 202]. Label interpolation used nearest-neighbor. These dMRI-space labels served as ground truth for both the diffusion-based and the T2w-based models. All transformations were saved for reproducibility.

5.2.4 Label definitions and model inputs

Labels The 87 Draw-EM regions were merged across hemispheres to yield 44 anatomical labels (Table A.4). For hierarchical evaluation, these were further aggregated into 15 lobar/structure groups and 8 fundamental tissue classes (WM, cortical GM, deep GM, cerebellum, brainstem, hippo-amyg, ventricles, CSF) (Table A.5). A complete label mapping is provided in the Supplementary Materials (link).

Model inputs Two distinct input configurations were used:

1. *dMRI model*: A 4-channel input comprising the four simple DTI-derived metrics: AD, RD, MD, and FA maps. Each channel was z-scored within the brain mask on a per-subject basis.

2. *T2w baseline*: A single-channel input of the T2w image, identically z-scored within the brain mask.

Critically, both models were trained to predict labels in the native dMRI space, ensuring an identical evaluation framework.

5.2.5 Network architecture, training and inference

We used the nnU-Net v2 framework, which automatically configures key parameters such as patch size, network topology, and training schedule based on input data. The core architecture was a 3D full-resolution U-Net with the following specifics:

1. Architecture: A five-stage encoder-decoder cascade. Each stage consisted of two 3×3×3 convolutional layers, followed by instance normalization and Leaky ReLU activation (slope = 0.01). The number of features started at 32 in the first stage and doubled at each downsampling step ($32 \rightarrow 64 \rightarrow 128 \rightarrow 256 \rightarrow 320$), mirroring in the decoder.

2. Optimization: Training used stochastic gradient descent (SGD) with Nesterov momentum 0.99; The initial learning rate was 0.01 with polynomial decay (power 0.9). The loss function was an equally weighted sum of Soft Dice loss and cross-entropy loss (Loss = 0.5 × Soft-Dice + 0.5 × cross-entropy). Mixed-precision training was used to accelerate the computation.

3. Cross-validation and ensembling inference: Models were trained using a 5-fold cross-validation scheme on the internal dHCP dataset. For final inference, an ensemble of the five cross-validation models was created by averaging their softmax probability outputs.

Segmentation accuracy was evaluated voxel-wise across three anatomical hierarchies: the primary 44-label set, the 15-group aggregation, and the 9-tissue map. We report the Dice Similarity Coefficient (Dice) as the primary endpoint, supplemented by Precision, Recall, 95th percentile Hausdorff Distance (HD_{95}), and Average Surface Distance (ASD). Metrics were calculated for each subject and summarized throughout the cohort as median and interquartile range (IQR), unless otherwise stated.

All models were trained on NVIDIA RTX-3060 GPUs ($\geq$ 8 GB). The software environment included PyTorch v2.7.1, DIPY 1.8.0. A fixed random seed (42) was used for all data splitting and stochastic processes.

5.2.6 Experimental design and statistical analysis

To verify stable optimization and guard against fold idiosyncrasies, we performed five-fold cross-validation on the training/validation split and reported the mean and standard deviation of performance across folds. The final hypothesis tests and error analyzes were conducted in held-out internal (dHCP) and external (CHUSJ) test sets that were not used for training or model selection.

To test our hypothesis that diffusion-only model is no worse than the T2w baseline model in the internal test, a paired one-sided t-test ($\text{Dice}_{\text{diffusion}} \geq \text{Dice}_{\text{T2w}}$, $p < 0.05$, if it does not meet the norm distribution, Wilcoxon would be used) was performed to compare the differences of all test subjects using two models.

To test our hypothesis that diffusion only model is better than T2w baseline model in external test, a paired one-sided t-test ($\text{Dice}_{\text{diffusion}} > \text{Dice}_{\text{T2w}}$, $p < 0.05$, if it does not meet the norm distribution, Wilcoxon would be used) was performed to compare the differences of all test subjects using two models with $p < 0.05$.

In addition, to better evaluate the dMRI performance, the global performance was profiled by reporting the mean and standard deviation for all metrics across the cohort. Furthermore, a detailed anatomical breakdown was performed by aggregating the 44 labels into 14 key anatomical regions and 8 fundamental tissue classes, allowing us to identify specific structures where each model excelled or faltered. To diagnose the nature and source of segmentation errors, particularly under domain shift, we generated and qualitatively analyzed row-normalized confusion matrices for 8 tissue classes. Finally, a visual assessment of the segmentation outlines was performed on representative subjects of both cohorts to provide a qualitative context for the quantitative findings and to illustrate the practical implications of the observed metric differences.

5.3 Results

5.3.1 Five-fold cross-validation performance

Table 5.3 Mean dice similarity coefficient (DSC) across five validation folds for each segmentation protocol. "44 labels" = full anatomical parcellation; "9 tissues" = tissue-level segmentation. Values range from 0 (no overlap) to 1 (perfect overlap).

Modality	**Individual Folds**					**Mean Dice**	**SD**
	Fold 1	Fold 2	Fold 3	Fold 4	Fold 5		
T2w-baseline (44 labels)	0.93	0.93	0.93	0.92	0.92	0.93	0.001
dMRI-proposed (44 labels)	0.88	0.88	0.88	0.88	0.87	0.88	0.004
T2w-baseline (9 labels)	0.97	0.97	0.96	0.97	0.96	0.96	0.001
dMRI-proposed (9 labels)	0.94	0.94	0.94	0.94	0.93	0.94	0.002

Five-fold cross-validation on the training set (Table 5.3): Both networks generalize consistently across folds:

1. For the full 44-label parcellation, the T2-weighted baseline averages 0.93 Dice with a very small fold-to-fold SD (0.004), whereas the diffusion-only model achieves 0.88 Dice ($SD = 0.004$). The around 5-percentage-point gap mirrors the outcome seen on the internal held-out test set.

2. When the task is coarsened to nine main tissue classes, the performance increases for both inputs: 0.96 Dice for the T2w model and 0.94 Dice for the dMRI model. The gain reflects the reduced complexity of the boundary at the tissue level.

3. The narrow standard deviations (< 0.01) in all rows indicate that neither model is sensitive to the particular fold split, suggesting that the training dataset is sufficiently large and the optimization procedure is stable.

These cross-validation results confirm that the diffusion-based network is competitive with the structural baseline, especially for tissue-level segmentation, while the T2w model retains a small but consistent advantage for the finer 44-structure task.

5.3.2 Internal (dHCP) and external (CHUSJ) test-set performance

Table 5.4 Internal dHCP test-set: segmentation performance of the diffusion-only model versus the T2-weighted baseline. Mean ± SD of six segmentation metrics computed over all 44 anatomical labels for the held-out dHCP test subjects. ΔMetric is the mean difference (dMRI – T2w). One-sided paired $t-$tests were performed with a zero-point non-inferiority margin (the diffusion model must equal or exceed baseline); "Decision" indicates whether non-inferiority was achieved at $\alpha = 0.05$ (✓= non-inferior, ✗ = not demonstrated).

Metric	T2w-baseline	dMRI-proposed	Δ Metric	$p-$value	Decision (test)
Dice	0.93 ± 0.00	0.88 ± 0.01	-0.05 ± 0.01	< 0.0001	Inferior ✓
Precision	0.93 ± 0.00	0.88 ± 0.01	-0.05 ± 0.01	< 0.0001	Inferior ✓
Recall	0.93 ± 0.00	0.88 ± 0.02	-0.05 ± 0.01	< 0.0001	Inferior ✓
HD_{95} (mm)	1.18 ± 0.01	1.21 ± 0.05	$+0.04 \pm 0.05$	$= 0.0014$	Inferior ✓
ASD (mm)	0.15 ± 0.01	0.27 ± 0.03	$+0.12 \pm 0.03$	< 0.0001	Inferior ✓

Across all six metrics (Table 5.4): Diffusion-only model scores lower than the structural baseline; the mean Dice difference is -0.05. Because the non-inferiority margin was set to 0 percentage-points (the dMRI model must be at least as good as T2w), the one-sided tests reject non-inferiority for every metric. Boundary (HD_{95}, ASD) and volumetric (VAE) errors also favor the T2w pipeline. These results confirm that, inside the dHCP domain, the structural model remains the stronger choice.

Table 5.5 External CHUSJ test-set: segmentation performance of the diffusion-only model (dMRI-proposed) versus the T2-weighted baseline (T2w-baseline). Mean ± SD of six segmentation metrics computed over all 44 anatomical labels for the external CHUSJ test subjects. ΔMetric is the mean difference (dMRI – T2w). One-sided paired $t-$tests were performed with a zero-point non-inferiority margin (the diffusion model must equal or exceed baseline); "Decision" indicates whether non-inferiority was achieved at $\alpha = 0.05$ (✓= non-inferior, ✗ = not demonstrated).

Metric	T2w-baseline	dMRI-proposed	Δ Metric	$p-$value	Decision
Dice	0.71 ± 0.08	0.78 ± 0.02	0.07 ± 0.08	0.0001	Non-inferior ✓
Precision	0.81 ± 0.05	0.77 ± 0.02	-0.04 ± 0.05	0.9998	Non-inferior ✗
Recall	0.68 ± 0.08	0.79 ± 0.01	0.10 ± 0.08	< 0.0001	Non-inferior ✓
HD_{95} (mm)	2.79 ± 0.95	1.65 ± 0.09	-1.14 ± 0.93	< 0.0001	Non-inferior ✓
ASD (mm)	0.58 ± 0.16	0.58 ± 0.05	0.02 ± 0.15	0.7278	Non-inferior ✗

In the CHUSJ cross-scanner cohort, the diffusion model gains +0.07 Dice and +0.10 Recall over the baseline T2w while reducing HD_{95} and VAE by approximately half. Given the 0 pp margin, noninferiority is demonstrated for Dice, Recall, HD_{95} and VAE; Precision and ASD remain statistically tied to the baseline. The diffusion model therefore generalizes better across vendors, outperforming or matching the structural approach on four of six metrics under the stricter zero-margin criterion.

On dHCP data (Fig. 5.1): Both the T2w-baseline and diffusion-only pipelines segment lobar GM, WM and key subcortical structures with near-perfect accuracy. Dice never drops below 0.87, and for 10 of 14 regions the diffusion model reaches the ≥ 0.90 "excellent" threshold.

Applied to the CHUSJ cohort (Fig. 5.2): Performance decreases for both inputs, but the drop is markedly greater for the structural pipeline: Only the four of fourteen diffusion classes and the three of fourteen T2w classes remain above the 0.90 benchmark. However, the diffusion model maintains a score ≥ 0.78 for every region and exceeds the structural baseline in ten of fourteen classes. In particular, the brain stem Dice rises by 45% and the hippocampus and amygdala by 16%, rescuing two areas where the T2w model suffers its steepest losses.

In particular, the standard deviation of the T2w predictions widens noticeably in the subcortical and frontal and posterior cortices, whereas the diffusion bars remain compact. These patterns reinforce the conclusion that diffusion-derived contrast is both more accurate and more stable under cross-scanner conditions.

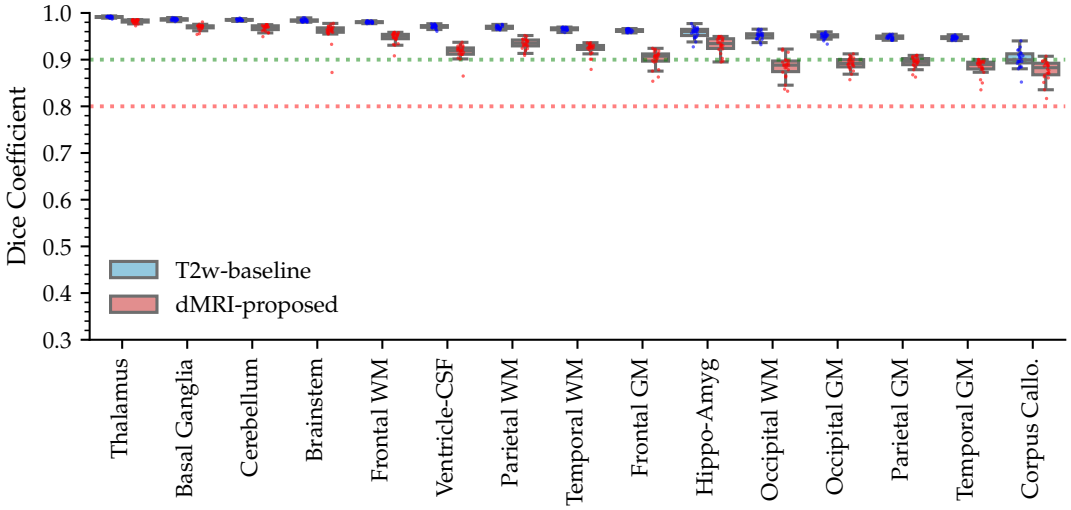

Figure 5.1 Per-class Dice coefficients for 14 aggregated regions – internal dHCP test set. Horizontal bars are sorted in descending order of the T2-weighted Dice. Green and red dotted lines mark Dice = 0.90 and Dice = 0.80, respectively. All T2w scores exceed 0.90; the diffusion model also exceeds 0.90 in 10/14 regions and remains ≥ 0.87 elsewhere (corpus callosum). The thalamus is the best-segmented structure (T2w 0.99, dMRI 0.98); the corpus callosum is the most challenging (T2w 0.90, dMRI 0.87).

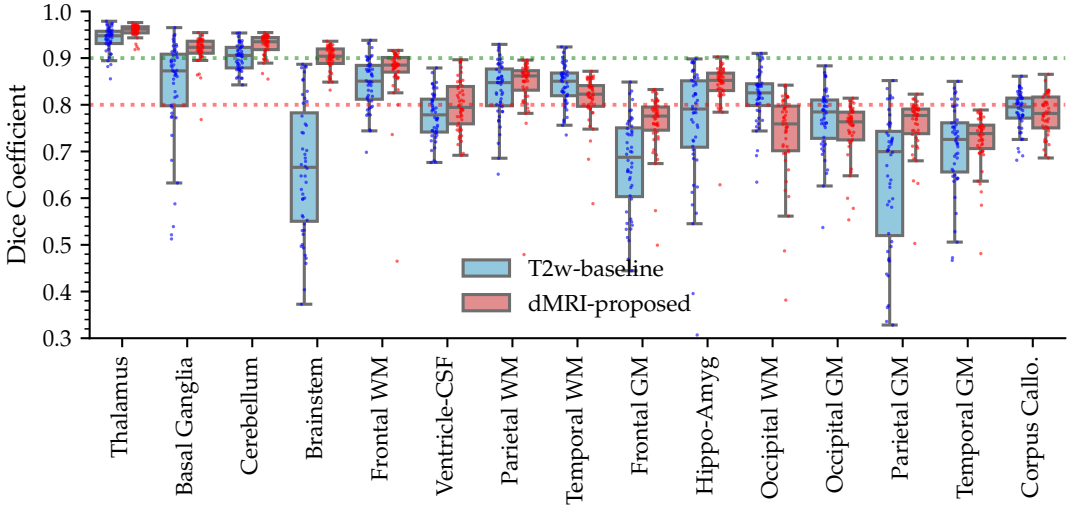

Figure 5.2 Per-class Dice coefficients for the same 14 regions–external CHUSJ test set. Bars appear in the same anatomical order as Fig. 5.1 to facilitate comparison. The vendor shift lowers accuracy for both models, pushing several T2w classes below the 0.90 threshold. By contrast, the diffusion-based model retains$\geq$ 0.80 Dice in every region and surpasses the structural baseline in hippocampus + amygdala, brain-stem, cerebellum, deep GM and CSF.

5.3.3 Qualitative assessment of segmentation

Comparison of two pipelines on a representative dHCP subject (Figure 5.3): Both pipelines trace the cortical ribbon with subvoxel precision (dark green arrow) and delineate the thalamus cleanly (light green arrow); in the mid-sagittal slice the automated contours even bridge a small discontinuity present in the Draw-EM reference. The near-identical outlines visually confirm the high Dice scores reported for the internal set (Table 5.5).

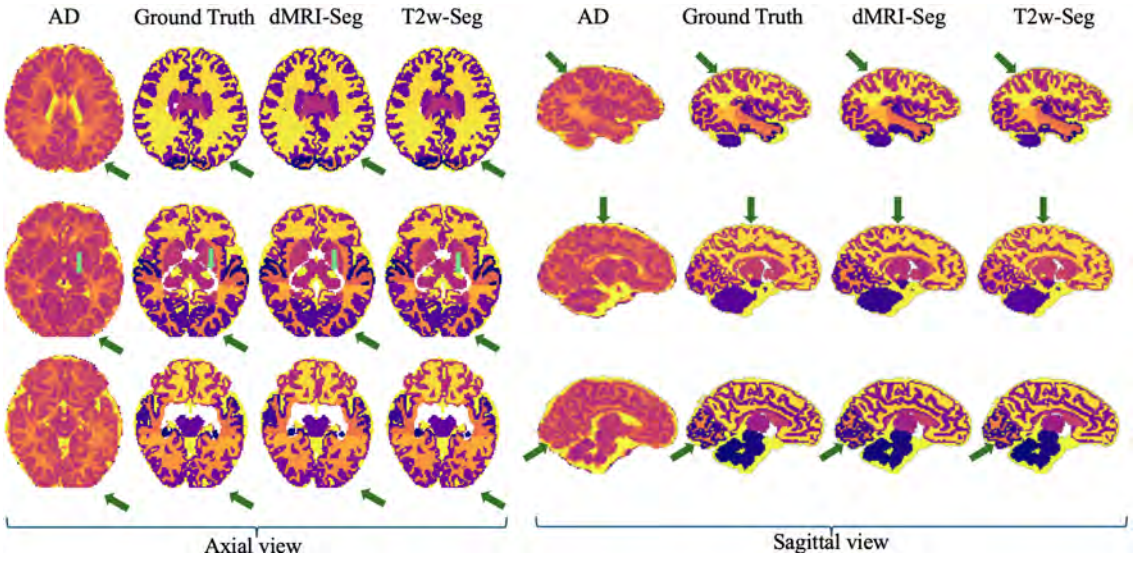

Figure 5.3 Representative internal-cohort infant (dHCP, subject ses-31801): three axial slices (left block) and three sagittal slices (right block). For each slice the four panels show (1) axial-diffusivity map, (2) Draw-EM reference, (3) Diffusion MRI prediction (Dice = 0.89) and (4) T2-weighted prediction (Dice = 0.94). Subject: Term male infant (ses-31801) were scanned at 40 weeks 6 days GA and born at 40 weeks 2 days GA. Both models reproduce a continuous cortical-GM ribbon (dark-green arrow) and accurately delineate the thalamus region (light-green arrow); the mid-sagittal contours even correct a small gap in the manual reference.

Typical segmentation quality in Siemens data from the external CHUSJ test set (Fig. 5.4): The diffusion model maintains an unbroken cortical GM band, whereas the T2w model shows clear fragmentation (dark green arrow). It also labels the thalamus correctly, while the structural model misses a substantial portion of that nucleus (light green arrow). These qualitative differences echo the numerical results in Table 5.5 (the dMRI segmentation gains 7% Dice overall) and highlight the robustness of diffusion-based segmentation when structural contrast deteriorates.

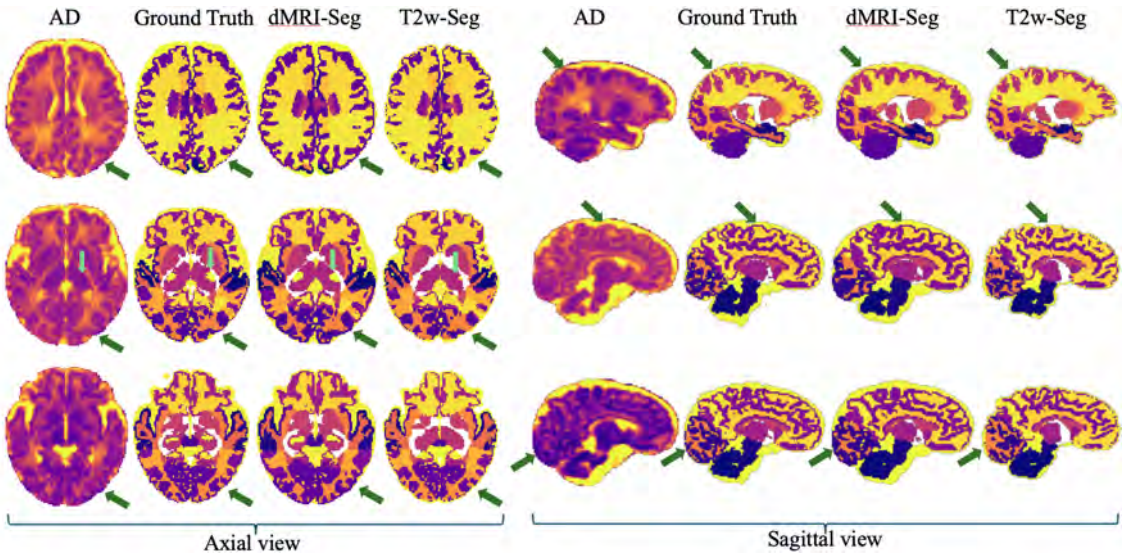

Figure 5.4 Representative external-cohort infant (CHUSJ, Siemens Skyra): three axial slices (left block) and three sagittal slices (right block). Within each slice, from left to right: axial diffusivity map, ground-truth labels, dMRI-based prediction (Dice = 0.79), and T2w-based prediction (Dice = 0.77). Subject: Male infant scanned at 41 weeks 6 days (GA); born at 34 weeks 5 days (GA). Green arrow: dMRI segmentation preserves a continuous cortical-gray-matter ribbon that is fragmented in the T2w prediction. Light-green arrow: dMRI segmentation correctly identifies the thalamus, which is missed by the T2w model.

5.3.4 Tissue-level performances

Internal dHCP set (Fig. 5.5): T2-weighted baseline outperforms the diffusion model in all eight tissues. The largest Dice gaps occur in the cortical GM and CSF (-9.2% each), whereas the deep GM and the cerebellum differ only by -2.3%. All differences are statistically significant ($p < 0.05$).

The confusion matrix in Fig. 5.6 (a) confirms near-perfect performance: every class exceeds the accuracy of 0.94 rows, with the highest cerebellum (0.99) and the lowest hippocampus-amygdala (0.94). The diffusion model (Fig. 5.6 (b)) remains robust accuracies ≥ 0.86 and cerebellum still 0.97, but shows more mixing between ventricles and CSF and between the hippocampus-amygdala and adjacent cortical GM.

External CHUSJ set (Fig. 5.6, bottom row): Performance drops for both models when applied to Siemens data. The T2w model is especially affected, losing 18% Dice overall and showing three major failure modes:

1. The accuracy of the brain stem falls to 0.48, with 29% of its voxels mislabeled as cerebellum (Fig. 5.6 (c)).

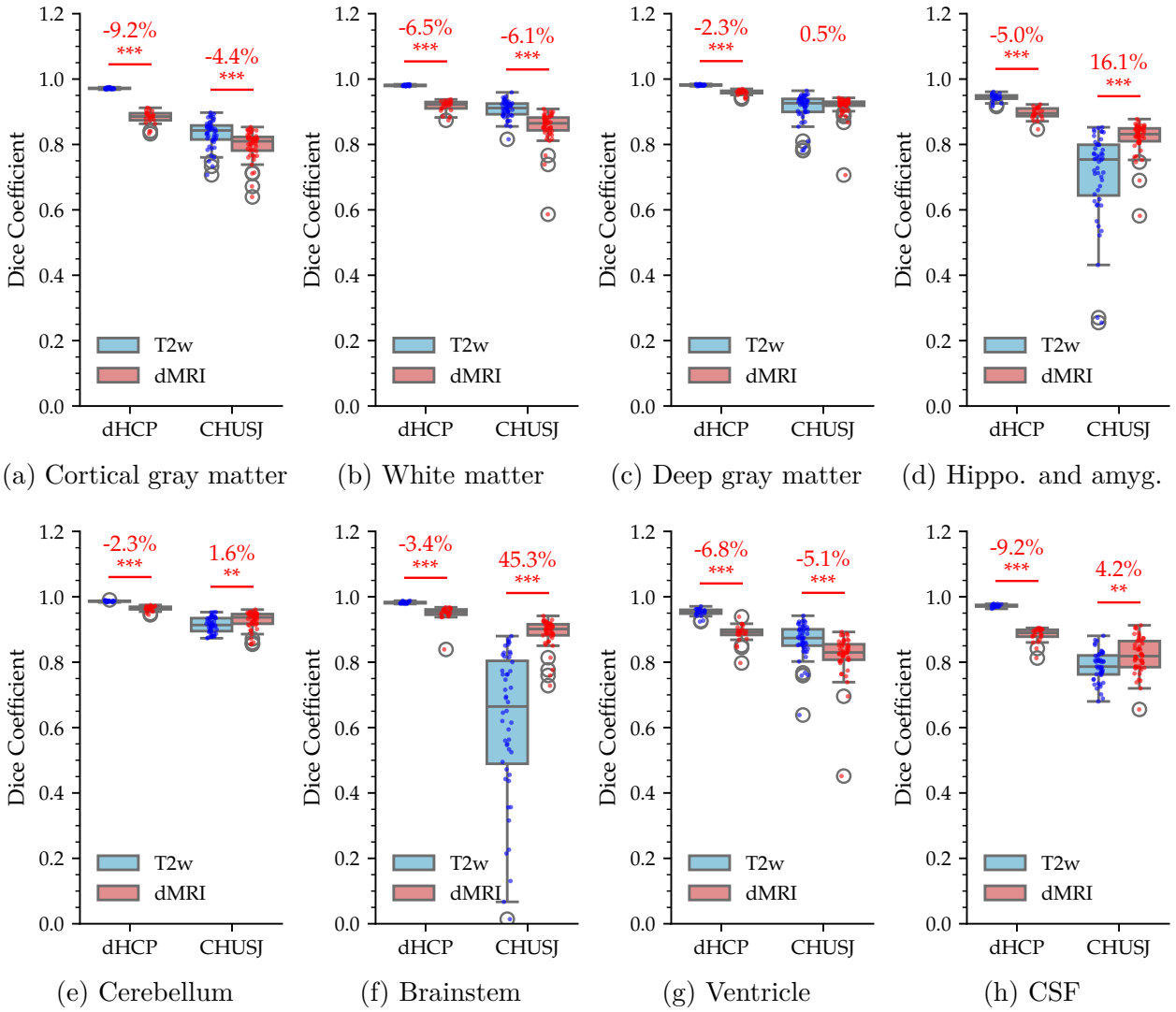

(a) Cortical gray matter (b) White matter (c) Deep gray matter (d) Hippo. and amyg.

(e) Cerebellum (f) Brainstem (g) Ventricle (h) CSF

Figure 5.5 Tissue-level Dice comparison on internal (dHCP) and external (CHUSJ) cohorts. Dice similarity for eight neonatal tissue classes: (a) cortical gray matter, (b) white matter, (c) deep gray matter, (d) hippocampus + amygdala, (e) cerebellum, (f) brain-stem, (g) lateral ventricles, (h) extra-ventricular CSF. For each class two colour-coded box-plots are shown: blue for T2w-based segmentation and red for dMRI-based segmentation. Left pair = dHCP internal test set; right pair = CHUSJ external set. Boxes mark median ± IQR, whiskers = 1.5× IQR, circled dots = outliers. Above each pair: percentage gain/loss of the diffusion model relative to T2w and paired two-tailed t-test significance ($*$ $0.01 < p < 0.05$, $**$ $0.001 < p < 0.01$, $***$ $p < 0.001$, no mark $p > 0.05$).

2. The hippocampal + amygdala drops to 0.59, mislabeled mainly as cortical GM (17%) and white matter (15%).

3. The cortical GM decreases to 0.76 due to leakage into white matter (14%) and CSF (9%).

In contrast, the diffusion model improves or matches T2w in five of the eight tissues (deep GM +0.5%, hippocampus + amygdala +16.1%, cerebellum +1.6%, brain stem +45.3%, CSF +4.2%). Dice remains lower for cortical GM (−4.4%), white matter (−6.1%) and ventricles (−5.1%), but the net effect is a statistically significant gain in mean Dice (+7%, Table 6-2). The confusion matrix (Fig. 5.6 (d)) shows that the brain stem and cerebellum are now well separated (row accuracy 0.83 and 0.97 respectively). Ventricles and CSF remain the weakest classes (row accuracy 0.76 each), with most errors arising from partial-volume voxels misassigned to cortical GM.

These figures visually support the quantitative tables:

1. *Internal data*: structural contrast still yields the highest Dice, but diffusion segmentation is competitive ($\leq 5\%$ gap) and anatomically coherent.

2. *External data*: diffusion contrast generalizes much better; the dMRI model rescues brain stem and limbic structures that the T2-weighted model does not recognize in single-shell scans.

3. Overall: diffusion-based segmentation offers a more scanner-agnostic solution, trading a modest in-domain Dice loss for substantial cross-domain gains, an outcome critical for multicenter neonatal studies.

5.4 Discussion

This chapter presents the development and validation of T2w and diffusion-only segmentation models for the neonatal brain. We compared two otherwise identical 3D nnU-Net pipelines for neonatal brain segmentation: T2w-baseline and diffusion-only model using DTI metrics, across three levels (44 labels, 14 aggregated regions, 9 tissue classes) on an internal dHCP set and a cross-scanner CHUSJ set. The results supported our hypothesis and showed that both models achieve strong internal performance and acceptable external generalizability, establishing a practical tool for enabling microstructure analysis in cohorts with missing structural scans.

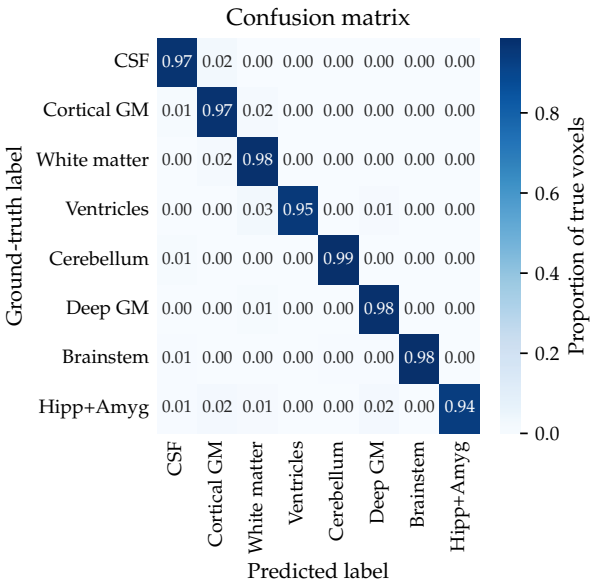

(a) T2w-internal test (dHCP)

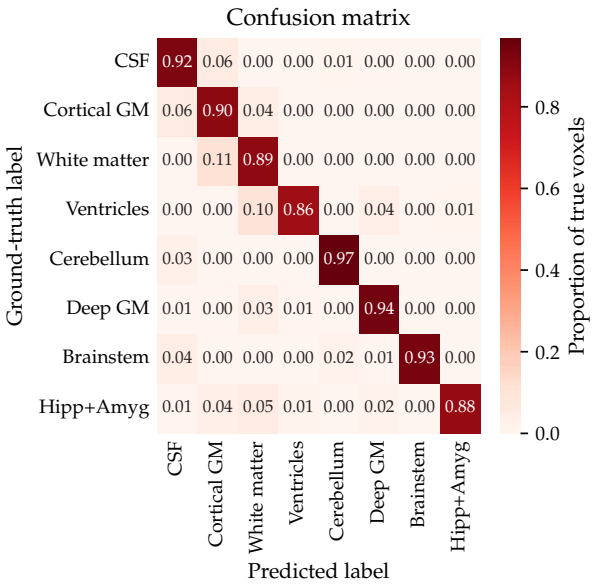

(b) dMRI-internal test (dHCP)

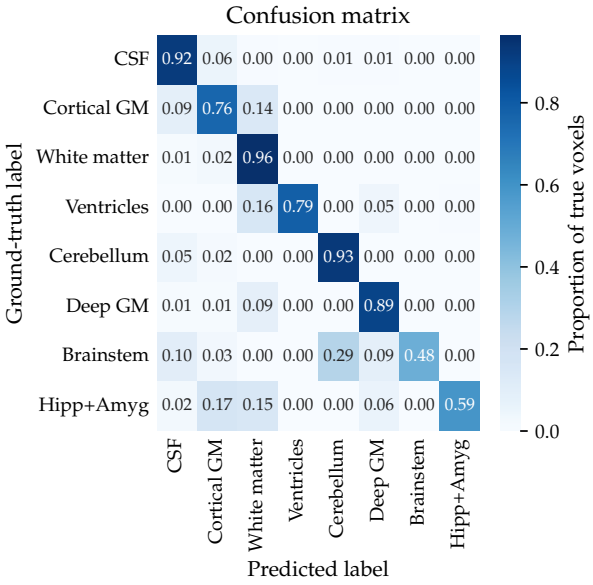

(c) T2w-external test (CHUSJ)

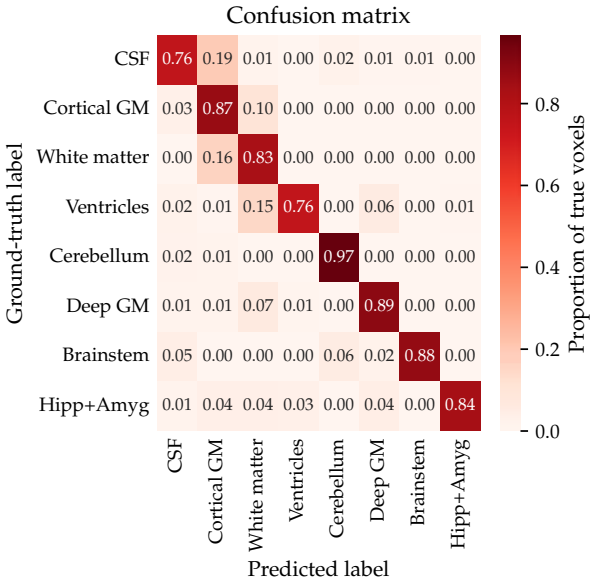

(d) dMRI-external test (CHUSJ)

Figure 5.6 Row-normalized confusion matrices for eight tissue classes. Voxel-wise classification performance for the two models. (a) T2w-based model – internal dHCP test set (blue); (b) dMRI-based model – internal dHCP test set (red); (c) T2w-based model – external CHUSJ test set (blue); (d) dMRI-based model – external CHUSJ test set (red). Rows = ground-truth class, columns = predicted class. Values are normalised so each row sums to 1, indicating the proportion of voxels from a given class assigned to every class.

Internal and external performance Internally, both models performed competitively. Our T2w segmentations (Dice > 0.90 across 14 labels) and dMRI results (Dice ≥ 0.87 on 10/14 labels) fall within and close to the established range reported in the infant neuroimaging literature (Dice $0.90-0.96$) [156, 163]. When evaluated on the out-of-domain CHUSJ cohort, performance declined (14−class: T2w 0.71, dMRI 0.78; 8-class: dMRI 0.87), reflecting the typical pattern in multicenter neonatal studies: strong in-domain performance followed by a measurable but manageable drop externally [163, 203, 204]. Our diffusion-only external Dice of $0.78-0.87$ aligns with reports from subcortical segmentation studies, which achieved Dice of 0.78 externally, increasing to $0.85-0.90$ after harmonization or fine-tuning [203]. Notably, our task is more challenging with different imaging contrast, more labels, and neonatal data, yet we achieved comparable generalization. This supports our claim that the dMRI model generalizes acceptably despite neonatal-domain shifts caused by acquisition heterogeneity, labeling protocols, and age-dependent contrast variations [162].

T2w outperforms dMRI internally but generalizes less well As expected, T2w MRI outperformed diffusion-derived inputs on internal evaluation (44-label Dice 0.93 vs. 0.88). This is attributable to several factors: (i) Neonatal structural pipelines are optimized for high-resolution T2w anatomy, while diffusion labels are transferred via registration, introducing residual distortion and label noise [177, 205]. (ii) Tissue boundaries exhibit stronger contrast in T2w than in scalar dMRI maps [206]. (iii) In addition, structural T2w volumes are reconstructed to 0.5 mm isotropic while neonatal dMRI is typically 1.5 mm ($1.17 \times 1.17 \times 1.5\,\text{mm}^3$ after preprocessing), increasing partial-volume effects [162].

However, the diffusion-only model generalized better externally, with a 10% Dice drop compared to 22% for T2w. This is likely because T2w contrast is highly scanner-specific, while DTI-derived scalars (FA, MD, AD, RD) are nominally intensity-standardized. Simple z-score normalization may not fully harmonize T2w differences across sites. The Multi-site infant T2w benchmarks also report notable cross site degradation unless explicit harmonization or adaptation is used [163, 203, 204, 207]. More surprising was that the diffusion model still lost 10% Dice, and we had expected a smaller drop ($\leq 5\%$) despite relying on biophysical scalars (FA, MD, AD, RD) that are nominally intensity-standardized. In practice (as also shown in our result, Chapter 4), DTI metrics are protocol-dependent ($b-$values, number of directions, TE/TR, gradient sampling) [22].

Limitations and future work

While our findings support the central hypotheses, several factors likely constrained performance and generalization. (i) First, the dHCP-tuned structural pipeline underperformed on CHUSJ T2w scans: when using Draw-EM to generate "ground truth" on CHUSJ data,

contrast mismatches between the CHUSJ T2w images and the dHCP template occasionally led to failed or suboptimal segmentations. This degrades label quality relative to dHCP and can bias both training and evaluation. (ii) Resolution differences between CHUSJ (2.0 mm isotropic) and dHCP ($1.17 \times 1.17 \times 1.5$ mm) may introduce resampling artifacts and shift FA and MD distributions, further complicating fair comparison. (iii) Third, acquisition protocols differ: constrained by clinical workflow, CHUSJ uses a short ($\approx$ 4 min) 25-direction, lower-b scheme. Although all DTI metrics were reconstructed using only $b \leq 1000\,\mathrm{s/mm^2}$ for consistency, protocol-dependent variability in scalars likely remains and can affect model transfer. (iv) Fourth, the external CHUSJ cohort contains a higher proportion of preterm infants; given known microstructural immaturity at TEA in preterm-born infants, this alters intensity and shape priors and can depress apparent external performance. (v) Finally, computational limits (8 GB GPU) restricted augmentation diversity and batch size during nnU-Net training, potentially hindering convergence to optimal hyperparameters.

Future directions Thus, in the future, We plan to (i) generate site-specific reference labels at CHUSJ by refining Draw-EM with local intensity harmonization and template adaptation, and to quantify label quality with inter-rater and replayability checks; (ii) We will standardize evaluation resolution (single target grid) and report sensitivity to resampling choices. (iii) Cross-protocol calibration will be pursued using multi-source training that includes 20–30% CHUSJ cases, complemented by domain adaptation and acquisition-aware augmentations. (iv) Cohort composition will be balanced or stratified (preterm versus term) to disentangle biological from domain effects, and downstream analyses will propagate segmentation uncertainty to mitigate label-noise bias. (v) Lastly, scaling training on larger-memory GPUs will enable richer augmentations and larger batches, which we expect to close much of the remaining external generalization gap while preserving the practicality of a dMRI-first workflow.

5.5 Conclusion

In conclusion, this study successfully developed and validated deep learning-based segmentation models for neonatal brain MRI, using both T2-weighted and diffusion-only inputs. The T2w model achieved state-of-the-art internal accuracy, while the diffusion-only model offered a compelling trade-off: a modest reduction in internal performance was offset by significantly better generalization to external data. This is a critical advantage in heterogeneous, multi-center clinical studies where structural scans are often unavailable or acquired under variable protocols.

By providing a robust and accessible tool for tissue segmentation, this work directly supports

the overarching aim of the thesis: to enable reproducible, large-scale microstructure analysis in neonatal populations. The diffusion-only pipeline, in particular, ensures that advanced models like DBM can be applied consistently across diverse cohorts, including those with missing T2w data. In the following chapters, we leverage this foundational tool to investigate both typical brain maturation and injury in preterm and term-born infants.

CHAPTER 6 RESULT 3: DBM FRAMEWORK APPLICATION I: COMPARATIVE STUDY OF PRETERM- AND TERM-BORN INFANTS

6.1 Introduction

Preterm birth is the arrival of babies less than 37 weeks of gestational age and is a major public health concern with a birth rate of around 10% worldwide in recent years [1]. It is associated with an elevated risk of later motor, cognitive, language, and behavioral difficulties [85, 87, 95, 97, 100, 101]. Magnetic resonance imaging (MRI) performed at term equivalent age (TEA; 40 weeks postmenstrual age, PMA) has become a standard window to assess early brain health in premature babies, offering a clinically practical time point when sedation-free images are more feasible and neuroanatomy is more mature [91, 92, 94]. However, despite widespread use, the extent to which brain microstructure in preterm infants has "caught up" to that of term-born peers in TEA remains debated and likely varies across tissue classes and regions [88, 89, 99, 101, 106, 107, 109].

Diffusion MRI (dMRI) is a powerful tool for probing tissue microstructure on a cellular scale non-invasively, linking the decay of the MRI signal to the random motion of water molecular in brain tissues [16]. Diffusion tensor imaging (DTI), the most widely used one-tensor dMRI model, has revealed general trends of decreasing mean diffusivity (MD) and increasing fractional anisotropy (FA) during the preterm to TEA period [90, 109]. The model's inherent assumption of Gaussian diffusion is frequently violated, and its metrics are nonspecific, conflating contributions from various diffusion levels. For instance, the decrease of MD can be caused by fast water clearance progress or slow diffusion water increasing caused by higher neuro cell density, or hindered diffusion water increasing caused by less ex-cellular space during brain maturation. To solve this problem, several multicompartment models based on DTI were developed, such as the NODDI, CHARMED and FWE model, which usually assume that there are limit distinct diffusive components in brain tissue and can be treated as a mixture of restricted, hindered, and fast diffusion independently [25, 26, 208]. However, the developing neonatal brain, characterized by a rapidly continuous water content, axonal progress, different neuro-cell architecture, and changes, poses fundamental challenges for these limited multicompartment models to capture the precise nature of maturational differences [94].

Spectrum-based diffusion models aim to address this limitation by decomposing the diffusion signal into distinct apparent diffusivity. Representative approaches include DSI, DBSI, RSI, and spherical mean imaging spectrum (SMIS) methods [13, 27, 28, 105]. Although promising,

their translation to neonatal brain analysis is hampered by requirements for high b-values, multi-shell sampling, longer acquisitions, and reconstruction complexity, which increase vulnerability to motion and limit clinical feasibility.

To bridge these limitations, we recently introduced the Diffusion Bubble Model (DBM), a novel spectrum-based dMRI model that can indicate where the injury- and other cased-leaded diffusion alteration occurs along its derived one-dimensional diffusion spectrum [24]. It has been used to identify stages of neonatal brain injury by observing the different changes in the tail and position of the diffusion spectrum [24]. Neonatal brain development that evolves fast-water content, microstructural restriction, and clearance processes may also change the diffusion spectrum in brain tissues. To date, DBM has not been applied to characterize the preterm versus term microstructure at TEA.

Currently, several critical gaps persist in characterizing preterm brain maturation at TEA. First, prior studies have predominantly focused on white matter tracts, leaving a systematic assessment of cortical gray matter and deep nuclei lacking. Second, most of the related studies used DTI or compartment models (e.g., NODDI, DKI), there remains a need to benchmark spectrum-based approaches, like DBM, under neonatal protocols against established metrics. Third, many studies are based on retrospective designs, limiting the ability to track longitudinal trajectories. Furthermore, although multiple reports confirm that preterm brains at TEA remain less mature, with heterogeneity tied to gestational age at birth, the fundamental nature of these differences is unclear. It is unknown whether they primarily reflect a timing shift (a simple delay in maturation onset) or a rate difference (a persistently slower pace of maturation), a distinction crucial for prognosis and intervention. Furthermore, rapid volumetric changes around TEA can confound microstructural estimates, a factor that is often not taken into account.

Objectives Leveraging our prospective cohort of preterm infants (scanned at 34 and 40 weeks PMA) and term-born controls (scanned at 40 weeks PMA), our general goal is to apply DBM and segmentation developed to quantify regional maturation trajectories from 34 to 40 wk PMA. Specifically, we aim to:

1. Establish a comprehensive map of preterm-term microstructural differences at TEA across cortical gray matter, deep gray matter nuclei, and white matter tracts, to resolve controversies regarding the regional heterogeneity of catch-up;

2. Model longitudinal trajectories of microstructural development from 34 to 40 weeks PMA in preterm infants, contrasting them against a term-born reference to empirically distinguish between a pure timing shift and a persistent rate difference;

3. Test the primary developmental mechanism by formally evaluating whether the observed differences are better explained by the timing-shift or rate-difference hypothesis, while rigorously controlling for volumetric confounds; and

4. Benchmark the added value of the Diffusion Bubble Model (DBM) against DTI by quantitatively comparing their effect sizes and biological specificity in detecting residual alterations under clinically feasible acquisition parameters.

Hypotheses We hypothesize that (i) Differences in microstructural maturation between 34 and 40 weeks of PMA are primarily explained by a timing shift (a uniform delay in the onset of maturation), rather than a rate difference (a persistently slower pace), reflecting a delayed but fundamentally intact postnatal development program. (ii) Residual microstructural gaps at TEA will be most pronounced in late-maturing association areas, particularly frontal and temporal white matter and gray matter. The more mature regions have smaller DBM positional metrics and fewer fast water fractions. (iii) DBM will detect these residual alterations with greater sensitivity and biological specificity than DTI by revealing distinct spectrum-localized shifts associated with processes such as altered axonal packing or extracellular matrix development.

6.2 Method

6.2.1 Participants

We prospectively enrolled 67 unique healthy infants (46 preterm-born; 21 term-born) at CHU Sainte-Justine Hospital (Montréal, Canada) from June 2021 to January 2025, with the approval of the CHU Sainte-Justine Recearch Center Authority. Participants contributed to three analysis groups defined by scan timepoint; note that preterm infants could contribute to both the 34-week and 40-week scans.

Preterm infants - 34-week scan (PT-34W): Thirty-six preterm infants were scanned at approximately 34 weeks PMA. Two diffusion series were excluded due to a scanner intensity scaling error that irreversibly corrupted the data, resulting in 34 analyzable scans.

Preterm infants-term-equivalent scan (PT-TEA): Thirty-five preterm infants were scanned near 40 weeks PMA, including 25 returning infants from the PT-34W cohort and 10 newly enrolled infants. One examination was unreconstructed due to uncompleted DICOM files, resulting in 34 retained scans.

Term-born controls - 40-week scan (TC-40W): Twenty-one term-born infants were scanned near 40 weeks PMA. One dataset exhibited the same intensity–rescaling artifact and was

excluded, leaving 20 control scans.

In total, after quality control we retained 88 diffusion datasets across the three groups (PT-34W: 34; PT-TEA: 34; TC-40W: 20). A subject-level index is provided in Table A.1, and demographic characteristics are summarized in Table 6.1.

Table 6.1 Demographic and perinatal characteristics of study cohorts. PT-33W = preterm infants scanned at 33 weeks wk GA; PT-TEA = same infants re-imaged at term-equivalent age; TC-40W = term-born controls scanned at 40 wk GA. GA = gestational age; wk = week(s); F/M = female/male. Values are mean ± SD except sex counts, which are number.

Group	N (M/F)	GA at birth (wk)	GA at scan (wk)	Weight (kg)	PA at scan (wk)
PT-34W	34(19/15)	32.30 ± 1.85	34.03 ± 1.44	1.75 ± 0.42	1.73 ± 1.08
PT-TEA	34(19/15)	32.16 ± 2.22	40.14 ± 1.76	3.14 ± 0.54	7.98 ± 2.34
TC-40W	20(14/06)	39.37 ± 0.88	40.86 ± 1.39	3.30 ± 0.57	1.50 ± 0.98

6.2.2 MRI acquisition

MRI imaging was performed on 3T GE (*Discovery MR750*) and 3T Siemens (*Skyra*) systems using a neonatal 32-channel head coil at CHU Sainte-Justine Hospital. Infants were fed, swaddled ($\approx$ 10 min), protected with ear defenders and silicone putty, and stabilized with a vacuum bean bag. The total scanning time was limited to $\leq$ 45 min.

T2-weighted scans were acquired using fast spin-echo sequences, with TR/TE = 5067/160 ms and resolution $1.0 \times 0.75 \times 0.75$ mm (GE scanner); with TR/TE = 11270/90 ms and resolution $0.625 \times 0.625 \times 2\,\mathrm{mm}^3$ (Siemens scanner).

Diffusion MRI data was acquired using dMRI-25-dir (research protocol) with 3 $b0$, 25 different b -values / directions with max $b \leq 800\,\mathrm{s/mm}^2$, anterior-posterior (AP) phase encoding direction, TR/TE = 8000/81 ms and resolution $2.0 \times 2.0 \times 2.0\,\mathrm{mm}^3$. When time allowed, a full reverse phase (PA) series was acquired with identical parameters; otherwise, a single PA $b0$ was collected for susceptibility correction.

6.2.3 Data preprocessing

Raw diffusion-weighted images (DWIs) were first denoised using MP-PCA (Marchenko–Pastur PCA) [178]. Susceptibility distortions were estimated with TOPUP from the acquired AP/PA calibration data and applied to the DWIs [209]. Next, all DWI volumes were rigidly aligned with a reference image b0 (typically the first b0) to mitigate the movement between volumes. Finally, all volumes were resampled to the target resolution of $1.17 \times 1.17 \times 1.5\,\mathrm{mm}^3$ [179].

DTI fitting used weighted least squares (DIPY v1.8.0), yielding AD, RD, MD and FA metric maps [180]. DBM was fitted using the nonlinear anisotropic adjustment and the nonnegative least squares optimization method to estimate the voxel-wise isotropic spectra (from 0 to 3.2 $\mu m^2/ms$), with the positional and general metrics derived (see the list in Table 3.1).

For region-based analyzes, a diffusion-only deep learning segmentation (trained on DTI maps) was used to produce 14 predefined ROIs covering lobar cortical GM and subjacent WM, deep GM, and midline structures. For each ROI and scan, we extracted the mean value within each ROI for all DBM and DTI metrics, as well as for absolute (V) and intracranial-volume-proportional (V/ICV) volumetric measures.

The complete list of 14 ROIs is provided in Table A.5; The segmentation details can be found in Chapter 5; The complete pre-processing workflow is summarized in Fig. 6.1.

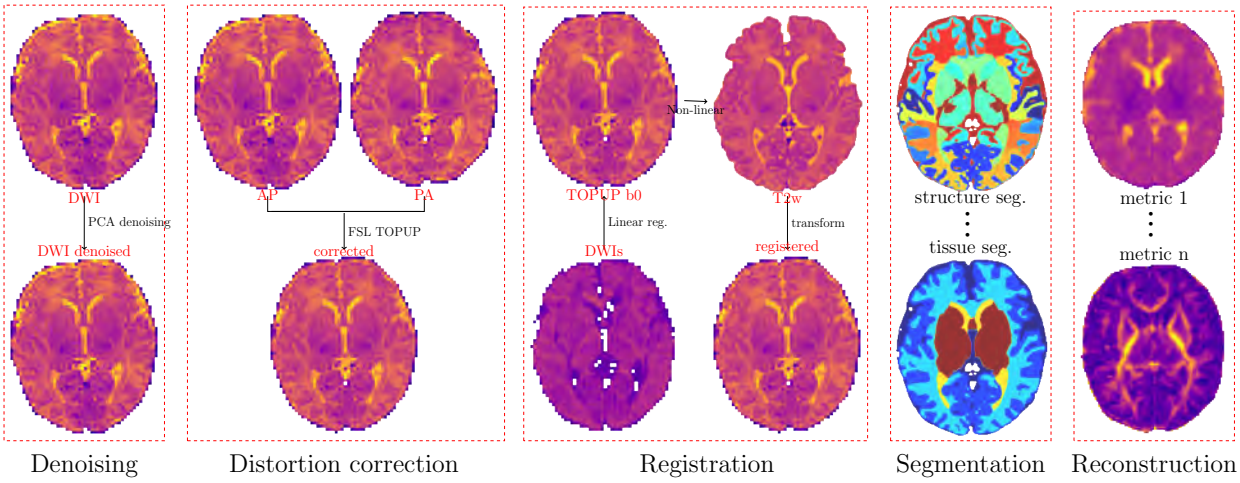

Figure 6.1 Overview of the Diffusion MRI Data Processing Pipeline. Example shown uses sub-B054S1 (male infant), born at 38 weeks 2 days (GA) and scanned at 40 weeks 5 days (PMA) on a 3T Siemens scanner in CHU Sainte-Justine Hospital. Segmentation maps were used method in Chapter 5.

6.2.4 Experimental design and statistical analysis

To systematically address this chapter's research objectives, we implemented a hierarchical analytical strategy. This framework progresses from comprehensively mapping neonatal brain group differences and developmental trajectories, to rigorously testing specific maturational mechanisms, and concludes with a comparative evaluation of our microstructural modeling approach.

Comprehensive Mapping of Microstructure Maturation

To achieve the aim of comprehensive mapping of microstructural maturation, we first computed standardized effect sizes for each ROI and dMRI metric: Hedges' g_{av} for longitudinal catch-up (PT-34W $\rightarrow$ PT-TEA) and Hedges' g for residual gaps at TEA (PT-TEA versus TC-40W). We then assessed statistical significance using linear mixed-effects models (LMMs) with a random intercept for subject for longitudinal contrasts, and ANCOVA (controlling for PMA at scan) for cross-sectional contrasts. False discovery rate (FDR) correction was applied within each metric family on all ROIs ($q < 0.05$). The results of this analysis are visualized as annotated effect-size heatmaps, which were generated at two anatomical levels to provide both a global overview and a system-level perspective aggregating ROIs into functional panels.

Characterization of Volumetric Growth Patterns

This aim sought to delineate the contribution of macroscopic structural development, specifically to separate absolute brain growth from proportional redistribution within the cranial vault. We applied the same effect size and statistical modeling framework from Aim 1 to both absolute (V) and intracranial-volume-proportional V/ICV volumes. This allowed us to generate four key contrasts: absolute and proportional catch-up, and absolute and proportional residual differences at TEA. Furthermore, to quantify growth rates in the preterm brain prior to TEA, we fitted LMMs within the preterm cohort for each ROI ($\log V \sim \mathrm{PMA}_c + (1 \mid \mathrm{Subject})$) , expressing slopes as percentage change per week, with an analogous model for $\log(V/ICV)$ to assess relative growth.

Disentangling Microstructure from Volume Confounds

The core purpose of this aim was to directly test our primary hypothesis regarding the nature of maturational differences—specifically, whether they reflect a timing shift or a rate difference that is independent of underlying volumetric changes. To this end, we fitted a unified linear mixed-effects model across a broad PMA window (31-45 weeks) for each dMRI metric, which included PMA_c, Group, their interaction term ($\mathrm{PMA}_c \times Group$), and $\log V$ as a covariate to adjust for the ROI's absolute volume. In this model, a significant interaction term indicates a rate difference (i.e., different slopes of maturation), whereas a significant Group effect in the absence of an interaction supports a timing shift (i.e., parallel trajectories with an offset). We also performed sensitivity analyzes using V/ICV for volumetric adjustment. FDR correction was applied within each metric family on all ROIs ($q < 0.05$).

Benchmarking DBM against Standard DTI

To quantitatively assess the added value of the DBM framework relative to the clinical standard of DTI, we compared the sensitivity of DBM and DTI by summarizing two key metrics across all ROIs for both catch-up and TEA residual contrasts: the proportion of statistically significant findings ($FDR < 0.05$) and the median absolute effect size ($|g|$). To ensure the robustness of these comparisons, we estimated bootstrap confidence intervals for the summaries and further decomposed the results by metric type and anatomical system to attribute performance gains.

6.3 Results

6.3.1 Diffusion microstructure maturation: robust catch-up versus persistent residual gaps

Our panoramic mapping of microstructural development (Fig. 6.2) revealed a fundamental dissociation: preterm infants exhibit robust catch-up growth in the specific regions, yet show persistent, anatomically distinct residual differences at term equivalent age comparing to term controls. This pattern was further characterized by the complementary sensitivity of DBM and DTI metrics.

DBM captures widespread development, particularly in deep & midline structures

PT-34W→PT-TEA (Catch-up) (Fig. 6.2 a): Longitudinal analysis within the preterm cohort revealed a consistent pattern of maturational decline in diffusivity. The Diffusion Bubble Model (DBM) proved particularly sensitive to these developmental changes, detecting significant catch-up (FDR $q < 0.05$) in 55/112 (49%, median effect size 0.74) of ROI-metric pairs, outperforming DTI's 32/70 (46%, median effect size 0.75) despite a more stringent multiple comparison burden.

Anatomically, the most robust catch-up was located in midline structures (e.g. corpus callosum) with median $|g| \approx 0.80$ and deep gray matter nuclei (e.g. thalamus) with median $|g| \approx 0.54$). Cortical gray matter (effect size ≈ 0.30) has the least maturation of the brain diffusion microstructure, right after white matter (≈ 0.46).

Metrically, the DBM spectral marker $D_{1/4}$ provided the broadest coverage, implicating 12 of 14 ROIs in the catch-up process.

DTI highlights widespread residual microstructural gaps at TEA in lobar networks

PT-TEA vs. TC-40W (Residual gap at TEA) (Fig. 6.2 b): In contrast, the cross-sectional comparison at TEA revealed a pervasive residual microstructural immaturity in the preterm group. Here, conventional DTI diffusivity metrics demonstrated superior sensitivity, with 69.6% (39/56, median $|g| = 1.00$) of cells surviving FDR correction compared to 50.0% (63/126, median $|g| = 0.83$) for DBM. The anatomical distribution of these residual gaps was starkly different from the catch-up pattern, being overwhelmingly concentrated in lobar cortical gray matter and white matter (median $|g| \approx 0.93$ and 0.82). The DTI metrics RD and MD were nearly globally significant (12/14 ROIs, 13/14 ROIs), underscoring the extensive nature of the residual differences in tissue organization at TEA.

The panoramic view highlights a posterior/WM-weighted catch-up and lobar GM/WM-dominant TEA residual, with midline/deep nuclei prominent in catch-up (Table 6.2).

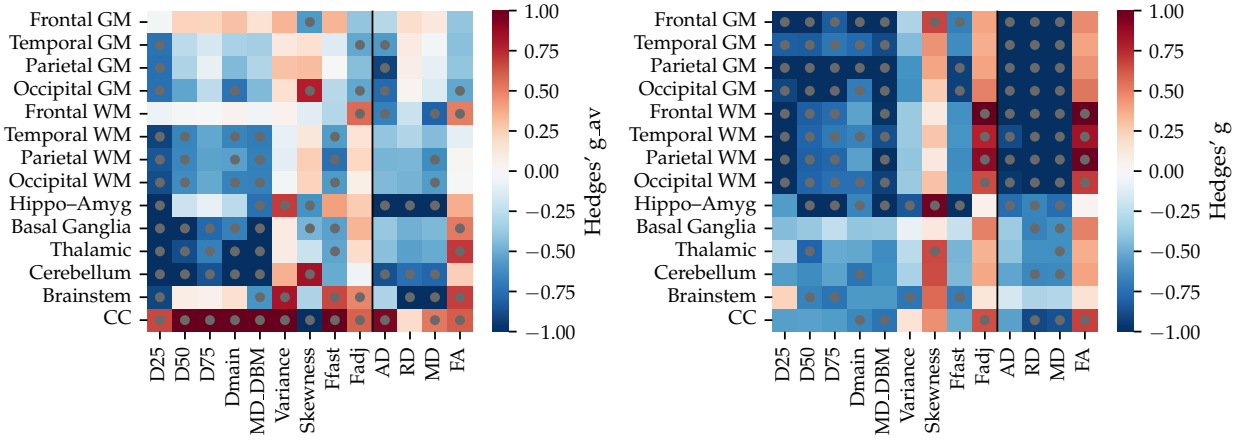

(a) PT-34W → PT-TEA (14-ROIs, no-adj.)

(b) PT-TEA vs. TC-40W (14-ROIs, no-adj.)

Figure 6.2 Whole-brain overview (14 ROIs): microstructural maturation summarized by Hedges' g (unadjusted). (a) Longitudinal catch-up within preterm infants (PT-34W → PT-TEA), effect size = Hedges' g_{av} (> 0 means PT-TEA $>$ PT-34W). (b) Residual gap at term-equivalent age (PT-TEA versus TC-40W), effect size = Hedges' g computed as TC − PT-TEA (> 0 means term controls higher). Rows: 14 ROIs ordered anterior–posterior and grouped GM → WM → deep-GM → midline. Columns: 13 core metrics (4 DBM positional, 5 DBM scalar/shape, 4 DTI). Color: cell color encodes effect size (red = higher in the second group, blue = lower), clipped to ±1. Significance: gray dots mark ROI–metric pairs remaining significant after BH–FDR within each panel and within metric family (DBM and DTI separately) across all 14 rows ($q < 0.05$). Models: panel (a) $value$ = timepoint + $(1|subject)$ mixed-effects; panel (b) ANCOVA with HC3 robust SEs.

Table 6.2 System-level DBM versus DTI summaries on the panoramic 14-ROI heatmaps (BH–FDR within metric). For each system and contrast we report significant cells (n_{sig}), total cells (n_{all}), their proportion, and the median absolute effect size $|g|$ across all cells and across significant cells.

System	Family	n_{sig}	n_{all}	Proportion	Median $\lvert g\rvert$ (all / sig)
Catch-up (PT-34W→PT-TEA)					
Lobar GM	DBM	10	32	0.31	0.31 / 0.65
	DTI	4	20	0.20	0.29 / 0.67
Lobar WM	DBM	13	32	0.41	0.41 / 0.66
	DTI	8	20	0.40	0.46 / 0.68
Subcortical GM	DBM	15	24	0.62	0.53 / 0.70
	DTI	10	15	0.67	0.61 / 0.66
Midline	DBM	17	24	0.71	0.83 / 1.02
	DTI	12	15	0.80	0.76 / 0.83
TEA residual (PT-TEA vs. TC)					
Lobar GM	DBM	19	32	0.59	0.75 / 0.94
	DTI	16	20	0.80	1.15 / 1.23
Lobar WM	DBM	18	32	0.56	0.69 / 0.80
	DTI	20	20	1.00	1.13 / 1.13
Subcortical GM	DBM	7	24	0.29	0.48 / 0.97
	DTI	9	15	0.60	0.61 / 0.66
Midline	DBM	7	24	0.29	0.56 / 0.67
	DTI	8	15	0.53	0.57 / 0.66

6.3.2 Macroscopic volumetric catch-up is largely complete at TEA

Next, we sought to determine whether the observed microstructural differences could be explained by macroscopic growth failure. We found that absolute brain volumes of preterm infants demonstrated robust catch-up growth, converging with term-born controls by TEA.

Volumes: catch-up and residuals (Fig.6.3 a,b): Longitudinal analysis revealed rapid, regionally heterogeneous growth in the preterm cohort. Lobar gray matter expanded most vigorously (e.g., parietal GM Hedges' $g_{av} = 3.78$), substantially outpacing white matter (e.g., parietal WM Hedges' $g_{av} = 1.62$). Crucially, at TEA, no regions showed significant differences in absolute volumes after FDR correction, demonstrating complete macroscopic volumetric catch-up.

Proportional volumes: catch-up and residuals (Fig.6.3 (c) and (d)) In proportional terms (V/ICV), occipital GM, basal ganglia, thalamus, brainstem, and corpus callosum were no longer significant, suggesting that their apparent growth largely tracked global intracranial expansion rather than representing disproportionate regional changes.

In TEA (PT-TEA versus TC-40W; Fig. 6.3 (c) and (d), second row of each subfigure), no ROI survived BH–FDR correction in absolute volumes. In proportional volumes, however, temporal GM, frontal WM, and temporal WM remained significant, indicating localized residual lags relative to global brain growth. To clarify whether these residuals represent slower ongoing growth (trajectory differences) or simply stable offsets, we next examined age-associated growth rates using longitudinal mixed-effects models.

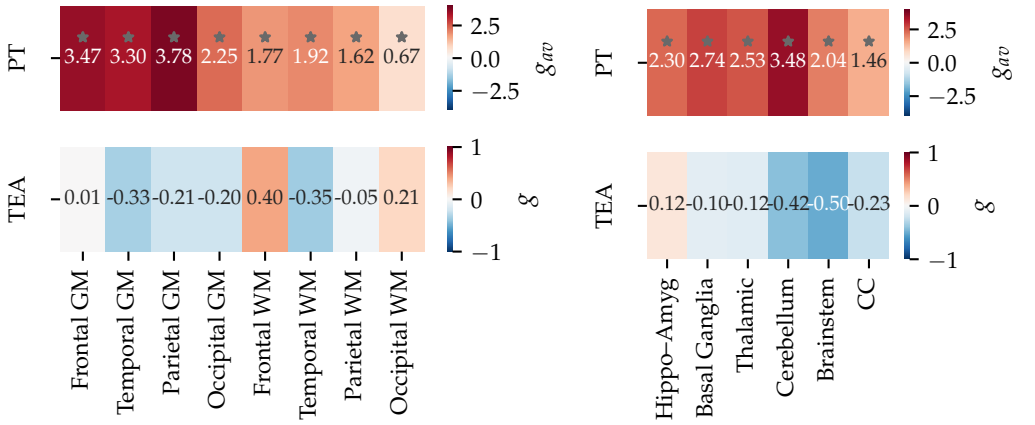

(a) Lobar GM and WM (V)

(b) Subcortical - midline (V)

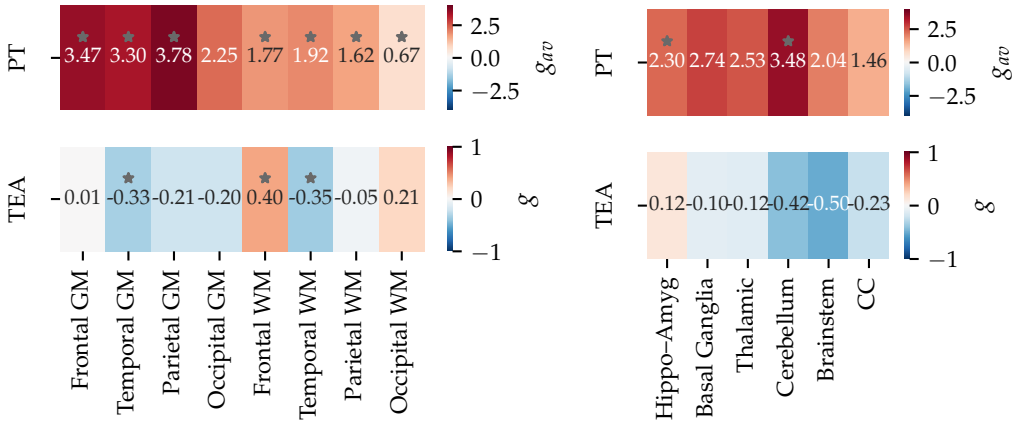

(c) Lobar GM and WM (V/ICV)

(d) Subcortical - midline (V/ICV)

Figure 6.3 Regional volume catch-up and residual gap: absolute (top) and proportional to ICV (bottom). Effect size: color-coded Hedges' g_{av} for PT (PT-34W → PT-TEA) and g for TEA (TC-40W versus PT-TEA), red/blue = higher/lower in the second group of each contrast, gray dots = significant after BH–FDR ($q < 0.05$) within each subpanel across its ROIs.

PMA-associated growth rates in regional volumes (Fig. 6.4): Within preterm infants, absolute growth rates from mixed-effects regressions on log volume were largest in the cerebellum (≈15%/week) and lobar GM (≈13–14%/week), moderate in lobar WM (≈5–6%/week),

with CC and occipital WM not significant after FDR correction.

For proportional volume (V/ICV), gram matter increased($\approx$ 4–5%/week, while white matter decreased typically ≈ -2.5 to -3.2%/week. The occipital white matter decreased largest (≈ -8.2%/week), and the cerebellar increased fastest ($\approx$5.3%/week) (Fig. 6.4).

These trajectories mirror the heat maps in showing that the cortical GM and the cerebellum accelerate volume growth during late gestation, while WM expands more slowly. Together with the nonsignificant absolute volume differences at TEA, this suggests that the residual microstructure gaps observed in dMRI are unlikely to be explained by volumetric lag but rather reflect tissue-level maturation processes beyond size growth.

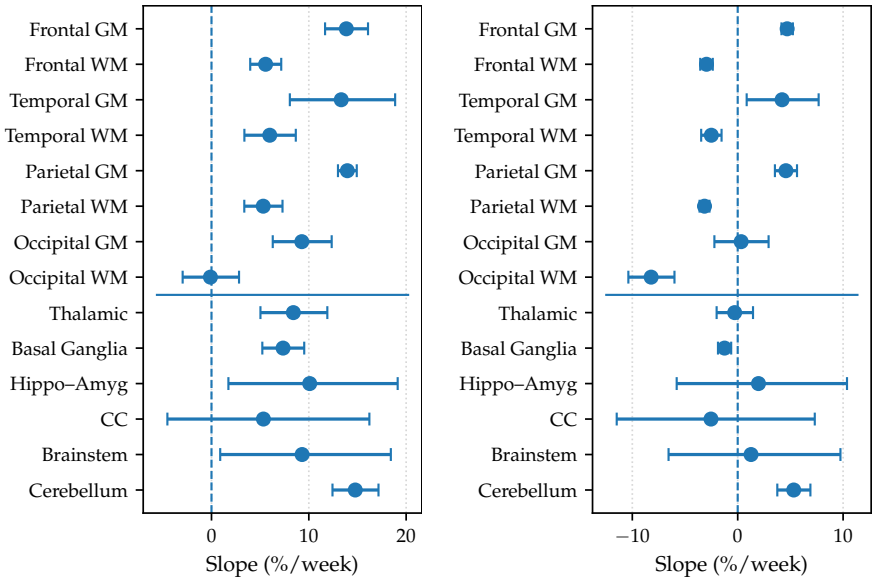

(a) Absolute growth rates (b) Relative growth rates

Figure 6.4 PMA-associated growth rates in regional volumes. Points show model-estimated slopes from mixed-effects regressions on log volume within preterm infants (PT-34W and PT-TEA): y=log(V)∼PMAc +(1|subj). Horizontal bars are 95% CIs. (a) Absolute slopes (% change per week); (b) Relative slopes for proportional volume V/ICV (% change per week relative to whole-brain growth). ROIs are grouped as lobar GM+WM (top) and subcortical+midline (bottom). See Table A.6 and Table A.7 for q values (BH–FDR across 14 ROIs).

6.3.3 Age-dependent trajectories of volume-adjusted dMRI metrics

Age-dependent trajectories (31 - 45 weeks GA) (Fig. 6.5): Linear mixed-effects models (age × group) across the full 31–45 wk window showed largely (92.3%, 155/168) parallel maturation in preterm and term infants, but 13 ROI-metric pairs showed a significantly

different age slope (FDR-corrected $q < 0.05$; Fig. 6.5) in three patterns:

1. Generally, all significant interactions reflected a flatter slope in preterm-born infants. No ROI–metric pair matured faster than the controls.

2. Anatomically, the effects clustered in the frontal and temporal tissues and in the white matter of the occipital area.

3. Metrically, the differences were driven almost exclusively by the DBM fast diffusion fraction, variance, and skewness.

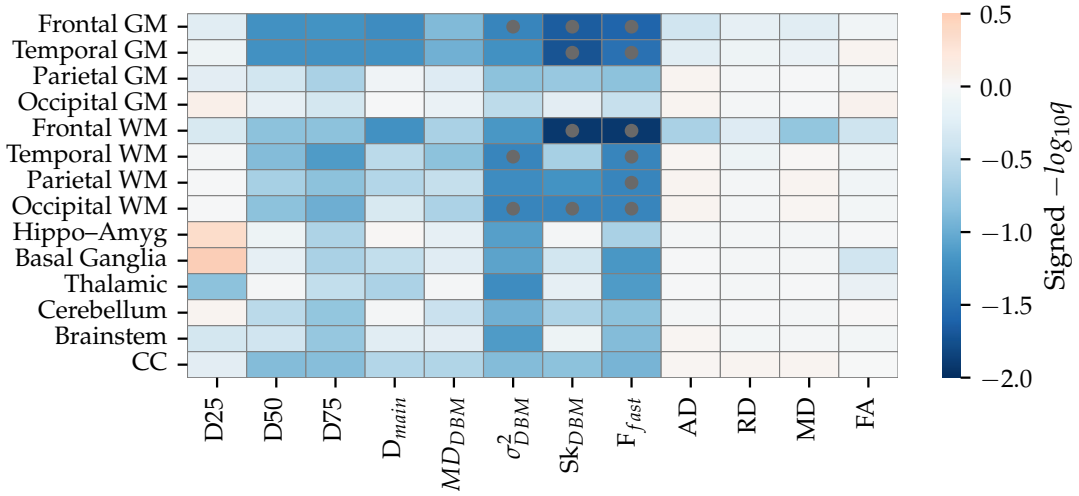

Figure 6.5 Direction and strength of Age × Group slope differences across regions and diffusion metrics. Rows list the 14 ROIs (grey-matter, white-matter, deep-GM and mid-line structures, anterior → posterior); columns list the 12 core DBM/DTI metrics. Cell colour encodes the signed interaction effect. Red: Preterm slope is steeper than the term-control slope and the metric changes faster per week; Blue: Preterm slope is flatter than the control slope (slower maturation). Deeper shades indicate stronger evidence, gray dots mark ROI–metric pairs that remain significant after Benjamini–Hochberg correction ($q < 0.05$).

This pattern is illustrated by two representative trajectories (Fig. 6.6). In the temporal white matter (Fig. 6.6 (a)), a late-maturing region, the fast-diffusion fraction declined at a significantly slower rate in preterm infants compared to term-born controls (−0.003 vs. −0.018 units/week, Δ slope $= -0.015\,\mu\text{m}^2/\text{ms/week}$, $q = 0.047$), indicating a slower clearance of free water or maturation of the extracellular space. In contrast, the thalamus (Fig. 6.6 (b)), a deep gray matter structure that matures earlier, exhibited perfectly parallel trajectories in mean diffusivity between groups (Δslope $= -0.004\,\mu\text{m}^2/\text{ms/week}$, $q = 0.903$). This direct

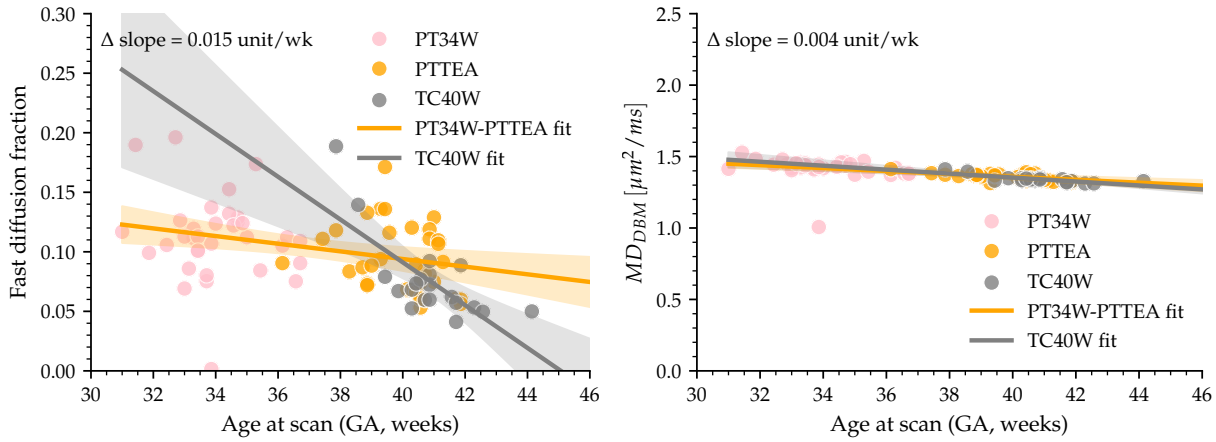

(a) Temporal WM (b) Thalamus

Figure 6.6 Age-related trajectories of two representative microstructural metrics and regions: (a) Temporal-white-matter fast-diffusion fraction; (b) Thalamic mean diffusivity (DBM-MD). Scatter points are individual scans: PT-34W (pink), PT-TEA (orange), and TC-40W (gray). Solid lines depict the fitted mean trajectory for the pooled preterm cohort (orange) and for term controls (gray); shaded ribbons are 95% confidence bands derived from linear mixed-effects models.

comparison underscores that the 'rate difference' is not a global phenomenon, but is specifically localized to vulnerable late-maturing circuits, while the 'timing shift' hypothesis holds for the majority of brain structures.

6.3.4 Complementary roles of DBM and DTI in developmental neuroimaging

DBM demonstrated superior sensitivity for detecting within-individual developmental change (Fig. 6.7). It identified a larger proportion of significant catch-up effects than DTI (DBM: 61/126,48%; DTI: 23/56, 41%) with a slightly higher median absolute effect size (DBM: $|\tilde{g}| = 0.51$; DTI: 0.46).

In contrast, DTI was more sensitive to persistent differences between cross-sectional groups in TEA. It detected a significantly larger proportion of residual gaps (DTI: 29/56, 52%; DBM: 26/126, 21%) with substantially larger effect sizes (DTI: $|\tilde{g}| = 0.86$; DBM: 0.65).

Robustness (Fig. A.3): Including CSF in the family-wise counting modestly increased detection rates for both families but did not alter the rank ordering (DBM catch-up 68/135 (50%); DTI 26/60 (43%); DTI TEA 32/60 (53%); DBM TEA 34/135 (25%)). Unless otherwise stated, CSF is excluded from the main family-wise counts and is shown only for sensitivity.

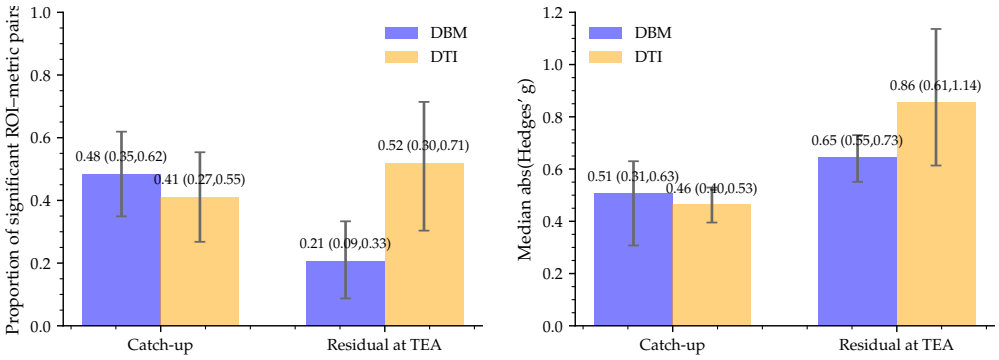

(a) Proportion of significant (overall) (b) Median Hedges' $|g|$ (overall)

Figure 6.7 DBM vs. DTI sensitivity to catch-up and residual gaps (with 95% CIs). Panels summarize detection and effect-size magnitude under the same multiple-comparison control as the heatmaps. (a) Bars show the proportion of FDR-significant ROI–metric pairs within family (DBM or DTI) for the two contrasts: Catch-up (PT-34W → PT-TEA) and Residual at TEA (PT-TEA vs. TC-40W). Numbers above bars indicate significant/total pairs and the percentage. Error bars are 95% CIs from ROI-cluster bootstrap (2,000 resamples). (b) Bars show the median absolute Hedges' g across ROI–metric pairs with 95% bootstrap CIs; catch-up uses g_{av} for PT-TEA-PT-34W, TEA residual uses g for TC-40W versus PT-TEA. BH–FDR is applied within each diffusion family across all ROIs × metrics (8 lobar + 6 subcortical/midline); longitudinal models use mixed-effects without PMA due to collinearity with timepoint.

Supplementary per-system analyses (Fig. 6.8) confirmed that the proportions of significant ROI-metric are highest in the midline and subcortical GM, and lowest in the Lobar GM for both the DTI and DBM analysis; In TEA, the proportions of significant residual ROI-metrics are higher in lobar tissues than in other regions, especially for DTI analysis.

This support DBM has advantages catch-up sensitive, while DTI remains more sensitive to tissue-specific microstructural lag in TEA.

Per-metric counts (Fig. 6.9) show that DBM sensitivity is mainly carried out by diffusion-spectrum quartiles (notably D_{25} and D_{50}), while DTI sensitivity is dominated by diffusivities (RD and MD).

These results support a complementary pattern: DBM tracks the rapid diffusion positional change (D_{25}, D_{50}) and geneal scalar ($\mathrm{MD}_{\mathrm{DBM}}$) in the diffusion spectrum for both catch-up and TEA residuals, while DTI tracks changes more depends on AD RD and MD for catch-up, and RD and MD for TEA residual.

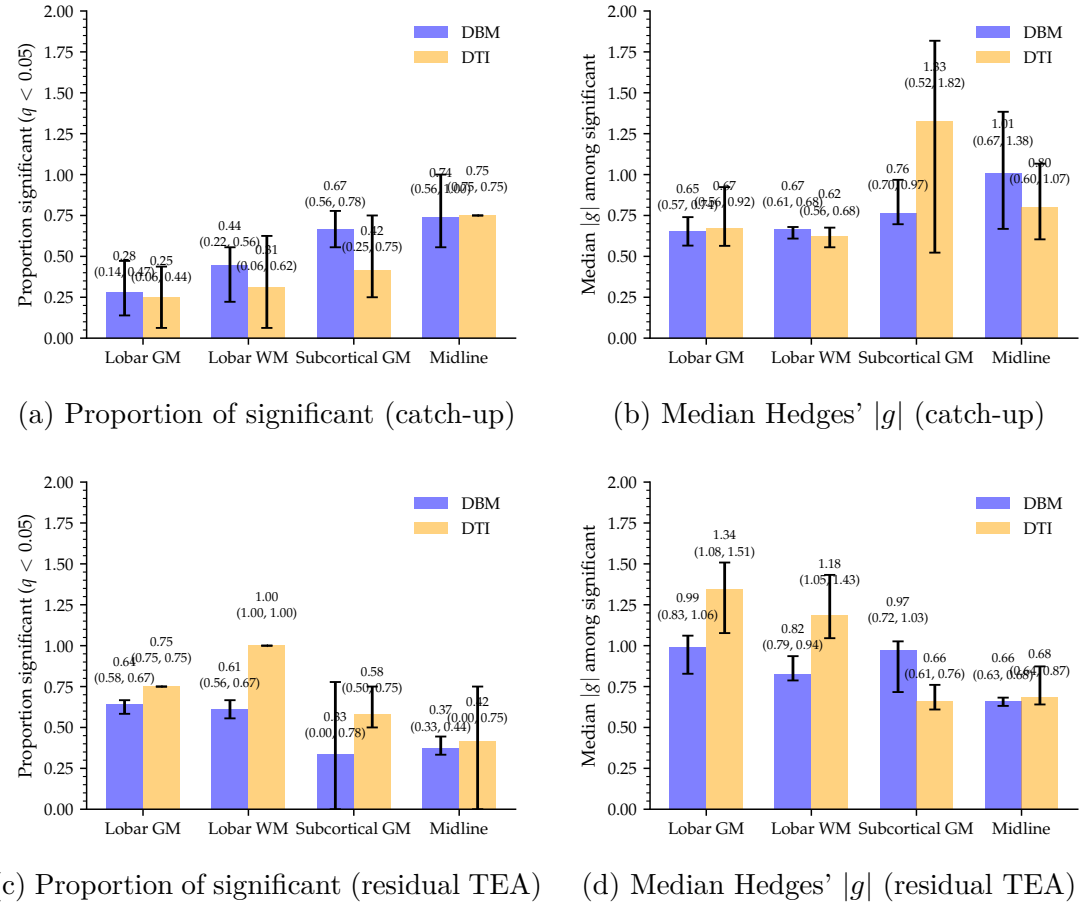

(a) Proportion of significant (catch-up)

(b) Median Hedges' $|g|$ (catch-up)

(c) Proportion of significant (residual TEA)

(d) Median Hedges' $|g|$ (residual TEA)

Figure 6.8 Per-system sensitivity (DBM versus DTI): catch-up and TEA residuals. (a–d) System-level sensitivity under matched BH–FDR control across ROI×metric cells. Top row for catch-up (PT-34W→PT-TEA): (a) proportion of significant cells ($q < 0.05$) by system; (b) median absolute effect size $|g|$ among significant cells. Bottom row for TEA residual (PT-TEA vs. TC-40W): (c) proportion significant; (d) median $|g|$ among significant. Color mapping: blue = DBM, orange = DTI. Error bars are ROI-cluster bootstrap 95% CIs (resampling ROIs within systems). Higher proportion indicates broader spatial detection; higher median $|g|$ indicates larger effect magnitudes among detected cells.

6.4 Discussion

This chapter provides the first comprehensive application of the Diffusion Bubble Model to map microstructural maturation and catch-up in the preterm brain from 34 weeks to term-equivalent age (TEA). By integrating volumetric and spectrally-resolved diffusion data, our findings delineate a clear developmental principle: while global brain size normalizes by TEA, widespread microstructural immaturity persists, best explained by a delayed onset of maturation rather than a persistently altered rate, which supports our hypothesis.

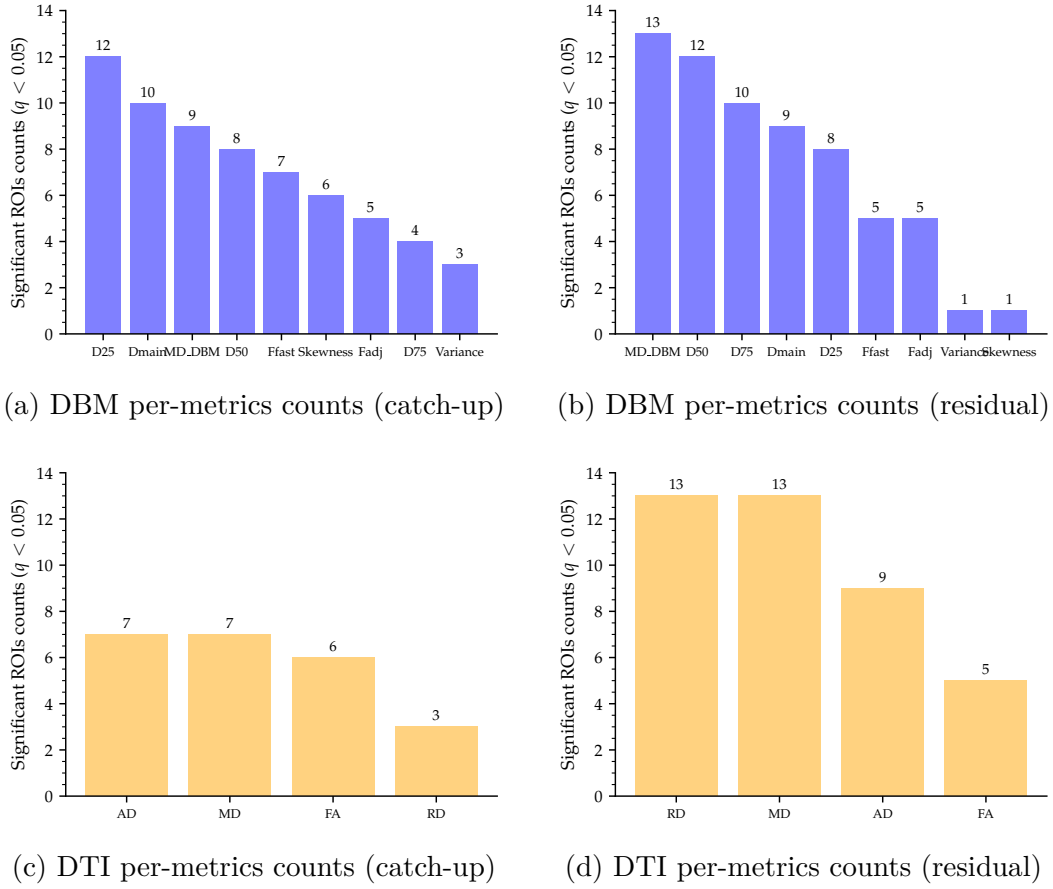

(a) DBM per-metrics counts (catch-up)

(b) DBM per-metrics counts (residual)

(c) DTI per-metrics counts (catch-up)

(d) DTI per-metrics counts (residual)

Figure 6.9 Per-metric contributions to sensitivity. Per-metric contributions to sensitivity (DBM versus DTI; catch-up and TEA residuals). (a–d) Number of ROIs (out of 14) that remain significant ($q < 0.05$, BH–FDR within family and within contrast) for each metric. Top row: DBM metrics for (a) catch-up (PT-34W $\rightarrow$ PT-TEA) and (b) TEA residual (PT-TEA vs. TC-40W). Bottom row: DTI metrics for (c) catch-up and (d) TEA residual. Bars quantify how much each metric drives detection in its family/contrast: taller bars indicate broader spatial significance across ROIs. Color mapping: blue = DBM, orange = DTI. This view highlights that DBM quartile/spectrum metrics (e.g., D25/D50) carry much of the catch-up signal, whereas DTI diffusivities (RD/MD) dominate the residual gap at TEA.

6.4.1 Volumetric catch-up masks underlying microstructural lag

Our volumetric analysis confirms significant brain growth across all regions from 34 to 40 weeks PMA, with a spatial gradient (parietal > frontal/temporal > occipital) in both GM and WM (Fig. 6.3), consistent with late-gestation surges [66]. Critically, after adjusting for intracranial volume, most regions did not show absolute volume differences in TEA. However, proportional volumetric differences (e.g., smaller temporal GM and WM, larger frontal WM) revealed persistent alterations in brain composition. This indicates that volumetric catch-up,

while substantial, is not synonymous with normative maturation [63, 64]. The co-occurrence of this volumetric stabilization with a systematic decrease in the DBM fast fraction points to a shared underlying process: the contraction of the extracellular space as the brain matures.

6.4.2 A delayed-onset, hierarchical model of microstructural maturation

After adjusting for head size and postmenstrual age, preterm–term diffusion trajectories were broadly parallel yet consistently offset, supporting a timing-shift account in which the maturational program is preserved but begins later after preterm birth [88, 187, 190]. The spatial layout of this delay follows a well-described hierarchy. In cortical gray matter, DBM revealed a predominant leftward shift of the isotropic spectrum with a concurrent reduction of the fast tail—patterns consistent with extracellular-space contraction and dendritic and synaptic maturation. Residual immaturity at TEA was most evident in temporal and parietal cortices, whereas frontal cortex showed the smallest interval change, in line with a posterior-to-anterior progression [190, 191]. In white matter, catch-up was strongest: fast fraction and MD declined steeply, aligning with rapid late-gestation myelination. Nonetheless, frontal WM retained the most pronounced fast-end elevation at TEA, underscoring its protracted timetable and heightened vulnerability relative to posterior bundles [4, 190]. Deep gray matter matured asymmetrically: the thalamus—hub of early sensorimotor circuits—approached normalization (low DBM fast fraction; normalized FA and MD), whereas the hippocampus–amygdala complex retained the largest residuals, consistent with limbic susceptibility in prematurity [186, 187]. Across midline structures, a posterior-to-anterior sequence was again apparent. The cerebellum showed substantial catch-up with only a small residual gap by TEA in our cohort, while the corpus callosum—particularly posterior segments—displayed persistent immaturity. Notably, the brainstem looked normalized on DTI, yet DBM still detected fast-end elevation, suggesting subtle extracellular-space differences that tensor averages can miss [210, 211].

Taken together, earlier-maturing projection systems (e.g., thalamus) exhibit smaller residuals than later-maturing association systems (e.g., frontal WM, callosum), a pattern that coheres with established models of developmental vulnerability and is captured with high fidelity by DBM's spectral readouts [88, 187, 190].

6.4.3 DBM provides superior sensitivity to maturational processes

A central contribution of this work is showing how DBM complements, and in key scenarios surpasses, conventional DTI for characterizing maturation. By reconstructing the isotropic diffusivity spectrum, DBM localizes where changes occur along the diffusivity axis, providing

biologically specific signatures of processes such as extracellular-water reduction and membrane proliferation that underlie scalar shifts in MD and FA. This added specificity translated into practical gains: DBM detected lingering fast-end elevations in regions (e.g., brainstem) that appeared normalized on DTI and offered greater statistical power to separate groups at TEA, especially in frontal and temporal pathways. In short, moving from scalar summaries to spectral localization revealed maturational dynamics—both regional and temporal—that would otherwise remain obscured by tensor averages [4, 190, 210].

6.4.4 Limitations and future directions

This study has several limitations. First, relying on a coarse four-lobar parcellation constrains anatomical specificity and may miss vulnerabilities within substructures (such as thalamic nuclei or callosal subsegments) or across cortical layers. Although our diffusion-only deep-learning pipeline already yields high-quality multi-label segmentations, the present analysis does not fully exploit that granularity. Second, the 34–40 week PMA window, combined with a two-time-point, cross-group design, effectively privileges linear approximations of maturation. Prior work indicates that diffusion metrics—including DTI-derived FA—often follow nonlinear age trajectories in late gestation, so linear models may oversimplify true developmental dynamics. Third, sampling is sparse: preterm infants were scanned at only two time points and term controls at a single time point, leaving rate estimates vulnerable to noise and outliers and limiting inference about inter-individual variability. In addition, we lack longitudinal neurodevelopmental outcomes, preventing direct tests of whether DBM-based maturational signatures predict later cognitive or motor performance. Finally, potential sex-related differences could not be evaluated because the cohort was imbalanced.

In future, thus, several steps would strengthen both inference and clinical relevance. Firstly, we will adopt finer, anatomy-informed parcellations (e.g., Draw-EM–style high-granularity segmentation), and cortical-depth profiling, so that region- and layer-specific trajectories can be quantified with greater precision. Secondly, we will use flexible modeling of nonlinear growth or Bayesian hierarchical approaches that capture subject-specific change. Third, we will expand the sampling window earlier than 34 weeks and beyond TEA and move the study to truly longitudinal designs. In addition, sex-balanced data will be acquired to avoid potential bias. Finally, long-term neuro-development outcomes will be evaluated.

6.5 Conclusion

In conclusion, this study maps late-gestation brain maturation in preterm infants (34 weeks to term-equivalent age) and answers our core questions. Although volumes largely "catch up" by TEA, microstructure lags behind: DBM and DTI reveal persistent differences that volumetry alone cannot. This lag follows an ordered, posterior-to-anterior hierarchy and is best explained by a timing shift (a delayed onset of maturation in preterm infants) rather than a fundamentally different growth rate.

The Diffusion Bubble Model was central to these insights. By localizing changes along the diffusion spectrum (e.g., fast-tail retreat and peak shifts consistent with extracellular-space reduction), DBM complements conventional DTI and provides a more biologically specific account of maturation. Moving beyond scalar averages to spectral signatures, we establish DBM as a practical, sensitive tool for developmental neuroscience. With this framework validated in typical maturation, next chapter applies it to a specific problem of neonatal brain injury, where spectral phenotyping may further clarify mechanisms and improve stratification.

CHAPTER 7 RESULT 4: DBM FRAMEWORK APPLICATION II: MICROSTRUCTURAL CHARACTERIZATION AND SUBTYPING OF NEONATAL PUNCTATE WHITE MATTER LESIONS

7.1 Introduction

Punctate white matter lesions (PWML) are a frequent form of neonatal brain injury, particularly in infants born preterm [6]. Although a substantial proportion of affected infants show apparent resolution on follow-up imaging [119], PWML are linked to later motor [6, 7], cognitive [212, 213], and behavioral difficulties [213, 214]. Precise phenotyping is therefore clinically important, because different lesion patterns likely reflect distinct pathologies and risk profiles [5, 6, 117, 137]. However, most existing classifications emphasize macroscopic features, location, burden, and gross geometry (e.g., punctate, clustered, linear), with relatively little attention to quantitative microstructural characterization.

Magnetic resonance imaging (MRI) is central to neonatal neuroimaging [9–11]. PWML typically appear as focal hyperintensities on T1-weighted (T1w) images and iso- to hypointense foci on T2-weighted (T2w) images [5, 116, 118–122]. Susceptibility-weighted imaging (SWI) can further distinguish ischemic from non-ischemic subtypes in some cases. Diffusion MRI (dMRI) adds sensitivity to microstructural injury; prior studies have reported restricted diffusion associated with PWML, sometimes with spatial extents that differ from the T1w footprint, suggesting lesion stage or subtype heterogeneity [5]. Yet, conventional models such as diffusion tensor imaging (DTI) mainly summarize the overall diffusion magnitude and anisotropy, providing limited insight into which diffusivity components are altered within the tissue.

To address this gap, we recently introduced the Diffusion Bubble Model (DBM), which decomposes diffusion-weighted signals into a set of isotropic diffusivity components with associated weights. By analyzing how the spectrum and its weights shift, DBM localizes where along the diffusivity axis microstructural changes occur, offering a more granular readout than aggregate DTI metrics and potentially improving sensitivity to subtle injury.

In this study, we focus on PWML that affects optical radiation (OR), a clinically relevant pathway sensitive to myelination, and apply DBM to characterize the microstructure of the lesion. We test whether the diffusion bubble model enhances the detection of PWML-related microstructural alterations in neonatal optic radiation. We hypothesize that PWML in the neonatal OR shift the isotropic diffusivity spectrum toward lower values and that DBM

outperforms DTI in detecting such changes. We also assess subtype-specific profiles (wet, dry), expecting a common leftward shift with differences in distributional characteristics.

7.2 Method

7.2.1 Participants

We used the second dataset release of the Developing Human Connectome Project (dHCP), acquired at King's College London with UK Health Research Authority approval [103, 162]. We searched the dHCP cohort for neonates with punctate white matter lesions. Candidate lesions had to appear as focal T1-weighted hyperintensities with corresponding T2-weighted iso- to hypointensities. Four trained raters independently screened all candidates while blinded to diffusion maps; disagreements were resolved by consensus, and a neonatal neurology researcher verified the final set.

To minimize etiological heterogeneity, we retained 20 infants whose PWML were confined to a unilateral optic radiation region. Each infant was paired $1:1$ with a dHCP control in sex, gestational age at birth, postmenstrual age at scan and birth weight. This yielded a three-arm comparison: (i) *Lesion group*: Twenty infants with a single PWML in optic radiation (mean gestational age at scan 37.82 ± 3.00 weeks; mean gestational age at birth 35.57 ± 3.76 weeks). (ii) *Contralateral group*: In each infant with PWML, the mirror region in the contralateral hemisphere was analyzed to provide a reference within the subject. (iii) *Control group*: Twenty dHCP infants matched one-to-one for sex, birth-weight, gestational age at birth, and age at scan (mean GA 37.97 ± 2.84 weeks; mean GA at birth 35.79 ± 3.75 weeks).

7.2.2 MRI acquisition

All infants underwent structural (T2w-weighted) and diffusion MRI on a 3T Philips Achieva system. The resolution of the T2w images was $0.5 \times 0.5 \times 0.5\,\mathrm{mm}^3$ with a repetition time of 12000 ms and an echo time of 156 ms [162]. The diffusion MRI data included 20 $b0$ images and three diffusion weighting shells (40 $b = 400\,\mathrm{s/mm}^2$, 88 $b = 1000\,\mathrm{s/mm}^2$, and 128 $b = 2600\,\mathrm{s/mm}^2$), with a spatial resolution of $1.172 \times 1.172 \times 1.5\,\mathrm{mm}^3$, TR / TE of 3800 / 90 ms [103].

7.2.3 Data processing

For each infant, T1w and T2w were rigidly aligned with each other and then registered to diffusion $b0$ image (target space for all analyzes) with a linear then non-nonlinear strat-

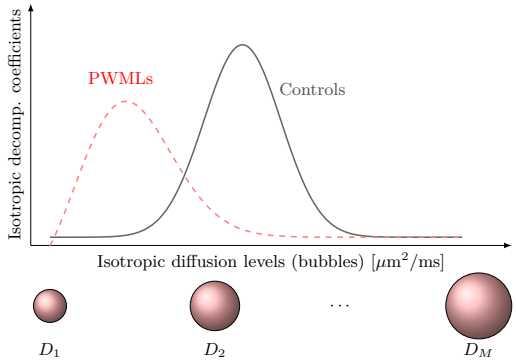

Figure 7.1 Conceptual DBM Isotropic Diffusion Spectrum Curves. These illustrative DBM-derived curves compare isotropic diffusion spectrum for tissues affected by punctate white matter lesions (PWMLs, dashed red) and healthy control tissues (Controls, gray). The x-axis represents isotropic bubble diameters (diffusion levels), and y-axis shows isotropic decomposition coefficients. This paper hypothesized curve shifts happened in the PWMLs compared to controls, because of restricted diffusion in PWMLs. Figure was from our prior open-access article with author permission [24].

egy [215, 216]. dHCP diffusion data were used as released (denoising, motion and eddy correction with outlier replacement, susceptibility correction) [103].

For the region of interest (ROI), the raters manually delineated the PWML boundary on T1w (hyperintense core), cross-validated against T2w and color-FA to confirm OR location. When minor cross-modality discrepancies occurred, T1w defined the boundary. Then we created (i) a contralateral ROI by placing in the anatomically equivalent position in the same neonatal brain, and (ii) a matched control ROI by placing an anatomically homologous mask in the OR of the paired control infant [24].

7.2.4 DBM, DTI, and FWE reconstruction

We fit three diffusion MRI models to the diffusion MRI data. Firstly, DBM was applied to the diffusion data to obtain the isotropic diffusion spectrum and the DBM metrics, namely $\mathrm{MD_{DBM}}$, $\mathrm{D_{25}}$, $\mathrm{D_{50}}$, $\mathrm{D_{75}}$, $\mathrm{F_{fast}}$, Variance σ^2_{DBM}, Skewness $\mathrm{Sk_{DBM}}$ [24]. $\mathrm{F_{fast}}$ is the sum of coefficients of the isotropic spectrum with diffusion level above 2.5 $\mathrm{mm^2/ms}$. For comparison, we computed the DTI-derived metrics (AD, RD, MD and FA) using the weighted least square DTI provided by DIPY [179, 180]. Furthermore, fast diffusion water volume fraction maps were generated by applying the free water elimination model to the same dMRI dataset, providing further insight into the microstructure of tissue beyond the standard DTI measures [181].

7.2.5 Experiment design and statistics

We evaluated PWML-related microstructural alterations in the optic radiation (OR) using a paired three-arm design (Lesion versus Contralateral; Lesion versus Matched control) and conducted analyses in three datasets: wet, dry, and all lesions (wet+dry). The lesions were first classified as wet or dry based on the fast water fraction of DBM (F_fast) measured in the ROI of the lesion relative to the OR of the paired control.

Our primary hypothesis is that PWML induces a leftward shift of the isotropic diffusivity spectrum within the OR relative to the contralateral and matched control OR (Fig. 7.1). Operationally, a shift to the left is defined as the lower DBM-derived diffusivity landmarks in lesions, that is, the mean diffusivity of the spectrum (MD_{DBM}) and the quartile diffusivities (D_{25}, D_{50}, D_{75}). Analyses were performed separately within the wet, dry, and wet+dry (combined) datasets. For each scalar outcome, we screened normality and used two-sided paired t-tests ($p < 0.05$) when assumptions were met, otherwise Wilcoxon signed-rank tests ($p < 0.05$) for the two contrasts (Lesion versus Contralateral; Lesion versus Matched-control).

To contextualize the findings of DBM, we also analyzed conventional DTI metrics (AD, RD, MD and FA) and structural MRI signal intensity (T1w, T2w) within the same ROIs and paired contrasts using the same statistical procedures. We then evaluated the added value of DBM in identifying and characterizing PWML-related tissue alterations by comparing the direction and percentage changes of effects across modalities.

7.3 Results

7.3.1 Results of inter-rater reliability of PWML lesion masks

Table 7.1 Pair-wise inter-rater similarity for PWML lesion masks. Each entry shows Cohen's κ, its 95 % confidence interval (CI), the Dice coefficient, and raw agreement. Values are rounded to three decimals, except raw agreement, which is shown to one decimal place.

Rater pair	κ	95 % CI	Dice	Raw agreement
Rater1–Rater2	0.912	(0.908–0.915)	0.912	100.0 %
Rater1–Rater3	0.884	(0.880–0.888)	0.884	99.9 %
Rater1–Rater4	0.887	(0.883–0.891)	0.888	99.9 %
Rater2–Rater3	0.884	(0.880–0.888)	0.885	99.9 %
Rater2–Rater4	0.889	(0.885–0.893)	0.889	99.9 %
Rater3–Rater4	0.848	(0.843–0.852)	0.848	99.9 %
Fleiss (4 raters)	0.884	(0.881–0.887)	—	99.9 %

For interrater reliability (Table 7.1), pairwise Cohen's values k in pairs ranged from 0.848 to 0.912, with 95% CI uniformly narrow (≤ 0.01 wide). Each pair of labels achieved almost perfect agreement ($k \geq 0.81$). The excellent Dice score (0.848–0.912) mirrored it, indicating a substantial spatial overlap of the binary lesion masks. Furthermore, overall Fleiss's k was 0.884 (95% CI 0.881–0.887), confirming excellent concordance across the four raters simultaneously.

7.3.2 DBM-based sub-typing of neonatal PWMLs

Data-driven identification of "wet" and "dry" lesions

When DBM was applied to all optic radiation PWMLs, the fast diffusion fraction (F_{fast}), displayed a clear bimodal distribution. Using the values in the contralateral and control regions as a threshold, the lesions were divided into two equally sized groups (10 infants each):

(1) *Wet-Type PWMLs*: F_{fast} is significantly higher than the mirror region (contralateral) and the matched controls, indicating excess free water.

(2) *Dry-Type PWMLs* F_{fast} is indistinguishable from reference tissue, suggesting a denser and less edematous microenvironment.

Figure 7.2 (a) plots F_{fast} against gestational age at scan. Wet lesions (pink circles) lie consistently above dry lesions (red circles), and both reference groups (orange triangles, gray squares). All groups show the expected decline in maturation F_{fast} with age, consistent with normal maturation of the neonatal brain and a gradual reduction in free water content [217].

A secondary analysis revealed that wet-type infants were imaged earlier after birth (median 5.50 days) than dry-type infants (median 14.00 days; Mann-Whitney one-sided $U = 26.0$, $p = 0.0376$; Figure 7.2 (b)). The gestational age at the scan did not differ ($p = 0.82$), confirming that the differences between subtypes are not explained by the general maturity of the brain.

Characteristic imaging signatures

Wet-type PWML example Figure 7.3 and Fig. B.1 illustrate a wet-type PWML in a neonate scanned at 35.00 weeks (GA at birth 34.14 weeks). On conventional MRI the lesion is hyperintense on T1-weighted images (Fig. 7.3 (a)), hypointense on T2-weighted images (Fig. B.1 (a)). The diffusion tensor imaging results demonstrated restricted diffusion within the lesion, with

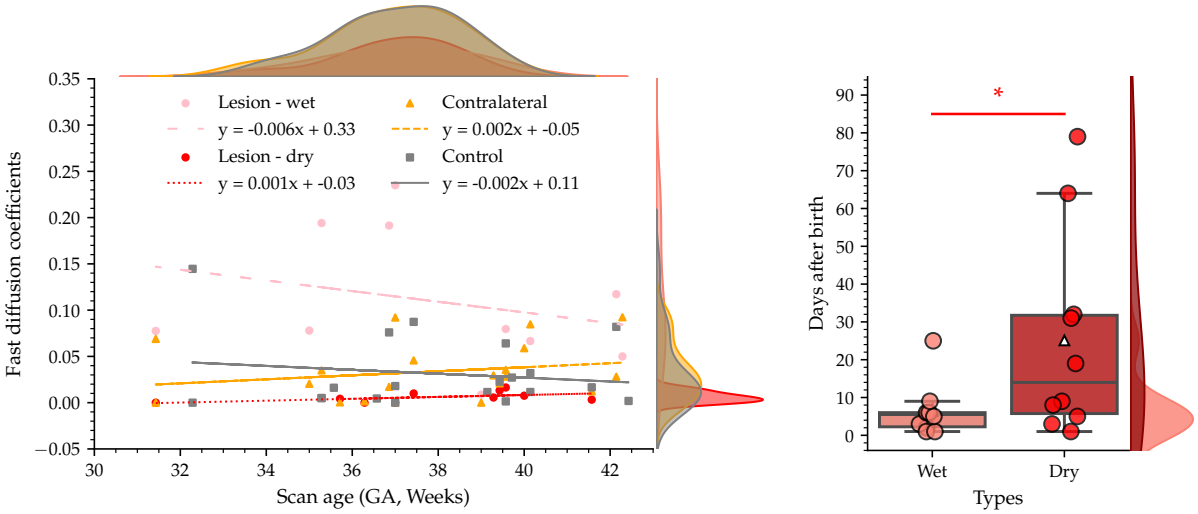

(a) Fast diffusion fraction vs. scan age

(b) Days after birth of subtypes

Figure 7.2 Subtype-specific trajectories of fast-diffusion metrics and postnatal age at MRI in PWML. (a) Averaged fast-diffusion coefficient in ROI plotted against scanning age for four regions: wet-type PWML (pink circles), dry-type PWML (red circles), contralateral OR (orange triangles), and matched-control OR (gray squares). Separate trend lines were fitted to visualize subtype- and region-specific age relationships. (b) Postnatal age at MRI by subtype. Box-and-whisker plots summarize wet-type (pink) and dry-type (red) PWML; the center line marks the median, the open triangle marks the mean, boxes span the interquartile range, and whiskers extend to 1.5× the inter-quartile range. A one-sided Mann–Whitney test (wet < dry) indicated lower postnatal age for wet lesions ($U = 26.0$, $p = 0.0376$). Figure was adapted from our prior open-access article with minor edits and is reused here with author permission [24].

reductions in both axial and radial diffusivity maps (Figs. B.1 (b) and (c)). These findings were consistent with classical imaging descriptions of PWML in the literature [5, 119, 122].

DBM analysis adds microstructural details:

(1) *Isotropic spectrum*: The curve is uniformly left-shifted and markedly broadened, with a pronounced fast-diffusion tail (Fig. 7.3 (g)). This pattern indicates abundant extracellular water consistent with vasogenic oedema.

(2) *Quartile diffusivity maps*: Due to the spectrum shift, the lesion appears as a characteristic "black hole" across all three area-specific (D_{25}, D_{50}, D_{75}) diffusion maps (Fig. 7.3 (d)-(f)).

(3) *Fast-water fraction*: An elevated fast-diffusion fraction makes the lesion stand out as bright foci on the water-fraction map (Fig. 7.3 (c)).

(4) *DBM mean diffusivity* (MD_{DBM}): The lesion remains restricted on the model-specific MD map (Fig. 7.3 (b)).

(5) *Spectrum spread and shape*: The deviation (width) map shows a prominent bright spot, while skewness is substantially increased within the lesion (Appendix Fig. B.1 (d) and (e)), both reflecting the broadened asymmetric spectrum.

Together, these findings support the wet-type phenotype: acute tissue disruption accompanied by vasogenic oedema and excess free water.

Dry-type PWML example Figure 7.4 and Fig. B.2 display a representative dry-type punctate white matter lesion located in the optic radiation of an infant scanned at 39.43 weeks gestational age (born at 39.29 weeks GA). On conventional MRI, the lesion is hyper-intense on T1-weighted image (Figure 7.4 (a)), hypo-intense on T2-weighted image (Figure B.2 (a)), and displays mild restriction on both axial and radial diffusivity maps (Figure B.2 (b) and (c)), characteristics it shares with wet-type PWMLs. However, DBM analysis highlights a distinct microstructural pattern:

(1) *Isotropic spectrum*: The lesion's spectrum is uniformly shifted toward a lower diffusivity and is slightly broader than that of the contralateral optic radiation, with the main difference confined to the beginning of slow diffusion (Fig. 7.4 (g)). This indicates a persistent microstructural change with little extracellular (fast) water.

(2) *Quartile diffusivity maps*: The lesion appears only slightly darker than the surrounding tissue on all three maps (Fig. 7.4 (d)-(f)), reflecting the modest spectrum shift.

(3) *Fast-water fraction*: There is no appreciable fast-diffusion tail, confirming minimal free-water accumulation (Fig. 7.4 (c)).

(4) *DBM mean diffusivity* (MD_{DBM}): The slight diffusion restriction is still evident (Fig. 7.4 (b)), but the contrast is less striking than in the wet-type example.

(5) *Spectrum shape*: The deviation (width) and skewness maps show only subtle changes (Appendix Fig. B.2 (d) and (e)), consistent with a slightly broadened, asymmetric spectrum.

These findings point to ongoing cellular reorganization or a chronic structural change after resolution of acute vasogenic oedema. In line with this interpretation, infants with dry-type lesions are typically scanned later than those with wet-type lesions (Fig. 7.2 (b)), suggesting that the dry phenotype represents a more later stage in the lesion-evolution continuum.

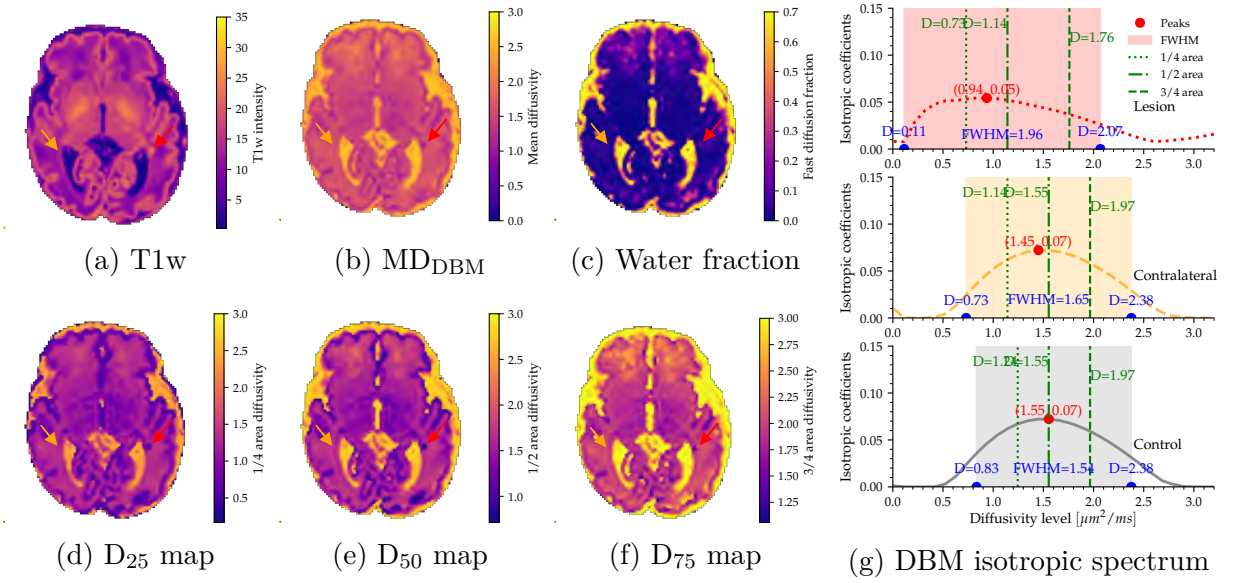

(a) T1w (b) MD_{DBM} (c) Water fraction

(d) D_{25} map (e) D_{50} map (f) D_{75} map (g) DBM isotropic spectrum

Figure 7.3 Wet-type punctate white-matter lesion in the optic radiation visualized with DBM. Subject ses-44704 from the dHCP cohort. (a) Axial T1-weighted image shows a focal hyperintense PWML (red arrow). (b) DBM-derived mean-diffusivity map (MD_{DBM}) confirms markedly redstricted diffusion at the same locus. (c) Fast-diffusion (free-water) fraction map reveals an elevated extracellular-water component, a hallmark of the "wet" phenotype. (d–f) Isotropic-spectrum area maps at the first, second and third quartiles (D_{25}, D_{50}, D_{70} area diffusion) illustrate the progressive signal inversion that accompanies increasing diffusion scales. Orange arrows mark the mirror (contralateral) region used for within-subject comparison; the matched control ROI is not displayed. (g) Isotropic decomposition coefficient curves for lesion (red), contralateral (orange) and control (grey) ROIs: the lesion spectrum is broadened, left-shifted and exhibits an exaggerated high-diffusion tail, consistent with oedematous tissue rich in free water.

7.3.3 Group spectrum analysis of lesion, contralateral, and control regions

When we averaged the isotropic spectra within each dataset (combined type: wet + dry, wet type and dry type, Fig. 7.5), the group patterns recapitulated the single subject examples shown previously (Fig. 7.3 and Fig. 7.4). In all three datasets, lesion spectra were left-shifted relative to contralateral and matched control OR, with a greater spectral weight at lower diffusivities (i.e. slower diffusion components). Contralateral spectra closely followed their corresponding controls, showing only a slight leftward displacement at the D_{25} landmark. The control spectra overlapped between the data sets without visible differences. Notably, the wet subtype exhibited the most pronounced high-diffusivity tail, the combined-type group was intermediate, and the dry subtype showed the smallest tail.

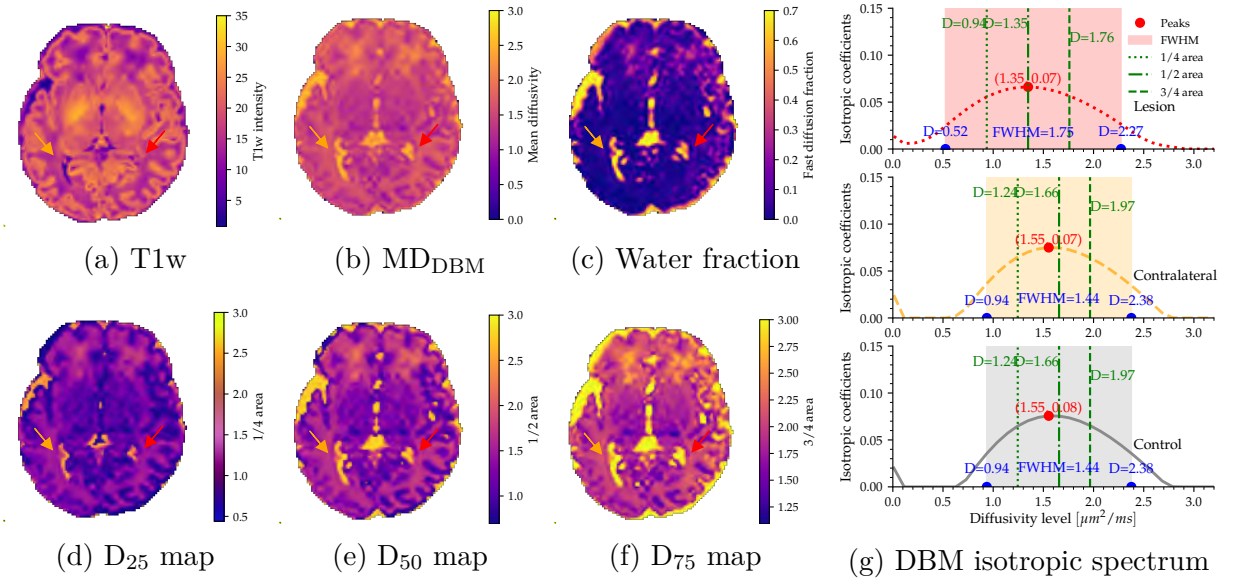

(a) T1w (b) MD_{DBM} (c) Water fraction

(d) D_{25} map (e) D_{50} map (f) D_{75} map (g) DBM isotropic spectrum

Figure 7.4 Dry-type punctate white-matter lesion in the optic radiation characterized with DBM. Subject ses-38001 from the dHCP cohort. (a) Axial T1-weighted image displays a focal hyper-intense PWML (red arrow). (b) DBM-derived mean-diffusivity map (MD_{DBM}) shows only mild diffusion restriction. (c) Fast-diffusion fraction map reveals no appreciable increase in free-water content, a defining feature of the "dry" phenotype. (d–f) Isotropic-spectrum area maps at the first, second, and third quartiles (D_{25}, D_{50}, D_{75} map) illustrate how the lesion signal diminishes with increasing diffusion scale, without developing the high-diffusion inversion seen in wet-type lesions. Orange arrows mark the contralateral mirror ROI; the matched control ROI is not displayed. (g) Isotropic decomposition coefficient curves for lesion (red), contralateral (orange), and control (gray) regions confirm a modest leftward shift and a narrower spectrum with no high-diffusion tail—consistent with a compact, gliotic micro-environment lacking excess extracellular water.

7.3.4 DBM analysis of three group of PWMLs

Combined Group Consistent with the spectra in Fig. 7.5 (a), the box plots in Fig. 7.6 (a) and Fig. 7.7 (a) confirmed a systematic leftward displacement of the lesion spectrum relative to both contralateral and control OR, indicating a higher proportion of slow-diffusing components within lesions. Specifically:

- D_{25} (1/4 area diffusivity) was lower in lesions by 29.1% versus controls ($p < 0.001$, $1.24\,\mu m^2/\,ms$ to $0.83\,\mu m^2/\,ms$) and by 25.1% vs. contralateral ($p < 0.001$, $1.14\,\mu m^2/\,ms$ to $0.83\,\mu m^2/\,ms$).

- D_{50} (1/2 area diffusivity) was lower in lesions by 21.5% versus controls ($p < 0.001$, $1.66\,\mu m^2/\,ms$ to $1.55\,\mu m^2/\,ms$) and by 19.2% versus contralateral ($p < 0.001$, $1.14\,\mu m^2/\,ms$

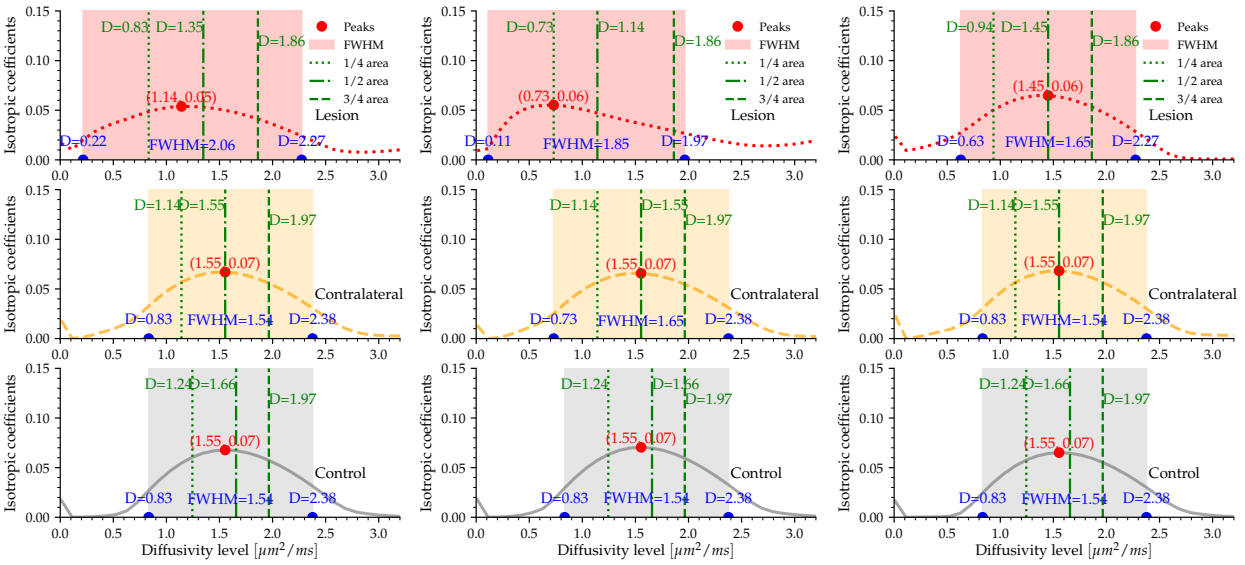

(a) Combined-Type PWMLs (b) Wet-Type PWMLs (c) Dry-Type PWMLs

Figure 7.5 Averaged Isotropic Decomposition Coefficient Curves for Lesion, Contralateral, and Control Regions in the Optic Radiation. This figure presents the averaged isotropic decomposition coefficient curves within the optic radiation for: (a) subjects with both wet and dry type punctate white matter lesions (PWMLs) ($N = 20$); (b) subjects with only Wet-type PWMLs ($N = 10$); (c) subjects with only Dry-type PWMLs ($N = 10$). Lesion regions: red solid curve; Contralateral regions: orange dashed curve, from the same subjects as the lesion regions; Control Regions: gray dashed curve, from 20 paired healthy controls.

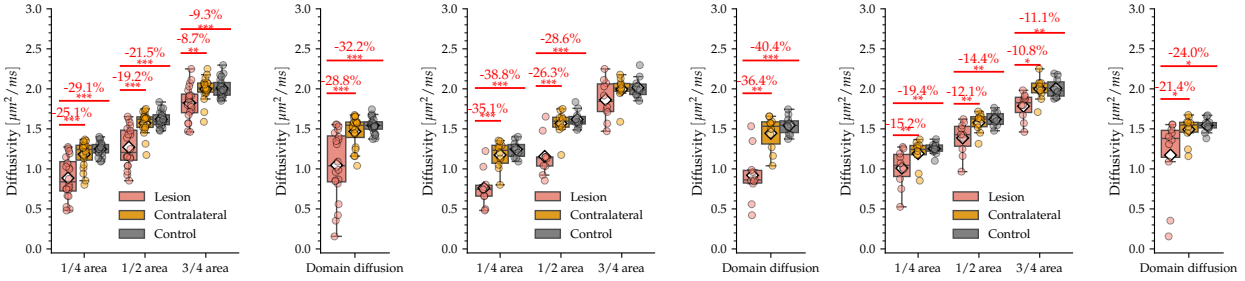

(a) Combined-Type PWMLs (b) Wet-Type PWMLs (c) Dry-Type PWMLs

Figure 7.6 DBM diffusion postional metrics in the optic radiation across lesion (red), contralateral (orange), and control regions (gray). Bar plots of D_{25} (1/4 area diffusivity, D_{50} (1/2 area diffusivity, D_{75} (3/4 area diffusivity, and domain diffusivity in the optic radiation for (a) all subjects with punctate white matter lesions (PWMLs) ($N = 20$), (b) subjects with only wet PWMLs ($N = 10$), and (c) subjects with dry PWMLs ($N = 10$). Pairwise contrasts were lesion versus contralateral and lesion versus matched control. Statistically significant differences are marked as * ($p < 0.05$), ** ($p < 0.01$), and *** ($p < 0.001$); percentage differences are annotated above significant bars.

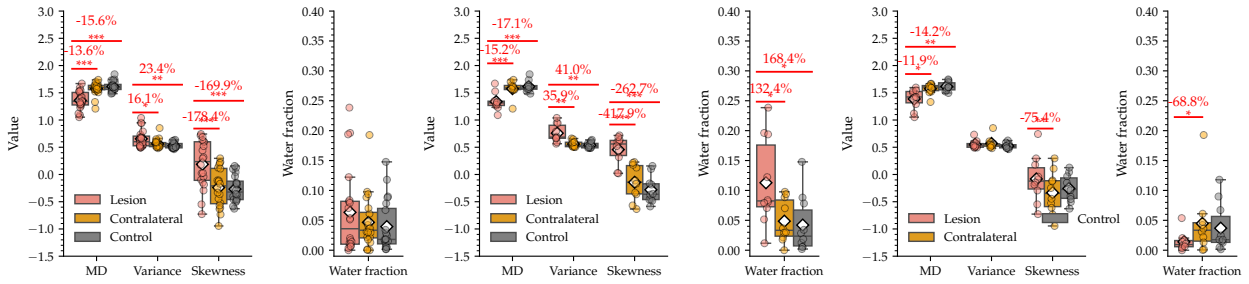

(a) Combined-Type PWMLs (b) Wet-Type PWMLs (c) Dry-Type PWMLs

Figure 7.7 General DBM metrics in the optic radiation across lesion (red), contralateral (orange), and control regions (gray). Bar plots of MD, Variance, Skewness, and Fast water fraction in the optic radiation for (a) all subjects with punctate white matter lesions (PWMLs) ($N = 20$), (b) subjects with only wet PWMLs ($N = 10$), and (c) subjects with dry PWMLs ($N = 10$). Pairwise contrasts were lesion versus contralateral and lesion versus matched control. Statistically significant differences are marked as * ($p < 0.05$), ** ($p < 0.01$), and *** ($p < 0.001$); percentage differences are annotated above significant bars.

to 1.35 $\mu m^2/ms$).

- D_{75} (3/4 area diffusivity) was lower in lesions by $< 10\%$ versus both controls and contralateral.
- The domain diffusivity exhibited a shift to the left of 32.2% versus controls ($p < 0.001$) and of 28.8% versus contralateral ($p < 0.001$).

Wet lesions accentuated the group-level pattern (Fig. 7.5 (b), Fig. 7.6 (b) and Fig. 7.7 (b)):

- D_{25} (1/4 area diffusivity) was lower by 38.8% vs. controls ($p < 0.001$, 1.24 $\mu m^2/ms$ to 0.73 $\mu m^2/ms$) and 35.1% vs. contralateral ($p < 0.001$, 1.14 $\mu m^2/ms$ to 0.73 $\mu m^2/ms$).
- D_{50} (1/2 area diffusivity) was lower by 28.6% vs. controls ($p < 0.001$, 1.66 $\mu m^2/ms$ to 1.14 $\mu m^2/ms$) and 26.3% vs. contralateral ($p < 0.001$, 1.55 $\mu m^2/ms$ to 1.14 $\mu m^2/ms$).
- D_{75} (3/4 area) did not show a significant change.
- *Domain diffusivity* d_{domain} shifted left by 40.4% and 36.4% vs. controls ($p < 0.001$) and contralateral ($p < 0.001$).
- Fast water fraction, comparing to the control group, increased more than 160% ($p < 0.05$), and the spectral variance and skewness increased dramatically (41.0%, $p < 0.01$ and 417.8%, $p < 0.001$), consistent with vasogenic oedema.

Dry lesions displayed a milder, more evenly distributed shift (Fig. 7.5 (c), Fig. 7.6 (c) and Fig. 7.7 (c)):

- D_{25} (1/4 area diffusivity) was lower by 19.4% vs. controls ($p < 0.01$) and 15.2% vs. contralateral ($p < 0.01$).
- D_{50} (1/2 area diffusivity) was lower by 14.4% vs. controls ($p < 0.01$) and 12.1% vs. contralateral ($p < 0.01$).
- D_{75} (3/4 area diffusivity) shifted left by 11.1% and 10.8% vs. controls ($p < 0.01$) and contralateral ($p < 0.05$).
- Domain diffusivity shifted left by 24.0% and 21.4% vs. controls ($p < 0.05$) and contralateral ($p < 0.05$).
- Fast water fraction decreased (68.8%, $p < 0.05$), and the variance did not show significant changes.

Thus, wet lesions showed the greatest left shift, broadening, and skewness with a large excess of fast water, while dry lesions retained a left shift without a rapid-water augmentation, together delineating subtype-specific microstructural phenotypes.

7.3.5 Conventional MRI findings in lesion, contralateral, and control regions

Diffusion tensor imaging metrics

Combined group: Lesions showed a uniform reduction in diffusivity relative to both references (Figure 7.8 (a)). AD decreased by ≈ 28% versus controls and by ≈ 26% versus contralateral OR; RD and MD drop by a comparable 25–27%. FA decreased only modestly (13.4%), reflecting the preserved but compressed fiber organization.

Wet-Type PWMLs: The attenuation was more pronounced (Fig. 7.8 (b)): AD was lower by ≈ 32% compared to both control and contralateral tissue, RD by ≈ 29% and MD by ≈ 30%. FA decreased by 15–17%. The magnitude and pattern of the reductions were compatible with acute injury accompanied by increased extracellular water, although the DTI itself does not specify a mechanism.

Dry-Type PWMLs: The changes were smaller, but they remained significant (Fig. 7.8 (c)). AD decreased by ≈ 25% vs. controls and ≈ 19% vs. contralateral tissue; RD and MD fell by roughly 22–24%. FA showed no significant differences.

Structural-MRI signal intensities

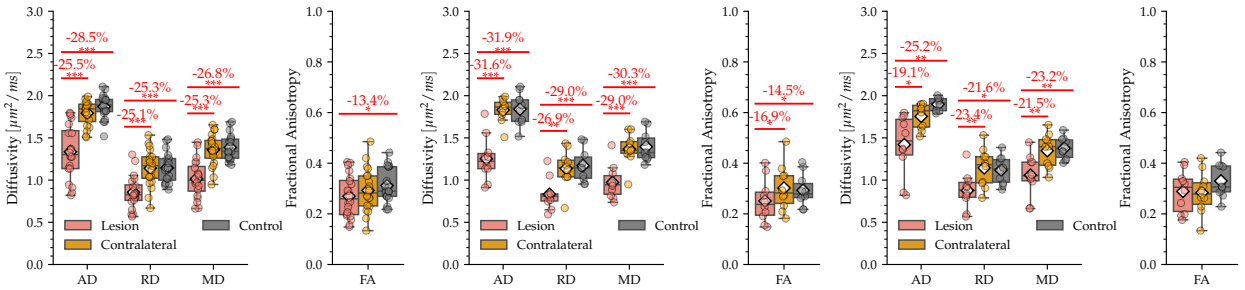

(a) Combined-Type PWMLs (b) Wet-Type PWMLs (c) Dry-Type PWMLs

Figure 7.8 DTI metrics in the optic radiation across lesion (red), contralateral (orange), and control regions (gray). Bar plots of AD, RD, MD, and FA in the optic radiation for (a) all subjects with punctate white matter lesions (PWMLs) ($N = 20$), (b) subjects with only wet PWMLs ($N = 10$), and (c) subjects with dry PWMLs ($N = 10$). Pairwise contrasts were lesion versus contralateral and lesion versus matched control. Statistically significant differences are marked as * ($p < 0.05$), ** ($p < 0.01$), and *** ($p < 0.001$); percentage differences are annotated above significant bars.

Across all lesion subgroups (Fig. 7.9), T1-weighted signal was $> 30\%$ higher than the contralateral side and $> 40\%$ higher than the control white matter, with wet lesions showing the highest elevation. T2-weighted signal was uniformly lower, decreasing by 11% to 13%, with a slightly greater reduction in dry lesions.

7.4 Discussion

This study applied the Diffusion Bubble Model to investigate the microstructural underpinnings of punctate white matter lesions. Our findings strongly support the hypothesis that DBM provides superior sensitivity and specificity compared to conventional metrics, revealing a consistent leftward shift in the isotropic diffusivity spectrum within PWMLs. Crucially, DBM resolved this population into two distinct subtypes, edema-dominant ("wet") and reorganization-dominant ("dry"), providing a mechanistic explanation for the heterogeneity of the lesion that is invisible to structural magnetic resonance imaging and DTI.

7.4.1 Resolving microstructural heterogeneity in PWMLs

Conventional imaging presented a uniform picture of PWMLs. Both subtypes showed similar, significant reductions in contralateral-normalized T2w signal (wet: -11.3%, dry: -12.5%) and mean diffusivity (20% to 30%). It was the decomposition of the diffusivity signal by DBM that uncovered the profound mechanistic divergence between them.

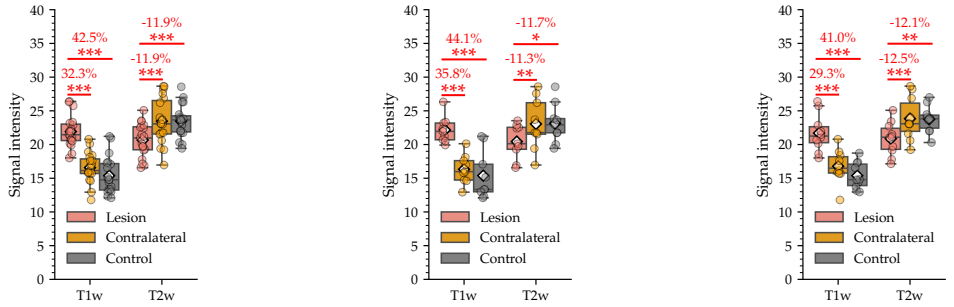

(a) Combined-Type PWMLs (b) Wet-Type PWMLs (c) Dry-Type PWMLs

Figure 7.9 Structural MRI signal intensity in the optic radiation across lesion (red), contralateral (orange), and control regions (gray). Bar plots of T1-weighted and T2-weighted signal intensity in the optic radiation for (a) all subjects with punctate white matter lesions (PWMLs) ($N = 20$), (b) subjects with only wet PWMLs ($N = 10$), and (c) subjects with dry PWMLs ($N = 10$). Pairwise contrasts were lesion versus contralateral and lesion versus matched control. Statistically significant differences are marked as * ($p < 0.05$), ** ($p < 0.01$), and *** ($p < 0.001$); percentage differences are annotated above significant bars.

Wet-type PWML Lesions classified as "wet" were characterized by a dramatic inflation of the fast-diffusing water fraction (+160%, $p < 0.05$) and a markedly higher spectral skewness (+418%, $p < 0.001$). On quartile diffusivity maps, these lesions presented a focal hypointense core (Fig. 7.3), indicating a local displacement of the entire spectrum. This pattern is highly consistent with vasogenic edema, where water redistributes into more freely diffusing extracellular pools. The concurrent changes at the slow-diffusion end may further reflect compartmental changes linked to inflammatory or cellular responses [25, 27, 50, 127, 183].

Dry-type PWML In contrast, "dry" lesions exhibited a predominant leftward shift of the isotropic spectrum with a significantly reduced fast fraction (−68.8%, $p < 0.05$) and no discrete hypointense core on quantile maps (Fig. 7.4). This profile is compatible with later-stage tissue reorganization processes, such as gliosis or elevated cellularity, which restrict water mobility with minimal free water contribution. The finding that infants with dry-type lesions were scanned at a later postnatal age (Fig. 7.2 (b)) supports a temporal progression from an acute, edematous phase to a chronic and reparative one.

In our data, the contrast of T1w tended to be more conspicuous in wet lesions than in dry lesions, while the reductions of T2w were similar between subtypes (see Fig. 7.3, 7.4), highlighting the complementary sensitivities of structural MRI and DBM.

7.4.2 Validation and clinical translation

Convergent Validity with Established Models The biological interpretation of the DBM subtypes is reinforced by a strong convergent validity with standard free water elimination. An exploratory FWE analysis in the same cohort showed a higher free-water fraction in wet lesions and no elevation in dry lesions, directly mirroring the DBM fast-fraction pattern. Furthermore, DBM's fast fraction was linearly associated with FWE's free-water fraction in both simulations and neonatal data (slope near unity, high R^2; Fig. 4.5 (d)), indicating that DBM provides a congruent but spectrally richer estimate of fast-diffusing water.

Towards a Microstructurally-Informed Clinical Pathway The ability to subtype PWMLs at baseline opens a pragmatic path for personalized monitoring. We propose a scheme where: (i) lesions are subtyped using DBM (fast-tail inflation/skewness for wet; slow-end shift for dry); (ii) spectral normalization is tracked on follow-up (wet: fast-tail decrease; dry: continued leftward shift or stabilization); and (iii) surveillance intervals are tailored accordingly, with short-interval scans for edema-dominant lesions and longer-horizon monitoring for reorganization-dominant ones. This DBM-based approach directly complements structural magnetic resonance imaging, which showed similar T2w reductions between subtypes, by pinpointing where along the diffusivity axis pathological changes occur.

7.4.3 Limitations and future directions

Limitations Although we had four raters to carefully delineate the region of PWML, the manual lesion delineation is potentially biased. Defining ROIs on T1w before transfer to other modalities introduces sensitivity to residual distortions. Our analysis focused on the cores of the lesion, leaving the perilesional gradients and the specific impacts of the tract unquantified. The cross-sectional design also precludes direct observation of longitudinal wet-to-dry transitions.

Future work Future work will focus on standardizing lesion masks using co-registered T2w and $\mathrm{MD}_{\mathrm{DBM}}$ with multi-rater consensus, and on quantifying perilesional and along-tract effects. Tracking the temporal evolution of lesions in a longitudinal cohort is a critical next step in validating the proposed wet-to-dry transition. Finally, to ensure clinical translation, we plan to package a NICU-ready pipeline, including quality-control protocols, harmonization scripts, and pretrained models, for broader validation and use.

7.5 Conclusion

In conclusion, this study demonstrates that the Diffusion Bubble Model moves beyond the descriptive limitations of conventional MRI to provide a mechanistic phenotyping of punctate white matter lesions. We have established that what appears as a homogeneous entity on structural and tensor-based images in fact comprises two distinct microstructural pathways: an acute, edema-dominant "wet" phenotype characterized by fast-water inflation and high spectral skewness, and a more chronic, reorganization-dominant "dry" phenotype defined by a predominant leftward spectral shift and reduced fast fraction.

The ability of DBM to resolve this heterogeneity fulfills a central promise of this thesis: to deliver a clinically feasible framework with superior sensitivity and specificity to neonatal brain injury. By pinpointing where along the diffusivity axis pathological changes occur, DBM offers a biologically-grounded explanation for PWML appearance and a principled basis for subtyping. This work directly builds on the validated foundation of DBM (Chapter 4), culminating in its successful application to a precise and common form of clinical injury, paving the way for connecting early-life lesion characteristics with long-term neurodevelopmental outcomes.

CHAPTER 8 DISCUSSION

8.1 Overview of the Research Journey

Characterizing neonatal brain maturation and focal injury is challenging: the third trimester features rapid, heterogeneous microstructural change, while conventional imaging often lacks the biological specificity needed to disentangle tissue processes under clinically feasible acquisition constraints. This thesis aimed to close that gap by developing and validating a diffusion-MRI framework that is both biophysically interpretable and practical at the bedside, and then using it to address core questions in segmentation, developmental assessment, and injury characterization in preterm and term-born infants.

We organized the work around a simple narrative: methodological innovation enabling biological insight and clinical utility (Fig. 1.4). First, we introduced and rigorously validated the Diffusion Bubble Model (DBM) (Chapter 3 and Chapter 4)—a spectrum-based approach that reconstructs the isotropic diffusivity spectrum to localize where changes occur along the diffusivity axis—thereby adding interpretability beyond tensor averages. To ensure this model's applicability to large-scale, we then built a diffusion-only segmentation pipeline that delivers precise tissue parcellation directly in dMRI space (Chapter 5).

Armed with this validated toolkit, we applied it to resolve fundamental questions in brain development and injury. In development, we found that the preterm-term diffusion trajectories between late-preterm and TEA are broadly parallel but time-shifted, indicating a delayed onset of maturation with residual immaturity concentrated in frontal and temporal pathways at term-equivalent age, despite volumetric catch-up (Chapter 6). In injury characterization, we identified two mechanistically distinct subtypes within punctate white-matter lesions (PWML) that are indistinguishable using conventional imaging (Chapter 7).

8.2 Main discussion

The work in this thesis can be read as defining and applying a new microstructural language for the neonatal brain. The Diffusion Bubble Model (DBM) establishes the alphabet and grammar of this language by decomposing complex diffusion signals into meaningful spectral units. The diffusion-only segmentation tool ensures that this language can be read consistently across heterogeneous datasets—even when structural images are missing—so that spectral information is anchored in a stable anatomical frame. Deployed together, these components allow us to interpret maturation and focal injury through a common, spectrum-based

vocabulary rather than through a collection of sequence-specific readouts.

8.2.1 Positioning DBM within diffusion MRI modeling

Diffusion models are often grouped into three families: (i) statistical signal descriptions (e.g., DTI) that summarize the attenuated signal [14–16]; (ii) discrete multi-compartment models that posit a small set of tissue pools with prescribed geometries [17, 25, 26, 29]; and (iii) spectrum-based models that represent diffusion as a continuum over diffusivity or restriction scales [13,23,24,27,28]. DBM belongs to the third family with an explicit but compact design: it reconstructs the one-dimensional isotropic diffusivity spectrum and handles anisotropy via a low-dimensional adjustment, thereby localizing where along the diffusivity axis changes occur while minimizing orientation dependence [24].

Relation to two-compartment models

Conceptually, the Diffusion Bubble Model can be viewed as a natural extension of multi-compartment modeling into a continuous domain. It preserves the intuitive notion of signal "fractions" while relaxing the strong geometric and diffusivity assumptions that are often unidentifiable in typical neonatal acquisitions.

In practice, DBM often behaves like a parsimonious two-term factorization of the diffusion signal: (i) a low-dimensional anisotropy adjustment that captures orientation-dependent effects, and (ii) an isotropic residual that is explicitly decomposed into a continuous diffusivity spectrum. This differs from classical two-compartment formulations that assign fixed compartments with predetermined diffusivity.

Free water elimination (FWE) model is a representative two-compartment approach: it models each voxel as an anisotropic tissue tensor plus a single fast isotropic pool intended to capture free water or partial-volume CSF [181, 189]. DBM makes a complementary choice in another direction. Rather than positing one fixed fast-isotropic compartment, DBM first compresses anisotropy into a minimal adjustment using an explicit fixed long thin anisotropic tensor and then models the entire isotropic residual as a nonparametric spectrum. As a result, the isotropic component in DBM is not solely identified with free water; it integrates all isotropic contributions—including hindered and restricted components—and localizes them along the diffusivity axis.

In essence, DBM does not seek to map anatomical compartments in a one-to-one manner. Instead, it interprets the voxel's isotropic signal as an aggregate spectral response, reflecting the confluence of multiple microstructure processes within a single, continuous diffusivity

profile. This design confers a critical advantage under neonatal imaging constraints—limited b-value bandwidth, modest angular sampling, and short scan times. By circumventing the need to enumerate multiple anisotropic tissue compartments, DBM significantly enhances model identifiability while preserving the ability to resolve microstructure changes at the spectral level [24].

Relation to existing spectrum-based models

Within spectrum-oriented dMRI, DBM occupies a pragmatic middle ground. Unlike DSI—which reconstructs the full displacement or spectrum at the cost of dense q-space sampling, high b-values, and long acquisitions—DBM recovers a compact one-dimensional isotropic diffusivity spectrum from short, neonatal-feasible protocols. Although conceptually inspired by DBSI and DSI, which fit multiple anisotropic fiber populations and/or restricted components per voxel (assigning per-bundle $(\lambda_{\parallel}, \lambda_{\perp})$ and weights) [27], DBM avoids a per-bundle orientation fitting and the growth of accompanying parameters that are sensitive to SNR and initialization in short neonatal scans [23]. The trade-off is deliberate: DBM forgoes tract-level parameters in exchange for stable, spectrum-aware readouts that localize change along the diffusivity axis (e.g., quantile and dominant diffusivities) and summarize distribution shape (e.g., fast fraction, variance, skewness), which proved sufficient to phenotype developmental and lesion-related effects in this thesis.

DBM is also closely related to implicit-spectrum statistical models such as DKI and the stretched-exponential and distributed diffusion coefficient (DDC) model [14, 15]. Those approaches assume an underlying distribution of diffusivity but summarize it via low-order moments or two-parameter summaries in the signal domain (e.g., kurtosis as a variance proxy; DDC and the heterogeneity index α). By contrast, DBM makes the distribution explicit: after a minimal anisotropy adjustment, it inverts the isotropic component to obtain the full spectrum, from which moments can be computed to cross-check DKI and stretched-exponential descriptors. In this way, DBM retains computational simplicity while exposing the spectrum's shape, yielding interpretable, visually inspectable features that were informative for neonatal development and injury characterization in our cohort.

Scope, strengths, and boundaries of DBM

DBM is a spectrum-first, geometry-light framework optimized for low-to-moderate anisotropy typical of neonatal WM and GM. By reducing voxel-level anisotropy before isotropic decomposition, it localizes changes along the isotropic diffusivity spectrum without fitting multiple fiber populations, hence it is not designed for tractography. This design is advantageous

in neonates, where lower FA, higher free-water content, motion, and EPI distortions challenge orientation-resolved methods [103,218]. In simulations at fixed MD (e.g., 1.5 $\mu m^2/ms$), very high FA (≥ 0.7) produced slight but noticeable shifts in the recovered isotropic spectrum due to coupling in the anisotropy adjustment step; increasing the axial diffusivity of the adjustment tensor can mitigate this but at the cost of bias in low-FA voxels (Chapter 4). We therefore prioritized stability in the neonatal range (most tissue FA ≤ 0.5 in our cohort; Chapter 6), which aligns with our dMRI-25-direction neonatal acquisition. For interoperability, DBM can output tensor-like scalars (an anisotropy index with FA-like behavior, DBM-derived MD_{DBM}, and a domain diffusivity D_{main}), but these are compatibility bridges, not primary readouts. Recent work also shows shape stability of the recovered spectrum across reasonable isotropic bases—basis choice mainly rescales coefficients without altering qualitative features [24]. In sum, DBM complements rather than replaces orientation-resolved models: it is more informative for tissue-structure–level inference in development and disease (e.g., regional maturation and PWML characterization), and its boundaries are clearest in high-FA regimes and tractography applications.

8.2.2 What DBM adds beyond tensors?

Added specificity over tensors: localization along the diffusivity axis The key advantage of DBM is localization: it resolves where diffusion alterations occur along the isotropic diffusivity spectrum rather than averaging them into a small number of averaged values. From late preterm to TEA, neonatal brain diffusion trends are well established—MD decreases and FA increases with age as extracellular water contracts and early myelination progresses [10,184]. DBM clarifies these effects by separating the fast-diffusion (free-water–like) tail content from the tissue-dominated peak. For example, the classic observation that WM has higher MD than GM can be attributed primarily to a right-shift of the tissue peak in WM rather than to a greater free-water fraction (Chapter 4). Across late preterm to 43 weeks, DBM shows monotonic decreases in the fast-water fraction in cortical GM, WM, and deep GM (GM > WM > deep GM at a given age; Chapter 6), consistent with extracellular-space contraction rather than edema [185]. This aligns with spectrum and FWE-style approaches that improve specificity by parsing high-diffusivity isotropic signal from hindered and restricted components [219].

PWML illustration: similar tensors, distinct spectra In punctate white-matter lesions (Chapter 7), tensor metrics and T2w signal changes can appear similar across lesions, yet DBM separates edema-dominant (“wet”) from reorganization-dominant (“dry”) phenotypes by revealing fast-tail inflation with increased skewness versus a left-shift with reduced fast

fraction. Thus, DBM's positional and shape metrics (e.g., diffusivity quantiles, skewness, fast fraction) provide mechanistic specificity that complements tensors and structural intensity. Structural MRI alone does not robustly distinguish these subtypes, whereas the spectral readout indicates where in the distribution the change occurs.

Convergent validity with FWE DBM quantifies fast-diffusion content by integrating the high-diffusivity tail of the isotropic spectrum rather than assigning a single "free-water" compartment. Across simulations and neonatal data (Chapter 4), DBM fast fraction is linearly associated with FWE's free-water fraction, indicating convergent—though not identical—estimates while DBM retains a fuller spectral description. Because FWE imposes one fast-isotropic pool, absolute magnitudes are not directly interchangeable; we therefore use FWE as a consistency check rather than a ground truth.

Complementary sensitivity profiles Under matched multiple-comparison control, DBM more often detected within-preterm catch-up effects (via positional metrics such as D_{25} and D_{50}), whereas DTI captured larger shares of TEA residuals (AD, RD and MD) (Chapter 6). This reflects the models' emphases: DBM localizes where along the spectrum maturation proceeds; DTI summarizes how much diffusivity lag remains at TEA. Using both yields a more complete picture.

8.2.3 Integrating development and injury within a unified spectral framework

DBM reveals a common "spectral grammar" that organizes both typical maturation and focal injury within the same coordinate system. During late-gestation development, the delayed-onset pattern observed in preterm infants can be interpreted as a progressive leftward shift of the tissue-dominated peak accompanied by compression of the fast-diffusion tail, consistent with extracellular-space reduction and increasing membrane density. Strikingly, the same axes help decode punctate white-matter lesions (PWML): edema-dominant ("wet") lesions exhibit fast-tail inflation, an extreme expression of extracellular water increase that lies on the same fast-diffusion end of the spectrum as normal developmental fluid changes, albeit with different magnitude and spatial extent; reorganization-dominant ("dry") lesions show a left shift with reduced fast fraction, suggestive of tissue reorganization and restricted-space dominance that diverges from, or "hijacks" the typical maturational trajectory.

Viewed this way, DBM does not provide two disconnected findings but a single, coherent narrative: both maturation and injury manifest as spectral displacements and deformations along the diffusivity axis. This perspective also clarifies why volumetry failed to capture microstructural lag at term-equivalent age: volume is a macroscopic, integrated quantity, whereas the DBM spectrum exposes uneven changes among underlying components, speci-

fying where along the diffusivity spectrum those changes occur.

8.2.4 Clinical feasibility and the diffusion-native workflow

Our original motivation for a diffusion-only segmentation pipeline was pragmatic: to analyze infants with missing or unusable T2-weighted images. In practice, the model's strong cross-site generalization indicates that dMRI-derived scalars—despite known protocol dependencies—can serve as robust tissue markers in multi-site neonatal studies. This directly reinforces the premise of DBM: clinically feasible diffusion acquisitions can contain sufficient information to recover microstructural signals (via the isotropic spectrum) without heavy reliance on external structural images. In other words, DBM helps align the scale of acquisition with the scale of interpretation.

Operationally, pairing DBM with diffusion-only segmentation yielded tangible benefits. The workflow increased the analyzable data by including 14/88 (16.0%) infants who lacked usable T2w scans in the preterm-term cohort, and supported stable regional analyses between scanners. More broadly, the development and injury applications show that isotropic diffusion information can be extracted natively from short, motion-tolerant neonatal protocols—without densely sampled, long multi-shell acquisitions—while still delivering spectrum-level interpretability. Multi-sequence or multi-shell data remain valuable when available, but a dMRI-native path is viable and scalable in routine clinical settings.

To make this workflow portable across clinical sites, we address protocol variability at both the model and data levels. First, on the acquisition–model side, DBM is designed for robustness: its minimal anisotropy-adjustment term reduces dependence on dense angular sampling, shifting the information burden toward a clinically manageable spread of b-values for spectral recovery within neonatal safety and SNR limits. Second, at the data level, fundamental dMRI normalization is critical: expressing diffusion signals as attenuation S/S_0 provides a unit-less input that is less sensitive to receive gain, coil differences, and main magnetic field strength, which is why diffusivity estimates (e.g., from DTI) are relatively comparable across scanners in practice. Our workflow adheres to this principle for DBM inputs, while acknowledging that protocol factors (TE and TR, noise and EPI distortions) may still introduce systematic bias in absolute metric values. Third, consistent preprocessing—including denoising, motion and susceptibility correction—further mitigates site-specific technical confounds in downstream statistics.

With these interconnected guardrails—a robust model, fundamental signal normalization, and consistent preprocessing—the combination of DBM and diffusion-only segmentation turns feasibility (short scans, fewer directions) and specificity (spectral localization) into

two sides of the same coin: a diffusion-native workflow that is both clinically compatible and biologically informative.

8.2.5 Translational outlook

The validation of the Diffusion Bubble Model (DBM) across this thesis lays the groundwork for translating it from a research prototype into a robust platform for discovery and clinical decision support. A pragmatic pathway comprises three interconnected stages: technical hardening, biological grounding, and clinical integration.

Technical hardening This work establishes a clinically feasible dMRI-25-direction protocol and the diffusion-only nnU-Net, forming a structural-agnostic pipeline. The immediate next step is to package the end-to-end workflow as a containerized, BIDS-compatible application with version-locked dependencies and embedded quality-control and uncertainty metrics (e.g., motion, eddy and susceptibility residuals, segmentation confidence, spectral-fit diagnostics) to guarantee multi-site reproducibility.

To maximize community adoption and benchmarking, we plan to integrate DBM into established quantitative MRI platforms. Implementation in qMRLab, a modular open-source project from our lab, provides a natural host for DBM with a graphical interface [220]. A complementary implementation in DIPY (Python) will enable a direct comparison with other diffusion models and facilitate integration into large-scale processing pipelines [179]. This dual-pathway strategy will transform DBM from a lab-specific tool into a standardized community-vetted resource. Finally, a prospective, pre-registered multi-site study will quantify test–retest repeatability, scanner and sequence variance components, and cross-protocol calibration, establishing scanner-specific reference norms.

Biological grounding Linking neonatal DBM metrics—such as maturation delay indices or PWML subtype patterns—to longitudinal neurodevelopmental outcomes will determine their prognostic value. Integration with complementary MRI modalities and histopathological correlation will further strengthen biological interpretation and refine the mechanistic meaning of spectral shifts.

Clinical integration DBM outputs (currently in NIfTI format) will be delivered through an automated reporting layer with DICOM-compatible exports—bridging research outputs to PACS—and concise, clinician-facing summaries (regional maturational percentile ranks and PWML subtype probabilities with suggested follow-up). Embedding these outputs into decision-support systems and longitudinal registry would enable risk stratification and early intervention planning.

Ultimately, the translation of DBM extends beyond adopting a new imaging model. It outlines a path toward precision neonatology in which microstructure health is quantified, monitored, and acted upon to improve outcomes for the most vulnerable infants.

8.2.6 Limitations and future work

Despite completing the initial phase of this project—model design, segmentation, evaluation of preterm catch-up, and PWML microstructure assessment—several inherent limitations and improvement areas remain.

Generalizability of the framework While DBM performs well in characterizing heterogeneity within PWML, an open question is whether the same spectral language can disentangle more complex mixed pathologies—for example, hypoxic–ischemic injury interleaved with inflammatory processes. Addressing this will require testing DBM on cohorts with richer etiological diversity and designing analyses that explicitly probe interaction patterns across the spectrum (e.g., concurrent fast-tail inflation and slow-end dominance), rather than assuming a single dominant process per voxel.

From association to mechanism The present work establishes strong imaging biomarkers, but the biological interpretation of spectral features must be consolidated through histopathological correlation and longitudinal outcome linkage. In particular, validating whether fast-tail inflation maps onto vasogenic edema and whether left-shifted, fast-reduced spectra reflect cellular reorganization will benefit from tissue studies and from prospective follow-up linking DBM metrics to neurodevelopmental outcomes at 6/12/24 months.

From framework to tool A critical next step is to translate the framework into a clinical tool: automating and standardizing the full pipeline, hardening it for multi-site use, and converting DBM spectral metrics into predictive decision support (e.g., risk scores indexed by PMA, trajectory alerts, and lesion-type likelihoods). This will involve protocol harmonization, uncertainty reporting, and prospective evaluation against actionable endpoints to demonstrate added value over conventional diffusion and structural imaging.

8.3 Concluding Perspective

In conclusion, the contribution of this thesis extends beyond the DBM model or any single application. Its central value is to articulate a pathway toward a unified, physics-grounded microstructural language that coherently explains both typical maturation and focal injury within the same diffusivity spectrum, moving away from piecemeal, sequence-specific readouts. By coupling a pragmatic dMRI-native workflow with spectral analysis, we outline

how neonatal diffusion MRI can deliver actionable, whole-brain assessment under clinically feasible protocols. This vision complements rather than replaces existing multi-sequence imaging, while providing a common substrate for multi-site harmonization and outcome-linked biomarkers in the at-risk neonatal brain. In this sense, DBM offers not only a model but a reproducible workflow on which routine, spectrum-resolved neonatal assessment could be built.

CHAPTER 9 CONCLUSION

This thesis set out to make diffusion MRI more informative and practical for the neonatal brain. We introduced the Diffusion Bubble Model (DBM), a spectrum-based framework that works within the constraints of neonatal dMRI: short scans, motion, and rapidly evolving microstructure, and demonstrated an end-to-end workflow from acquisition and modeling to diffusion-based segmentation, developmental inference in preterm and term infants, and lesion characterization. Across simulations, in vivo analyses and two application domains (punctate white matter lesions, PWML; and maturation around term equivalent age, TEA), DBM provides specific and biomedical interpretable diffusion readouts while remaining compatible with neonatal practice. In short, DBM increases the information content of neonatal dMRI without sacrificing feasibility, and the diffusion-first workflow operates when structural images are unavailable.

Summary of Contributions

1. *Neonatal-first diffusion model*: developed the Diffusion Bubble Model (DBM) to recover an isotropic diffusivity spectrum and derive compact, robust metrics: mean diffusivity, fast diffusion fraction, slow diffusion fraction, and spectral variance and skewness; validated key behaviors in simulations, including invariance to anisotropy changes at fixed mean diffusivity, linear scaling of the anisotropy-adjusted fraction with FA, and faithful recovery of fast and slow components; enabling specific, interpretable neonatal diffusion markers that remain estimable under short scans and motion.
2. *Practical deployment under clinical constraints*: optimized acquisition and preprocessing for neonatal-feasible protocols and showed DTI comparability (25- versus 32-direction) with narrow Bland–Altman limits and high reliability; demonstrated that DBM metrics remain stable for cohort studies despite modest differences in direction counts and b-value shell sampling; DBM behaved consistently in vivo under clinically feasible sampling, supporting reproducible neonatal dMRI pipelines.
3. *Diffusion-first workflow*: integrated acquisition, modeling, segmentation, and inference to operate with diffusion MRI alone when structural images are unavailable; verified feasibility via diffusion-only tissue segmentation and DBM biomarker stability across cohorts; allowing processing and analysis in time-limited scans, motion-degraded studies, and retrospective datasets lacking usable T1w and T2w.
4. *Diffusion-only tissue segmentation*: trained a diffusion-only nnU-Net using dMRI-

derived features to produce tissue maps without reliance on T2w contrast; evaluated performance in-domain and out-of-domain to show internal accuracy and acceptable cross-site generalization, mitigating known T2w variability; enabling diffusion-first workflows where microstructure mapping and segmentation share the same acquisition.

5. *Preterm vs. term maturation at TEA and across late-preterm to* 43 *weeks*: modeled maturation with mixed-effects analyses at TEA and longitudinally across late-preterm to 43 weeks; found largely parallel between groups with a delayed onset (offset) in preterm infants, yielding regional TEA residuals despite volume catch-up after head-size adjustment.
6. *PWML characterization with spectral insight*: quantified differences among the lesion, contralateral and matched control region using spectral readouts; Observed two PWML subtypes: wet (fast-tail inflation, skewness ↑, with a left shift) and dry (predominant left shift with reduced fast fraction) phenotypes, despite similar reductions in T2w and comparable decreases in MD tensors between subtypes.

Interpretation and Impact

1. *Microstructural specificity*: focusing on the isotropic spectrum separates faster (more extracellular) from slower (more restricted) components; providing interpretable biomarkers for edema-like processes, myelination trajectories, and lesion microenvironments.
2. *Practicality*: working with short neonatal scans and tolerates moderate protocol variation; supporting translation beyond a single scanner or study.
3. *Workflow minimalism:* operating on diffusion data alone reduces dependence on site-specific structural contrast; simplifying cross-site deployment and expanding utility to settings where structural images are unavailable or unusable.
4. *Decision-support potential:* in PWML, compact spectral metrics distinguish subtypes; in development, they reveal timing shifts and residual gaps—promising for risk stratification, subtyping, and longitudinal monitoring (pending prospective validation).

Concluding Remarks

This thesis advances neonatal diffusion MRI along two axes that rarely meet—biophysical specificity and clinical feasibility—by introducing DBM and a diffusion-first workflow. By moving beyond scalar averages to a spectrum-resolved representation, DBM clarifies both typical maturation and PWML heterogeneity, providing a foundation for deployable, reproducible biomarkers for the vulnerable neonatal brain and laying the groundwork for precise, non-invasive microstructural assessment in routine neonatal care.

REFERENCES

[1] E. O. Ohuma *et al.*, "National, regional, and global estimates of preterm birth in 2020, with trends from 2010: A systematic analysis," *Obstet. Anesth. Dig.*, vol. 44, no. 3, pp. 150–151, Sep. 2024.

[2] J. L. Y. Cheong *et al.*, "Neurodevelopment at age 9 years among children born at 32 to 36 weeks' gestation," *JAMA Netw. Open*, vol. 7, no. 11, p. e2445629, Nov. 2024.

[3] J. H. Jin *et al.*, "Long-term cognitive, executive, and behavioral outcomes of moderate and late preterm at school age," *Clin. Exp. Pediatr.*, vol. 63, no. 6, pp. 219–225, Jun. 2020.

[4] D. Pecheva *et al.*, "A tract-specific approach to assessing white matter in preterm infants," *Neuroimage*, vol. 157, pp. 675–694, Aug. 2017.

[5] A. L. A. Nguyen *et al.*, "The brain's kryptonite: Overview of punctate white matter lesions in neonates," *Int. J. Dev. Neurosci.*, vol. 77, pp. 77–88, Oct. 2019.

[6] C. A. M. de Bruijn *et al.*, "Neurodevelopmental consequences of preterm punctate white matter lesions: a systematic review," *Pediatr. Res.*, vol. 93, no. 6, pp. 1480–1490, May 2023.

[7] N. Tusor *et al.*, "Punctate white matter lesions associated with altered brain development and adverse motor outcome in preterm infants," *Sci. Rep.*, vol. 7, no. 1, p. 13250, Oct. 2017.

[8] Y. Zhang *et al.*, "Quantitative analysis of punctate white matter lesions in neonates using quantitative susceptibility mapping and R2* relaxation," *AJNR Am. J. Neuroradiol.*, vol. 40, no. 7, pp. 1221–1226, Jul. 2019.

[9] J. P. Lerch *et al.*, "Studying neuroanatomy using MRI," *Nat. Neurosci.*, vol. 20, no. 3, pp. 314–326, Feb. 2017.

[10] J. Dubois *et al.*, "MRI of the neonatal brain: A review of methodological challenges and neuroscientific advances," *J. Magn. Reson. Imaging*, vol. 53, no. 5, pp. 1318–1343, May 2021.

[11] A. L. Alexander *et al.*, "Diffusion tensor imaging of the brain," *Neurotherapeutics*, vol. 4, no. 3, pp. 316–329, Jul. 2007.

[12] D. Le Bihan *et al.*, "MR imaging of intravoxel incoherent motions: application to diffusion and perfusion in neurologic disorders," *Radiology*, vol. 161, no. 2, pp. 401–407, Nov. 1986.

[13] V. J. Wedeen *et al.*, "Mapping complex tissue architecture with diffusion spectrum magnetic resonance imaging," *Magn. Reson. Med.*, vol. 54, no. 6, pp. 1377–1386, Dec. 2005.

[14] K. M. Bennett *et al.*, "Characterization of continuously distributed cortical water diffusion rates with a stretched-exponential model," *Magn. Reson. Med.*, vol. 50, no. 4, pp. 727–734, Oct. 2003.

[15] J. Jensen *et al.*, "Quantifying non-gaussian water diffusion by means of pulsed-field-gradient MRI," *Proc. Intl. Soc. Mag. Reson. Med.*, vol. 11, p. 2154, 2003.

[16] C. Pierpaoli *et al.*, "Diffusion tensor MR imaging of the human brain," *Radiology*, vol. 201, no. 3, pp. 637–648, Dec. 1996.

[17] M. Palombo *et al.*, "SANDI: A compartment-based model for non-invasive apparent soma and neurite imaging by diffusion MRI," *Neuroimage*, vol. 215, no. 116835, p. 116835, Jul. 2020.

[18] I. O. Jelescu *et al.*, "Neurite exchange imaging (NEXI): A minimal model of diffusion in gray matter with inter-compartment water exchange," *Neuroimage*, vol. 256, no. 119277, p. 119277, Aug. 2022.

[19] S. G. Waxman *et al.*, *The axon: Structure, function and pathophysiology*, S. G. Waxman *et al.*, Eds. New York, NY: Oxford University Press, Mar. 1995.

[20] D. S. Novikov *et al.*, "Quantifying brain microstructure with diffusion MRI: Theory and parameter estimation: Brain microstructure with dMRI: Theory and parameter estimation," *NMR Biomed.*, vol. 32, no. 4, p. e3998, Apr. 2019.

[21] C. Beaulieu, "The basis of anisotropic water diffusion in the nervous system - a technical review," *NMR Biomed.*, vol. 15, no. 7-8, pp. 435–455, Nov. 2002.

[22] D. K. Jones *et al.*, "White matter integrity, fiber count, and other fallacies: the do's and don'ts of diffusion MRI," *Neuroimage*, vol. 73, pp. 239–254, Jun. 2013.

[23] I. O. Jelescu *et al.*, "Design and validation of diffusion MRI models of white matter," *Front. Phys.*, vol. 28, Nov. 2017.

[24] E. Zhang *et al.*, "Diffusion bubble model: A novel MRI approach for detection and subtyping of neonatal punctate white matter lesions," *Neuroimage*, vol. 317, no. 121324, p. 121324, Aug. 2025.

[25] N. S. White *et al.*, "Probing tissue microstructure with restriction spectrum imaging: Histological and theoretical validation," *Hum. Brain Mapp.*, vol. 34, no. 2, pp. 327–346, Feb. 2013.

[26] H. Zhang *et al.*, "NODDI: practical in vivo neurite orientation dispersion and density imaging of the human brain," *Neuroimage*, vol. 61, no. 4, pp. 1000–1016, Jul. 2012.

[27] Y. Wang *et al.*, "Quantification of increased cellularity during inflammatory demyelination," *Brain*, vol. 134, no. Pt 12, pp. 3590–3601, Dec. 2011.

[28] C. C. Conlin *et al.*, "Improved characterization of diffusion in normal and cancerous prostate tissue through optimization of multicompartmental signal models," *J. Magn. Reson. Imaging*, vol. 53, no. 2, pp. 628–639, Feb. 2021.

[29] D. A. Yablonskiy *et al.*, "Statistical model for diffusion attenuated MR signal," *Magn. Reson. Med.*, vol. 50, no. 4, pp. 664–669, Oct. 2003.

[30] D. Varadarajan *et al.*, "A theoretical signal processing framework for linear diffusion MRI: Implications for parameter estimation and experiment design," *Neuroimage*, vol. 161, pp. 206–218, Nov. 2017.

[31] D. S. Tuch, "Q-ball imaging," *Magn. Reson. Med.*, vol. 52, no. 6, pp. 1358–1372, Dec. 2004.

[32] E. Özarslan *et al.*, "Mean apparent propagator (MAP) MRI: a novel diffusion imaging method for mapping tissue microstructure," *Neuroimage*, vol. 78, pp. 16–32, Sep. 2013.

[33] A. V. Avram *et al.*, "Clinical feasibility of using mean apparent propagator (MAP) MRI to characterize brain tissue microstructure," *Neuroimage*, vol. 127, pp. 422–434, Feb. 2016.

[34] F. Sun *et al.*, "Research progress in diffusion spectrum imaging," *Brain Sci.*, vol. 13, no. 10, p. 1497, Oct. 2023.

[35] A. Tobisch *et al.*, "Compressed sensing diffusion spectrum imaging for accelerated diffusion microstructure MRI in long-term population imaging," *Front. Neurosci.*, vol. 12, p. 650, Sep. 2018.

[36] Q. Tian *et al.*, "Generalized diffusion spectrum magnetic resonance imaging (GDSI) for model-free reconstruction of the ensemble average propagator," *Neuroimage*, vol. 189, pp. 497–515, Apr. 2019.

[37] C.-W. Chiang *et al.*, "Quantifying white matter tract diffusion parameters in the presence of increased extra-fiber cellularity and vasogenic edema," *Neuroimage*, vol. 101, pp. 310–319, Nov. 2014.

[38] Y. Wang *et al.*, "Differentiation and quantification of inflammation, demyelination and axon injury or loss in multiple sclerosis," *Brain*, vol. 138, no. Pt 5, pp. 1223–1238, May 2015.

[39] Z. Ye *et al.*, "Diffusion histology imaging combining diffusion basis spectrum imaging (DBSI) and machine learning improves detection and classification of glioblastoma pathology," *Clin. Cancer Res.*, vol. 26, no. 20, pp. 5388–5399, Oct. 2020.

[40] T.-H. Lin *et al.*, "Noninvasive quantification of axonal loss in the presence of tissue swelling in traumatic spinal cord injury mice," *J. Neurotrauma*, vol. 36, no. 15, pp. 2308–2315, Aug. 2019.

[41] R. H. Han *et al.*, "Diffusion basis spectrum imaging as an adjunct to conventional MRI leads to earlier diagnosis of high-grade glioma tumor progression versus treatment effect," *Neurooncol. Adv.*, vol. 5, no. 1, p. vdad050, Apr. 2023.

[42] Q. Wang *et al.*, "Quantification of white matter cellularity and damage in preclinical and early symptomatic alzheimer's disease," *NeuroImage Clin.*, vol. 22, no. 101767, p. 101767, Mar. 2019.

[43] X. Wang *et al.*, "Diffusion basis spectrum imaging detects and distinguishes coexisting subclinical inflammation, demyelination and axonal injury in experimental autoimmune encephalomyelitis mice: DBSI detects subclinical pathologies," *NMR Biomed.*, vol. 27, no. 7, pp. 843–852, Jul. 2014.

[44] D. Jayasekera *et al.*, "Analysis of combined clinical and diffusion basis spectrum imaging metrics to predict the outcome of chronic cervical spondylotic myelopathy following cervical decompression surgery," *Journal of neurosurgery. Spine*, vol. 37, no. 4, pp. 1–11, May 2022.

[45] A. E. Rodríguez-Soto *et al.*, "Characterization of the diffusion signal of breast tissues using multi-exponential models," *Magn. Reson. Med.*, vol. 87, no. 4, pp. 1938–1951, Apr. 2022.

[46] C. E. Palmer *et al.*, "Microstructural development from 9 to 14 years: Evidence from the ABCD study," *Dev. Cogn. Neurosci.*, vol. 53, no. 101044, p. 101044, Feb. 2022.

[47] R. A. Carper *et al.*, "Restriction spectrum imaging as a potential measure of cortical neurite density in autism," *Front. Neurosci.*, vol. 10, p. 610, 2016.

[48] N. S. White *et al.*, "Improved conspicuity and delineation of high-grade primary and metastatic brain tumors using "restriction spectrum imaging": quantitative comparison with high B-value DWI and ADC," *AJNR Am. J. Neuroradiol.*, vol. 34, no. 5, pp. 958–64, S1, May 2013.

[49] N. S. White, "Diffusion-weighted imaging in cancer: physical foundations and applications of restriction spectrum imaging," *Cancer Res.*, vol. 74, no. 17, pp. 4638–4652, Sep. 2014.

[50] R. L. Brunsing *et al.*, "Restriction spectrum imaging: An evolving imaging biomarker in prostate MRI," *J. Magn. Reson. Imaging*, vol. 45, no. 2, pp. 323–336, Feb. 2017.

[51] K. M. Bennett *et al.*, "Water diffusion heterogeneity index in the human brain is insensitive to the orientation of applied magnetic field gradients," *Magn. Reson. Med.*, vol. 56, no. 2, pp. 235–239, Aug. 2006.

[52] T. C. Kwee *et al.*, "Intravoxel water diffusion heterogeneity imaging of human high-grade gliomas," *NMR Biomed.*, vol. 23, no. 2, pp. 179–187, Feb. 2010.

[53] Y. Bai *et al.*, "Grading of gliomas by using monoexponential, biexponential, and stretched exponential diffusion-weighted MR imaging and diffusion kurtosis MR imaging," *Radiology*, vol. 278, no. 2, pp. 496–504, Feb. 2016.

[54] X. Chen *et al.*, "Stretched-exponential model diffusion-weighted imaging as a potential imaging marker in preoperative grading and assessment of proliferative activity of gliomas," *Am. J. Transl. Res.*, vol. 10, no. 8, pp. 2659–2668, Aug. 2018.

[55] R. Bedair *et al.*, "Assessment of early treatment response to neoadjuvant chemotherapy in breast cancer using non-mono-exponential diffusion models: a feasibility study comparing the baseline and mid-treatment MRI examinations," *Eur. Radiol.*, vol. 27, no. 7, pp. 2726–2736, Jul. 2017.

[56] N. Chaudhary *et al.*, "Monoexponential, biexponential and stretched exponential models of diffusion weighted magnetic resonance imaging in glioma in relation to histopathologic grade and ki-67 labeling index using high B values," *Am. J. Transl. Res.*, vol. 13, no. 11, pp. 12 480–12 494, Nov. 2021.

[57] C. C. Conlin *et al.*, "A multicompartmental diffusion model for improved assessment of whole-body diffusion-weighted imaging data and evaluation of prostate cancer bone metastases," *Radiol. Imaging Cancer*, vol. 5, no. 1, p. e210115, Jan. 2023.

[58] E. H. Kim *et al.*, "An artificial intelligence model using diffusion basis spectrum imaging metrics accurately predicts clinically significant prostate cancer," *J. Urol.*, p. 4456, Jan. 2025.

[59] Z. Ye *et al.*, "Deep neural network analysis employing diffusion basis spectrum imaging metrics as classifiers improves prostate cancer detection and grading," *bioRxiv*, p. 2021.03. 22.436514, Mar. 2021.

[60] S. Loubrie *et al.*, "Discrimination between benign and malignant lesions with restriction spectrum imaging MRI in an enriched breast cancer screening cohort," *J. Magn. Reson. Imaging*, vol. 61, no. 4, pp. 1876–1887, Apr. 2025.

[61] J. K. Zhang *et al.*, "Diffusion MRI metrics characterize postoperative clinical outcomes after surgery for cervical spondylotic myelopathy," *Neurosurgery*, vol. 96, no. 1, pp. 69–77, Jan. 2025.

[62] M. Pietsch *et al.*, "A framework for multi-component analysis of diffusion MRI data over the neonatal period," *Neuroimage*, vol. 186, pp. 321–337, Feb. 2019.

[63] L. Gui *et al.*, "Longitudinal study of neonatal brain tissue volumes in preterm infants and their ability to predict neurodevelopmental outcome," *Neuroimage*, vol. 185, pp. 728–741, Jan. 2019.

[64] J. Romberg *et al.*, "MRI-based brain volumes of preterm infants at term: a systematic review and meta-analysis," *Arch. Dis. Child. Fetal Neonatal Ed.*, vol. 107, no. 5, pp. 520–526, Sep. 2022.

[65] M. Bouyssi-Kobar *et al.*, "Third trimester brain growth in preterm infants compared with in utero healthy fetuses," *Pediatrics*, vol. 138, no. 5, p. e20161640, Nov. 2016.

[66] A. Benavides *et al.*, "Sex-specific alterations in preterm brain," *Pediatr. Res.*, vol. 85, no. 1, pp. 55–62, Jan. 2019.

[67] Y. T. Khan *et al.*, "Sex differences in human brain structure at birth," *Biol. Sex Differ.*, vol. 15, no. 1, p. 81, Oct. 2024.

[68] A. Lind *et al.*, "Associations between regional brain volumes at term-equivalent age and development at 2 years of age in preterm children," *Pediatr. Radiol.*, vol. 41, no. 8, pp. 953–961, Aug. 2011.

[69] J. L. Y. Cheong *et al.*, "Brain volumes at term-equivalent age are associated with 2-year neurodevelopment in moderate and late preterm children," *J. Pediatr.*, vol. 174, pp. 91–97.e1, Jul. 2016.

[70] K. Keunen *et al.*, "Brain volumes at term-equivalent age in preterm infants: Imaging biomarkers for neurodevelopmental outcome through early school age," *J. Pediatr.*, vol. 172, pp. 88–95, May 2016.

[71] D. K. Thompson *et al.*, "Neonate hippocampal volumes: prematurity, perinatal predictors, and 2-year outcome," *Ann. Neurol.*, vol. 63, no. 5, pp. 642–651, May 2008.

[72] C. J. L. Murray *et al.*, "Disability-adjusted life years (DALYs) for 291 diseases and injuries in 21 regions, 1990-2010: a systematic analysis for the global burden of disease study 2010," *Lancet*, vol. 380, no. 9859, pp. 2197–2223, Dec. 2012.

[73] L. Liu *et al.*, "Global, regional, and national causes of under-5 mortality in 2000-15: an updated systematic analysis with implications for the sustainable development goals," *Lancet*, vol. 388, no. 10063, pp. 3027–3035, Dec. 2016.

[74] S. Chawanpaiboon *et al.*, "Global, regional, and national estimates of levels of preterm birth in 2014: a systematic review and modelling analysis," *Lancet Glob. Health*, vol. 7, no. 1, pp. e37–e46, Jan. 2019.

[75] C. Lebel *et al.*, "The development of brain white matter microstructure," *Neuroimage*, vol. 182, pp. 207–218, Nov. 2018.

[76] J. Dubois *et al.*, "Mri of the neonatal brain: A review of methodological challenges and neuroscientific advances," *Journal of Magnetic Resonance Imaging*, vol. 53, no. 5, pp. 1318–1343, 2021.

[77] S. C. L. Deoni *et al.*, "Mapping infant brain myelination with magnetic resonance imaging," *Journal of Neuroscience*, vol. 31, no. 2, pp. 784–791, 2011.

[78] S. C. L. Deoni, "Investigating white matter development in infancy and early childhood using myelin water fraction and relaxation time mapping," *NeuroImage*, vol. 63, no. 3, pp. 1038–1053, 2012.

[79] P. I. Yakovlev *et al.*, "The myelogenetic cycles of regional maturation of the brain," in *Regional Development of the Brain in Early Life*, A. Minkowski, Ed. Oxford: Blackwell Scientific Publications, 1967, pp. 3–70.

[80] M. Ouyang *et al.*, "Differential cortical microstructural maturation in the preterm human brain with diffusion kurtosis and tensor imaging," *Proceedings of the National Academy of Sciences of the USA*, vol. 116, no. 10, pp. 4681–4688, 2019.

[81] M. Anjari *et al.*, "Diffusion tensor imaging with tract-based spatial statistics reveals local white matter abnormalities in preterm infants," *Neuroimage*, vol. 35, no. 3, pp. 1021–1027, Apr. 2007.

[82] C. van Pul *et al.*, "Quantitative fiber tracking in the corpus callosum and internal capsule reveals microstructural abnormalities in preterm infants at term-equivalent age," *AJNR Am. J. Neuroradiol.*, vol. 33, no. 4, pp. 678–684, Apr. 2012.

[83] Y. Liu *et al.*, "White matter abnormalities are related to microstructural changes in preterm neonates at term-equivalent age: a diffusion tensor imaging and probabilistic tractography study," *AJNR Am. J. Neuroradiol.*, vol. 33, no. 5, pp. 839–845, May 2012.

[84] Y. Arzoumanian *et al.*, "Diffusion tensor brain imaging findings at term-equivalent age may predict neurologic abnormalities in low birth weight preterm infants," *AJNR Am. J. Neuroradiol.*, vol. 24, no. 8, pp. 1646–1653, Sep. 2003.

[85] E. G. Duerden *et al.*, "Tract-based spatial statistics in preterm-born neonates predicts cognitive and motor outcomes at 18 months," *AJNR Am. J. Neuroradiol.*, vol. 36, no. 8, pp. 1565–1571, Aug. 2015.

[86] T. Hasegawa *et al.*, "Development of corpus callosum in preterm infants is affected by the prematurity: in vivo assessment of diffusion tensor imaging at term-equivalent age," *Pediatr. Res.*, vol. 69, no. 3, pp. 249–254, Mar. 2011.

[87] B. J. M. van Kooij *et al.*, "Fiber tracking at term displays gender differences regarding cognitive and motor outcome at 2 years of age in preterm infants," *Pediatr. Res.*, vol. 70, no. 6, pp. 626–632, Dec. 2011.

[88] J. A. Kimpton *et al.*, "Diffusion magnetic resonance imaging assessment of regional white matter maturation in preterm neonates," *Neuroradiology*, vol. 63, no. 4, pp. 573–583, Apr. 2021.

[89] D. C. Dean, 3rd *et al.*, "Mapping white matter microstructure in the one month human brain," *Sci. Rep.*, vol. 7, no. 1, p. 9759, Aug. 2017.

[90] Z. Eaton-Rosen *et al.*, "Longitudinal measurement of the developing grey matter in preterm subjects using multi-modal MRI," *Neuroimage*, vol. 111, pp. 580–589, May 2015.

[91] R. Dimitrova *et al.*, "Preterm birth alters the development of cortical microstructure and morphology at term-equivalent age," *Neuroimage*, vol. 243, no. 118488, p. 118488, Nov. 2021.

[92] W. Wang *et al.*, "Altered cortical microstructure in preterm infants at term-equivalent age relative to term-born neonates," *Cereb. Cortex*, vol. 33, no. 3, pp. 651–662, Jan. 2023.

[93] J. Shi *et al.*, "Initial application of diffusional kurtosis imaging in evaluating brain development of healthy preterm infants," *PLoS One*, vol. 11, no. 4, p. e0154146, Apr. 2016.

[94] X. Zhao *et al.*, "The value of diffusion kurtosis imaging in detecting delayed brain development of premature infants," *Front. Neurol.*, vol. 12, p. 789254, Dec. 2021.

[95] X. Li *et al.*, "Mapping white matter maturational processes and degrees on neonates by diffusion kurtosis imaging with multiparametric analysis," *Hum. Brain Mapp.*, vol. 43, no. 2, pp. 799–815, Feb. 2022.

[96] K. Pannek *et al.*, "Fixel-based analysis reveals alterations is brain microstructure and macrostructure of preterm-born infants at term equivalent age," *NeuroImage Clin.*, vol. 18, pp. 51–59, Jan. 2018.

[97] K. Pannek, "Brain microstructure and morphology of very preterm-born infants at term equivalent age: Associations with motor and cognitive outcomes at 1 and 2 years," *Neuroimage*, vol. 221, no. 117163, p. 117163, Nov. 2020.

[98] D. Pecheva *et al.*, "Fixel-based analysis of the preterm brain: Disentangling bundle-specific white matter microstructural and macrostructural changes in relation to clinical risk factors," *NeuroImage Clin.*, vol. 23, no. 101820, p. 101820, Apr. 2019.

[99] D. Batalle *et al.*, "Early development of structural networks and the impact of prematurity on brain connectivity," *Neuroimage*, vol. 149, pp. 379–392, Apr. 2017.

[100] J.-W. Jeong *et al.*, "Neonatal encephalopathy prediction of poor outcome with diffusion-weighted imaging connectome and fixel-based analysis," *Pediatr. Res.*, vol. 91, no. 6, pp. 1505–1515, May 2022.

[101] M. Ouyang *et al.*, "Diffusion-MRI-based regional cortical microstructure at birth for predicting neurodevelopmental outcomes of 2-year-olds," *Elife*, vol. 9, Dec. 2020.

[102] C. J. Kelly *et al.*, "Abnormal microstructural development of the cerebral cortex in neonates with congenital heart disease is associated with impaired cerebral oxygen delivery," *J. Am. Heart Assoc.*, vol. 8, no. 5, p. e009893, Mar. 2019.

[103] M. Bastiani *et al.*, "Automated processing pipeline for neonatal diffusion MRI in the developing human connectome project," *Neuroimage*, vol. 185, pp. 750–763, Jan. 2019.

[104] D. Christiaens *et al.*, "Scattered slice SHARD reconstruction for motion correction in multi-shell diffusion MRI," *Neuroimage*, vol. 225, no. 117437, p. 117437, Jan. 2021.

[105] K. M. Huynh *et al.*, "Probing tissue microarchitecture of the baby brain via spherical mean spectrum imaging," *IEEE Trans. Med. Imaging*, vol. 39, no. 11, pp. 3607–3618, Nov. 2020.

[106] P. S. Bobba *et al.*, "Age-related topographic map of magnetic resonance diffusion metrics in neonatal brains," *Hum. Brain Mapp.*, vol. 43, no. 14, pp. 4326–4334, Oct. 2022.

[107] W. Liang *et al.*, "A comparative study of the superior longitudinal fasciculus subdivisions between neonates and young adults," *Brain Struct. Funct.*, vol. 227, no. 8, pp. 2713–2730, Nov. 2022.

[108] A. S. Verschuur *et al.*, "Feasibility study to unveil the potential: considerations of constrained spherical deconvolution tractography with unsedated neonatal diffusion brain MRI data," *Front. Radiol.*, vol. 4, p. 1416672, Jun. 2024.

[109] N. Kunz *et al.*, "Assessing white matter microstructure of the newborn with multi-shell diffusion MRI and biophysical compartment models," *Neuroimage*, vol. 96, pp. 288–299, Aug. 2014.

[110] A. P. Kansagra *et al.*, "Microstructural maturation of white matter tracts in encephalopathic neonates," *Clin. Imaging*, vol. 40, no. 5, pp. 1009–1013, Sep. 2016.

[111] S. Karmacharya *et al.*, "Advanced diffusion imaging for assessing normal white matter development in neonates and characterizing aberrant development in congenital heart disease," *NeuroImage Clin.*, vol. 19, pp. 360–373, May 2018.

[112] D. Fenchel *et al.*, "Development of microstructural and morphological cortical profiles in the neonatal brain," *Cereb. Cortex*, vol. 30, no. 11, pp. 5767–5779, Oct. 2020.

[113] A. Uus *et al.*, "Multi-channel 4D parametrized atlas of macro- and microstructural neonatal brain development," *Front. Neurosci.*, vol. 15, p. 661704, Jun. 2021.

[114] X. Wang *et al.*, "Application of diffusion kurtosis imaging in neonatal brain development," *Front. Pediatr.*, vol. 11, p. 1112121, Mar. 2023.

[115] M. A. DiPiero *et al.*, "Gray matter based spatial statistics framework in the 1-month brain: insights into gray matter microstructure in infancy," *Brain Struct. Funct.*, vol. 229, no. 9, pp. 2445–2459, Sep. 2024.

[116] L. G. Cornette *et al.*, "Magnetic resonance imaging of the infant brain: anatomical characteristics and clinical significance of punctate lesions," *Arch. Dis. Child. Fetal Neonatal Ed.*, vol. 86, no. 3, pp. F171–7, May 2002.

[117] K. J. Kersbergen *et al.*, "Different patterns of punctate white matter lesions in serially scanned preterm infants," *PLoS ONE*, vol. 9, no. 10, p. e108904, Oct. 2014.

[118] X. Sun *et al.*, "Automatic detection of punctate white matter lesions in infants using deep learning of composite images from two cases," *Sci. Rep.*, vol. 13, no. 1, p. 4426, Mar. 2023.

[119] M. Hayman *et al.*, "Punctate white-matter lesions in the full-term newborn: Underlying aetiology and outcome," *Eur. J. Paediatr. Neurol.*, vol. 23, no. 2, pp. 280–287, Mar. 2019.

[120] M. Kobayashi *et al.*, "Diagnostic specificity of cerebral magnetic resonance imaging for punctate white matter lesion assessment in a preterm sheep fetus model," *Reprod. Sci.*, vol. 28, no. 4, pp. 1175–1184, Apr. 2021.

[121] J. Pavaine *et al.*, "Diffusion tensor imaging-based assessment of white matter tracts and visual-motor outcomes in very preterm neonates," *Neuroradiology*, vol. 58, no. 3, pp. 301–310, Mar. 2016.

[122] T. Niwa *et al.*, "Punctate white matter lesions in infants: new insights using susceptibility-weighted imaging," *Neuroradiology*, vol. 53, no. 9, pp. 669–679, Sep. 2011.

[123] A. M. Childs *et al.*, "Magnetic resonance and cranial ultrasound characteristics of periventricular white matter abnormalities in newborn infants," *Clin. Radiol.*, vol. 56, no. 8, pp. 647–655, Aug. 2001.

[124] L. T. Sie *et al.*, "Early MR features of hypoxic-ischemic brain injury in neonates with periventricular densities on sonograms," *AJNR Am. J. Neuroradiol.*, vol. 21, no. 5, pp. 852–861, May 2000.

[125] L. A. Ramenghi *et al.*, "Magnetic resonance imaging assessment of brain maturation in preterm neonates with punctate white matter lesions," *Neuroradiology*, vol. 49, no. 2, pp. 161–167, Feb. 2007.

[126] L. Bassi *et al.*, "Diffusion tensor imaging in preterm infants with punctate white matter lesions," *Pediatr. Res.*, vol. 69, no. 6, pp. 561–566, Jun. 2011.

[127] Y. Nanba *et al.*, "Magnetic resonance imaging regional T1 abnormalities at term accurately predict motor outcome in preterm infants," *Pediatrics*, vol. 120, no. 1, pp. e10–9, Jul. 2007.

[128] T. Y. Jeon *et al.*, "Neurodevelopmental outcomes in preterm infants: comparison of infants with and without diffuse excessive high signal intensity on MR images at near-term-equivalent age," *Radiology*, vol. 263, no. 2, pp. 518–526, May 2012.

[129] X. Li *et al.*, "Characterization of extensive microstructural variations associated with punctate white matter lesions in preterm neonates," *AJNR Am. J. Neuroradiol.*, vol. 38, no. 6, pp. 1228–1234, Jun. 2017.

[130] S. A. Back, "Cerebral white and gray matter injury in newborns: new insights into pathophysiology and management," *Clin. Perinatol.*, vol. 41, no. 1, pp. 1–24, Mar. 2014.

[131] J. J. Volpe *et al.*, "The developing oligodendrocyte: key cellular target in brain injury in the premature infant," *Int. J. Dev. Neurosci.*, vol. 29, no. 4, pp. 423–440, Jun. 2011.

[132] O. Khwaja *et al.*, "Pathogenesis of cerebral white matter injury of prematurity," *Arch. Dis. Child. Fetal Neonatal Ed.*, vol. 93, no. 2, pp. F153–61, Mar. 2008.

[133] N. R. Saunders *et al.*, "Barrier mechanisms in the developing brain," *Front. Pharmacol.*, vol. 3, p. 46, Mar. 2012.

[134] S. A. Back, "White matter injury in the preterm infant: pathology and mechanisms," *Acta Neuropathol.*, vol. 134, no. 3, pp. 331–349, Sep. 2017.

[135] J. I. Berman *et al.*, "Quantitative fiber tracking analysis of the optic radiation correlated with visual performance in premature newborns," *AJNR Am. J. Neuroradiol.*, vol. 30, no. 1, pp. 120–124, Jan. 2009.

[136] R. Trò *et al.*, "Diffusion kurtosis imaging of neonatal spinal cord in clinical routine," *Front. Radiol.*, vol. 2, p. 794981, May 2022.

[137] A. J. Hughes *et al.*, "Motor development interventions for preterm infants: A systematic review and meta-analysis," *Pediatrics*, vol. 138, no. 4, Oct. 2016.

[138] I. Despotovic *et al.*, "Mri segmentation of the human brain: Challenges, methods, and applications," *Computational and Mathematical Methods in Medicine*, vol. 2015, p. 450341, 2015.

[139] I. S. Gousias *et al.*, "Magnetic resonance imaging of the newborn brain: Manual segmentation of labelled atlases in term-born and preterm infants," *NeuroImage*, vol. 62, no. 3, pp. 1499–1509, 2012.

[140] A. Makropoulos *et al.*, "A review on automatic fetal and neonatal brain mri segmentation," *NeuroImage*, vol. 170, p. ???, 2018.

[141] J. E. Iglesias *et al.*, "Multi-atlas segmentation of biomedical images: A survey," *Medical Image Analysis*, vol. 24, no. 1, pp. 205–219, 2015.

[142] S. K. Warfield *et al.*, "Simultaneous truth and performance level estimation (staple): An algorithm for the validation of image segmentation," *IEEE Transactions on Medical Imaging*, vol. 23, no. 7, pp. 903–921, 2004.

[143] H. Wang *et al.*, "Multi-atlas segmentation with joint label fusion," *IEEE Transactions on Pattern Analysis and Machine Intelligence*, vol. 35, no. 3, pp. 611–623, 2013.

[144] A. Makropoulos *et al.*, "Automatic whole brain mri segmentation of the developing neonatal brain," *IEEE Transactions on Medical Imaging*, vol. 33, no. 9, pp. 1818–1831, 2014.

[145] A. Makropoulos, "The developing human connectome project: A minimal processing pipeline for neonatal cortical surface reconstruction," *NeuroImage*, vol. 173, pp. 88–112, 2018.

[146] Y. Zhang *et al.*, "Segmentation of brain mr images through a hidden markov random field model and the expectation-maximization algorithm," *IEEE Transactions on Medical Imaging*, vol. 20, no. 1, pp. 45–57, 2001.

[147] K. Van Leemput *et al.*, "Automated model-based tissue classification of MR images of the brain," *IEEE Trans. Med. Imaging*, vol. 18, no. 10, pp. 897–908, Oct. 1999.

[148] K. Van *et al.*, "Automated model-based bias field correction of mr images of the brain," *IEEE Trans. Med. Imaging*, vol. 18, no. 10, pp. 885–896, Oct. 1999.

[149] P. Anbeek *et al.*, "Probabilistic brain tissue segmentation in neonatal magnetic resonance imaging," *Pediatric Research*, vol. 63, pp. 158–163, 2008.

[150] L. Wang *et al.*, "Links: Learning-based multi-source integration framework for segmentation of infant brain images," *NeuroImage*, vol. 108, pp. 160–172, 2015.

[151] M. Kass *et al.*, "Snakes: Active contour models," *International Journal of Computer Vision*, vol. 1, no. 4, pp. 321–331, 1988.

[152] S. Osher *et al.*, "Fronts propagating with curvature-dependent speed: Algorithms based on hamilton–jacobi formulations," *Journal of Computational Physics*, vol. 79, no. 1, pp. 12–49, 1988.

[153] M. Prastawa *et al.*, "Automatic segmentation of mr images of the developing newborn brain," *Medical Image Analysis*, vol. 9, no. 5, p. ???, 2005.

[154] L. Gui *et al.*, "Morphology-driven automatic segmentation of mr images of the neonatal brain," *Medical Image Analysis*, vol. 16, no. 8, pp. 1565–1579, 2012.

[155] O. Ronneberger *et al.*, "U-net: Convolutional networks for biomedical image segmentation," in *Medical Image Computing and Computer-Assisted Intervention – MICCAI 2015*, ser. Lecture Notes in Computer Science, vol. 9351. Springer, 2015, pp. 234–241.

[156] L. Wang *et al.*, "Benchmark on automatic 6-month-old infant brain segmentation algorithms: The iSeg-2017 challenge," *IEEE Trans. Med. Imaging*, vol. 38, no. 9, pp. 2219–2230, Feb. 2019.

[157] F. Milletari *et al.*, "V-net: Fully convolutional neural networks for volumetric medical image segmentation," in *2016 Fourth International Conference on 3D Vision (3DV)*. IEEE, 2016, pp. 565–571.

[158] F. Isensee *et al.*, "nnu-net: A self-configuring method for deep learning-based biomedical image segmentation," *Nature Methods*, vol. 18, no. 2, pp. 203–211, 2021.

[159] Y. Tang *et al.*, "Self-supervised pre-training of swin transformers for 3d medical image analysis," in *Proceedings of the IEEE/CVF Conference on Computer Vision and Pattern Recognition (CVPR) Workshops*, 2022, also available as arXiv:2111.14791.

[160] A. Hatamizadeh *et al.*, "Unetr: Transformers for 3d medical image segmentation," in *Proceedings of the IEEE/CVF Winter Conference on Applications of Computer Vision (WACV)*, 2022, also available as arXiv:2103.10504.

[161] L. Richter *et al.*, "Accurate segmentation of neonatal brain mri with deep learning," *Frontiers in Neuroinformatics*, vol. 16, p. 1006532, 2022.

[162] A. Makropoulos *et al.*, "The developing human connectome project: A minimal processing pipeline for neonatal cortical surface reconstruction," *Neuroimage*, vol. 173, pp. 88–112, Jun. 2018.

[163] F. Zhang *et al.*, "Deep learning based segmentation of brain tissue from diffusion MRI," *Neuroimage*, vol. 233, no. 117934, p. 117934, Jun. 2021.

[164] M. O. Irfanoglu *et al.*, "Evaluating corrections for eddy-currents and other EPI distortions in diffusion MRI: methodology and a dataset for benchmarking: Magnetic resonance in medicine," *Magn. Reson. Med.*, vol. 81, no. 4, pp. 2774–2787, Apr. 2019.

[165] X. Gu *et al.*, "Evaluation of six phase encoding based susceptibility distortion correction methods for diffusion MRI," *Front. Neuroinform.*, vol. 13, p. 76, Dec. 2019.

[166] M. O. Irfanoglu *et al.*, "Improved reproducibility of diffusion MRI of the human brain with a four-way blip-up and down phase-encoding acquisition approach," *Magn. Reson. Med.*, vol. 85, no. 5, pp. 2696–2708, May 2021.

[167] I. Havsteen *et al.*, "Are movement artifacts in magnetic resonance imaging a real problem?-a narrative review," *Front. Neurol.*, vol. 8, p. 232, May 2017.

[168] F. Zhang *et al.*, "Deep learning based segmentation of brain tissue from diffusion MRI," *Neuroimage*, vol. 233, no. 117934, p. 117934, Jun. 2021.

[169] G. Theaud *et al.*, "DORIS: A diffusion MRI-based 10 tissue class deep learning segmentation algorithm tailored to improve anatomically-constrained tractography," *Front. Neuroimaging*, vol. 1, p. 917806, Sep. 2022.

[170] D. Karimi *et al.*, "Diffusion MRI with machine learning," *Imaging Neurosci. (Camb.)*, vol. 2, Nov. 2024.

[171] S. N. Jespersen *et al.*, "Modeling dendrite density from magnetic resonance diffusion measurements," *Neuroimage*, vol. 34, no. 4, pp. 1473–1486, Feb. 2007.

[172] I. O. Jelescu *et al.*, "Degeneracy in model parameter estimation for multi-compartmental diffusion in neuronal tissue: Degeneracy in model parameter estimation of diffusion in neural tissue," *NMR Biomed.*, vol. 29, no. 1, pp. 33–47, Jan. 2016.

[173] D. S. Novikov *et al.*, "Rotationally-invariant mapping of scalar and orientational metrics of neuronal microstructure with diffusion MRI," *arXiv [physics.bio-ph]*, Sep. 2016.

[174] A. Ramirez-Manzanares *et al.*, "Diffusion basis functions decomposition for estimating white matter intravoxel fiber geometry," *IEEE Trans. Med. Imaging*, vol. 26, no. 8, pp. 1091–1102, Aug. 2007.

[175] M. DiPiero *et al.*, "Applications of advanced diffusion MRI in early brain development: a comprehensive review," *Brain Struct. Funct.*, vol. 228, no. 2, pp. 367–392, Mar. 2023.

[176] M. Jenkinson *et al.*, "FSL," *Neuroimage*, vol. 62, no. 2, pp. 782–790, Aug. 2012.

[177] A. Makropoulos *et al.*, "Automatic whole brain MRI segmentation of the developing neonatal brain," *IEEE Trans. Med. Imaging*, vol. 33, no. 9, pp. 1818–1831, Sep. 2014.

[178] J. V. Manjón *et al.*, "Diffusion weighted image denoising using overcomplete local PCA," *PLoS One*, vol. 8, no. 9, p. e73021, Sep. 2013.

[179] E. Garyfallidis *et al.*, "Dipy, a library for the analysis of diffusion MRI data," *Front. Neuroinform.*, vol. 8, p. 8, Feb. 2014.

[180] S. Chung *et al.*, "Comparison of bootstrap approaches for estimation of uncertainties of DTI parameters," *Neuroimage*, vol. 33, no. 2, pp. 531–541, Nov. 2006.

[181] O. Pasternak *et al.*, "Free water elimination and mapping from diffusion MRI," *Magn. Reson. Med.*, vol. 62, no. 3, pp. 717–730, Sep. 2009.

[182] T. K. Koo *et al.*, "A guideline of selecting and reporting intraclass correlation coefficients for reliability research," *J. Chiropr. Med.*, vol. 15, no. 2, pp. 155–163, Jun. 2016.

[183] E. Zhang *et al.*, "A novel method for detecting neuroinflammation in mouse brain with sanfilippo syndrome," in *ISMRM*, Jun. 2023.

[184] P. S. Hüppi *et al.*, "Microstructural development of human newborn cerebral white matter assessed in vivo by diffusion tensor magnetic resonance imaging," *Pediatr. Res.*, vol. 44, no. 4, pp. 584–590, Oct. 1998.

[185] S. Yoshida *et al.*, "Diffusion tensor imaging of normal brain development," *Pediatr. Radiol.*, vol. 43, no. 1, pp. 15–27, Jan. 2013.

[186] G. Ball *et al.*, "The effect of preterm birth on thalamic and cortical development," *Cereb. Cortex*, vol. 22, no. 5, pp. 1016–1024, May 2012.

[187] A. Aeby *et al.*, "Maturation of thalamic radiations between 34 and 41 weeks' gestation: a combined voxel-based study and probabilistic tractography with diffusion tensor imaging," *AJNR Am. J. Neuroradiol.*, vol. 30, no. 9, pp. 1780–1786, Oct. 2009.

[188] J. Rose *et al.*, "Neonatal brain microstructure correlates of neurodevelopment and gait in preterm children 18-22 mo of age: an MRI and DTI study," *Pediatr. Res.*, vol. 78, no. 6, pp. 700–708, Dec. 2015.

[189] A. R. Hoy *et al.*, "Optimization of a free water elimination two-compartment model for diffusion tensor imaging," *Neuroimage*, vol. 103, pp. 323–333, Dec. 2014.

[190] A. Qiu *et al.*, "Diffusion tensor imaging for understanding brain development in early life," *Annu. Rev. Psychol.*, vol. 66, no. 1, pp. 853–876, Jan. 2015.

[191] K. J. Kersbergen *et al.*, "Microstructural brain development between 30 and 40 weeks corrected age in a longitudinal cohort of extremely preterm infants," *Neuroimage*, vol. 103, pp. 214–224, Dec. 2014.

[192] P. G. Batchelor *et al.*, "Anisotropic noise propagation in diffusion tensor MRI sampling schemes," *Magn. Reson. Med.*, vol. 49, no. 6, pp. 1143–1151, Jun. 2003.

[193] A. H. Cross *et al.*, "A new imaging modality to non-invasively assess multiple sclerosis pathology," *J. Neuroimmunol.*, vol. 304, pp. 81–85, Mar. 2017.

[194] A. Makropoulos *et al.*, "A review on automatic fetal and neonatal brain MRI segmentation," *Neuroimage*, vol. 170, pp. 231–248, Apr. 2018.

[195] C. N. Devi *et al.*, "Neonatal brain MRI segmentation: A review," *Comput. Biol. Med.*, vol. 64, pp. 163–178, Sep. 2015.

[196] F. Isensee *et al.*, "nnU-net: a self-configuring method for deep learning-based biomedical image segmentation," *Nat. Methods*, vol. 18, no. 2, pp. 203–211, Feb. 2021.

[197] D. Karimi *et al.*, "Detailed delineation of the fetal brain in diffusion MRI via multi-task learning," *ArXiv*, Sep. 2024.

[198] L. Richter *et al.*, "Accurate segmentation of neonatal brain MRI with deep learning," *Front. Neuroinform.*, vol. 16, p. 1006532, Sep. 2022.

[199] Y. Sui *et al.*, "Isotropic MRI super-resolution reconstruction with multi-scale gradient field prior," *Med. Image Comput. Comput. Assist. Interv.*, vol. 11766, pp. 3–11, Oct. 2019.

[200] Y. Sui, "Learning a gradient guidance for spatially isotropic mri super-resolution reconstruction," *Med. Image Comput. Comput. Assist. Interv.*, vol. 12262, pp. 136–146, Oct. 2020.

[201] S. Fadnavis *et al.*, "Patch2Self: Denoising diffusion MRI with self-supervised learning," *arXiv [cs.LG]*, Nov. 2020.

[202] B. Avants *et al.*, "Advanced normalization tools: V1.0," *Insight J.*, Jul. 2009.

[203] L. Chen *et al.*, "An attention-based context-informed deep framework for infant brain subcortical segmentation," *Neuroimage*, vol. 269, no. 119931, p. 119931, Apr. 2023.

[204] Y. Sun *et al.*, "Multi-site infant brain segmentation algorithms: The iSeg-2019 challenge," *IEEE Trans. Med. Imaging*, vol. 40, no. 5, pp. 1363–1376, May 2021.

[205] A. Albi *et al.*, "Image registration to compensate for EPI distortion in patients with brain tumors: An evaluation of tract-specific effects," *J. Neuroimaging*, vol. 28, no. 2, pp. 173–182, Mar. 2018.

[206] Y. Ding *et al.*, "Using deep convolutional neural networks for neonatal brain image segmentation," *Front. Neurosci.*, vol. 14, p. 207, Mar. 2020.

[207] R. T. Shinohara *et al.*, "Statistical normalization techniques for magnetic resonance imaging," *NeuroImage Clin.*, vol. 6, pp. 9–19, Aug. 2014.

[208] Y. Assaf *et al.*, "Composite hindered and restricted model of diffusion (CHARMED) MR imaging of the human brain," *Neuroimage*, vol. 27, no. 1, pp. 48–58, Aug. 2005.

[209] J. L. R. Andersson *et al.*, "How to correct susceptibility distortions in spin-echo echo-planar images: application to diffusion tensor imaging," *Neuroimage*, vol. 20, no. 2, pp. 870–888, Oct. 2003.

[210] L. G. Matthews *et al.*, "Longitudinal preterm cerebellar volume: Perinatal and neurodevelopmental outcome associations," *Cerebellum*, vol. 17, no. 5, pp. 610–627, Oct. 2018.

[211] D. K. Thompson *et al.*, "Corpus callosum alterations in very preterm infants: perinatal correlates and 2 year neurodevelopmental outcomes," *Neuroimage*, vol. 59, no. 4, pp. 3571–3581, Feb. 2012.

[212] T. Guo *et al.*, "Quantitative assessment of white matter injury in preterm neonates: Association with outcomes," *Neurology*, vol. 88, no. 7, pp. 614–622, Feb. 2017.

[213] F. T. de Bruïne *et al.*, "Clinical implications of MR imaging findings in the white matter in very preterm infants: a 2-year follow-up study," *Radiology*, vol. 261, no. 3, pp. 899–906, Dec. 2011.

[214] C. Arberet *et al.*, "Isolated neonatal MRI punctate white matter lesions in very preterm neonates and quality of life at school age," *J. Neonatal Perinatal Med.*, vol. 10, no. 3, pp. 257–266, Jan. 2017.

[215] M. Jenkinson *et al.*, "Improved optimization for the robust and accurate linear registration and motion correction of brain images," *Neuroimage*, vol. 17, no. 2, pp. 825–841, Oct. 2002.

[216] D. N. Greve *et al.*, "Accurate and robust brain image alignment using boundary-based registration," *Neuroimage*, vol. 48, no. 1, pp. 63–72, Oct. 2009.

[217] I. O. Jelescu *et al.*, "Challenges for biophysical modeling of microstructure," *J. Neurosci. Methods*, vol. 344, no. 108861, p. 108861, Oct. 2020.

[218] A. M. Heemskerk *et al.*, "Acquisition guidelines and quality assessment tools for analyzing neonatal diffusion tensor MRI data," *AJNR Am. J. Neuroradiol.*, vol. 34, no. 8, pp. 1496–1505, Aug. 2013.

[219] M. Bergamino *et al.*, "Applying a free-water correction to diffusion imaging data uncovers stress-related neural pathology in depression," *NeuroImage Clin.*, vol. 10, pp. 336–342, 2016.

[220] A. Karakuzu *et al.*, "qMRLab: Quantitative MRI analysis, under one umbrella," *J. Open Source Softw.*, vol. 5, no. 53, p. 2343, Sep. 2020.

APPENDIX A ADDITIONAL MATERIAL: COMPARATIVE STUDY OF PRETERM- AND TERM-BORN INFANTS

Detailed Neonatal Participant and Scan Information

Table A.1: Preterm Infants Scanned at Preterm Age. This table lists preterm infants scanned at their preterm age. The "Multi-scan" column indicates whether an additional scan at term-equivalent age was performed (2) or not (1). The first 25 infants with a value of 2 in the "Multi-scan" column also appear in the second table.

No.	Subject	Scan time	Birth age	Scan age	Sex	Weight	Scanner	Scans
1	sub-B008S1	2021-06-17	32W2D	33W2D	F	1.70	GE	2
2	sub-B009S1	2021-10-04	29W6D	35W0D	F	1.80	GE	2
3	sub-B010S1	2021-10-06	32W5D	33W6D	F	2.00	GE	2
4	sub-B012S1	2021-11-01	33W5D	34W5D	M	2.50	GE	2
5	sub-B013S1	2021-11-01	33W5D	34W5D	M	1.99	GE	2
6	sub-B015S1	2021-11-09	30W1D	33W0D	M	2.10	GE	2
7	sub-B016S1	2021-11-23	32W0D	32W6D	F	1.36	GE	2
8	sub-B017S1	2021-11-26	32W0D	33W2D	F	1.38	GE	2
9	sub-B018S1	2021-12-09	29W6D	33W0D	F	1.29	GE	2
10	sub-B019S1	2021-12-09	34W6D	36W1D	F	1.70	GE	2
11	sub-B023S1	2022-04-28	32W0D	33W3D	M	1.70	GE	2
12	sub-B024S1	2022-05-05	32W0D	34W3D	M	2.35	GE	2
13	sub-B029S1	2023-03-07	34W1D	35W2D	F	1.00	GE	2
14	sub-B030S1	2023-03-09	31W2D	33W6D	F	1.00	GE	2
15	sub-B031S1	2023-03-13	29W0D	31W3D	M	1.40	GE	2
16	sub-B032S1	2023-04-04	33W3D	34W4D	M	1.14	GE	2
17	sub-B035S1	2023-06-08	31W4D	33W1D	M	2.00	SIEMENS	2
18	sub-B059S1	2024-01-29	27W0D	32W3D	F	1.79	SIEMENS	2
19	sub-B065S1	2024-03-11	33W6D	35W3D	F	1.30	SIEMENS	2
20	sub-B071S1	2024-05-22	30W4D	31W6D	M	1.65	SIEMENS	2
21	sub-B072S1	2024-06-04	32W6D	33W5D	M	2.28	SIEMENS	2
22	sub-B073S1	2024-06-04	32W6D	33W5D	M	2.28	SIEMENS	2
23	sub-B084S1	2024-08-27	34W2D	36W2D	M	2.20	SIEMENS	2

Continued A.1

No.	Subject	Scan time	Birth age	Scan age	Sex	Weight	Scanner	Scans
24	sub-B085S1	2024-09-17	34W5D	36W4D	M	2.30	SIEMENS	2
25	sub-B086S1	2024-09-18	34W5D	36W5D	M	2.24	SIEMENS	2
26	sub-B021S1	2022-02-10	33W1D	34W3D	F	2.02	GE	1
27	sub-B025S1	2022-05-05	31W6D	32W5D	M	1.70	GE	1
28	sub-B033S1	2023-04-06	33W3D	34W6D	M	2.10	GE	1
29	sub-B036S1	2023-06-15	30W6D	32W6D	M	1.70	SIEMENS	1
30	sub-B037S1	2023-06-20	30W0D	31W0D	F	1.00	SIEMENS	1
31	sub-B049S1	2023-09-14	35W4D	36W5D	M	1.85	SIEMENS	1
32	sub-B062S1	2024-02-19	32W3D	34W0D	F	2.00	SIEMENS	1
33	sub-B067S1	2024-04-25	31W6D	33W6D	F	1.50	SIEMENS	1
34	sub-B082S1	2024-08-02	32W2D	33W3D	M	1.80	SIEMENS	1
35	sub-B083S1	2024-08-02	32W2D	33W3D	M	1.70	SIEMENS	1
36	sub-B095S1	2025-01-06	31W4D	33W1D	M	1.50	SIEMENS	1

Table A.2: Follow-Up Term-Equivalent Age Scans of Preterm Infants. This table provides the second scans for preterm infants who were rescanned at term-equivalent age. Only infants who had "2" in the "Multi-scan" column of the first table are included here.

No.	Subject	Scan Time	Birth age	Scan age	Sex	Weight	Scanner	Scans
1	sub-B008S2	2021-07-29	32W2D	39W2D	F	3.00	GE	2
2	sub-B009S2	2021-10-21	29W6D	37W3D	F	2.50	GE	2
3	sub-B010S2	2021-11-25	32W5D	41W0D	F	3.30	GE	2
4	sub-B012S2	2021-12-14	33W5D	40W6D	M	3.80	GE	2
5	sub-B013S2	2021-12-14	33W5D	40W6D	M	3.82	GE	2
6	sub-B015S2	2021-12-23	30W1D	39W2D	M	3.60	GE	2
7	sub-B016S2	2022-01-20	32W0D	41W1D	F	3.10	GE	2
8	sub-B017S2	2022-01-14	32W0D	40W2D	F	2.80	GE	2
9	sub-B018S2	2022-01-24	29W6D	39W4D	F	3.60	GE	2
10	sub-B019S2	2022-01-13	34W6D	41W1D	F	3.00	GE	2
11	sub-B023S2	2022-06-09	32W0D	39W3D	M	2.70	GE	2
12	sub-B024S2	2022-06-09	32W0D	39W3D	M	2.70	GE	2
13	sub-B029S2	2023-04-18	34W1D	41W2D	F	2.40	GE	2
14	sub-B030S2	2023-04-28	31W2D	41W0D	F	3.40	GE	2
15	sub-B031S2	2023-04-27	29W0D	37W6D	M	2.70	GE	2

Continued A.2

No.	Subject	Scan Time	Birth age	Scan age	Sex	Weight	Scanner	Scans
16	sub-B032S2	2023-06-28	33W3D	46W5D	M	3.40	SIEMENS	2
17	sub-B035S2	2023-07-27	31W4D	40W1D	M	3.60	SIEMENS	2
18	sub-B059S2	2024-04-03	27W0D	41W5D	F	3.60	SIEMENS	2
19	sub-B065S2	2024-04-15	33W6D	40W3D	F	2.10	SIEMENS	2
20	sub-B071S2	2024-07-22	30W4D	40W4D	M	4.00	SIEMENS	2
21	sub-B072S2	2024-07-23	32W6D	40W5D	M	4.00	SIEMENS	2
22	sub-B073S2	2024-07-23	32W6D	40W5D	M	3.00	SIEMENS	2
23	sub-B084S2	2024-08-27	34W2D	36W2D	M	2.20	SIEMENS	2
24	sub-B085S2	2024-10-24	34W5D	41W6D	M	4.00	SIEMENS	2
25	sub-B086S2	2024-10-24	34W5D	41W6D	M	3.80	SIEMENS	2
26	sub-B049S2	2023-09-25	35W4D	38W2D	F	2.50	SIEMENS	1
27	sub-B063S1	2024-03-05	34W4D	40W3D	M	3.20	SIEMENS	1
28	sub-B069S1	2024-05-17	31W0D	40W4D	M	3.00	SIEMENS	1
29	sub-B070S1	2024-05-17	31W0D	40W4D	F	2.73	SIEMENS	1
30	sub-B076S1	2024-07-02	35W5D	38W5D	M	3.00	SIEMENS	1
31	sub-B077S1	2024-07-09	34W0D	39W0D	M	2.00	SIEMENS	1
32	sub-B081S1	2024-08-02	27W5D	36W1D	M	2.70	SIEMENS	1
33	sub-B087S1	2024-10-16	33W5D	38W6D	M	3.50	SIEMENS	1
34	sub-B090S1	2024-11-08	29W3D	38W6D	F	2.90	SIEMENS	1
35	sub-B091S1	2024-11-08	29W3D	38W6D	F	3.30	SIEMENS	1

Table A.3: Term Control Infant Scans. This table displays the full-term control infants. Each entry has only one scan, indicated by "1" in the "Multi-scan" column, as no additional follow-up scans were performed.

No.	Subject	Scan Time	Birth age	Scan age	Sex	Weight	Scanner	Scans
1	sub-B007S1	2021-06-23	39W4D	39W6D	F	1.73	GE	1
2	sub-B011S1	2021-10-28	39W1D	39W3D	F	3.10	GE	1
3	sub-B026S1	2022-09-08	38W2D	38W4D	M	3.28	GE	1
4	sub-B027S1	2022-09-15	40W6D	41W6D	M	3.30	GE	1
5	sub-B028S1	2022-09-22	37W5D	37W6D	M	2.97	GE	1
6	sub-B034S1	2023-05-11	39W0D	40W0D	F	3.10	SIEMENS	1
7	sub-B038S1	2023-07-11	38W5D	41W4D	M	3.70	SIEMENS	1

Continued A.3

No.	Subject	Scan Time	Birth age	Scan age	Sex	Weight	Scanner	Scans
8	sub-B039S1	2023-07-18	39W1D	40W6D	M	4.70	SIEMENS	1
9	sub-B040S1	2023-07-28	39W0D	40W2D	M	3.40	SIEMENS	1
10	sub-B042S1	2023-08-15	41W0D	42W2D	F	3.17	SIEMENS	1
11	sub-B045S1	2023-09-05	40W4D	41W5D	M	3.70	SIEMENS	1
12	sub-B047S1	2023-09-12	39W2D	40W2D	F	3.10	SIEMENS	1
13	sub-B052S1	2023-10-30	40W1D	42W4D	F	3.40	SIEMENS	1
14	sub-B053S1	2023-11-01	39W0D	40W6D	M	3.00	SIEMENS	1
15	sub-B054S1	2023-11-06	38W2D	40W5D	M	3.30	SIEMENS	1
16	sub-B055S1	2023-11-10	38W4D	40W6D	M	2.80	SIEMENS	1
17	sub-B057S1	2023-12-27	40W1D	44W1D	M	3.60	SIEMENS	1
18	sub-B058S1	2024-01-24	39W2D	40W4D	M	3.45	SIEMENS	1
19	sub-B061S1	2024-02-14	40W0D	40W6D	F	3.70	SIEMENS	1
20	sub-B066S1	2024-03-21	39W0D	40W3D	M	2.70	SIEMENS	1
21	sub-B068S1	2024-05-15	39W5D	41W5D	M	3.80	SIEMENS	1

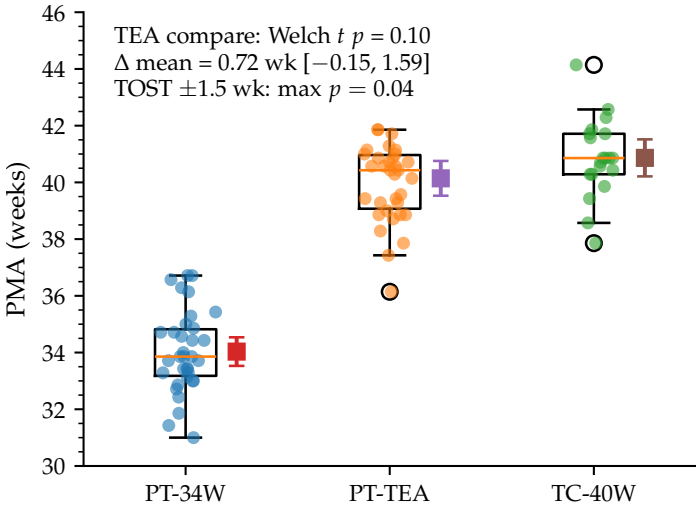

Figure A.1 PMA distributions at PT-34W, PT-TEA, and TC-40W. Box-and-jitter plots of postmenstrual age (PMA) at scan for the three cohorts. Boxes denote median and IQR; dots are individuals; squares indicate group means with 95% CIs. At TEA, PMA did not differ significantly between PT-TEA and TC-40W (Welch's t $p = 0.103$; mean difference 0.72 weeks, 95% CI [−0.15, 1.59]) and met TOST equivalence under ±1.5 weeks (max one-sided $p = 0.0395$). All TEA contrasts in the main analyses include PMA as a covariate (ANCOVA with HC3).

Region of Interest List

Table A.4 List of the 44 merged regions of interest used in this study, obtained by combining left and right hemisphere labels from the 87-label neonatal atlas. IDs correspond to the merged index used throughout the chapter; background labels are excluded.

44 ROIs (IDs 1–22)		**44 ROIs (IDs 23–44)**	
1	Hippocampus	23	Subthalamic nucleus
2	Amygdala	24	Lentiform nucleus
3	Anterior temporal lobe, medial part GM	25	Corpus callosum
4	Anterior temporal lobe, lateral part GM	26	Lateral ventricle
5	Gyri parahippocampalis et ambiens anterior GM	27	Anterior temporal lobe, medial part WM
6	Superior temporal gyrus, middle part GM	28	Anterior temporal lobe, lateral part WM
7	Med/Inf temporal gyri anterior part GM	29	Gyri para. et ambiens anterior part WM
8	Fusiform gyrus anterior part GM	30	Superior temporal gyrus, middle part WM
9	Cerebellum	31	Med/Inf temporal gyri anterior part WM
10	Brainstem	32	Fusiform gyrus anterior part WM
11	Insula GM	33	Insula WM
12	Occipital lobe GM	34	Occipital lobe WM
13	Gyri para. et ambiens posterior GM	35	Gyri para. et ambiens posterior WM
14	Fusiform gyrus posterior part GM	36	Fusiform gyrus posterior part WM
15	Med/Inf temporal gyri posterior part GM	37	Med/Inf temporal gyri posterior part WM
16	Superior temporal gyrus, posterior GM	38	Superior temporal gyrus, posterior WM
17	Cingulate gyrus anterior part GM	39	Cingulate gyrus anterior part WM
18	Cingulate gyrus posterior part GM	40	Cingulate gyrus posterior part WM
19	Frontal lobe GM	41	Frontal lobe WM
20	Parietal lobe GM	42	Parietal lobe WM
21	Caudate nucleus	43	CSF
22	Thalamus (T2 high)	44	Thalamus (T2 low)

Table A.5 System-level regions of interest (ROIs) for microstructural analysis. The complete set includes 15 consolidated ROIs; for the main analyses (14 ROIs), the Ventricles–CSF region was excluded to focus on brain parenchyma. Abbreviations: GM, gray matter; WM, white matter; Hippo-Amyg, hippocampus-amygdala complex; CC, corpus callosum; CSF, cerebrospinal fluid.

15 ROIs (IDs 1–8 long & short names)			**15 ROIs (IDs 9–15 long & short names**		
1	Frontal Lobe GM	Frontal GM	9	Hippocampus–Amygdala Complex	Hippo-Amyg
2	Temporal Lobe GM	Temporal GM	10	Basal Ganglia	Basal Ganglia
3	Parietal Lobe GM	Parietal GM	11	Thalamic Complex	Thalamic
4	Occipital Lobe GM	Occipital GM	12	Cerebellum	Cerebellum
5	Frontal Lobe WM	Frontal WM	13	Brainstem	Brainstem
6	Temporal Lobe WM	Temporal WM	14	Corpus Callosum	CC
7	Parietal Lobe WM	Parietal WM	15	Ventricles–CSF	CSF
8	Occipital Lobe WM	Occipital WM			

Supplemental Figures

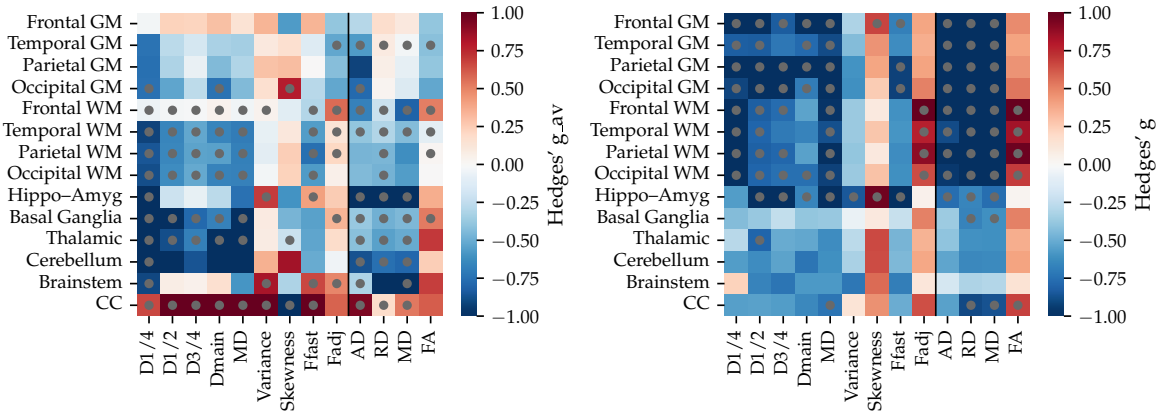

(a) PT-34W → PT-TEA (14-ROIs, vol-adj.) (b) PT-TEA vs. TC-40W (14-ROIs, vol-adj.)

Figure A.2 Whole-brain overview (14 ROIs): microstructural maturation summarized by Hedges' g (volume-adjusted). Panels and conventions as in Fig. 6.2. Models additionally include centered ROI volume as a covariate; dots reflect $p-$values from the volume-adjusted models and BH–FDR control within panel and family (across 14 rows, $q < 0.05$). Color scale and clipping as in Fig. 6.2.

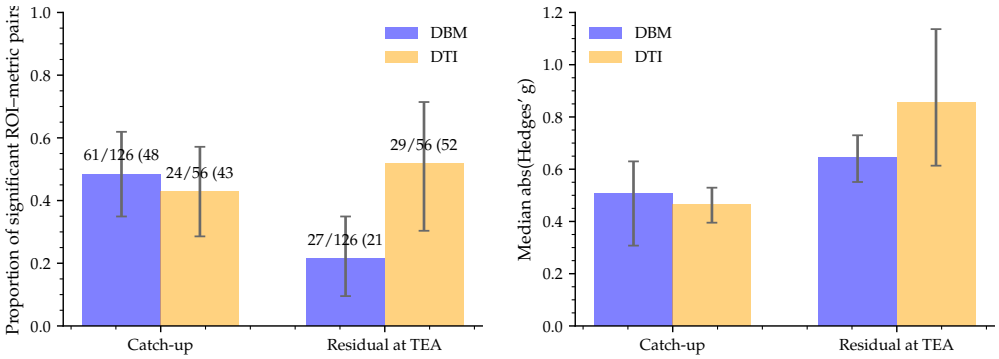

(a) Proportion of FDR-significant (b) median absolute Hedges' g

Figure A.3 DBM versus DTI sensitivity to catch-up and residual gaps (with 95% CIs, CSF included). (a) Bars show the proportion of FDR-significant ROI–metric pairs within family (DBM or DTI) for the two contrasts: Catch-up (PT-34W → PT-TEA) and Residual at TEA (PT-TEA versus TC-40W). Numbers above bars indicate significant/total pairs and the percentage. Error bars are 95% CIs from ROI-cluster bootstrap (2,000 resamples). (b) Bars show the median absolute Hedges' g across ROI–metric pairs with 95% bootstrap CIs; catch-up uses g_{av} for PT-TEA-PT-34W, TEA residual uses g for TC-40W versus PT-TEA. BH–FDR is applied within family across all ROIs × metrics (8 lobar + 6 subcortical/midline); longitudinal models use mixed-effects without PMA due to collinearity with timepoint.

Table A.6 PMA-associated growth rates in absolute ROI volumes within preterm infants. Slopes (% change per week) come from a mixed-effects model on log-volume, $y = \log V \sim \mathrm{PMA}_c + (1|\mathrm{subj})$. p: p-value; q: BH–FDR across the 14 ROIs.

ROI	Slope (%/week)	95% CI (%/week)	p(PMA)	q(PMA)	Sig. (q<.05)
Lobar GM + WM					
Frontal GM	13.9	11.7–16.1	$2.48e{-39}$	$1.28e{-38}$	Yes
Frontal WM	5.6	4.0– 7.2	$2.13e{-12}$	$7.47e{-12}$	Yes
Temporal GM	13.3	8.0–18.9	$2.74e{-07}$	$4.80e{-07}$	Yes
Temporal WM	6.0	3.4– 8.7	$4.77e{-06}$	$6.67e{-06}$	Yes
Parietal GM	14.0	13.0–14.9	$8.96e{-201}$	$1.25e{-199}$	Yes
Parietal WM	5.3	3.4– 7.3	$5.18e{-08}$	$1.04e{-07}$	Yes
Occipital GM	9.3	6.3–12.3	$3.42e{-10}$	$7.98e{-10}$	Yes
Occipital WM	-0.1	-3.0– 2.8	0.941	0.941	No
Subcortical + midline					
Thalamic	8.4	5.0–11.9	$5.89e{-07}$	$9.16e{-07}$	Yes
Basal Ganglia	7.4	5.2– 9.5	$4.04e{-12}$	$1.13e{-11}$	Yes
Hippo–Amyg	10.1	1.7–19.1	0.0169	0.0216	Yes
CC	5.3	-4.5–16.2	0.300	0.323	No
Brainstem	9.3	0.9–18.4	0.029	0.034	Yes
Cerebellum	14.8	12.4–17.2	$2.75e{-39}$	$1.28e{-38}$	Yes

Table A.7 PMA-associated growth rates in **relative** ROI volumes (proportion of ICV) within preterm infants. Slopes come from a mixed-effects model on log-proportion, $y = \log(V/\mathrm{ICV}) \sim \mathrm{PMA}_c + (1|\mathrm{subj})$, and can be read as % change per week *relative to whole-brain growth.* p is the coefficient p-value; q is BH–FDR across the 14 ROIs in this table.

ROI	Slope (%/week)	95% CI (%/week)	p(PMA)	q(PMA)	Sig. (q<.05)
Lobar GM + WM					
Frontal GM	4.69	4.15– 5.24	$1.53e{-67}$	$2.14e{-66}$	Yes
Frontal WM	-2.96	-3.56– -2.36	$7.94e{-22}$	$3.71e{-21}$	Yes
Temporal GM	4.21	0.85– 7.68	$1.36e{-02}$	$2.12e{-02}$	Yes
Temporal WM	-2.50	-3.47– -1.53	$5.41e{-07}$	$1.08e{-06}$	Yes
Parietal GM	4.57	3.53– 5.63	$2.27e{-18}$	$7.94e{-18}$	Yes
Parietal WM	-3.15	-3.62– -2.68	$3.96e{-38}$	$2.77e{-37}$	Yes
Occipital GM	0.33	-2.21– 2.93	0.803	0.803	No
Occipital WM	-8.21	-10.37– -6.00	$1.81e{-12}$	$5.06e{-12}$	Yes
Subcortical + midline					
Thalamic	-0.29	-2.00– 1.45	0.744	0.803	No
Basal Ganglia	-1.25	-1.87– -0.62	$1.05e{-04}$	$1.83e{-04}$	Yes
Hippo–Amyg	1.97	-5.79–10.37	0.629	0.800	No
CC	-2.54	-11.48– 7.31	0.601	0.800	No
Brainstem	1.27	-6.56– 9.75	0.759	0.803	No
Cerebellum	5.32	3.76– 6.90	$9.82e{-12}$	$2.29e{-11}$	Yes

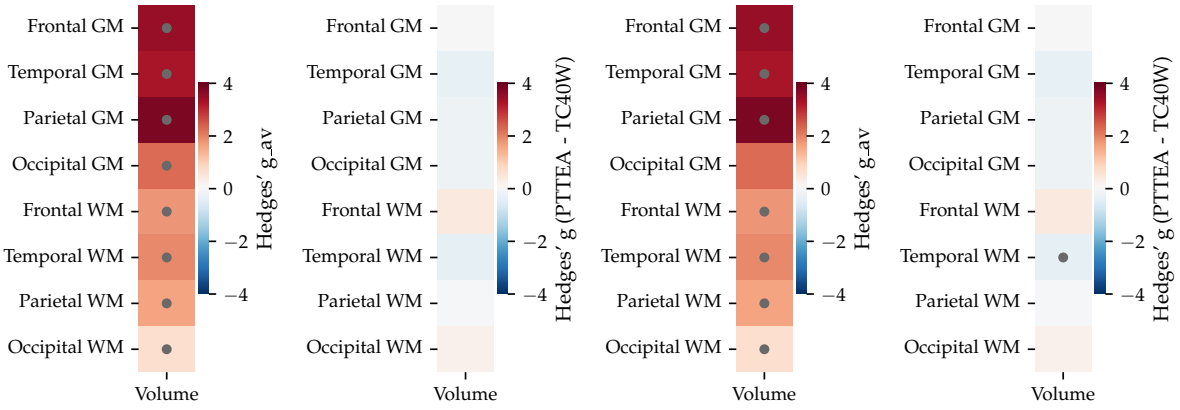

(a) PT-34W → PT-TEA (b) PT-TEA vs. TC-40W (c) PT-34W → PT-TEA (d) PT-TEA vs. TC-40W

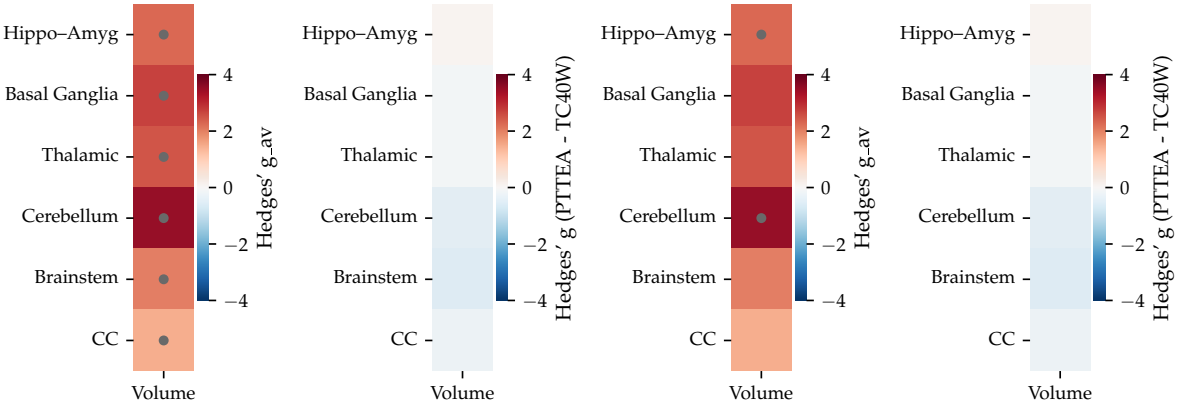

(e) PT-34W → PT-TEA (f) PT-TEA vs. TC-40W (g) PT-34W → PT-TEA (h) PT-TEA vs. TC-40W

Figure A.4 Regional volumes: catch-up and residual gap with PMA adjustment (absolute and proportional to ICV). Top row: lobar cortical GM with adjacent WM. Bottom row: subcortical nuclei and midline structures. Columns: (a,e) Absolute volumes—within-preterm catch-up (PT-34W → PT-TEA). (b,f) Absolute volumes—residual gap at TEA (PT-TEA vs. TC-40W). (c,g) Proportional volumes V/ICV—within-preterm catch-up. (d,h) Proportional volumes V/ICV—residual gap at TEA. Effect size shows in color (Hedges' g_{av} for PT-34W → PT-TEA and g for TC-40W versus PT-TEA), red/blue = higher/lower in the second group of each contrast, gray dots = significant after BH–FDR ($q < 0.05$) within each subpanel across its ROIs.

APPENDIX B ADDITIONAL MATERIAL: STUDY OF NEONATAL PUNCTATE WHITE MATTER LESIONS

PWML infant list

Table B.1 PWML infants and their paired healthy controls (optic radiation). Rows are sorted by lesion subtype (wet first), ages are in weeks (GA). Subtypes: wet = fast-water elevated by DBM; dry = no fast-water elevation.

	PWML infants					Paired control infants			
No.	**Subject**	**Session**	**Age**	**Birth age**	**Type**	**Subject**	**Session**	**Age**	**Birth age**
1	00723XX14	211900	31.43	30.14	wet	00284BN13	90801	32.29	30.71
2	00135BN12	44704	35.00	34.14	wet	00563XX11	153900	35.29	34.71
3	00571AN11	159101	35.29	34.86	wet	00563XX11	153900	35.29	34.71
4	00418BN14	125300	36.86	36.00	wet	00281AN10	90400	36.86	36.14
5	00853XX12	7330	42.14	41.29	wet	00117XX10	38200	42.14	41.57
6	00255XX08	84400	42.29	42.14	wet	00433XX13	132000	42.43	42.14
7	00418BN14	130300	39.57	36.00	wet	00771XX13	17710	39.71	35.57
8	00103XX04	35300	40.14	40.00	wet	00067XX10	20200	40.14	40.00
9	00723XX14	211900	31.43	30.14	wet	00284BN13	90801	32.29	30.71
10	00231XX09	77701	37.00	36.29	wet	00132XX09	44400	37.00	36.57
11	00723XX14	224100	39.29	30.14	dry	00830XX14	30710	39.57	30.43
12	00547XX20	157300	39.00	38.71	dry	00313XX08	100000	39.14	38.86
13	00695XX20	202600	39.57	36.86	dry	00418AN14	130200	39.57	36.00
14	00116XX09	38001	39.43	39.29	dry	00080XX07	30300	39.43	39.29
15	00301XX04	113001	40.00	28.71	dry	00121XX06	41700	40.14	28.14
16	00231XX09	77701	37.00	36.29	dry	00132XX09	44400	37.00	36.57
17	00517XX14	145000	36.29	35.14	dry	00492AN15	140900	36.57	35.14
18	00688XX21	199500	37.43	37.00	dry	00308XX11	98900	37.43	37.29
19	00688XX21	205500	41.57	37.00	dry	00332XX11	105700	41.57	39.00
20	00395XX17	121300	35.71	31.29	dry	00361XX07	111700	35.57	32.29

Figures for PWML examples

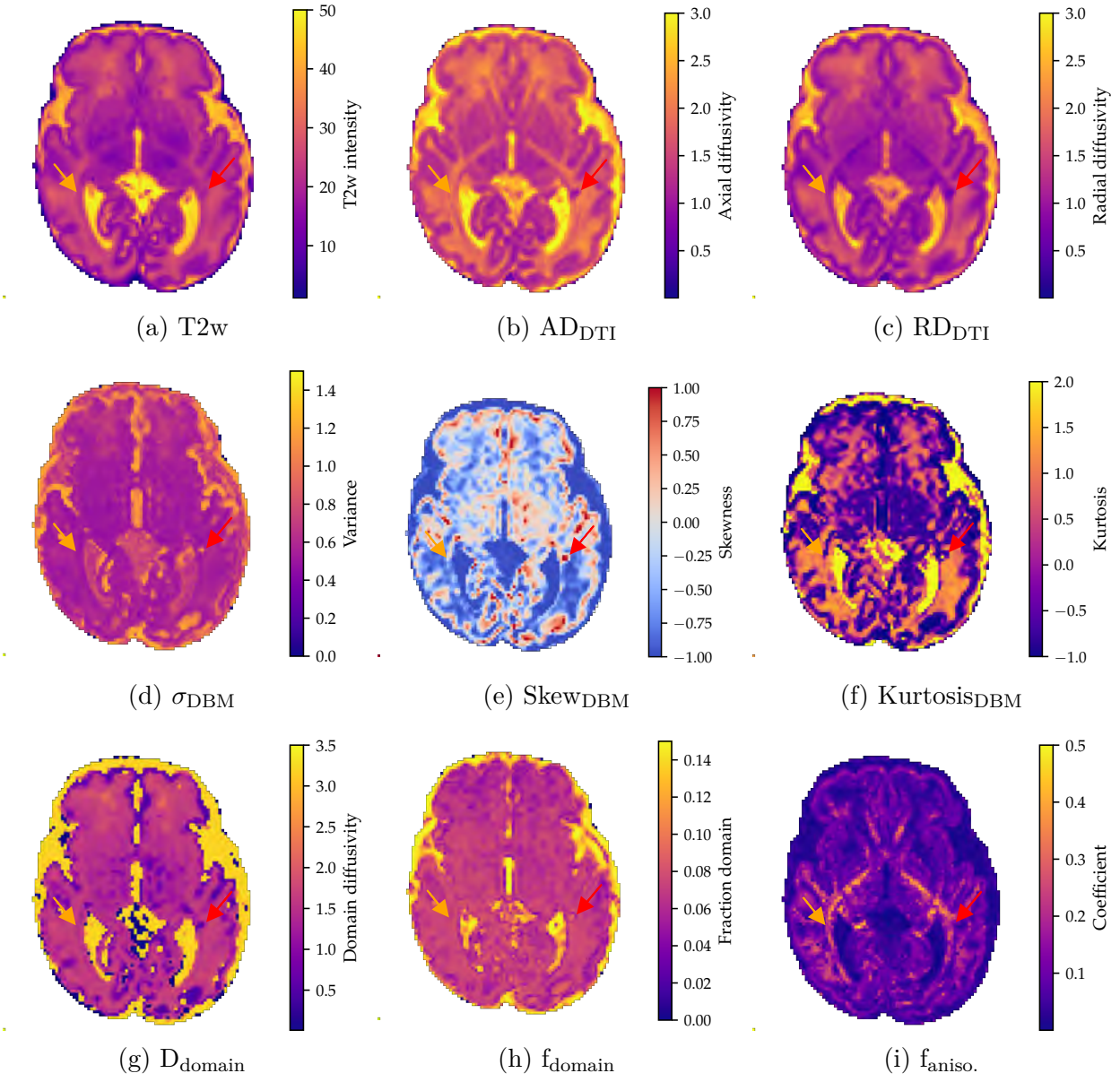

(a) T2w (b) AD_{DTI} (c) RD_{DTI}

(d) σ_{DBM} (e) $Skew_{DBM}$ (f) $Kurtosis_{DBM}$

(g) D_{domain} (h) f_{domain} (i) $f_{aniso.}$

Figure B.1 Wet-type punctate white-matter lesion: multi-parametric DBM assessment (subject ses-44704). (a) Axial T2-weighted reference image with the PWML highlighted (red arrow). (b) Axial diffusivity (AD_{DTI}) and (c) radial diffusivity (RD_{DTI}) from the conventional DTI model illustrate reduced axial and elevated radial diffusion within the lesion. (d) DBM isotropic-spectrum width, σ_{DBM}, demonstrates local broadening of the diffusion spectrum. (e) Spectrum skewness and (f) kurtosis maps further characterise the distribution's asymmetry and peakedness, respectively. (g) Dominant diffusivity d_{domain} pinpoints the most probable isotropic diffusivity in each voxel, while (h) isotropic volume fraction f_{domain} estimates the relative contribution of free-water–like diffusion. (i) Anisotropic fraction $f_{aniso.}$ maps the proportion of directionally constrained diffusion. Together, these parametric maps reveal the combined effects of vasogenic oedema and microstructural disruption that define the wet-type PWML phenotype.

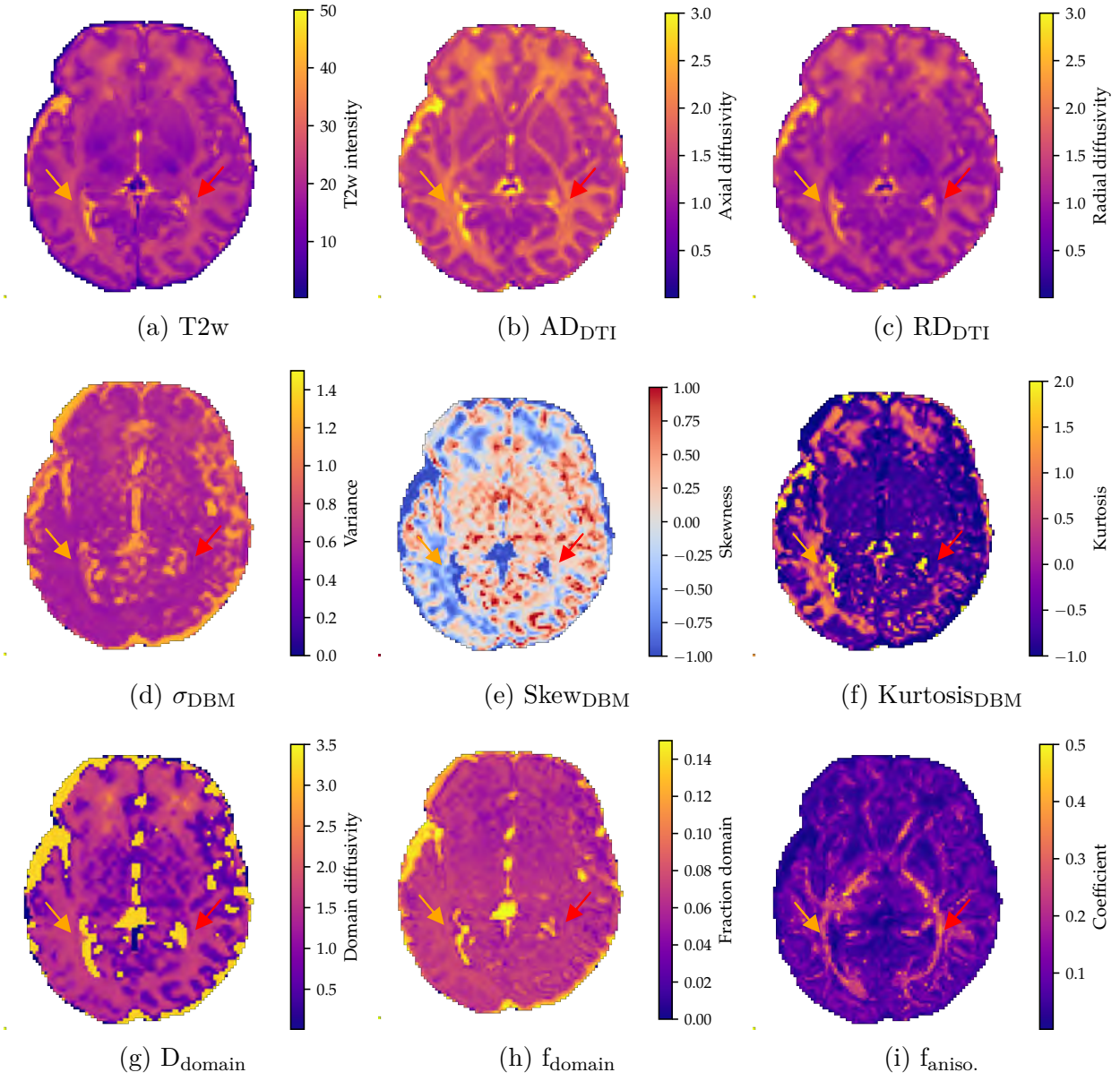

(a) T2w (b) AD_{DTI} (c) RD_{DTI}

(d) σ_{DBM} (e) $Skew_{DBM}$ (f) $Kurtosis_{DBM}$

(g) D_{domain} (h) f_{domain} (i) $f_{aniso.}$

Figure B.2 ry-type punctate white-matter lesion: multi-parametric DBM assessment (subject ses-38001). (a) Axial T2-weighted reference slice with the optic-radiation PWML indicated (red arrow). (b) Axial diffusivity (AD_{DTI}) and (c) radial diffusivity (RD_{DTI}) show a mild decrease in AD and RD relative to the contralateral tract, consistent with restricted but non-cystic tissue change. (d) DBM isotropic-spectrum width, σ_{DBM}, reveals non-apparent broadening of the diffusion spectrum, while (e) spectrum skewness and (f) kurtosis maps indicate subtle asymmetry and flattening—markers of heterogenous, cell-rich microstructure. (g) Dominant diffusivity d_{domain} shifts toward lower values, reflecting a global leftward displacement of the spectrum. Crucially, (h) isotropic volume fraction f_{domain} remains low, indicating minimal free-water content, and (i) anisotropic fraction $f_{aniso.}$ is no apparent reduction, suggesting preserved axonal organization. Together, these parametric maps depict a lesion dominated by chronic cellular remodeling with limited vasogenic oedema, the hallmark of the dry-type PWML phenotype.

APPENDIX C ADDITIONAL FIGURES FOR SEGMENTATION STUDY

Per-class Dice coefficients of dHCP and CHUSJ data test

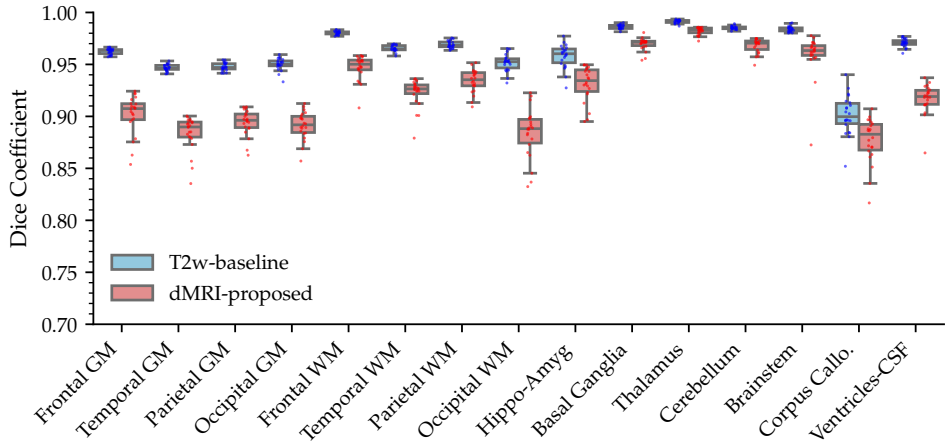

Figure C.1 Per-class Dice coefficients for 14 aggregated regions – internal dHCP test set. Horizontal bars are sorted in descending order of the T2-weighted Dice. Green and red dotted lines mark Dice = 0.90 and Dice = 0.80, respectively. All T2w scores exceed 0.90; the diffusion model also exceeds 0.90 in 10/14 regions and remains ≥ 0.87 elsewhere (corpus callosum). The thalamus is the best-segmented structure (T2w 0.99, dMRI 0.98); the corpus callosum is the most challenging (T2w 0.90, dMRI 0.87).

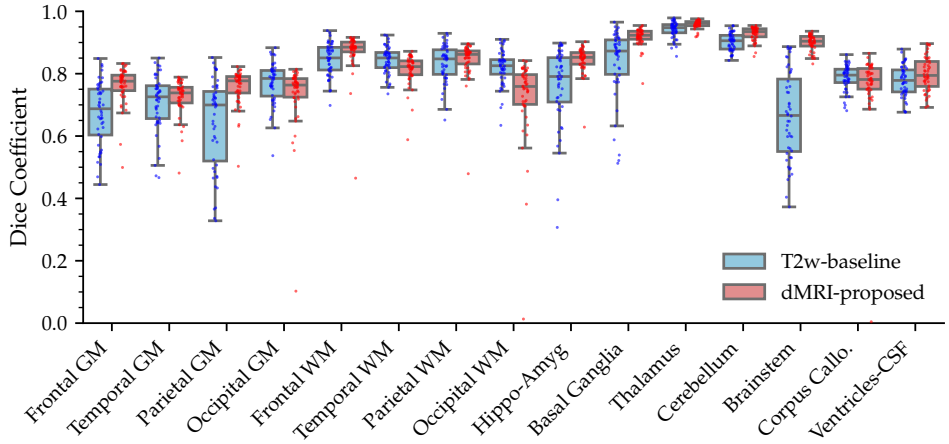

Figure C.2 Per-class Dice coefficients for the same 14 regions – external CHUSJ test set. Bars appear in the same anatomical order as Fig. 5.1 to facilitate comparison. The vendor shift lowers accuracy for both models, pushing several T2w classes below the 0.90 threshold. By contrast, the diffusion-based model retains$\geq$ 0.80 Dice in every region and surpasses the structural baseline in hippocampus + amygdala, brain-stem, cerebellum, deep GM and CSF.

APPENDIX D PUBLICATIONS DURING PHD STUDY

Journal Publications

[1] Diffusion Bubble Model: A novel MRI approach for detection and subtyping of neonatal punctate white matter lesions *Neuroimage* 2025, 317: 121324
Zhang, Erjun and De Leener, Benjamin and Lodygensky, Gregory A

[2] Severe central nervous system demyelination in Sanfilippo disease *Front. Mol. Neurosci.* 2023, 16: 1323449
Taherzadeh, Mahsa and Zhang, Erjun and Londono, Irene and De Leener, Benjamin and Wang, Sophie and Cooper, Jonathan D and Kennedy, Timothy E and Morales, Carlos R and Chen, Zesheng and Lodygensky, Gregory A and Pshezhetsky, Alexey V

[3] Non-invasive in vivo MRI detects long-term microstructural brain alterations related to learning and memory impairments in a model of inflammation-induced white matter injury *Behav. Brain Res.* 2022, 428: 113884
Pierre, Wyston C and Zhang, Erjun and Londono, Irène and De Leener, Benjamin and Lesage, Frédéric and Lodygensky, Gregory A

Conference Publications

[1] Diffusion Bubble Model: A Novel Method For Detecting Neuroinflammation in Mouse Brain With Sanfilippo Syndrome *ISMRM* 2023, Toronto, Canada
Zhang, Erjun and Londono, Irene and Fouquet, Jérémie and Pshezhetsky, Alexey and De Leener, Benjamin and Lodygensky, Gregory

[2] T1w/T2w Ratio Improves Detection of Neonatal Punctate White Matter Lesions *CNPRM / DOHaD / ENRICH / CAMCCO* 2025, Toronto, Canada
Zhang EJ, Emadoye J, Xu K, Ton That H, De Leener B., Lodygensky G.

[3] A Novel Method For Evaluation of Neonatal Brain Development *10th CNPRM* 2023, Montebello, Canada
Zhang EJ, Emadoye J, Xu K, Ton That H, De Leener B., Lodygensky G.

[4] Major White Matter and Hippocampal Alterations in a Mouse Model of Sanfilippo Syndrome at 7T MRI *OHBM* 2023, Montreal, Canada
Zhang EJ, Taherzadeh M, Londono I, Fouquet J, DeLeener B, Pshezhetsky A, Lodygensky G.

[5] Impacts of Prematurity on Neonatal Deep Gray Matter Using Diffusion Basis Spectrum Imaging *OHBM* 2023, Montreal, Canada

Zhang EJ, Londono I, Paquette N, Deschenes S, Petitpas L, Damien J, Pinchefsky E, Gallagher A, DeLeener B, Lodygensky

[6] Evaluation Of Neonatal Brain White Matter Development Using Diffusion Basis Spectrum Imaging *PAS* 2023, Washington, D.C., USA
Zhang EJ, DeLeener B, Lodygensky G.

[7] Severe Neuronal Demyelination in Sanfilippo Disease *WORLDSymposium* 2023, Orlando, USA.
Taherzadeh M, Zhang EJ, Kennedy, T, Morales CR, Lodygensky G, Pshezhetsky A

[8] Assessment of White Matter Maturation in Preterm Infants Using Diffusion Basis Spectrum Imaging *CNPRM* 2022, Canada
Zhang EJ, Song SK, Deschenes S, Enguix V, Paquette N, Petitpas L, Damien J, Fondrouge K, Pinchefsky E, Gallagher A, DeLeener B, Lodygensky G.

[9] Assessment Of White Matter Maturation In Preterm Infants Using DBSI *CPRME* 2022, Montreal, Canada
Zhang EJ, Song SK, Deschenes S, Enguix V, Paquette N, Petitpas L, Damien J, Fondrouge K, Pinchefsky E, Gallagher A, DeLeener B, Lodygensky G.

[10] An Assessment of the Development and Maturation of Neonatal Brain Tissues Using Diffusion MRI *91e Congrès de l'Acfas* 2024, Ottawa, Canada
Xu K, Hernandez S, Zhang EJ (mentor), Lodygensky G.

[11] Characterizing Neonatal PWMLs: A Cohort Study from the dHCP *92e Congrès de l'Acfas* 2025, Quebec, Canada
Emadoye J, Ton That H, Xu K, Zhang EJ (mentor), Nadeau H, Cox S, Lodygensky G., De Leener B.